

FINAL REPORT

Analysis of Petroleum Systems on the Scotian Slope Using Thermal and Seismic Techniques

Start Date: 9 August 2007

Reporting Period: 1 July 2009 to 31 July 2010

Name and Affiliation of Recipient

**Keith Loudon
Department of Oceanography
Dalhousie University**

Date of Report: 16 August 2010

2. Summary Year 3

Historical Background. Petroleum systems models of rifted continental margins are widely used by industry to predict the general pressure and temperature conditions suitable for hydrocarbon generation and storage within sediment layers during their geological formation. These calculations depend on numerous assumptions concerning the thermal properties of the sediment and basement layers and the model boundary conditions (e.g. input of heat over time from the crust). Significant variations of temperature over time can additionally be caused by mobile salt layers due to its high thermal conductivity. The models require the interpretation of seismic data to define the various sediment layers as a function of distance and depth across the margin. The seismic data are also analyzed to determine the physical properties of layers that are likely targets of petroleum accumulation. Testing of the model predictions normally requires observations from deep boreholes which is very expensive or impractical for ultra deep water targets on the continental slope. The purpose of this project is to reexamine such models and explore alternative methods for verifying their predictions.

General Objectives. The approach of this project is to produce new petroleum systems and high resolution seismic velocity models along several transects across the central and NE sectors of the Scotian slope. Ground-truth from existing wells on the upper slope will be used as benchmarks. New marine heat flow observations and better definition of deeper structures on recent seismic depth sections will place important new constraints on the model parameters. Each transect uses recent high quality pre-stack migrated seismic profiles, which have greatly improved the definition of the salt and sub-salt structures relative to earlier profiles. An important goal is that all data and models will be published and thus available for any future industry initiatives.

Summary of Results. (a) Measurements of present-day sea-floor heat flow have been taken on three transects across the Scotian margin. Values reduce slightly from approximately 43 mW/m² in the ultra deep-water basin to 38 mW/m² on the upper slope. These values are approximately 10-15 mW/m² lower than predicted by earlier models. Values in the offshore region are uniform along the margin. These observations agree with standard pure-shear rifting models. (b) Large positive anomalies in heat flow are observed over salt structures, both diapiric and tabular, with values up to 73 mW/m². In general, the observations agree with predictions of higher heat flow in the models due to the high conductivity associated with salt. However, structures in general have higher observed than predicted values and some structures indicated significant second-order fluctuations on the edges of the diapiric structure. (c) Revised 2D petroleum systems models indicate that all conceptual reservoirs may contain more oil than previously estimated, especially those within the late Jurassic and early Cretaceous. Preliminary 3D models give similar results, indicating that 2D models are sufficient to define the primary petroleum maturation potential of the margin. (d) Travel-time and waveform tomography have been implemented for the 9-km-offset pre-stack seismic reflection data across the Torbrook well site. Results indicate that refraction tomography significantly improves the long-wavelength velocity model of sediment structures down to a depth of approximately 2.5 km. The velocity images show higher-frequency variations that define complex laterally-varying velocity contrasts for the major reflection boundaries. Deeper structures require a combined analysis of both MCS and OBS datasets.

3. Objectives of Project:

The work is focused on constraining thermal and petroleum systems models for two deep to ultra-deep water regions of the Nova Scotia slope. The results will lead to a better understanding of the nature of basement and salt structures and their effect on petroleum maturation, and will provide groundwork for seismic characterization of sedimentary physical properties for improved definition of petroleum reservoirs. In particular:

- New heat flow observations and petroleum systems models will be undertaken on 4-6 seismic profiles to study regions surrounding salt structure and a recently-imaged zone of early rifting sediments. The researchers will contrast results from two sub-regions of the margin: one with expected lower heat flow and autochthonous salt structures (diapirs), and the other with expected higher heat flow that is dominated by allochthonous salt structures (salt canopies).
- Analysis of seismic reflection data, recently collected by GXT using a 9-km-long, 360 channel streamer, together with new multi-component ocean bottom seismometer data. The researchers will use advanced travel-time and waveform modeling techniques for enhanced imaging and resolution of physical properties that are important for assessment of potential reservoirs. They will contract structures at two well sites: Torbrook C-15 well (without reservoir) and the Annapolis G-24 well (with reservoir)

4. Description of Progress

(A) Results of heat flow survey (*see Appendix A*).

- Processing of the heat flow data taken in 2008 has been finalized by Eric Negulic as part of his MSc thesis. His thesis will be defended in October 2010. Presentations of his work were made at the GeoCanada 2010 Conference and at the Nova Scotia Energy Research & Development Forum in May 2010 where he was awarded a prize for best geoscience and engineering student award.
- Heat flow values reduce slightly from approximately 43 mW/m² in the ultra deep-water basin to 38 mW/m² on the upper slope. These values are approximately 10-15 mW/m² lower than predicted by our previous petroleum systems models. Values in the offshore region are uniform along the margin.
- Large positive anomalies in heat flow are observed over salt structures, both diapiric and tabular, with values up to 73 mW/m². In general, the observations agree with predictions of higher heat flow in the models due to the high conductivity associated with salt. However, most structures have higher than predicted values and one prominent structure on Profile 88-1A indicated significant second-order fluctuations on the edges of the diapiric structure.
- A request to NSERC for additional ship time on CCGS HUDSON in 2009 to complete the heat flow survey and take new refraction profiles was submitted in September 2009. The proposal was successful. However, subsequent application to DFO for ship time on the CCGS HUDSON was not granted. We have since been able to find a private vessel to

do the refraction profiles but this vessel does not have necessary heavy winch and wire capability to do the heat flow measurements.

(B) Revised Petroleum Systems Models (*see Appendix B*)

- Revised 2-D petroleum systems models were conducted at IES (Aachen, Germany) between May and December 2009. A specific goal was to determine if lower basal heat flow in agreement with our surface measurements will reduce the maturation level and over pressures of the potential lower Jurassic source rocks, thereby enhancing their future resource potential. Preliminary to this work, seismic stratigraphic horizons were revised for profiles GXT Line 1400 and Lithoprobe Line 88-1A. and new horizons were picked for GXT Line 1600. The horizons included revised salt horizons based on salt tectonic studies of C. MacDonald and C. Campbell as part of their M.Sc. theses.
- Results of the new models yield reservoirs that contain more oil than previously estimated, especially for sedimentary units within the late Jurassic and early Cretaceous. The comparative mass balance of hydrocarbons illustrate that: (a) the seismic line 88-1a has the highest amount of hydrocarbons generated and expelled from four deeper source rocks, and accumulated in the Upper Jurassic and Triassic reservoirs; (b) the seismic line 88-1a accumulated at least five times more hydrocarbons in various reservoirs compared to lines NOVSPAN 1400 and NOVSPAN 1600; and (c) the main HC accumulations in lines 88-1a and NOVSPAN 1600 (in lower saturations) are concentrated in the late Triassic, late Jurassic, and early Cretaceous reservoirs while the main accumulation is restricted to the late Jurassic reservoir in the line NOVSPAN 1400.
- A final 3-D petroleum systems model will be made by Eric Negulic for the region of the central slope along the Lithoprobe 88-1A seismic line as a final part of his thesis. In preparation for this work, existing TGS profiles in the region were digitized from paper records of data that became available through the CNSOPB. We had requested digital data from TGS but this request was denied. A primary objective of this final study will be to use basement temperature models determined from extensional models consistent with the heat flow data, and to model the temperature (and heat flow) anomalies related to the salt structures.

(C) Processing and analysis of pre-stack seismic reflection data along GXT Lines 5100 and 1400 across Torbrook C15 well site (*see Appendix C and D*).

- Programs for modeling of travel-time tomography and full waveform tomography have been implemented. Program modification was required for the MCS geometry to allow the travel-time tomography code to work when direct waves occur as first arrivals.
- Analyses were performed on GXT NovaSpan Lines 5100 and 1400 across the Torbrook C-15 well site using the long-offset pre-stack seismic reflection data. Results indicate that refraction tomography improves the long-wavelength velocity model of sediment structures down to a depth of approximately 2.5 km. The velocity images show higher-frequency variations that define complex laterally-varying velocity contrasts for the major reflection boundaries. Results have been submitted for publication in Geophysics.
- Analysis of refracted arrivals with longer offsets from coincident ocean bottom seismometer (OBS) data will be required to constrain deeper velocity structures, such as

those at the Annapolis G-24 well. Preliminary modelling results on OBS data across the Torbrook well indicate that such data must be densely sampled (including both shots and receivers) but also include arrivals from very long offsets. The only OBS data that exists on the Nova Scotia margin which satisfies these criteria were collected recently on the NovaSPAN profile 2000. We have received the OBS data as part of a Play Fairway Analysis Plate Tectonic Special Project. We are in process of refining the original data processing to improve the receiver-shot geometry that our work shows is critical to successful inversions. We have requested the pre-stack MCS data from ION//GX in order to conduct inversions using both MCS and OBS data along the profile.

5. Dissemination and Technology Transfer

European Geophysical Union, Annual Meeting, Vienna, Austria, May 2-7, 2010.

-- Delescluse, M., Loudon, K.E., and Nedimović, M.R., Waveform Tomography Applied to Long Streamer MCS Data from the Scotian Slope.

GeoCanada 2010 Conference, Calgary, AB, May 4-8, 2010.

-- Negulic, E., Loudon, K.E., Mukhopadhyay, P.K., Wielens, H. and Nedimović, M.R., Thermal Modelling of the Central Scotian Slope, Offshore Nova Scotia: The Effects of Salt on Heat Flow and Implications for Hydrocarbon Maturation

Nova Scotia Energy Research & Development Forum, Halifax, NS, May 26-27, 2010

-- Loudon, K., Mosher, D., Pre-Piper, G., and MacMulin, S., Academic Panel on Geosciences
-- Negulic, E., Loudon, K.E., Mukhopadhyay, P.K., Wielens, H., and Nedimović, M.R., Thermal models of the central Scotian Slope and the effects of salt on heat flow. (*best geoscience & engineering student award*)
-- Delescluse, M., M.R. Nedimović, K.E. Loudon, Waveform Tomography Applied To Long Streamer MCS Data from the Scotian Slope

Central & North Atlantic Conjugate Margins Conference, Lisbon, Portugal, 29 Sept to 1 Oct 2010

-- Negulic, E., Loudon, K.E., Wielens, H., Mukhopadhyay, P.K., and Nedimović, M.R., Thermal modelling of the central Scotian Slope, offshore Eastern Canada: Seafloor heat flow data, hydrocarbon maturation potential and the effects of salt on heat flow.
-- Delescluse, M., Nedimović, M.R., and Loudon, K.E., Waveform tomography applied to long streamer MCS data from the Scotian Slope, offshore Eastern Canada.

6. Publications

Delescluse, M., Nedimovic, M., and Loudon, K., 2010. 2D Waveform Tomography Applied to Long Streamer MCS Data from the Scotian Slope, Geophysics, submitted 12-Jul-2010.

Negulic, E., Louden, K.E., Mukhopadhyay, P.K., Wielens, H. and Nedimović, M.R., 2010. Thermal Modelling of the Central Scotian Slope, Offshore Nova Scotia: The Effects of Salt on Heat Flow and Implications for Hydrocarbon Maturation, GeoCanada 2010 Meeting, May 4-8, extended abstract.

7. Additional Funding Secured

Pengrowth Petroleum Innovation Grant to Eric Negulic for 2-yr MSc fellowship (2008-9 and 2009-10) to continue research on Petroleum Systems Models of the Nova Scotia Slope

..... \$15,000

NSERC Ship time for heat flow measurements in 2010 (10 days on CCGS HUDSON)

..... \$212,475

* Partial support from Pengrowth Petroleum Innovation Grant

see Appendix C ## see Appendix A

10. Final Steps

We request that the termination date of the research grant be extended for an additional year. This extension will allow us to use remaining project funds for the following activities:

- 3-D petroleum systems models for the central margin using the heat flow data as constraints on the basement thermal flux will be finalized in September 2010 by Eric Negulic as a last part of his MSc thesis.
- Results of our work will be presented at the Central & North Atlantic Conjugate Margins Conference in Lisbon (29 Sept to 1 Oct 2010). Eric Negulic will present a talk on the thermal modeling and Matthias Delescluse and Mladen Nedimovic will present a poster on the waveform tomography.
- A paper on the heat flow acquisition and processing will be prepared for submission in Oct-Nov 2010.
- We will begin analysis of further seismic data based on results from the seismic inversion techniques and the availability of additional MCS and/or new OBS seismic datasets. New OBS data along MCS NovaSPAN Profile 2000 have been received and are being reprocessed as part of a Play Fairway Analysis Plate Tectonic Special Project. A proposal to ION/GX for access to the pre-stack MCS data along the same profile has been submitted (*see Appendix D*). It is expected that this work will be completed in a follow-up year (2010-2011), using remaining funds for the PDF.

**Excerpt from Eric Negulic's MSc Thesis,
Department of Earth Sciences, Dalhousie University**

Chapter 3: Nova Scotia Margin Heat flow data and simple crustal models

3.1 Introductory Remarks

The focus of this chapter is on the heat flow through the central Scotian Slope. Heat flow is measured in ocean basins using shallow penetrating seafloor heat flow probes. The methodology of seafloor heat flow data acquisition and processing has been discussed in detail by others (e.g. Lister 1979, Hyndman et al. 1979, Villinger and Davis 1979). The general acquisition and processing methodology is presented in Appendix B. In this chapter we introduce the 2008 Hudson heat flow cruise across the central Scotian Slope and present the 47 new seafloor heat flow measurements acquired on the cruise, as well as four unpublished measurements acquired in 2004. We will discuss corrections to the data associated with bottom water temperature (BWT) variations, the effects of sedimentation and high thermal conductivity salt bodies on heat flow. This will allow us to better constrain the basal heat flux of the study area. Corrected seafloor heat flow data will then be compared with predictions from simple crustal rift models to constrain simple lithospheric models across the central Scotian Slope.

The rate of heat loss across the Earth's surface is not laterally uniform. Large variations in crustal heat flow occur between continental and oceanic crust as a result of variations in crustal composition and thickness. In summarizing the global heat flow dataset, Pollack et al. (1993) proposed that the global mean crustal heat flow is $\sim 87 \text{ mWm}^{-2}$, where heat flow through the oceans and continents average $\sim 101 \text{ mWm}^{-2}$ and

$\sim 65 \text{ mWm}^{-2}$ respectively. As oceanic crust is composed primarily of basalt with low concentrations of radioactive elements, the major source of oceanic heat is the cooling of young lithosphere generated at ocean spreading centers upon thinning of the lithosphere during extension (Lister, 1980). The primary source of heat in the thicker continental crust is radiogenic heat produced during the radioactive decay of potassium, uranium and thorium which occur in much greater concentrations in continental than oceanic crust.

3.2 Passive Continental Margin Heat Flow

The specific thermal evolution of rifted passive continental margins results in unique heat flow histories sensitive to the rift style, geometry and amount of initial lithospheric thinning prior to continental breakup. Numerous simple 2D numerical thermal models such as the pure shear model (McKenzie 1978), the dual stretching model (Royden and Keen 1980) and the simple shear model (Wernicke 1981, Wernicke 1985) have been proposed to predict the basement heat flux and subsidence histories across rifted continental margins following the onset of rifting. Each model predicts different seafloor heat flux histories based on the amount of initial lithospheric extension associated with rifting. Brief introductions to these models are included in Appendix F.

The pure shear model assumes instantaneous thinning of the entire lithosphere by a factor β at the onset of rifting. This thinning is accompanied by increased crustal heat flux immediately following rifting, followed by conductive cooling with time returning to original unstretched values as time approaches infinity (McKenzie 1978). Royden and Keen (1980) proposed the addition of a second, lower lithospheric layer, to the pure shear model of McKenzie. This dual stretching pure shear model allows for varying components of upper (β) and lower (δ) lithospheric stretching which will in turn effect

the subsidence and basal heat flux experienced by the margin. Young margins experience significantly increased present day basal heat fluxes due to varying amounts of upper and/or lower lithospheric stretching. However, old margins, such as the Scotian Margin (~200 Ma), yield similar present day heat flux values independent of variations in β and δ due to the extensive period of conductive cooling.

These simple crustal rift models have been applied to the margins of the North Atlantic in attempts to better constrain crustal structure, subsidence histories and heat flow. These models, when coupled with present day seafloor heat flow measurements and seismic interpretations, can be used to further constrain lithospheric models and the margins evolution. Loudon et al. (1991, 1997) coupled pure and simple shear rift models with seafloor heat flow data across the Goban Spur, Galicia Bank and Iberian margins to better constrain lithospheric models for the region. Seafloor heat flow data corrected for sedimentation and basement structure were compared with the predicted present day heat flux values from pure and simple shear rift models with stretching factors constrained by available seismic reflection and refraction data. This same workflow will be followed later in this chapter to better constrain lithospheric models across the Scotian Slope, and to determine the basal heat flux history through time.

3.2.1 Scotian Basin Heat Flow

The Scotian Basin's heat flow is relatively poorly constrained, especially in the deeper water regions of the Scotian Slope (Fig. 3.1). Seafloor heat flow measurements from the deepwater Sohm abyssal plain yield values of 53 mWm^{-2} (Loudon et al. 1989). A recent study by Goutorbe et al. (2007) presented an average heat flow of $47 \pm 07 \text{ mWm}^{-2}$ for the Scotian Basin. The study used bottom hole temperatures for gradient

analysis and a combination of commonly available well logs to determine sediment thermal conductivity. Data from available Scotian Basin wells were used from which average heat flow was determined. The study did not take into account the effects of salt bodies on heat flow, and thus the reported value of $47 \pm 07 \text{ mWm}^{-2}$ may be a slight overestimate of the present day heat flow as many wells target salt flank and salt crest traps, thus, experiencing elevated gradients.

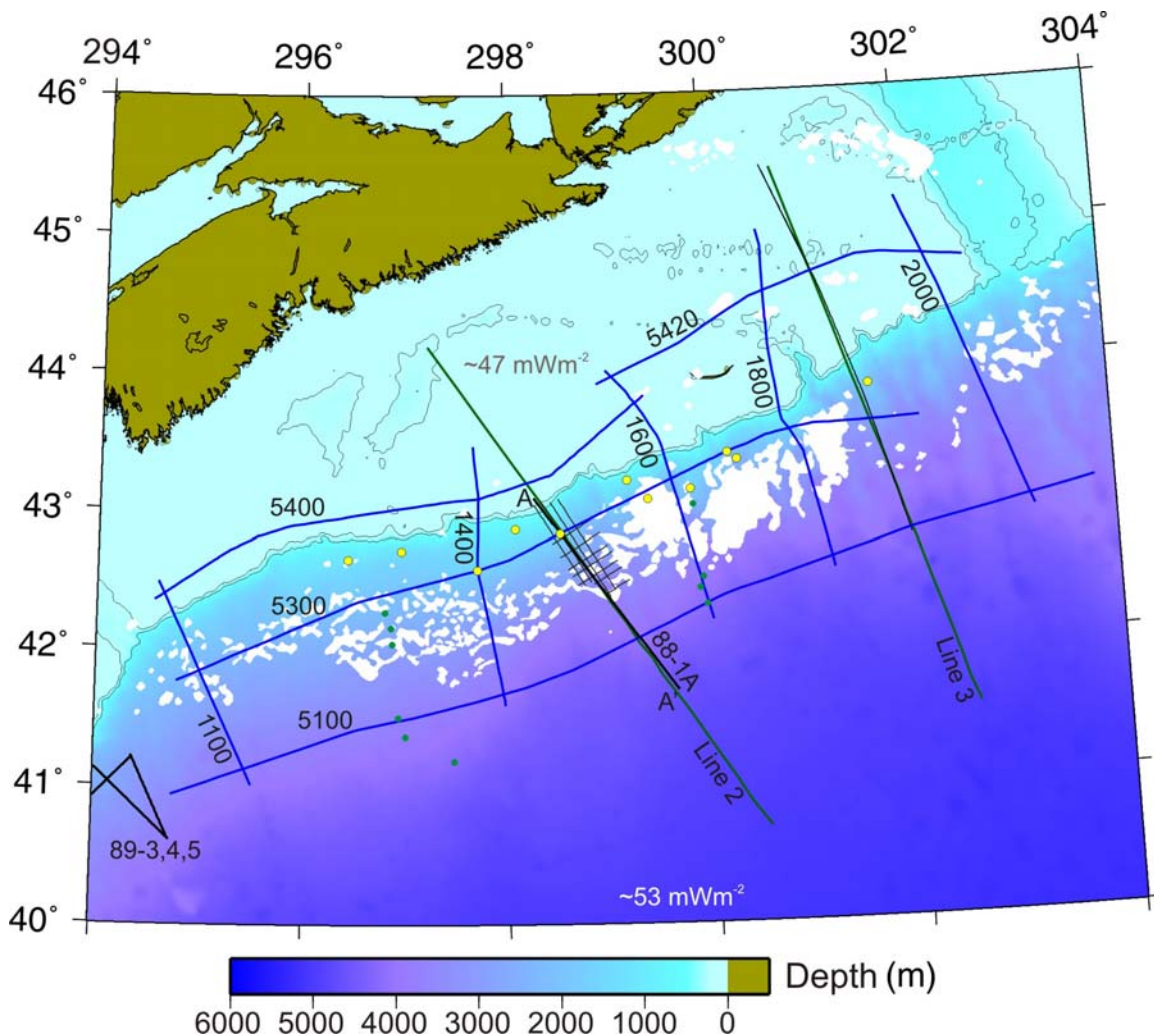


Figure. 3.1: Location map of Scotian basin showing seismic lines of the NovaSPAN survey (blue), Lithoprobe survey (thick black), SMART refraction lines (green) and TGS-Nopec NS-100 (thin grey). Scotian Slope well locations are represented with yellow circles and Lewis and Hyndman heat flow station locations (1976) are shown with green. Background map shows water depth and white represents location of shallow salt after Shimeld (2004). Measured Sohm abyssal plain heat flow is shown in white after Loudon et al. (1989) and Scotian basin average after Goutorbe et al. (2007) is shown in brown.

The only published seafloor heat flow measurements from the Scotian Basin to date are ten measurements reported by Lewis and Hyndman (1976) from two transects across the Scotian Slope (Fig. 3.1). These measurements record a large variability in seafloor heat flow from 24-75 mWm⁻². A mean value of 52 ± 5 mWm⁻² was reported. The variation in measured heat flow has been attributed to the presence of salt diapiric structures underlying the Scotian Slope. Large salt diapirs have a focusing effect as they work as low resistance thermal conduits funneling heat to the seafloor above them, thus resulting in the observed variations. The effects of salt on heat flow are discussed in further detail in Section 3.4.3.

3.3 Hudson 2008 Heat Flow Cruise

The 2008 Hudson heat flow cruise was designed to measure seafloor heat flow across the central Scotian Slope. Seven days of ship time aboard the CCGS Hudson were allotted for the measurement of heat flow from the central Scotian Slope using the 32 thermistor Dalhousie heat flow probe (Appendix B-3). The goal of the cruise was two-fold: determine the regional heat flow trends across the central Scotian Slope, including any along strike or down dip variations in heat flow; and measure the local effects of high thermal conductivity salt bodies on seafloor heat flow. In total 47 successful heat flow measurements were acquired from the Torbrook gas hydrates mound and along the traces of three 2D seismic reflection profiles, NovaSPAN lines 1400 (heat flow transect Line 1) and 1600 (heat flow transect Line 3) and Lithoprobe line 88-1A (heat flow transect Line 2) (Fig. 3.2). We were unable to obtain measurements from all sites due to limited ship time and coarse surface sediments preventing penetration of the probe in certain regions. Of the 47 successful measurements, 7 were located at the Torbrook gas hydrates mound,

18 were taken along Line 1, 13 were taken along Line2, and 9 were taken along Line 3 (Fig. 3.2). The results of the cruise are summarized in Table 3.1, and further data tables for each station are included in Appendix C.

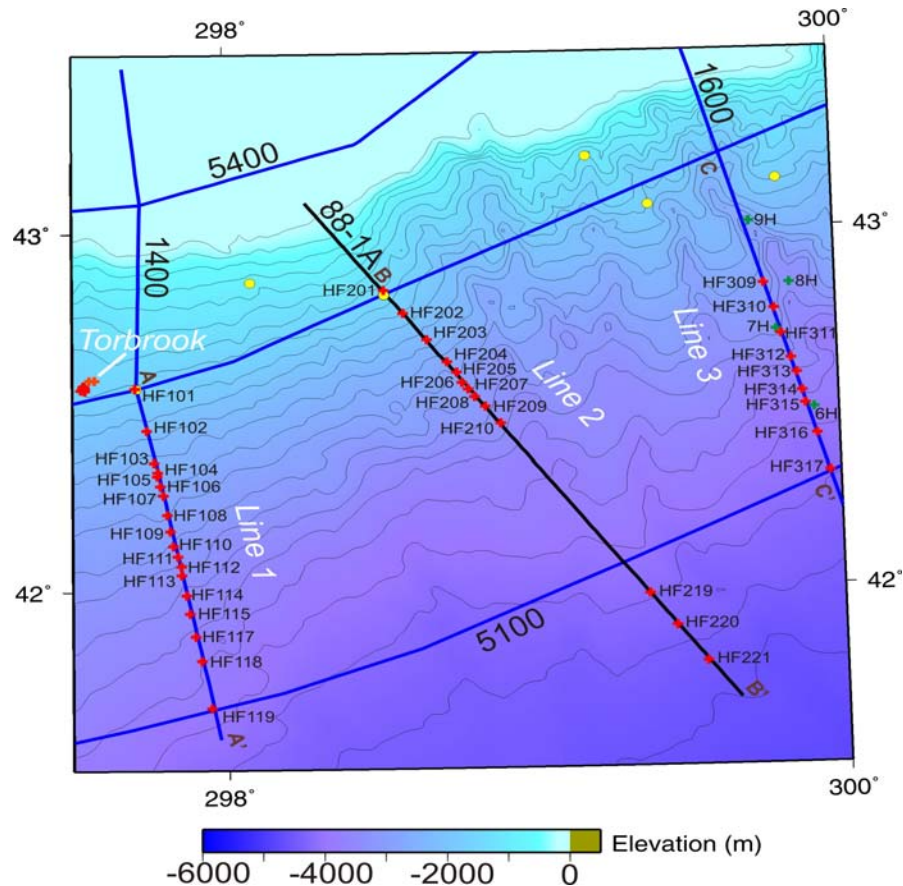


Figure 3.2: Location map of the central Scotian Slope showing 2D seismic lines of the NovaSPAN survey in blue and the Lithoprobe survey in black. Background map shows seafloor topography. Heat flow transects of the Torbrook mound and Lines 1-3 are shown in white text. 2008 heat flow stations are shown as red crosses, 2004 stations as orange crosses, and Lewis and Hyndman stations (1976) are shown as green crosses. Yellow circles represent Scotian Slope well locations and cross sections locations corresponding to figures 3.4-3.6 are shown by brown letters.

3.3.1 Torbrook Results

Seven new seafloor heat flow measurements were acquired at the Torbrook gas hydrates mound in 2008 (Fig. 3.3). Two additional heat flow measurements were acquired from the Torbrook mound on a previous cruise in 2004 and will be compared with the more recent data recorded on the 2008 cruise in order to determine the precision

of conductivity values recorded by the probe between different cruises. Recorded geothermal gradients may vary between cruises if bottom water temperature variations exist; however, sediment thermal conductivity values should remain constant providing a good test for the consistency of the probe.

Station No.	Lat. (N)	Long. (W)	X	Y	Offset (m)	Shot Point	E.S. Depth (m)	CTD Depth (m)	BWT (°C)	No. Temp. Points	Gradient (mK/m)	σ	No. of Cond. Points	Thermal Cond.	σ	Heat Flow (mW/m ²)	σ	Bullard Heat Flow (mW/m ²)	σ	Tilt
<i>Line 1 (1400 profile)</i>																				
HF101	42°34.07	62°17.48	557731.47	4713136.40	100700	3177	1700.00	1672.00	3.74	20	20.29	0.86	20	1.191	0.161	24.18	4.3	23.9	0.8	1.5
HF102	42°26.62	62°15.32	560933.71	4700057.71	114200	2908	2180.00	2140.00	3.31	25	34.2	0.55	25	1.065	0.112	36.43	4.41	34.7	0.6	1.5
HF103	42°21.42	62°13.71	562881.08	4690215.09	124300	2708	2467.00	2438.00	3.10	23	37.63	0.3	23	1.013	0.104	38.12	4.23	37.3	0.4	1
HF104	42°20.07	62°13.29	563876.25	4687289.61	127300	2646	2530.00	2503.00	3.06	23	37.76	0.32	23	1.031	0.053	38.94	2.32	38.1	0.5	1
HF105	42°18.89	62°12.98	563678.13	4686122.53	128500	2626	2616.00	2585.00	3.03	23	45.36	0.24	23	0.999	0.084	45.33	4.04	46.9	0.3	2.5
HF106	42°17.50	62°12.60	564565.41	4683077.27	131700	2563	2685.00	2655.00	2.92	24	39.74	0.43	24	0.941	0.088	37.4	3.9	39.3	0.4	0
HF107	42°16.15	62°12.24	565420.07	4680149.96	134800	2500	2750.00	2726.00	2.88	23	40.72	0.25	23	0.959	0.087	39.04	3.77	40.3	0.2	1
HF108	42°13.00	62°11.40	566488.09	4674153.31	140900	2378	2888.00	2864.00	2.74	24	35.99	0.19	24	0.983	0.091	35.39	3.48	37.1	0.2	1.5
HF109	42°10.15	62°10.65	567341.83	4669073.51	146100	2276	3031.00	3009.00	2.61	23	39.32	0.44	23	1.007	0.058	39.61	2.74	39.4	0.3	1.5
HF110	42°07.45	62°09.93	568113.59	4664439.62	150900	2182	3095.00	3075.00	2.55	22	45.02	0.46	22	0.945	0.052	42.53	2.79	43.3	0.4	1.5
HF111	42°05.61	62°09.38	569409.65	4661258.96	154300	2114	3191.00	3167.00	2.40	28	64.05	0.24	28	0.966	0.092	61.88	6.11	65.7	0.5	0
HF112	42°04.19	62°09.03	570250.24	4658122.33	157600	2050	3301.00	3253.00	2.40	22	51.99	0.33	22	1.047	0.129	54.41	7.04	54.9	0.3	2
HF113	42°02.51	62°08.61	570317.60	4655408.38	160300	1995	3370.00	3345.00	2.33	26	42.94	0.38	26	0.93	0.12	39.95	5.5	43.1	0.3	1
HF114	41°58.88	62°07.66	571647.14	4649142.90	166800	1868	3475.00	3459.00	2.31	24	43.71	0.28	24	0.964	0.067	42.13	3.22	43.4	0.3	0
HF115	41°55.85	62°06.87	572606.96	4643508.66	172600	1753	3520.00	3503.00	2.30	23	52.63	1.05	23	1.029	0.163	54.19	9.64	56.6	0.5	1
HF117	41°51.93	62°05.80	574221.49	4636377.85	180000	1606	3778.00	3699.00	2.25	22	47.09	0.56	22	1.079	0.082	50.82	4.47	51.7	0.7	1
HF118	41°47.85	62°04.74	575833.58	4628743.21	187800	1451	3789.00	3783.00	2.22	26	41.31	0.46	26	1.054	0.087	43.54	4.09	43.3	0.4	3.5
HF119	41°40.29	62°02.83	578541.73	4614105.16	201700	1178	3910.00	3906.00	2.19	21	44.34	0.64	22	0.987	0.108	43.75	5.4	46	0.7	0.5
<i>Line 2 (88-1a profile)</i>																				
HF201	42°49.75	61°28.46	624265.79	4743901.45	34300	2492	1482.00	1466.00	3.82	19	22.55	1.56	19	1.243	0.145	28.02	5.2	29.1	1.4	2
HF202	42°46.25	61°24.59	629556.52	4736882.50	43100	2602	1890.00	1871.00	3.43	16	30.49	1.88	17	1.187	0.132	36.2	6.25	31.7	1.7	2
HF203	42°42.55	61°20.22	636002.1336	4728696.165	53500	2731	2341	2359	3.16	20	41.48	1.2	20	1.027	0.132	42.61	6.72	43.9	0.7	1
HF204	42°37.68	61°16.32	641390.7036	4721797.612	62200	2841	2671	2652	2.85	13	53.77	2.28	13	0.991	0.243	53.27	15.34	54.7	2	0.5
HF205	42°35.84	61°14.42	643952.2479	4718624.638	66300	2893	2763	2741	2.79	21	56.2	0.61	22	1.114	0.097	62.59	6.13	65.5	0.8	1
HF206	42°34.40	61°13.00	645449.1237	4715442.52	70000	1605	2920	2899	2.76	22	59.76	1.08	22	0.997	0.113	59.61	7.85	61.3	1.1	0
HF207	42°33.32	61°11.91	647061.2141	4713378.41	72600	2970	3010	2995	2.7	22	67.76	0.38	22	1.055	0.074	71.49	5.38	72.8	0.4	1
HF208	42°32.13	61°10.75	648830.8865	4710985.725	75600	3007	3170	3157	2.59	21	57.08	1.11	21	1.041	0.145	59.41	9.44	60.7	1	0.5
HF209	42°30.36	61°09.11	651737.4651	4708062.383	79500	3057	3249	3229	2.49	22	45.78	0.64	22	0.98	0	44.87	0.63	N/A	N/A	1
HF210	42°27.51	61°06.22	655833.0709	4702850.292	86000	3139	3535	3501	2.33	16	45.14	0.8	16	0.922	0.158	41.62	7.89	47.1	1	4
HF219	41°58.54	60°37.64	695968.9103	4650443.79	152000	3964	4180	4184	2.19	23	41.19	0.39	23	1.072	0.093	44.15	4.27	42.6	0.4	2.5
HF220	41°53.29	60°32.54	703388.3668	4640612.751	164500	4120	4337	4344	2.18	22	43.29	0.42	22	1.039	0.054	44.98	2.78	44.5	0.5	0.5
HF221	41°47.24	60°26.66	711751.4859	4629585.37	178200	4292	4464	4470	2.2	20	40.81	0.76	20	0.986	0.154	40.25	7.03	41.1	0.4	2
<i>Line 3 (1600 profile)</i>																				
HF309	42°49.85	60°13.60	726101.8034	4746783.642	150400	2406	2915	2893	2.65	21	45.8	0.59	21	1.043	0.063	47.76	3.52	47	0.4	2
HF310	42°45.70	60°12.05	728958.3947	4739021.285	158700	2242	3085	3066	2.49	19	45.38	0.72	19	1.063	0.043	48.22	2.73	48.3	0.7	0.5
HF311	42°41.52	60°10.51	730914.9098	4731120.244	166800	2077	3256	3240	2.31	19	48.82	0.71	19	1.058	0.041	51.66	2.77	51.4	0.5	2
HF312	42°37.46	60°09.03	733626.4161	4723602.946	174800	1919	3539	3530	2.23	15	39.04	0.64	16	1.075	0.053	41.96	2.77	41.4	0.4	0
HF313	42°34.77	60°08.05	735106.5278	4719050.445	179500	1824	3650	3640	2.21	19	33.82	0.54	19	1.018	0.039	34.44	1.87	34.4	0.4	0
HF314	42°32.15	60°07.08	736643.6373	4713450.953	185300	1708	3785	3780	2.2	17	42.86	0.66	18	1.04	0	44.57	0.69	N/A	N/A	1
HF315	42°30.07	60°06.32	737558.9535	4709570.841	189300	1626	3890	3883	2.2	13	39.7	0.63	13	1.086	0.038	43.11	2.18	43.1	0.5	0
HF316	42°24.60	60°04.31	740639.5733	4700195.174	199200	1429	4065	4061	2.21	19	40.66	0.3	20	1.064	0.054	43.26	2.53	43.1	0.2	0
HF317	42°18.54	60°02.10	744260.9093	4689008.382	211000	1196	4220	4221	2.18	21	41.18	0.61	21	1.01	0.072	41.57	3.59	41.4	0.5	0.5
<i>Torbrook Site</i>																				
HF001	42°33.95	62°27.49					1563	1541	3.71	22	21.78	0.62	22	1.067	0.159	23.24	4.12	20.6	1.2	3
HF002	42°33.80	62°27.45					1567	1550	3.7	25	21.29	0.47	25	1.098	0.116	23.37	2.99	21.5	0.5	2
HF003	42°33.48	62°27.39					1594	N/A	N/A	24	22.25	0.52	24	1.146	0.078	25.49	2.33	24.9	0.3	2
HF004	42°33.54	62°27.84					1590	1572	3.7	24	19.56	0.59	24	1.192	0.15	23.32	3.64	21.9	0.9	3
HF005	42°33.78	62°27.65					1592	1563	3.69	24	22.02	0.31	24	1.132	0.141	24.92	3.45	23.7	0.4	2
HF006	42°33.88	62°27.56					1564	N/A	N/A	25	22.34	0.32	25	1.154	0.118	25.77	2.99	24.2	0.4	2
HF007	42°34.11	62°27.34					1572	1549	3.7	23	22.49	0.46	23	1.093	0.101	24.57	2.77	24.4	0.4	3
<i>2004 Data</i>																				
HYD401	44°34.10	54°51.79					1703	N/A	N/A	8	26.7	0.4	10	1.186	0.054	31.6	1.9	28.9	0.6	4
HYD402	44°33.45	54°52.63					1730	N/A	N/A	10	26.0	0.5	12	1.171	0.070	30.4	2.4	28.2	0.6	6.5
HYD503	42°34.92	62°25.46					1526	1535	3.73	24	31.5	0.4	23	1.143	0.114	36.0	4.1	36.8	0.3	0
HYD504	42°35.30	62°26.44					1545	1544	3.73	22	37.6	0.3	19	1.146	0.100	43.1	4.2	42.3	0.4	1

Table 3.1: Summary table of heat flow data acquired during the July 2008 Hudson heat flow cruise as well as unpublished data from 2004. E.S. = echo sounder, BWT = Bottom Water Temperature.

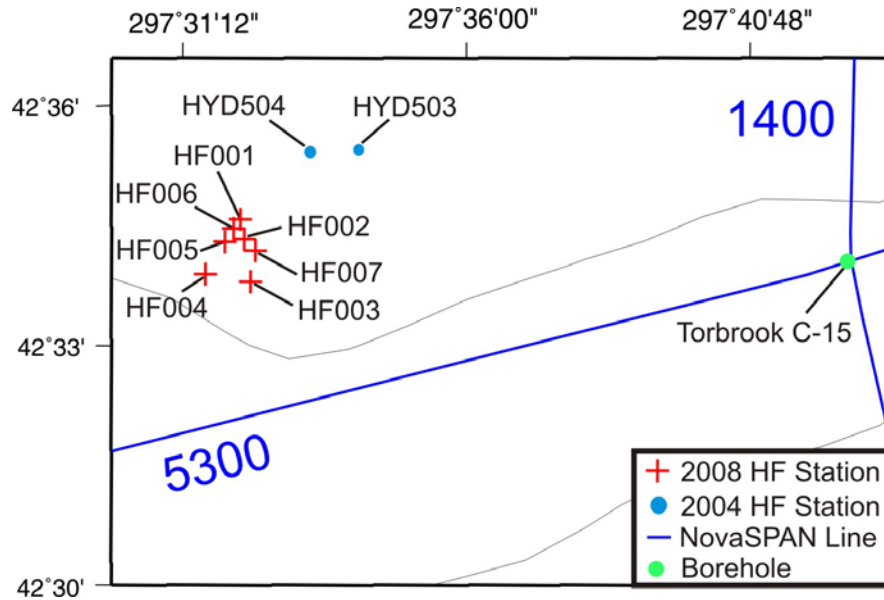


Figure 3.3: Location map showing seafloor heat flow stations recorded in 2008 (red crosses) and 2004 (blue circles).

For all stations, recorded gradients are roughly linear over the length of the probes penetration with the exception of some disturbances of thermistors in the uppermost 2 m resulting in a slight change in gradient (Fig. 3.4). The uppermost 2 m of temperature data are likely effected by penetration of water from above upon penetration of the probe and thus are not included in our gradient calculation. Gradient measurements showed little variation between stations with the exception of a low gradient of $19.6 \pm 0.6 \text{ mK m}^{-1}$ recorded at site HF004. Geothermal gradients varied from $19.6 \pm 0.6 - 22.5 \pm 0.5 \text{ mK m}^{-1}$ with a mean gradient of $21.7 \pm 0.5 \text{ mK m}^{-1}$. Thermal conductivity values ranged from $1.07 \pm 0.16 - 1.19 \pm 0.15 \text{ W m}^{-1} \text{ K}^{-1}$, with a mean conductivity of $1.13 \pm 0.12 \text{ W m}^{-1} \text{ K}^{-1}$. Heat flow values for the Torbrook sites ranged from $20.6 \pm 1.2 - 24.4 \pm 0.4 \text{ mW m}^{-2}$, with a mean heat flow of $23.0 \pm 0.6 \text{ mW m}^{-2}$ for the Torbrook gas hydrates mound. The maximum distance between heat flow sites at the Torbrook mound was $\sim 1000 \text{ m}$, and

with little assumed lateral variation in lithology between sites and consistent measured conductivity and gradient values we can assume that the probe is functioning well.

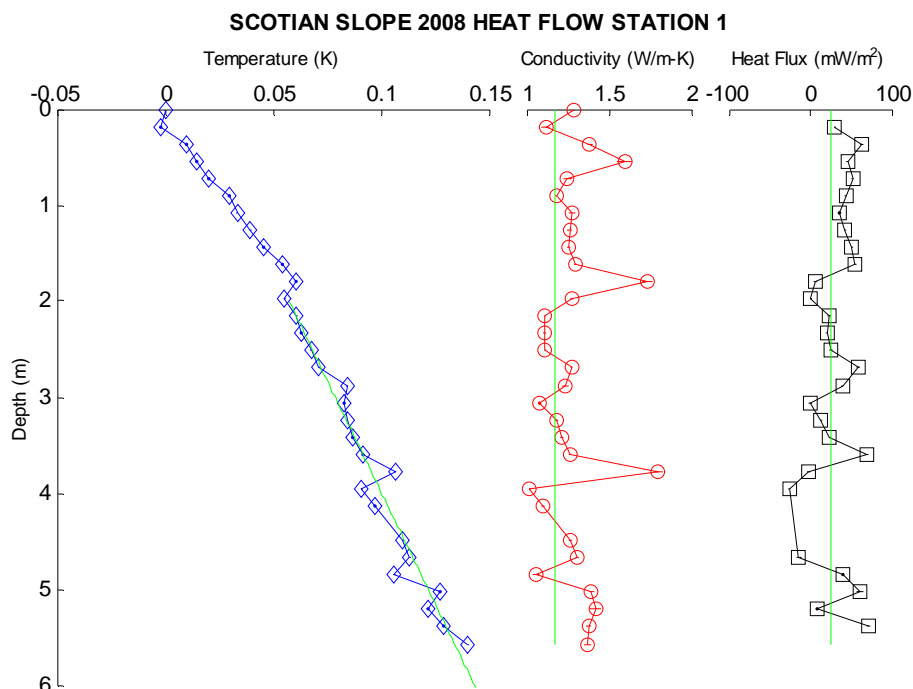


Figure 3.4: Example plot of 2008 Hudson heat flow station showing temperature, conductivity, and heat flux vs. depth plots.

We will also take this opportunity to report the results of two unpublished heat flow measurements acquired from the Torbrook gas hydrates mound in 2004. Measurements were acquired using the Dalhousie heat flow probe following the same method as described in Appendix B. The data have not previously been publicly released and are presented in Table 3.1. Gradients measured for stations HYD503 and HYD504 were $31.5 \pm 0.4 \text{ mK m}^{-1}$ and $37.6 \pm 0.3 \text{ mK m}^{-1}$ respectively, with thermal conductivity values of $1.14 \pm 0.11 \text{ W m}^{-1} \text{ K}^{-1}$ and $1.15 \pm 0.10 \text{ W m}^{-1} \text{ K}^{-1}$. Heat flow values of $36.8 \pm 0.3 \text{ mW m}^{-2}$ and $42.4 \pm 0.4 \text{ mW m}^{-2}$ for stations HYD503 and HYD504 are significantly higher than those recorded at the Torbrook mound on the 2008 cruise due to the notably higher gradients. This suggests that in addition to purely conductive vertical heat transfer

a second mechanism such as convective heat transfer through the upper sediments or varying bottom water temperatures may have effected the measured gradient. Variations in BWT's are investigated in Section 3.4.1.

3.3.2 Line 1 Results

Line 1 resulted in the successful acquisition of 18 of the 19 heat flow measurements planned along the trace of GXT NovaSPAN 2D seismic reflection profile 1400. Station HF116 was skipped to save time. From this line 13 measurements were taken in regions unaffected by salt structures to determine the regional trends across the slope, and 5 measurements were taken above salt bodies to quantify the effects of salt on heat flow (Fig. 3.5).

Measurements in regions unaffected by salt showed a general increase in the seaward direction. Ignoring the abnormally low value of 23.9 mWm^{-2} at station HF101, the background heat flow values in the landward regions of the survey range from $\sim 35\text{-}40 \text{ mWm}^{-2}$, while the more seaward stations show values of $\sim 43\text{-}46 \text{ mWm}^{-2}$. Increased heat flow above salt bodies is evident in the data. The increase in measured heat flow above salt varies from one diapir to another. Values above the most landward diapir (D1) increase by $\sim 8 \text{ mWm}^{-2}$ from the surrounding background values of $\sim 39 \text{ mWm}^{-2}$ to 46.9 mWm^{-2} above the salt body at heat flow station HF105. The small salt body which underlies HF107 does not have a significant effect on seafloor heat flow likely because its increased distance from the seafloor and welded, non-rooted, feeder. Stations HF109 and HF110 are both located above what is interpreted as a deeply buried salt canopy, and similar to station HF107 do not record significantly elevated heat flow values, likely as a result of the depth of salt. Values above the central salt diapir D2 show the

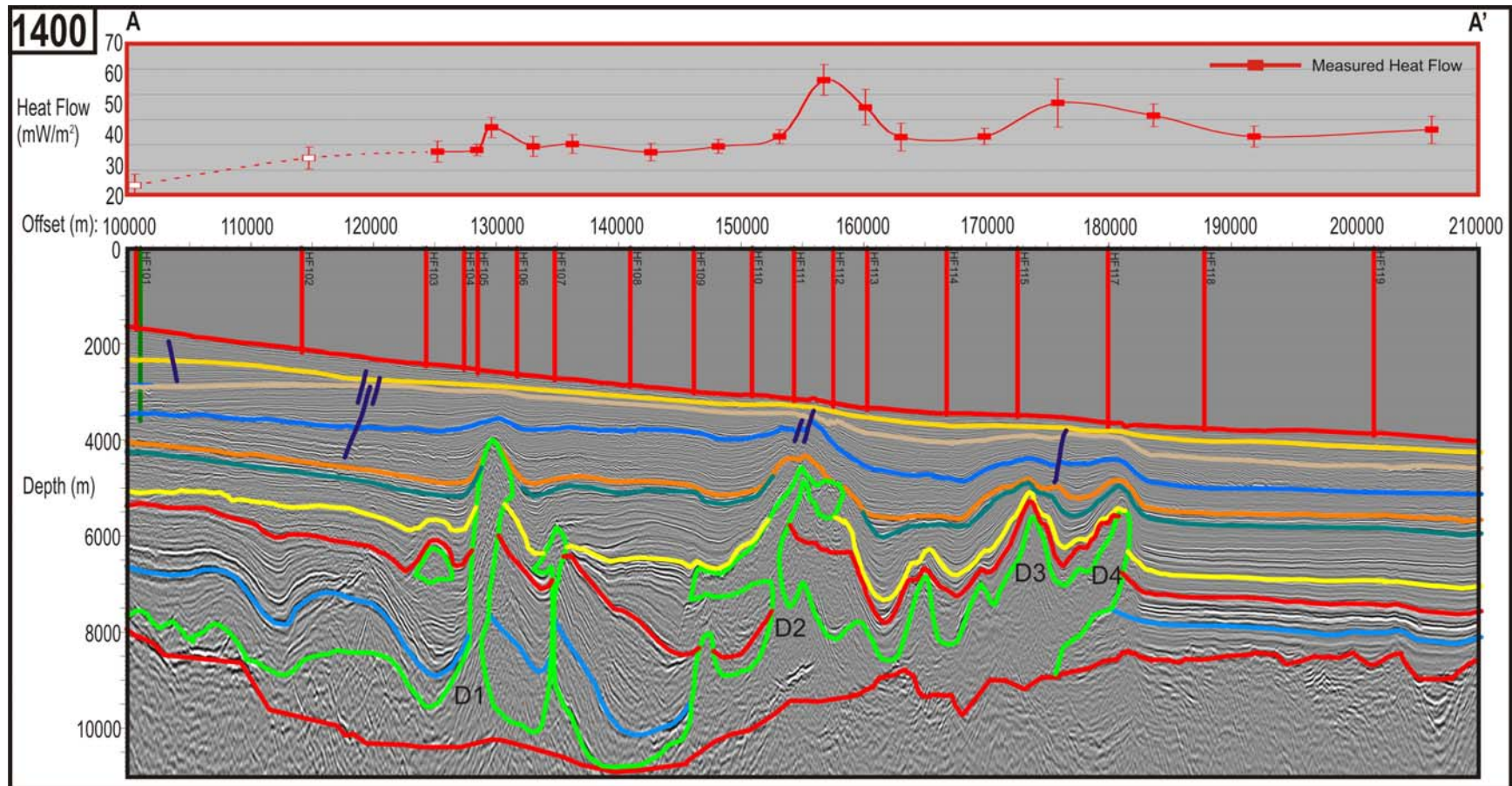


Figure 3.5: Seismic interpretation of NovaSPAN line 1400 from A-A' as shown in Figure 3.3. Colored horizons represent lithological units as shown in Figure 2.???. Vertical red lines show locations of seafloor heat flow measurements, steep blue lines represent faults and the vertical green line represents the Torbrook C-15 well. Above the seismic interpretation is a plot of measured seafloor heat flow in red; hollow boxes are likely erroneous and may be disregarded.

largest increase in heat flow, reaching upwards of 65.7 mWm^{-2} at station HF111, $\sim 23 \text{ mWm}^{-2}$ above the surrounding background values of $\sim 43 \text{ mWm}^{-2}$. This station is located directly above the squeezed feeder and is the second shallowest salt body identified on Line 1400. Station HF112 is located above a shallow salt canopy fed by the attached diapir underlying HF111, thus, recording a high heat flow value of $54.9 \pm 0.3 \text{ mWm}^{-2}$. The most seaward salt bodies show increases of $\sim 8\text{-}13 \text{ mWm}^{-2}$ above the background values of $\sim 43 \text{ mWm}^{-2}$, reaching values of $51.7 \pm 0.7 \text{ mWm}^{-2}$ and $56.6 \pm 0.5 \text{ mWm}^{-2}$ at stations HF115 and HF117 above diapirs D3 and D4 respectively.

It is noted that the largest increase in measured seafloor heat flow does not correspond to the tallest, shallowest diapir (D1). However, as neither station HF105 or HF106 are located directly above the crest of this diapir, they may not have recorded the maximum associated heat flow. Station HF111, located directly above the crest of the second tallest and shallowest salt body (D2), records the highest seafloor heat flow value of heat flow transect Line 1.

3.3.3 Line 2 Results

In total, 13 of the 21 proposed measurements were successfully acquired along heat flow transect Line 2. Successful stations include HF201-210 and HF219-221 (Fig. 3.6); however, station 209 recorded only a measure of gradient, and thus conductivity values were averaged from stations HF210 and HF208 yielding a conductivity value of $0.98 \text{ Wm}^{-1}\text{K}^{-1}$. This value is a low value for conductivity and reflects the anomalously low value of $0.92 \pm 0.16 \text{ Wm}^{-1}\text{K}^{-1}$ recorded at station HF210. Stations HF217 and HF218 were attempted, however problems were encountered in penetrating the seafloor due to the presence of coarse sediments. Stations HF216-211 were skipped as they appeared to

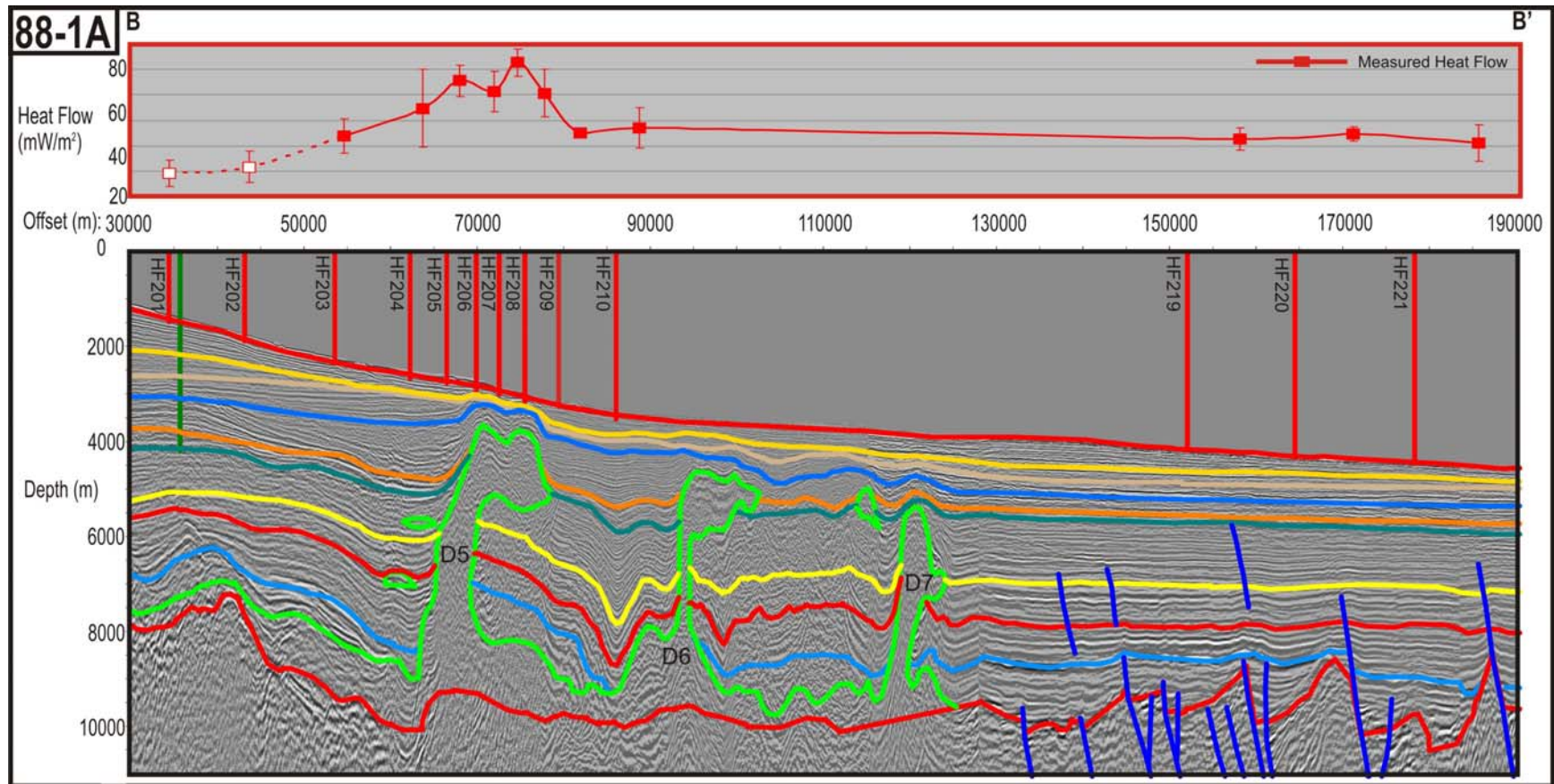


Figure 3.6: Seismic interpretation of Lithoprobe line 88-1a from B-B' as shown in Figure 2.1. Colored horizons represent different lithological units. Vertical red lines show locations of seafloor heat flow measurements, steep blue lines represent faults and the vertical green line represents the Shubenacadie H-100 well. Above the seismic interpretation is a graph showing plots of measured heat flow values in red; hollow boxes are likely erroneous and may be disregarded.

be located in a large channel where accumulations of coarser sediments would make successful penetration of the probe unlikely. Of the 13 measurements acquired across Line 2, four measurements were taken above a salt structure D5, while the rest were taken in regions unaffected by salt.

Similar to Line 1, we see a general increase in heat flow in the seaward direction. In line 2 we record low heat flow values of $\sim 30 \text{ mWm}^{-2}$ at the landward limit of the line increasing to $\sim 43 \text{ mWm}^{-2}$ at the seaward limit similar to Line 1. The low heat flow values at stations HF201 and HF202 are associated with the anomalously low geothermal gradients of $22.6 \pm 1.6 \text{ mK}^{-1}$ and $30.5 \pm 1.2 \text{ mK}^{-1}$ respectively as the corresponding thermal conductivities of $1.24 \pm 0.14 \text{ Wm}^{-1}\text{K}^{-1}$ and $1.19 \pm 0.13 \text{ Wm}^{-1}\text{K}^{-1}$ are actually higher than the mean values of $1.05 \pm 0.13 \text{ Wm}^{-1}\text{K}^{-1}$ for the line. Salt structure D5 has been interpreted as a large, thick, salt canopy fed by a broad vertical feeder. The heat flow spike above D5 is not uniform across the structure. A range of heat flow values from $60.7 \pm 1.0 - 72.8 \pm 0.4 \text{ mWm}^{-2}$ are identified above the salt structure. Little variation in depth to salt in the seismic images coupled with large variations in measured heat flow above the salt diapir suggests that the variations in heat flow above this diapir are not the result of purely conductive heat transfer and that there is likely a second mechanism effecting the measured temperature gradients.

3.3.4 Line 3 Results

Line 3 resulted in the successful acquisition of data from 9 of the 17 planned heat flow stations (Fig. 3.7). Measurements were made at stations HF317-309. Many stations required two penetrations as the jog sensor was not triggered on the first attempt, thus no

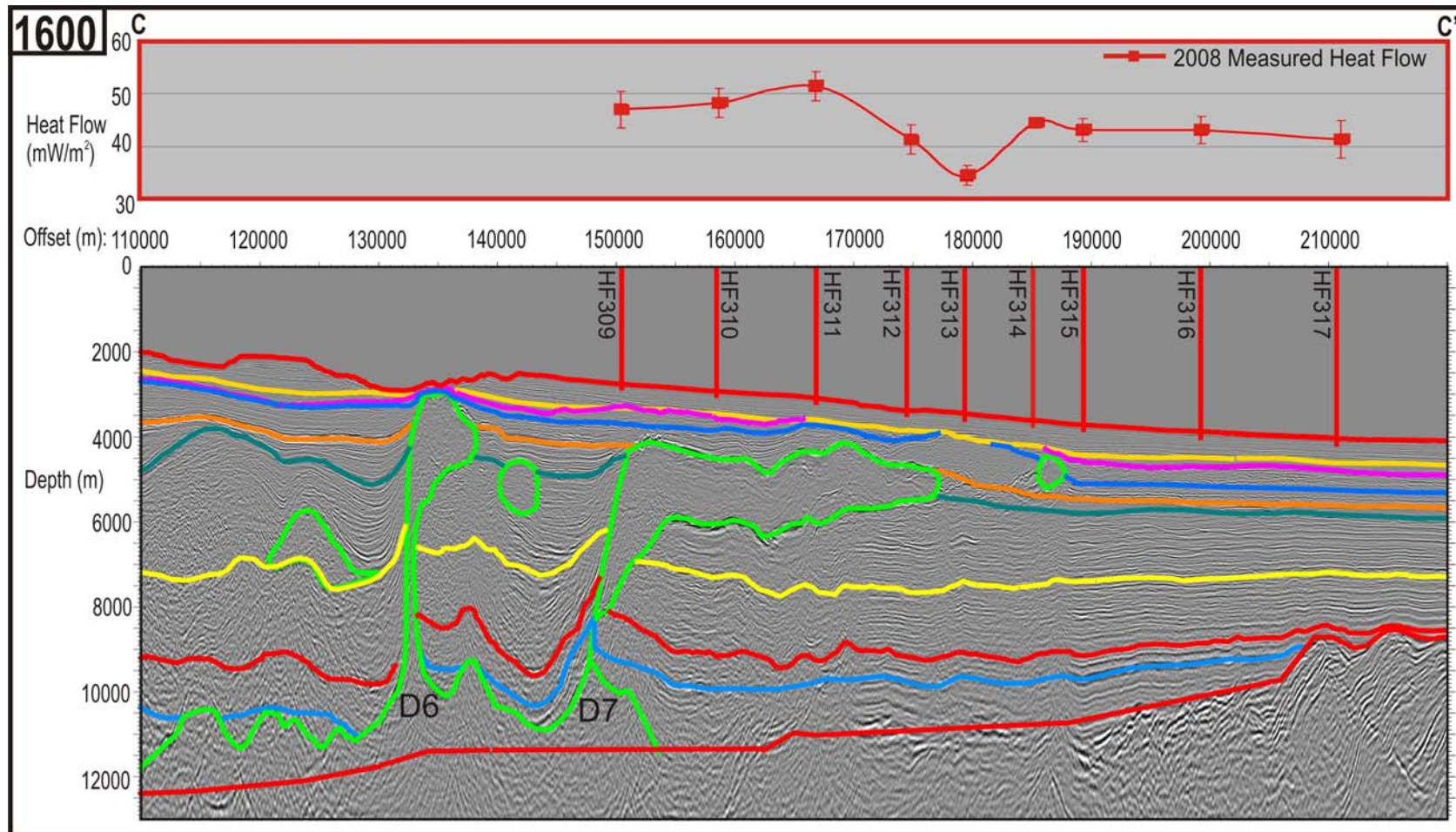


Figure 3.6: Seismic interpretation of NovaSPAN line 1600 from C-C' as shown in Figure 2.1. Colored horizons represent different lithological units. Vertical red lines show locations of seafloor heat flow measurements. Above the seismic interpretation is a graph showing plots of measured heat flow values in red.

heat pulse was released from the central heater wire (Appendix B-3). This gave us the opportunity to check gradient values between penetrations. No significant variations in gradient were recorded between penetrations at the same site (Table 3.2). Little variation in conductivity with depth occurred for any station in this line. Therefore the results of the Bullard heat flow calculations were very similar to the uniform conductivity heat flow calculations (Table 3.1).

Station HF314 had no heat pulse on either attempt, and thus conductivity values for heat flow analysis at this station were taken from surrounding stations HF316 and HF313. Time did not permit completion of the Line 3 heat flow survey; however, multi-beam imaging beneath the more landward portions of this line suggest that the region is cut by a large submarine canyon and thus penetration of the associated coarser seafloor sediments may not have been possible even had time permitted (Fig. 3.8). It is unfortunate we were unable to take measurements from this region as the most landward diapir (D6) penetrates within ~200 m of the seafloor, and is the shallowest diapir seen in the available seismic images. Of the nine measurements acquired, one station is located above a large salt diapir stalk (D7), four are located over a shallow salt canopy, while only three are located in regions unaffected by salt (Fig. 3.7).

Station No.	First Penetration (<i>No Heat Pulse</i>)			Second Penetration (<i>Heat Pulse</i>)		
	No. Temp. Points	Gradient (mK/m)	σ	No. Temp. Points	Gradient (mK/m)	σ
HF317	22	42.4	0.1	21	41.2	0.6
HF316	19	42.2	0.8	19	40.7	0.3
HF313	19	35.1	0.4	19	33.8	0.5
HF312	21	40.3	0.6	15	39.0	0.6
HF311	20	48.9	0.8	19	48.8	0.7
HF310	20	45.8	0.5	19	45.4	0.7
HF309	18	45.1	0.9	21	45.8	0.6

Table 3.2: Comparison between gradients recorded for stations which required multiple penetrations.

Figure 3.8: Multi-beam image of seafloor **Get from Keith or Calvin**

Heat Flow measurements recorded seaward of salt ranged from 41.4 ± 0.5 - $43.1 \pm 0.5 \text{ mWm}^{-2}$ and were in good agreement with measurements from the seaward limits of Lines 1 and 2. Heat flow stations HF309-312 were located above a large diapir/canopy. Stations HF309-311 yielded heat flow values from 47.0 ± 0.4 - $51.4 \pm 0.5 \text{ mWm}^{-2}$, notably higher than those in regions unaffected by salt. Station HF312, located at the seaward tip of the canopy, recorded a low heat flow value of only $41.4 \pm 0.4 \text{ mWm}^{-2}$. Station HF314 recorded a final measurement above salt. It was located above a detached salt canopy. The measured value of $44.6 \pm 0.7 \text{ mWm}^{-2}$ is higher than both the adjacent values at stations HF313 and HF315 which do not overly salt bodies.

The lack of heat flow measurements from the landward regions of Line 3 is problematic in our analysis of regional heat flow trends across the central Scotian Slope as we have no constraints on the landward heat flow for Line 3. According to the trends measured at Lines 1 and 2 we expect that heat flow values will decrease in the landward direction, however, further measurements are required to verify these assumptions. Further landward measurements in regions unaffected by salt would also be useful in assessing the effects of the salt canopies on heat flow. For now we assume that the higher heat flow above the canopies is due to the high thermal conductivity of the salt; however, verifying this requires lower heat flow values be found in the adjacent regions unaffected by salt diapirism/canopies.

3.4 Heat Flow Data Analysis

In order to analyze our seafloor heat flow data in terms of crustal heat flux we must account for the effects of sedimentation, salt, and bottom water temperature

variations on the measured heat flow data. We examine BWT variations using water column temperature data recorded by a CTD probe contained within the Dalhousie heat flow probe, the 6 m of sediment temperature data recorded by the heat flow probe, and temperature gradients determined by Leblanc et al. (2006) from the Torbrook gas hydrates mound (Section 3.4.1). We correct for the effects of sedimentation on seafloor heat flow using the equations of Loudon and Wright (1989) (Section 3.4.2) and the effects of salt on heat flow using simple 2D conductivity based numerical models (Section 3.4.3)

3.4.1 Bottom Water Temperature Variations

To address the possible effects of BWT variations on seafloor heat flow measurements we have compared bottom water temperatures and water column temperature gradient profiles recorded at the Torbrook mound from both the 2004 and 2008 cruises. Water column data were recorded with a Conductivity (salinity)-Temperature-Depth (CTD) probe located within the instrument housing of the Dalhousie heat flow probe. Further plots of water column temperature gradients are included in Appendix D. Temperature data recorded through the water column are used to determine the stability of bottom water gradients and if significant variations exist in BWT between stations and cruises. If bottom water currents exist they may explain the variations in measured near surface geothermal gradients noted between 2004 and 2008 as associated varying BWT can penetrate downward into the near surface sediments. Finally, in addition to the CTD temperature data we will also investigate heat flow at the Torbrook gas hydrates mound using a geothermal gradient sourced from measured seafloor

temperatures and depth to a Bottom Simulating Reflector (BSR) associated with the methane gas hydrates phase boundary after Leblanc et al. (2007).

The CTD probe was employed to record changes in the structure of the water column. The temperature trend recorded through the water column is particularly useful in identifying anomalous temperature variations associated with bottom water currents. As expected, the general trend recorded by the CTD probe shows increasingly stable temperatures and smaller variations in temperature with increasing depth (Fig. 3.9).

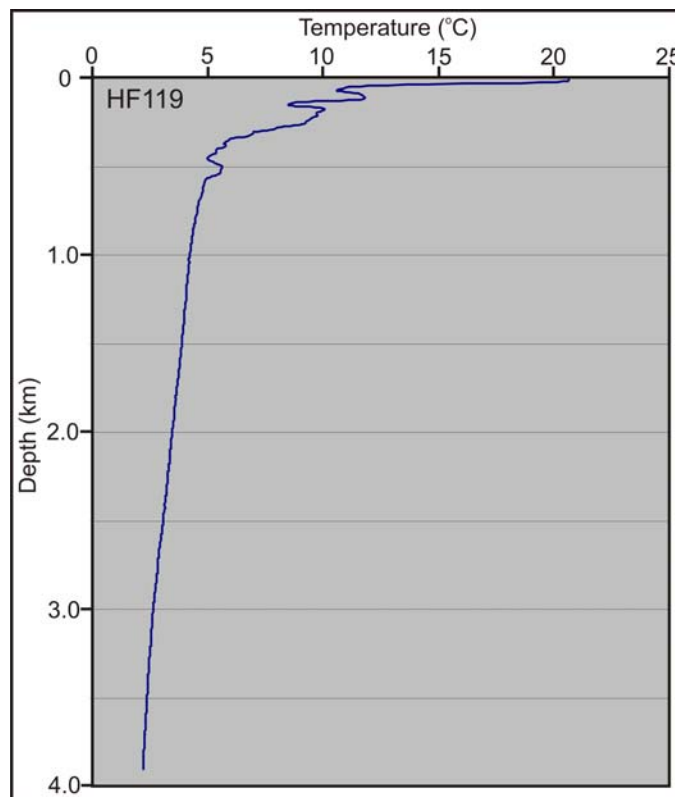


Figure 3.9: Temperature vs. Depth plot showing temperatures recorded by the CTD probe as it descended through the water column.

At shallow depths up to ~700 m water temperatures vary at a daily to seasonal time period induced by surface temperature variations and shallow penetrating currents.

Smaller temperature variations can persist to depths greater than 700 m and may effect near surface sediment temperatures. Appendix D contains temperature vs. depth profiles

for the bottom 600 m of the water column for all heat flow stations with CTD data.

Deeper stations show more stable BWT (Fig. 3.10). Water column temperature gradients become increasingly stable with increasing water depth. Notable increases in water column gradient stability occur below ~2000 m. Very little variation in bottom water temperature gradients occurred at depths greater than ~3300 m (Appendix D).

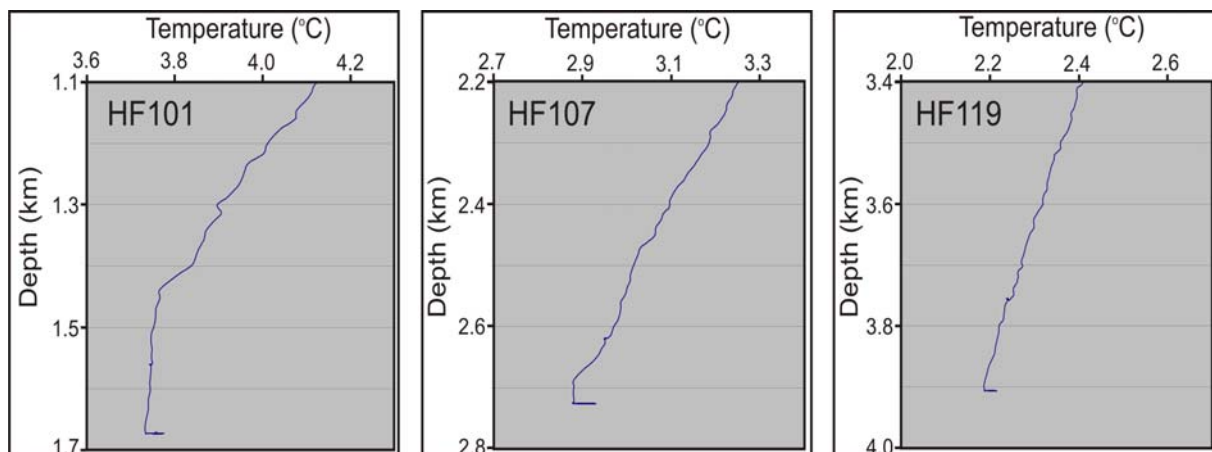


Figure 3.10: Comparison of bottom water temperatures for different heat flow stations along line 1.

As described in Section 3.4.1 and shown in Table 3.1 the mean seafloor heat flow of $23.0 \pm 0.6 \text{ mWm}^{-2}$ from the 2008 Torbrook data were significantly lower than the mean values of $39.6 \pm 0.4 \text{ mWm}^{-2}$ from the 2004 Torbrook data. The mean gradient of $34.5 \pm 0.4 \text{ mKm}^{-1}$ recorded during the 2004 cruise was much higher than the mean gradient of $21.7 \pm 0.5 \text{ mKm}^{-1}$ in 2008. However, this relatively high value is still notably lower than all other gradients ($>37 \text{ mWm}^{-2}$) recorded across the margin with the exception of four other measurements made in shallow water regions near the gas hydrates mound and station HF313 on heat flow transect Line 3. The mean sediment thermal conductivity values of $1.13 \pm 0.12 \text{ Wm}^{-1}\text{K}^{-1}$ in 2008 and $1.14 \pm 0.11 \text{ Wm}^{-1}\text{K}^{-1}$ in 2004 were similar. As thermal conductivity values remained essentially constant it is the change in temperature gradient that was responsible for the significantly lower estimates

of seafloor heat flow in 2008. In order to determine if these changes in gradient were the result of variations in BWT penetrating into the upper sediments we have compared the BWT data from the two cruises.

The CTD data from the 2008 cruise showed greater changes in temperature with depth than the more stable bottom water column temperatures recorded in 2004 (Fig. 3.11). The mean BWT of 3.70 °C recorded in 2008 is only 0.03 °C lower than the mean BWT value of 3.73 °C recorded in 2004. The absolute BWT's are similar between the two cruises; however, non-linearity's observed in the water column temperature gradient for the few hundred meters of seawater above the seafloor suggests bottom water currents may exist (Fig. 3.11).

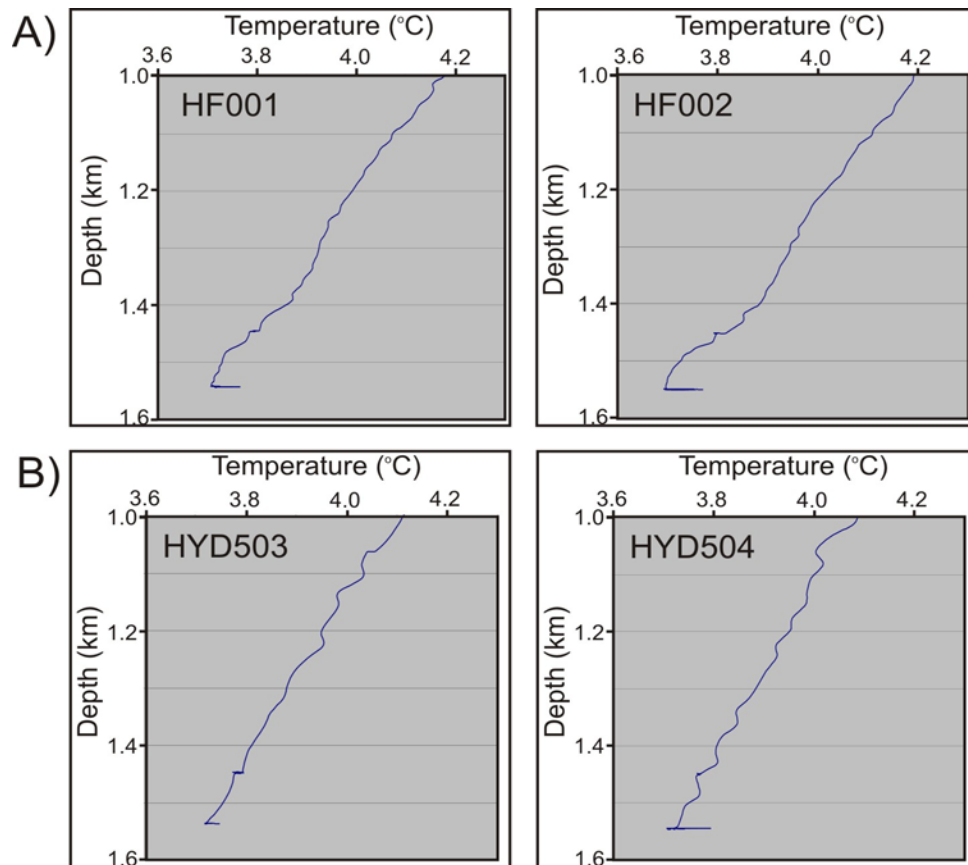


Figure 3.11: Comparison of BWT data from Torbrook mound in A) 2008 and B) 2004.

The effects of seasonal variations in BWT's penetrating downward into the seafloor sediments should be greatest at the surface, decreasing towards the undisturbed sediment temperatures sourced from earth's interior with depth. Therefore, all temperature vs. depth plots for the 6 m of temperature data recorded by the seafloor heat flow probe should converge with depth when plotted from the associated BWT recorded by the CTD probe. Similar geothermal gradients should be experienced at depths beneath the penetration of environmental perturbations. Environmental perturbations due to seasonal or annual BWT variations should not penetrate beneath the uppermost few meters of the sediment column (Louden and Wright 1989). The data recorded by the seafloor heat flow probe for the uppermost 6 m of the sediment column should be found to converge with depth between the 2004 and 2008 cruises if the data are affected by short wavelength seasonal or annual BWT variations. However, this expected convergence is not observed in our data when comparing the temperature vs. depth plots from the 2008 and 2004 cruises (Fig. 3.12).

This suggests that the near surface sediment temperature gradient for both datasets has been effected by deeper penetrating temperature variations extending to depths greater than 6 m. These may be the result of longer wavelength bottom water temperature variations operating at a period longer than the four years we recorded, or possibly an effect of convective fluid flow within the sediments. More data over a longer sample period are required to determine the true cause of the variations in sediment temperatures recorded between the two cruises. From our early analysis we are unable to conclude if BWT are effecting the recorded gradients.

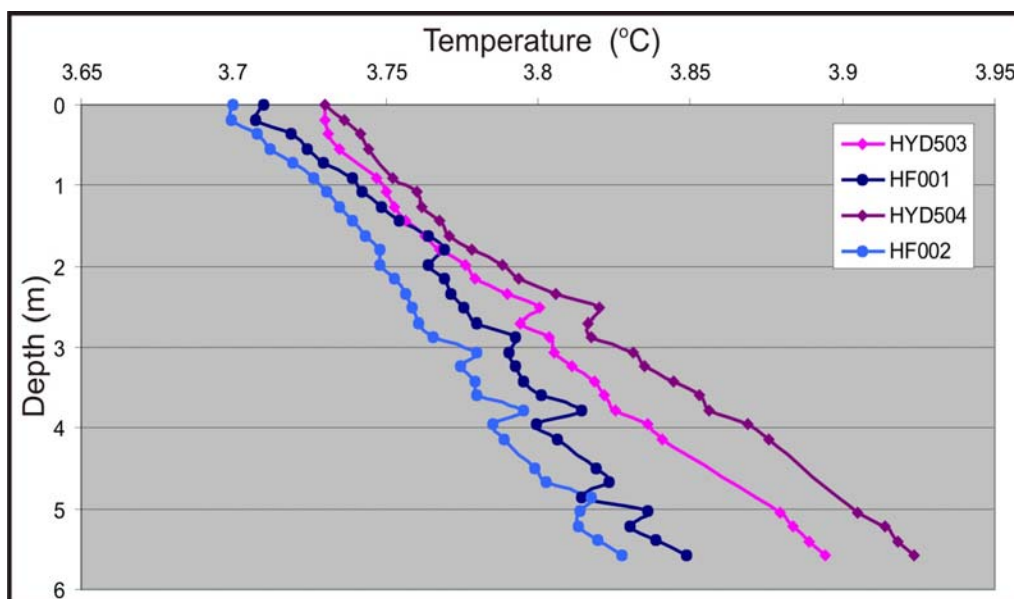


Figure 3.12: Plots of Temperature vs. Depth recorded by the 32 thermistor Dalhousie heat flow probe showing temperature gradient in the upper 6 m of sediments. Gradient is plotted from the bottom water temperature recorded by the CTD probe at the seafloor (0 m).

In addition to BWT analysis a second method of seafloor heat flow calculation for the Torbrook gas hydrate mound has been applied to help us interpret the anomalously low geothermal gradients recorded at the Torbrook mound during the 2004 and 2008 heat flow cruises. The method involves calculation of gradient using measured seafloor temperatures and temperatures associated with the methane gas hydrates phase boundary (Fig. 3.13). Leblanc et al. (2007) have identified a BSR associated with the methane gas hydrates phase boundary at a depth of 363 m below seafloor. Using a measured seafloor temperature of 3.7 °C and the depth to phase boundary under hydrostatic and lithostatic pressure, geothermal gradients of 45-50 mK^m⁻¹ were determined. Leblanc et al. (2007) report a sediment thermal conductivity of 1.1 Wm⁻¹K⁻¹ at the seafloor. As vertical heat flow is simply the product of geothermal gradient and sediment thermal conductivity, a seafloor heat flow value of 49.5 mWm⁻² has been calculated at the Torbrook gas hydrates mound using the low (hydrostatic) end member geothermal gradient of 45 mK^m⁻¹. The

gradient of 45 mK m^{-1} is slightly higher than most gradients recorded in regions unaffected by salt ($\sim 40\text{--}44 \text{ mK m}^{-1}$), however, the Leblanc et al. (2006) gradient is much better agreement with these stations than with the low gradients ($< 35 \text{ mK m}^{-1}$) recorded with our probe for the shallow water stations.

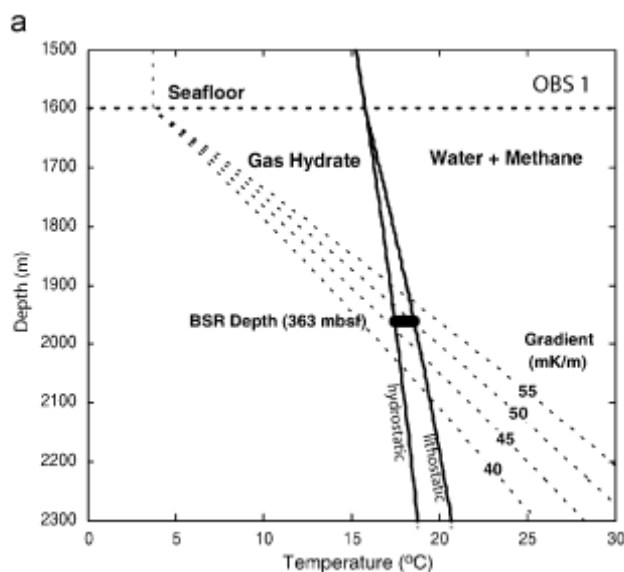


Figure 3.13: BSR depth at the Torbrook gas hydrates mound. Horizontal dashed black line represents seafloor depth and diagonal dashed black lines represent sediment temperatures based on varying geothermal gradients from $40\text{--}55 \text{ mK m}^{-1}$. Solid black lines represent solid to gas phase change boundary for methane gas hydrates under both lithostatic and hydrostatic pressures (From Leblanc et al. 2007).

Despite minor fluctuations recorded in the water column temperatures we have no definitive evidence suggesting bottom water temperature variations have effected our seafloor heat flow data in the shallower water regions. However, we do observe large variations in geothermal gradients recorded in 2004 and 2008 suggesting that something is effecting the near surface sediment temperatures. BWT recorded in 2004 and 2008 ($3.73 \text{ }^{\circ}\text{C}$ and $3.70 \text{ }^{\circ}\text{C}$) were very close, and should not significantly effect shallow sediment temperatures. Furthermore, had near surface sediment temperatures been effected by BWT variations the temperature vs. depth curves recorded by the shallow penetrating probe should converge with depth as BWT variations have a greater affect on

shallower sediment temperatures. Finally, the agreement between the heat flow calculated using the gradient derived from the depth to gas hydrates phase boundary with our deeper water heat flow values in regions unaffected by salt suggests that the higher gradient is likely representative of the true gradient for the region. To determine what is causing the anomalously low temperatures recorded at the landward limits of heat flow transects Line 1 and 2, as well as the Torbrook gas hydrates mound, requires further investigation. Shallow temperature variations may be associated with the gas hydrates in the area, or with fluid flow through the upper sediments.

3.4.2 Correction for Sedimentation

Sedimentation atop crystalline basement following rifting often results in a temporary decrease in observed heat flow at the seafloor. The influx of new sediments are deposited at the bottom water temperature which is commonly assumed to be 0 °C, although may be higher in shallow water regions (Louden and Wright 1989). Time is required to warm the new cool sediments and reestablish the geothermal gradient at the seafloor, prior to which, anomalously low geothermal gradients may be recorded in the seafloor sediments if conduction of heat from below cannot keep pace with sedimentation (Louden and Wright 1989). For this reason, the seafloor heat flow measurements acquired in 2008 are not expected to match the predicted basement heat flux's after McKenzie (1978) and Royden and Keen (1980) without applying a correction for the effects of sedimentation. A study by Nagihara and Opre Jones (2005) in the Gulf of Mexico showed notably decreased seafloor heat flow values with increasing sedimentation rates associated with the Mississippi Fan suggesting that depressed seafloor heat flow values are not unlikely in regions of continued sedimentation.

In order to correct for the effects of sedimentation on seafloor heat flow, Loudon and Wright (1989) have proposed correction factor (C_s).

$$C_s = 1 - (1 - 2X^2)\text{erfc}(X) - (2/\pi)X\exp(-X^2) \quad (?1)$$

$$X = v_s * (\text{sqrt}(t)/\text{sqrt}(\kappa)) \quad (?2)$$

Here v_s refers to a constant sedimentation rate derived from the compacted sediment thickness and the period of deposition (t) in Ma. κ is thermal diffusivity and radiogenic heat production is ignored. This method allows for the quick, simple, calculation of C_s using compacted sediment thickness' in order to remove the effects of sedimentation from seafloor heat flow measurements to predict a more realistic present day basement heat flux. Loudon and Wright (1989) suggest that calculating a sediment correction factor using this simplified method yields results in relative agreement with the results calculated by Hutchinson (1985) using a more complete method involving decompacted sediment thicknesses. For all sedimentation models an inverse relationship between rate of sedimentation and seafloor heat flux has been predicted (e.g. Hutchinson 1985, Wang and Davis 1992)

We have calculated a correction for sedimentation for all seafloor heat flow measurements acquired along heat flow transects Line 1 and 2 during the 2008 Hudson heat flow cruise (Table 3.3). Calculations were made using sediment thicknesses derived from seismic interpretations and depositional velocities calculated using compacted sediment thicknesses. A depositional period of 200 Ma was used for all stations not overlying salt bodies (Table 3.3). The sediment thickness for stations overlying salt diapirs refers to sediment above salt. Salt diapirs migrate upwards through the sediment column from depth rather than being deposited at the seafloor, therefore, salt

Heat Flow Station	Offset (m)	Bullard Heat Flow (mW/m ²)	Sediment Thickness (m)	Depositional Period (Ma)	Depositional Velocity (m/Ma)	Stretching Factor (β)	Cs	Diapir	Salt Increase	Sed. Cor. Basal Heat Flux (mW/m ²)	Salt Corrected Basal Heat Flux (mW/m ²)	Model 1 HF (mW/m ²)	Model 2 HF (mW/m ²)
Line 1													
HF101	100700	23.9	6400	200	32.0	2.01	0.123			26.83731	26.83731	35.85	44.81
HF102	114200	34.7	7700	200	38.5	2.42	0.156			40.11667	40.11667	36.1428	45.17
HF103	124300	37.3	8000	200	40.0	2.84	0.164			43.4172	43.4172	36.33	45.42
HF104	127300	38.1	7900	200	39.5	3.05	0.161			44.24934	44.24934	36.4	45.5
HF105	128500	46.9	2600	90	28.9	3.12	0.065	D1	1.08	49.95788	46.05423529	36.42	45.53
HF106	131700	39.3	7700	200	38.5	3.28	0.156			45.43473	45.43473	36.46	45.58
HF107	134800	40.3	7900	200	39.5	3.4	0.161			46.80442	46.80442	36.49	45.61
HF108	140900	37.1	8100	200	40.5	3.7	0.167			43.28457	43.28457	36.55	45.69
HF109	146100	39.4	3700	120	30.8	3.9	0.085	D2	0.94	42.7293	45.37624779	36.58	45.73
HF110	150900	43.3	3100	120	25.8	4.1	0.068	D2	1.05	46.23141	43.96013629	36.61	45.76
HF111	154300	65.7	1800	90	20.0	4.3	0.042	D2	1.23	68.43969	55.72832454	36.63	45.79
HF112	157600	54.9	1700	70	24.3	4.43	0.045	D2	1.16	57.38697	49.66521203	36.65	45.81
HF113	160300	43.1	5900	200	29.5	4.46	0.111			47.87117	47.87117	36.65	45.81
HF114	166800	43.4	5900	200	29.5	4.6	0.111			48.20438	48.20438	36.66	45.83
HF115	172600	56.6	3000	145	20.7	4.81	0.058	D3	1.11	59.8828	53.96032527	36.68	45.85
HF117	180000	51.7	2500	145	17.2	5	0.046	D4	1.11	54.09371	48.74378264	36.7	45.87
HF118	187800	43.3	4800	200	24.0	5.06	0.070			46.31368	46.31368	36.7	45.88
HF119	201700	46	4800	200	24.0	5.2	0.070			49.2016	49.2016	36.71	45.89
Line 2													
HF201	34300	29.1	6500	200	32.5	2.01	0.125			32.7	32.7	35.82	44.7772
HF202	43100	31.7	5900	200	29.5	2.24	0.111			35.2	35.2	36	44.9995
HF203	53500	43.9	7000	200	35.0	2.59	0.138			50	50	36.2	45.2434
HF204	62200	54.7	6000	200	30.0	3.12	0.161			63.5	47.8	36.38	45.4799
HF205	66300	65.5	3000	80	37.5	3.35	0.084	D5	1.330	71	53.4	36.44	45.5516
HF206	70000	61.3	1000	40	25.0	3.51	0.034	D5	1.330	63.4	47.6	36.51	45.5938
HF207	72600	72.8	1000	40	25.0	3.63	0.034	D5	1.330	75.3	56.6	36.54	45.6221
HF208	75600	60.7	800	40	20.0	3.75	0.026	D5	1.330	62.3	46.8	36.56	45.6478
HF209	79500	N/A	6300	200	31.5	3.9	0.120			50.3	50.3	36.58	45.6768
HF210	86000	47.1	6500	200	32.5	4.22	0.125			53	53	36.62	45.7291
HF219	152000	42.6	5500	200	27.5	4.46	0.101			46.9	46.9	36.65	45.7614
HF220	164500	44.5	5200	200	26.0	4.04	0.094			48.7	48.7	36.6	45.7012
HF221	178200	41.1	5300	200	26.5	4.45	0.097			45.1	45.1	36.65	45.7602

Table 3.3: Corrections table showing correction for sedimentation and correction for both salt and sedimentation. In addition, modelled basal heat flux after McKenzie (1978) using a lithospheric thickness of 100 km (Model 1) and 125 km (Model 2) are shown. Cs is correction for sedimentation, stretching factor after Wu (2006).

emplacement will not have a cooling effect as surface sedimentation does and should not be included in our correction for cooling due to sedimentation. The age associated with the sediments overlying salt, as required for depositional velocity calculation, are inferred from stratigraphic boundaries as picked in our seismic interpretations.

Corrections for sedimentation were applied to determine the basal heat flux rather than the present day seafloor heat flux for later comparisons with predictions from crustal rift models. As measurements above salt diapirs recorded anomalously high geothermal gradients due to the focusing effects of salt on heat flow, these measurements are not representative of the true underlying basal heat flux and require an additional correction for the conductive effects of salt, as described in section 3.4.3. It should also be noted that the predicted values after McKenzie (1978) and Royden and Keen (1980) do not account for any additional heat generation due to radioactive decay of uranium, potassium and thorium which likely occur in the sediment pile overlying the basement.

3.4.3 Effects of Salt on Heat Flow

The thermal conductivity of salt is approximately 6 W/m/°C at room temperature, decreasing as temperature increases to a value of ~4.5 W/m/°C at temperatures of 50-100 °C (Birch and Clark 1940). This conductivity value is significantly higher than the values for most clastic and carbonate sediments which range from 1.5-2.5 W/m/°C dependant on lithology, burial depth, compaction and water content (Clark 1966). As salt has a significantly higher thermal conductivity than most sediments, heat preferentially flows through salt, resulting in thermal anomalies above, beside, and beneath salt structures. Salt bodies are overlain by positive and underlain by negative thermal anomalies (Fig. 3.14) (O'Brien and Lerche 1987, Yu et al. 1992). Assuming a static salt body and purely

conductive heat transfer the thermal anomaly predicted is directly proportionate to the shape, height and volume of the salt body, as well as the contrast in thermal conductivities between the salt and surrounding sediments (Jensen 1983).

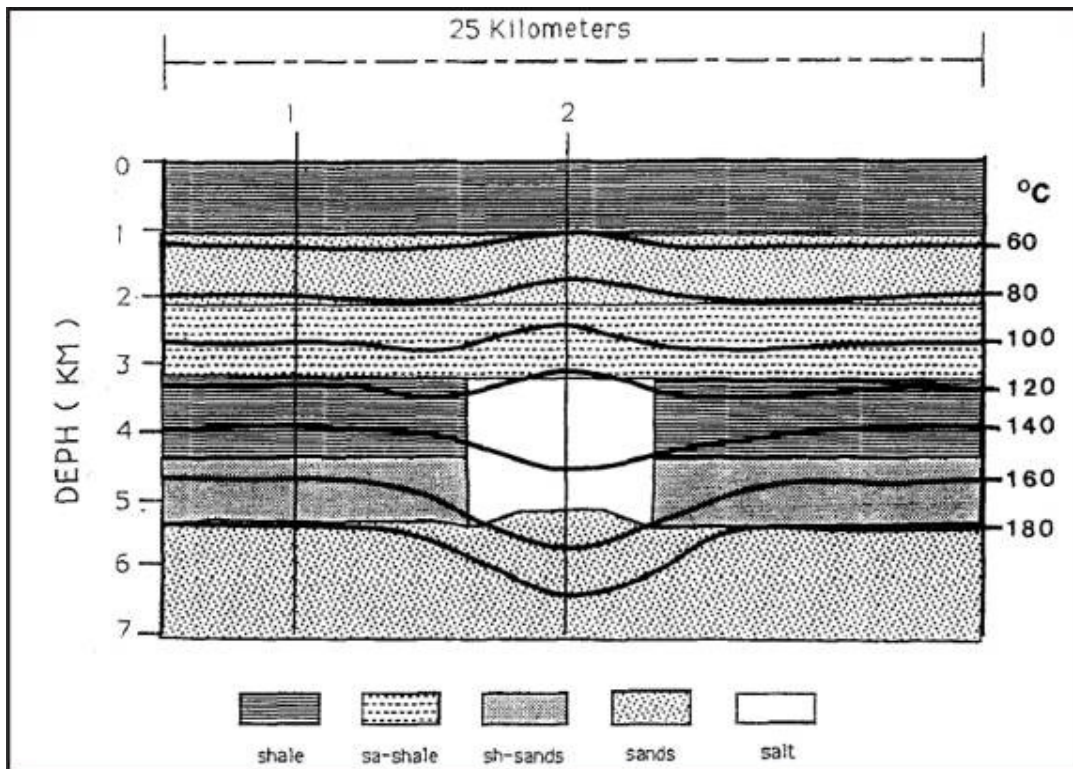


Figure 3.14: Simple 2D conductivity based numerical model showing the effects of a square shaped salt body on temperature distribution in the case of constant uniform basal heat flux (from Yu et al. 1992).

To determine the effects of salt diapirs on seafloor heat flow, a series of static, purely conductive, 2D numerical models were run (Appendix E). The models were designed to replicate the effects of salt bodies present in lines 1400 and 88-1A on seafloor heat flow. The relative increase in seafloor heat flow above salt diapirs observed in the models is used to remove the effects of salt on measured seafloor heat flow in an attempt to determine the basal heat flux across the central Scotian Slope. Models were run replicating diapirs D1-D4 on line 1400, and D5 on line 88-1A. Our modelling script does not allow for the presence of salt overhangs/canopies only allowing us to model

vertical salt diapirs (Appendix E). As a result, the slight overhangs observed in our seismic interpretations of the salt diapirs had to be removed.

Our model is a simple two layer model consisting of a basal salt layer with a thermal conductivity of $5.9 \text{ Wm}^{-1}\text{K}^{-1}$ overlain by sediments with increasing conductivity with depth from $2.2 \text{ Wm}^{-1}\text{K}^{-1}$ at the seafloor to $3.1 \text{ Wm}^{-1}\text{K}^{-1}$ at the salt/sediment boundary (Fig. 3.15). The increase in thermal conductivity with depth in the sediment pile is included to account for increasing conductivity due to compaction. A constant basal heat flux of 50 mWm^{-2} was assigned in the models. This value is slightly higher than the measured sediment corrected seafloor heat flow values of $\sim 47 \text{ mWm}^{-2}$ at the seaward limit of lines 1400 and 88-1A. The basal heat flux of 50 mWm^{-2} was used as a high end member in an attempt to match the measured values above salt diapirs.

It was noted by Yu et al. (1992) that in order to allow the basement heat flux to flow preferentially through the less resistant, higher thermal conductivity, material that the model must be wide enough for the heat pathways to be affected only by the conductivity of the materials and not by the edges of the models. Thus, varying distances between the salt body and the edges of the models were tested to determine how edge effects affected the model output and how far laterally the models needed to be extended in order to escape these effects. To escape significant seafloor heat flow variations due to edge effects a distance equivalent to twice the width of the salt body on either side of the diapir was required in the models.

As with all salt bodies, multiple interpretations of salt diapirs size, shape and distribution are possible. Two possible interpretations of diapir D5 are shown in Figure 3.15 showing the salt body as a large salt canopy with a thick vertical feeder (A), and as a

thick vertical diapir (B). The heat flow measurements recorded above this salt body are anomalously high, reaching values upwards of 72 mW/m^2 , and thus in the simple models the salt was interpreted as a thick vertical diapir as a high heat flow end member. In total, eight simple salt models were run. Of these five were modelled after diapir D5 in line 88-1A, and one was run for each diapir D1, D2 and D3/D4 in line 1400. The numerous runs for diapir D5 were done to test the effects of variations in the diapirs height/proximity to the seafloor, as well as variations on basal heat flux effects modelled seafloor heat flow (Appendix E). Of the models run after diapir D5 it was determined that Salt Model 2 was in best agreement with the observed seafloor heat flow data.

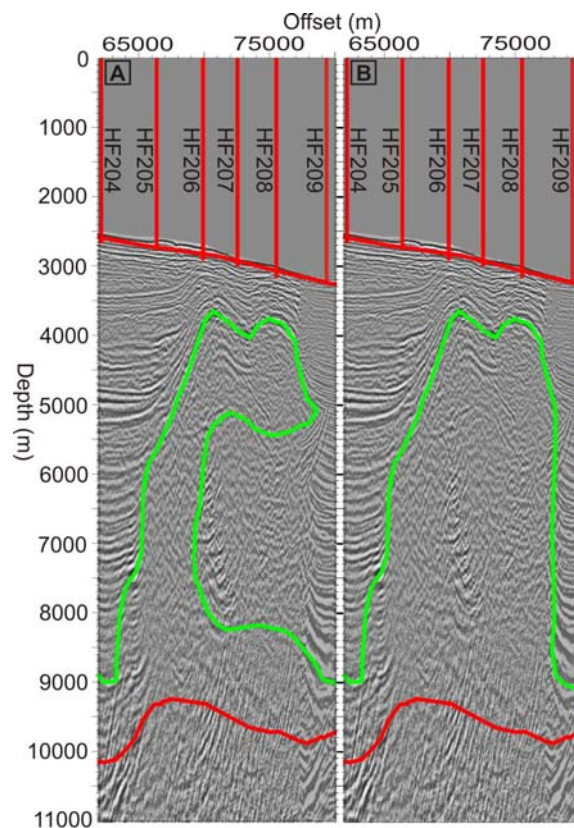


Figure 3.15: Two possible interpretations of salt diapir D5 on Lithoprobe Line 88-1A (Fig. 3.5) showing A) large tongue canopy with thick, squeezed, feeder and B) large vertical salt diapir.

In an attempt to better constrain the basal heat flux across the central Scotian Slope, sediment corrected heat flow values were further corrected for the conductive

effects of salt on heat flow for heat flow stations overlying salt bodies. To do this we use the relative increase in modelled heat flow above diapirs D1-D5 to remove the associated increase in heat flow associated with the purely conductive effects of salt from our measured, sediment corrected, heat flow measurements. The sediment corrected measured heat flow values are simply divided by the ratio modelled heat flow above salt over modelled heat flow unaffected by salt in a simple attempt to remove the conductive effects of salt as measured at the seafloor from true basal heat flux. Salt and sediment corrected heat flow data are included in Table 3.3.

Salt Model 2 is modelled directly after D5 mimicking height and shape. With lateral distances of 40 km between the diapir and edges of the models the model is wide enough to escape any edge effects as noted by Yu et al. (1992). As large variations in measured seafloor heat flow occurred across diapir D5 despite little variation in diapir height or proximity to seafloor, we used one simple correction factor for all measurements above this diapir. This model predicts a maximum heat flux above the salt diapir of $\sim 56 \text{ mWm}^{-2}$ and surrounding background values in regions unaffected by salt of $\sim 42 \text{ mWm}^{-2}$ (Fig. 3.16). The modelled increase in heat flow above salt is 1.33 times that of the surrounding regions unaffected by salt.

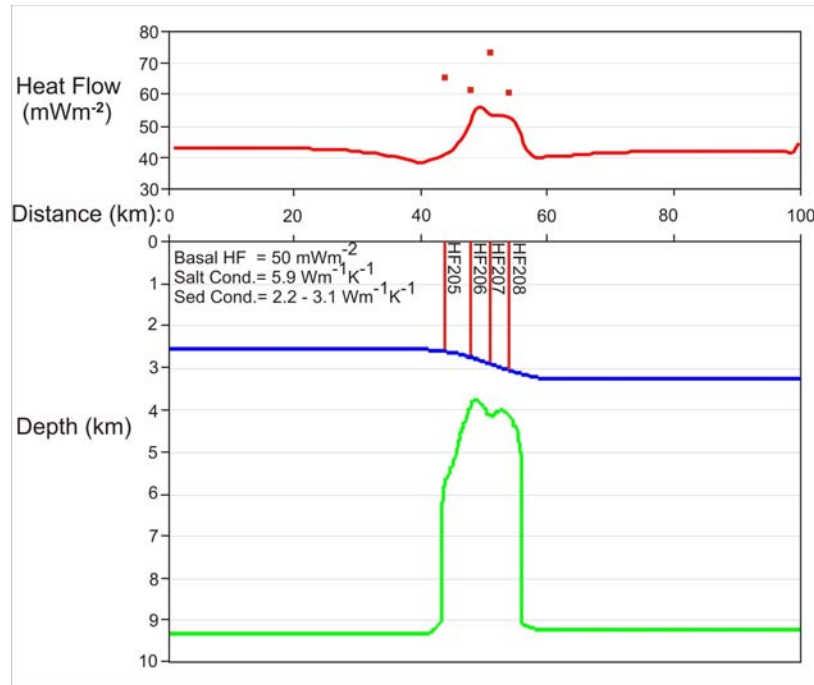


Figure 3.16: Simple 2D conductivity based thermal model of diapir D5 showing effects of salt on seafloor heat flow. Salt is outlined in green, and the seafloor in blue. The modelled seafloor heat flow is plotted above as a red line and measured values are plotted as red squares.

Salt Model 6, representative of diapir D1 in line 1400, is overlain by heat flow station HF105. The modelled seafloor heat flow of 45.6 mWm^{-2} is 1.08 times higher than the modelled background values of $\sim 42 \text{ mWm}^{-2}$ in regions unaffected by salt (Fig. 3.17). Salt Model 8 is modelled after both diapirs D3 and D4 and is overlain by heat flow stations HF115 and HF116. A modelled increase from $\sim 41 \text{ mWm}^{-2}$ in regions unaffected by salt to 45.5 mWm^{-2} above salt was observed for both diapir D3 and D4. Both heat flow stations are located just off the crest of diapirs the salt diapirs, and experience a relative increase in modelled heat flow of 1.11 mWm^{-2} due to the conductive effects of salt on seafloor heat flow (Fig. 3.18).

Salt diapir D2 is overlain by heat flow stations HF209-HF212. Salt Model 7 is representative of this diapir, however, as canopies are not possible in our models, the diapir has been inferred as a thick, vertical, basement rooted salt body (Fig. 3.19).

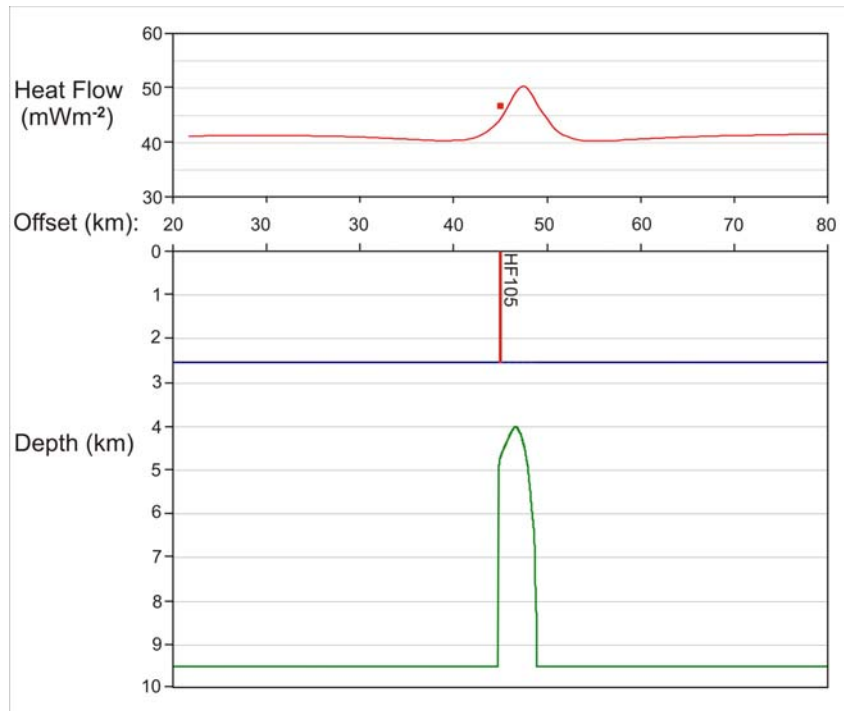


Figure 3.17: Simple 2D conductivity based thermal model of diapir D1 showing effects of salt on seafloor heat flow. Salt is outlined in green, and the seafloor in blue. The modelled seafloor heat flow is plotted above as a red line and measured values are plotted as red squares.

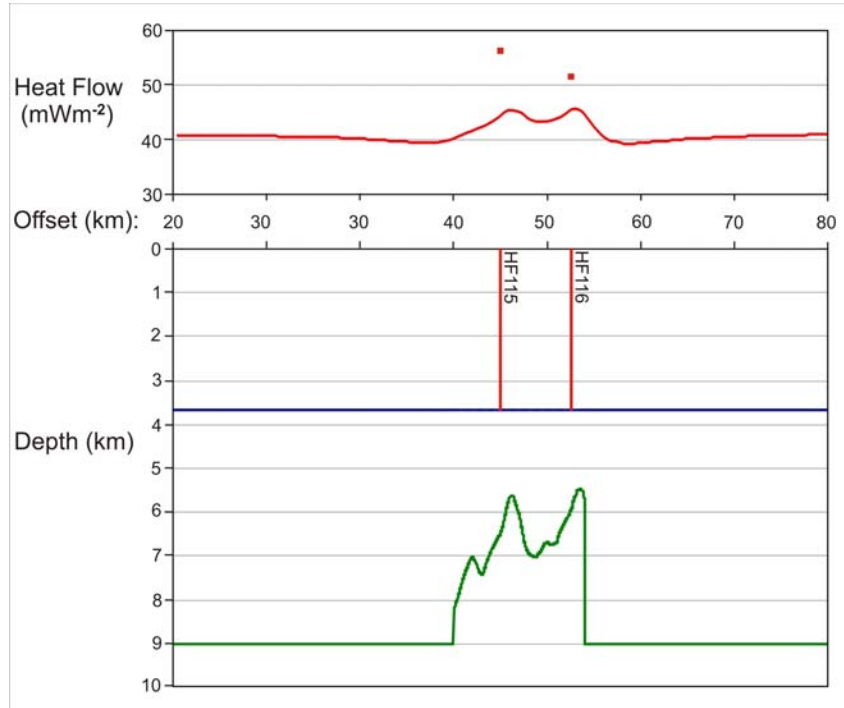


Fig. 3.18: Simple 2D conductivity based thermal model of diapir D3/D4 showing effects of salt on seafloor heat flow. Salt is outlined in green, and the seafloor in blue. The modelled seafloor heat flow is plotted above as a red line and measured values are plotted as red squares.

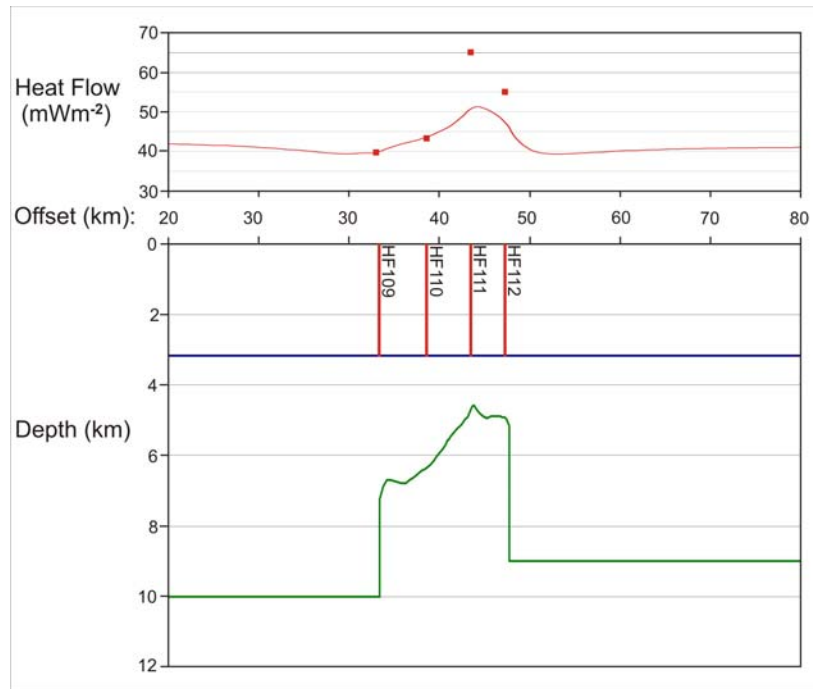


Figure 3.19: Simple 2D conductivity based thermal model of diapir D2 showing effects of salt on seafloor heat flow. Salt is outlined in green, and the seafloor in blue. The modelled seafloor heat flow is plotted above as a red line and measured values are plotted as red squares.

Modelled heat flow in regions unaffected by salt yielded a value of $\sim 42 \text{ mWm}^{-2}$.

Modelled seafloor heat flow values above salt varied from one station to the next, thus different correction factors were applied for the different stations located across the diapir. Station HF209, located at the very edge of diapir D2, recorded a modelled value of 39.5 mWm^{-2} , only 0.94 times the background value of $\sim 42 \text{ mWm}^{-2}$. This low heat flow value associated with the stations location at the edge of the diapir will actually require an increase in heat flow to correct for the conductive effects of salt. Stations HF110, HF110 and HF112 recorded modelled seafloor heat flow values of 44.2 mWm^{-2} , 51.8 mWm^{-2} and 48.5 mWm^{-2} , yielding respective correction factors of 10.5, 1.23 and 1.16.

Our simple modelling suggests that the increase observed above salt bodies in our measured heat flow data can not be reproduced by the strictly conductive effects of salt alone. In general, the purely conductive 2D models under-predict the heat flow above

salt. A second mechanism such as convection of fluids is likely affecting the temperatures observed above the salt bodies. Keen (1983) ran a series of similar conductivity based 2D models in an attempt to determine if the conductive effects of salt could sufficiently increase temperatures above the Primrose diapir on the Scotian Shelf to account for an observed maturation anomaly (Rashid and MacAlary 1977). While the temperature increase due to the conductive effects of salt were calculated to be 10-20 °C, this alone was not enough to result in the observed maturation anomaly.

Keen (1983) hypothesized that upon diapiric intrusion, faulting and fracturing of the sediments adjacent to the diapir could create a migration pathway for hot fluids from depth to the top of the diapir, which could cause significant increases in temperature and thus maturation above the diapir. Under favourable circumstances, it was found that in addition to the conductive effects of salt, migration of hot fluids from depth could produce the observed maturation anomaly above the Primrose diapir. Keen suggests that much of the rising fluid will likely continue to flow vertically beyond the crest of the diapir towards the surface, which supports the idea that convection of fluids could be effecting our observed variation in seafloor heat flow measurements. However, further modelling is required in order to test this hypothesis.

3.5 Simple Crustal Models

Once measured heat flow data have been corrected for the effects of sedimentation and salt to give approximations of present day basal heat flux are were able to begin analysis and comparisons of our measured data with predictions from simple crustal rift models. To theoretically predict the basement heat flux across our study area the uniform stretching model of McKenzie (1978) and the dual stretching model of

Royden and Keen (1980) were employed. We attempt to match modelled present day basal heat flux with our sediment and salt corrected measured heat flux data to constrain basal lithospheric temperatures and lithospheric thicknesses while predicting the margins heat flux history. An introduction to simple rift models and our MatLab scripts used in modelling are included in Appendix F.

To determine the basal heat flux across the central Scotian Slope we must first determine the crustal stretching factors across the margin. The pure shear model assumes uniform extension of the crust upon initiation of rifting. The predicted basal heat flux as a function of time is directly related to the initial crustal stretching factor (β), athenospheric temperature (T_1), and total lithospheric thickness (A). Varying crustal stretching factors (β) were defined by Wu (2007) along the trace of SMART refraction Line 2 based on crustal thicknesses derived from velocity modelling (Fig. 3.20). SMART Line 2 runs coincident with Lithoprobe line 88-1A. An offset of 156 km on SMART Line 2 corresponds with the 0 offset of Lithoprobe Line 88-1A. Using this, we were able to determine crustal stretching factors at known positions (thus at our heat flow stations) on line 88-1A.

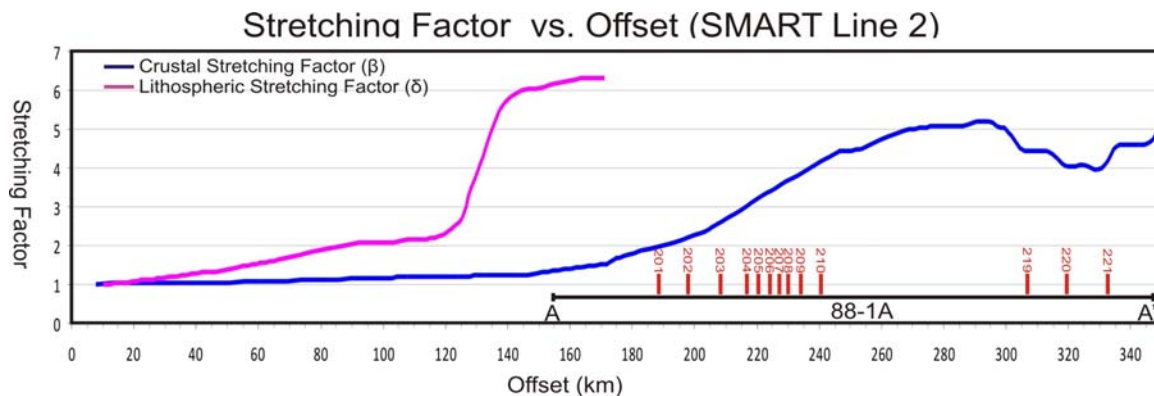


Figure 3.20: Stretching factor (β and δ) vs. Offset (km) for SMART Line 2 after Wu (2007) and Keen and Beaumont (1990). Black line represents the trace of coincident seismic reflection profile 88-1A. Vertical red lines represent seafloor heat flow locations. Corresponding location of Lithoprobe line 88-1A is shown from A to A' in Figure 3.1.

The predicted values for present day basal heat flux are calculated according to a rift age of 200 Ma with crustal stretching factors derived from Wu (2007). Stretching factors range from 2.01 at station HF201 on the upper continental slope to 4.46 at station HF219 towards the seaward limit of the Scotian Slope (Table 3.3). As expected, no significant variation in present day heat flux is predicted by the models associated with variations in β . All modelled present day basal heat flux values are within 1 mW/m^2 , independent of β values used. However, variations in β across the margin do significantly effect the heat flow history over the past 200 Ma (Fig. 3.21, Fig. 3.22). Therefore, although no present day heat flow variations exist associated with varying β , varying stretching factors across the margin may still have implications for hydrocarbon maturation and the thermal evolution of the margin. Using the pure shear crustal rift model present day heat flow was predicted at all heat flow stations as constrained by associated crustal thicknesses after Wu (2007) and lithospheric thicknesses (A) of both 125 km (Crustal Model 1) and 100 km (Crustal Model 2). Varying lithospheric thicknesses were tested in an attempt to match predicted heat flow to corrected measured data while maintaining the confines set by the known crustal thicknesses.

The dual stretching model predictions for the regions heat flow history vary depending on the amounts of upper lithospheric stretching (β) and lower lithospheric stretching (δ). Keen and Beaumont (1990) used large δ values in comparison with the small β values to explain the observed uplift of the Lahave Platform on the central Scotian Shelf. The proportions of lower lithospheric stretching are uncertain across the central Scotian Slope. We are able to obtain varying crustal heat flux histories while maintaining known crustal thickness' by varying the amount of sub-crustal thinning.

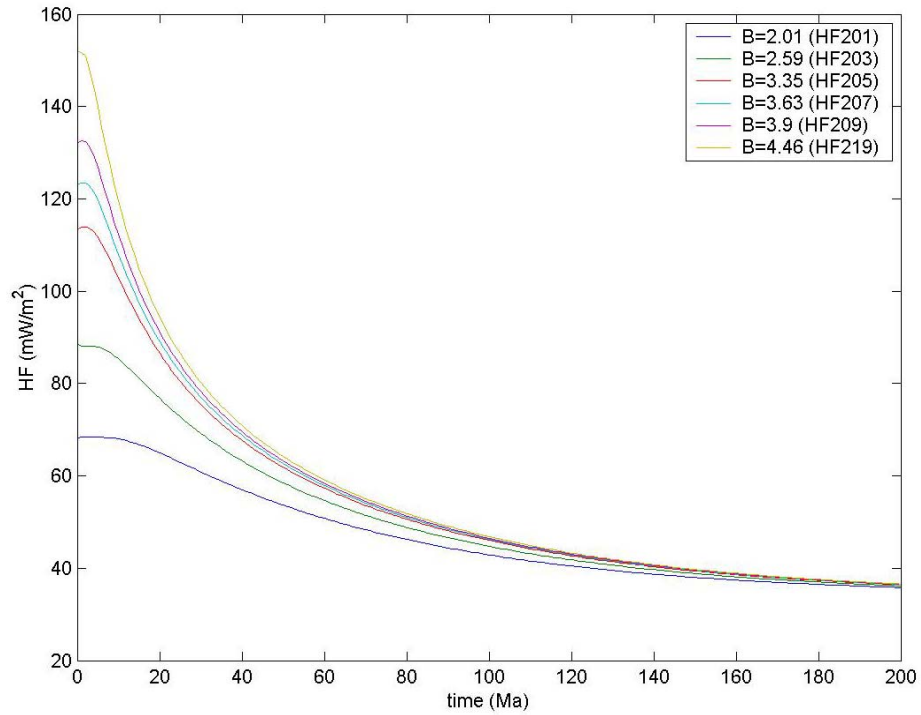


Figure 3.21: Heat flux vs. Time graph for Crustal Model 1 showing change in crustal heat flux with time for select heat flow stations based on associated crustal stretching factors as shown in Fig. 3.14 and $A = 125$ km. Time (in Ma) represents time following rifting.

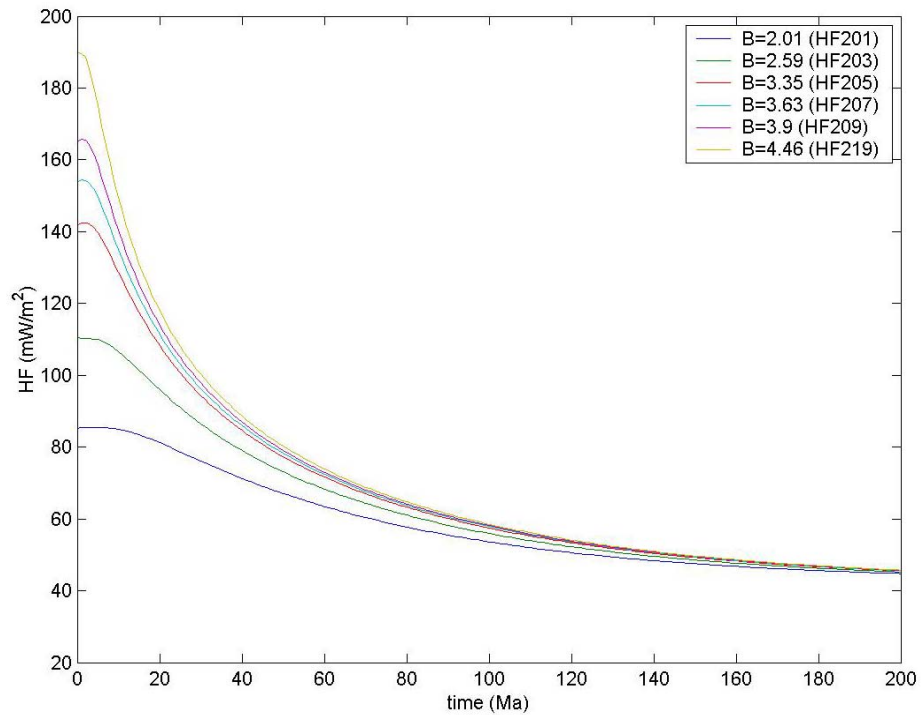


Figure 3.22: Heat flux vs. Time graph showing change in crustal heat flux with time for select heat flow stations based on associated crustal stretching factors as shown in Fig. 3.14 and $A = 100$ km. Time (in Ma) represents time following rifting.

Applying a large sub-crustal stretching factor has a negligibly small effect on present day basal heat flux when compared to the uniform stretching model predictions. However, it should be noted that uniform and dual stretching models, although arriving at similar present day heat flux values, have very different heat flux histories, particularly over the first ~50 Ma (Fig. 3.21, Fig. 3.23). This may significantly effect the hydrocarbon maturation history of the margin and is discussed in further detail in Chapter 4.

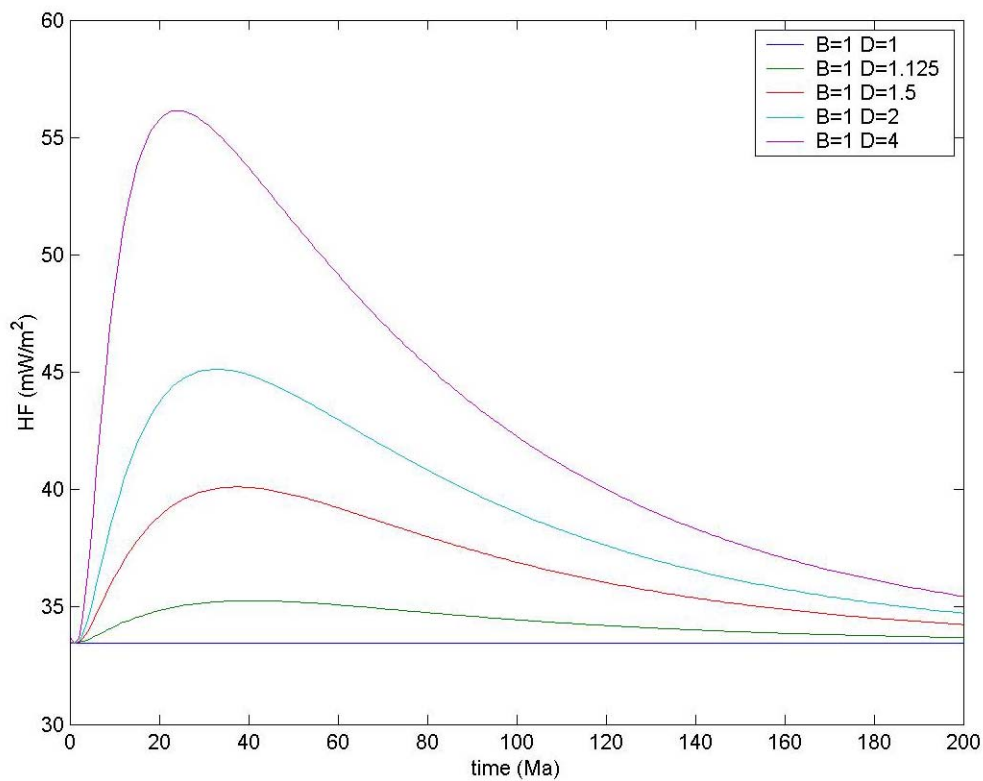


Figure 3.23: Dual stretching heat flow plot showing effects of varying δ on crustal heat flux with lithospheric thickness $A = 125$ km.

Our goal is to use the predicted basement heat flux histories from the uniform and dual stretching models in combination with measured sea floor heat flow values to produce a self consistent 3D thermal model of the central Scotian Slope where modelled seafloor heat flow values match measured values. Once the 3D model configuration has been set we are able to test the effects of varying basement heat flux histories as defined

by crustal thickness and varying β and δ on predicted seafloor heat flow. By testing various basement heat flux histories and comparing the predicted seafloor heat flow from the 3D models with the measured seafloor heat flow values of the 2008 Hudson cruise we are able to produce a 3D model constrained by both measured seafloor heat flow data and modelled basement heat flux data that remains consistent with observed crustal thicknesses.

3.6 Heat Flow Data Discussion and Interpretations

After analysis of our measured seafloor heat flow data we conclude that all stations from the Torbrook gas hydrates mound and shallow water stations HF101, HF102, HF201 and HF202 recording gradients $<35 \text{ mK m}^{-1}$ are not representative of purely conductive heat transfer sourced from Earth's interior. At present we are unable to determine the cause of these anomalously low gradients, however, after comparison with the deeper sourced temperature data from the gas hydrates phase boundary after Leblanc et al. (2006) we suggest the data should not be included in our overall analysis of the study areas heat flux. Corrections for the effects of sedimentation and salt on measured seafloor heat flow have been applied to approximate the present day basal heat flux from our measured seafloor data. Plots of corrected seafloor heat flow data are compared with present day basal heat flux predictions from the McKenzie uniform shearing model across both seismic lines 1400 and 88-1A in Figure 3.24.

For heat flow transect Line 2 (Lithoprobe line 88-1A) the general basal heat flux trend varies slightly across the margin increasing from $\sim 45\text{-}48 \text{ mW m}^{-2}$ towards the seaward limit of the line to $\sim 47\text{-}53 \text{ mW m}^{-2}$ in the central/landward regions of the line. These values exclude the slightly elevated values above stations HF205 and HF207 and

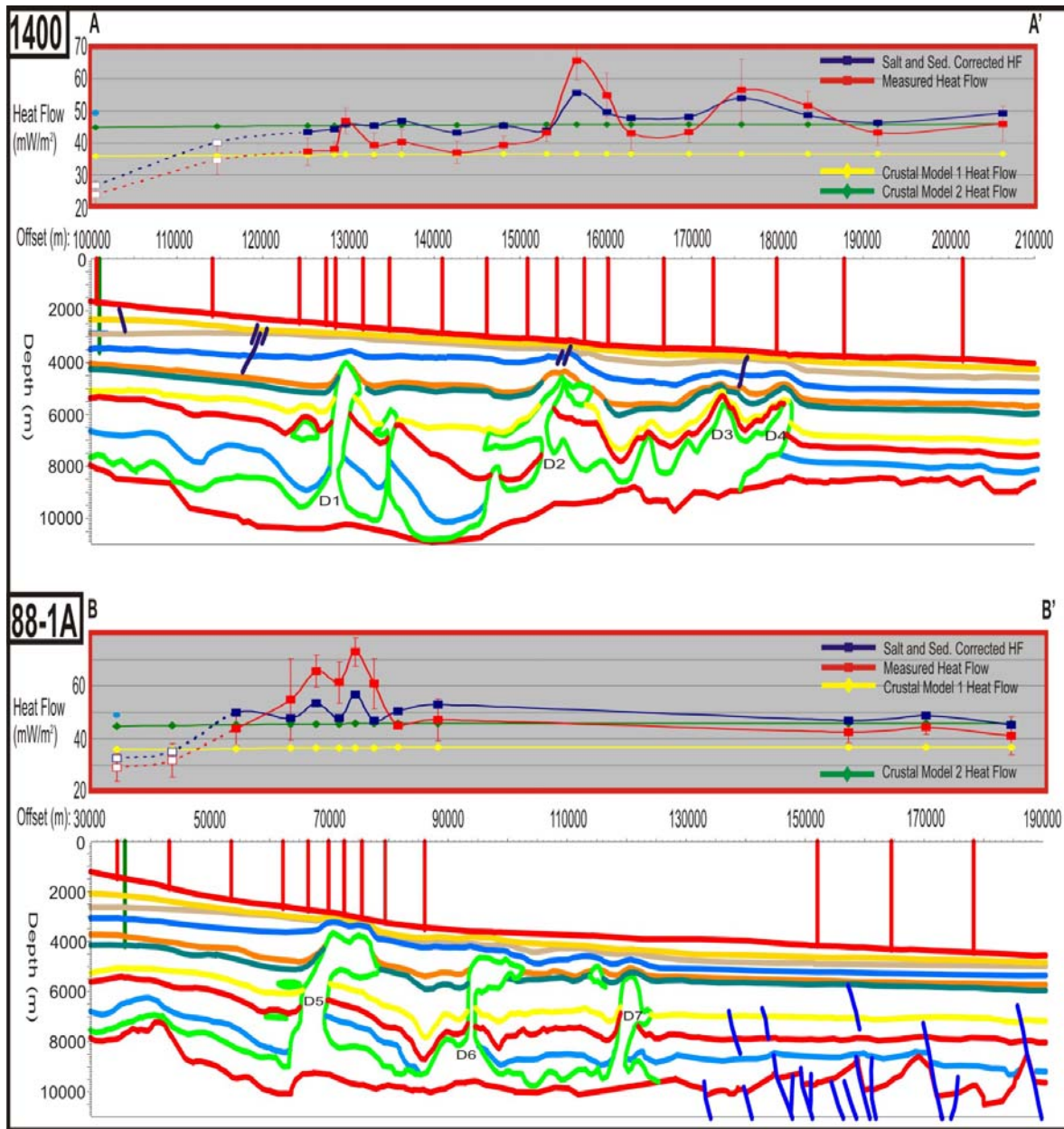


Fig.3.24: Comparisons between sediment and salt corrected measured heat flow data and modelled basement heat flux data for different lithospheric thicknesses and crustal stretching models after the uniform shear model of McKenzie (1978) for both line 1400 and 88-1A. White squares represent stations with anomalously low gradients and the blue circle represents heat flow value calculated after Leblanc et al. (2006) from the Torbrook gas hydrates mound. Below the heat flow plots are our stratigraphic interpretations from the seismic images as shown in Figures 3.5 and 3.6 for lines 1400 and 88-1A respectively.

the anomalously low values for stations HF201 and HF202. This increase in heat flow in the direction of thickening continental crust is counter to what one would expect for a young margin, however, for an old margin such as ours the majority of increased heat

flow associated with thinning during rifting has decayed. The increase in heat flow in the landward direction is possibly due to the increase in radiogenic heat production associated with the thickening continental crust. Our simple 2D models do not account for radiogenic heat production in the crust or sediments and the effects of adding radiogenic heating will be investigated in further detail in Chapter 4.

The corrected basal heat flux values calculated above salt diapir D5 are in relatively good agreement with the surrounding measurements at stations HF203, HF209 and HF210. We note that the increase in measured heat flow above salt is not uniform and cannot be entirely removed using a correction factor derived from a simple, static, 2D conductivity based numerical model as large variations in measured heat flow above salt persist even after correction for the conductive effects of salt. Other factors such as salt movement, out of plane variations in salt geometry or convective fluid flow through sediments overlying the diapir may also be effecting the measured heat flow values (Keen 1983).

In comparing our corrected measured seafloor heat flow data from heat flow transect Line 2 with the predictions for present day basal heat flux from the McKenzie (1978) uniform shear rifting model we find that the thinner lithospheric thickness of 100 km (Model 2) yields a better fit to the corrected heat flow data (Fig.3.24). There is a relatively good fit between our measured and modelled data, particularly towards the seaward limits of the line. When the heat flow calculated from the Torbrook gas hydrates phase boundary is extrapolated onto heat flow transect Line 2 and used in place of the anomalously low values calculated from HF201 and HF202 we see fairly constant heat flow across the line. Above the central region of the transect the measured data records

slightly higher basal heat flux values than Crustal Model 2 predicts. The two most landward measured data points show good agreement with the Model 1 ($A=125$ km) results (Fig. 3.21). However, as these data points recorded anomalously low measured geothermal gradients, this fit is most likely coincidental and not representative of the true basal heat flux as constrained by simple crustal rift models.

Heat flow transect Line 1 (NovaSPAN line 1400) recorded a corrected basal heat flux of and $\sim 42\text{--}47$ mWm^{-2} in the landward portions of the line $\sim 46\text{--}49$ mWm^{-2} towards the seaward end excluding anomalously high measurements above salt which persisted even following salt correction. Here we ignore stations HF101 and HF102 due to their anomalously low measured gradients. The slight increase in basal heat flux in the seaward direction recorded for this transect is opposite to the decrease identified in Line 2. However, as the error in measured heat flow is $\sim 2\text{--}7$ mWm^{-2} for regions unaffected by salt an interpretation that for both lines a average basal heat flux between ~ 44 and 50 mWm^{-2} is not unreasonable for the region.

After the correction for salt was applied, only stations HF111 (55.7 mWm^{-2}) and HF115 (54.0 mWm^{-2}) recorded anomalously high heat flow values. Again, we see the increase in heat flux above salt is not uniform and cannot be corrected using a simple conductivity based 2D model. All other heat flow stations are in relatively good agreement with the predictions from Crustal Model 2 (fig. 3.24). The increase in heat flow in the seaward direction agrees with the model predictions, however, the measured increase is slightly greater than the modelled increase. The heat flow of 49.5 mWm^{-2} calculated from the depth to BSR after Leblanc et al. (2006) at the Torbrook mound is slightly higher than the other recorded landward gradients at stations HF103-107 ($43\text{--}47$

mWm^{-2}); however, it is still in much better agreement than with the anomalously low measurement of 26.8 mWm^{-2} at HF101.

Our sediment and salt corrected basal heat flux is plotted against crustal stretching factor (β) in Figure 3.25 along with our modelled results for both Crustal Models 1 and 2. The general trend shows good agreement between our corrected heat flux data and the predicted values using the high heat flow end member Crustal Model 2. Although there exists notable scatter in our measured corrected data, we see that with the exception of station HF209, which has an extremely small error bar due to the lack of in-situ conductivity analysis for this station, that all modelled data from Model 2 fall within the error of the measured heat flow.

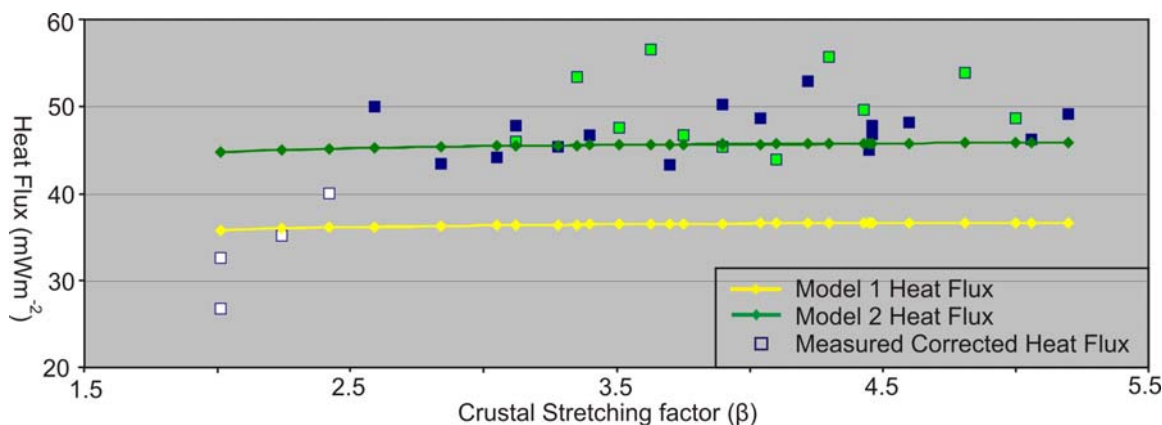


Figure 3.25: Heat flux vs. Crustal stretching factor (β) plot showing corrected (sediment and salt) measured seafloor heat flow data as blue squares. Filled green squares represent measurements above salt bodies and white filled squares represent stations with anomalously low gradients.

We can conclude that using simple 2D crustal rift models without including the effects of radiogenic heating that Crustal Model 2 with the thinner lithosphere yields a much better match to our corrected measured data. With the addition of radiogenic heating within the sediment pile and underlying crust we may find that the thinner lithospheric model over predicts the present day heat flux when compared with our modelled data and that, in fact, the thicker lithosphere yields a better fit to our measured

data. To test this hypothesis and to determine how significantly 3D effects of salt bodies effect heat flow we will run a series of more complex, dynamic 3D models in Chapter 4 using PetroMod 11 software.

Thermal & Petroleum System Modelling (Phase II) of seismic line NOVASPAN 1600 and the revision of 2D PS modelling of Seismic Lines NOVASPAN 1400 and FGP 88-1A, Scotian Basin, Offshore Nova Scotia based on new heat flow data of 2008

(Final Report Submitted to OETR-Dalhousie Contract 2007-2009)

*Submitted
To*

**Professor Keith Loudon
Project Coordinator, OETR Project
Oceanography Department, Dalhousie University
Life Sciences Centre, 1355 Oxford Street
Halifax, Nova Scotia
B3H 4J1**

Submitted by



**Dr. P. K. Mukhopadhyay (Muki)
Global Geoenergy Research Ltd.
P.O. Box 9469, Station A
(1657 Barrington Street, Suite 427)
Halifax, Nova Scotia
B3K 5S3 (B3J 2A1)**

January 14, 2009

Table of Contents

A. EXECUTIVE SUMMARY

- A.1. Modelled and Measured Heat Flow Calibration
- A.2. Maturity Trends and Hydrocarbon Accumulations
- A.3. Hydrocarbon Mass Balance

1. INTRODUCTION

- 1.1. Administrative Aspects
- 1.2. Objectives

2. PETROLEUM SYSTEM MODELLING: GEOLOGY, WELLS AND INPUT PARAMETERS

- 2.1. Petrobuilder: Input Parameters
- 2.2. Heat Flow
- 2.3. Source Rocks
- 2.4. Assigned Petroleum Systems

3. PETROLEUM SYSTEM MODELLING: RESULTS AND DISCUSSIONS

- 3.1. Seismic Line NOVSPAN 1400
- 3.2. Seismic Line FGP 88-1a
- 3.3. Seismic Line NOVSPAN 1600

4. PETROLEUM SYSTEM MASS BALANCE CALCULATIONS

5. CONCLUSIONS

- 5.1. Seismic Line NOVSPAN 1400
- 5.2. Seismic Line FGP 88-1a
- 5.3. Seismic Line NOVSPAN 1600

6. ACKNOWLEDGMENTS

7. REFERENCES AND BIOLOGRAPHY

Thermal & Petroleum System Modelling (Phase II) of seismic line NOVASPAN 1600 and the revision of 2D PS modelling of Seismic Lines NOVASPAN 1400 and FGP 88-1A, Scotian Basin, Offshore Nova Scotia based on new heat flow data of 2008

A. EXECUTIVE SUMMARY

This final Phase II report has established a complete evaluation and interpretation of two-dimensional thermal and petroleum system modeling of three seismic lines (NOVASPAN 1400, FGP 88-1a and NOVASPAN 1600) from the central portion of the Scotian Basin, offshore Nova Scotia. The Petroleum System Modelling used the PetroMod 2D modelling software (version 11.03; IES Inc., Germany [currently of Schlumberger Inc.]). The report is an extension of the Phase I study of the OETR-Dalhousie contractual agreement that was completed in 2007 and the report was submitted in January 2008 (Mukhopadhyay, 2008). The final report includes a revision of two-dimensional petroleum system modelling on seismic lines NOVASPAN 1400 and FGP 88-1a based on newly acquired heat flow data (Table 1; Loudon et al., 2009). In addition, a new composite petroleum system modelling was carried out on seismic line NOVASPAN 1600.

As a requirement of the modeling parameters, a complete suite of geological, geophysical, and geochemical parameters have been incorporated as input parameters. Other than basic geological properties included the timing of the salt movement (both diapiric and allochthonous stages), data on the individual faults (opened or closed), reservoir properties, multi-component kinetics of candidate source rocks from the Scotian Margin, and the phase behavior of the individual hydrocarbons.

The final report of the Phase II research of two-dimensional petroleum system modelling of three seismic lines for the OETR-Dalhousie University contract established the following conclusions:

A. 1. Modelled and Measured Heat Flow Calibration

- The modelled (used transient heat flow since the rifting) and measured heat flow values in all three seismic lines (NOVSPAN 1400, FGP 88-1a and NOVSPAN 1600) suggest that with the exception of a few heat flow values in all three lines, other measured values are closely correlated. The anomalous heat flow values are usually situated around the periphery of salt diapirs.
- The discrepancy of heat flow trends between the measured and modeled heat flow values is caused by: (a) an outline of the salt in the upper part of the section may not correctly drawn on each of the seismic line; and (b) problems in attaining a well-defined basement heat flow along the 2-D seismic section
- The heat flow values on top of the salt diapirs indicate that they are comparatively hotter in comparison than the heat flow values on the flank of the salt diapirs. However, the amount of heat flow variations depend on the thickness of individual salt structures and the proximity of the salt diapirs to the sediment water interface locations,
- Comparative heat flow values indicate that this part of the Scotian Basin (between western Sable Subbasin and eastern Shelburne Subbasin) is much cooler than was previously thought.

A.2. Maturity Trends and Hydrocarbon Accumulations

- In all three seismic lines, the present day temperature and the maturity profiles illustrate a higher temperature and maturity on top of the salt diapirs compared to the flank region. Moreover, because of lower heat flow history in this part of the Scotian Basin, the maturity data indicates that even the late Triassic source rocks could lie within the main dry gas generation zone. Similarly, the pore pressure profiles in all three seismic lines indicate that all of the late Triassic or early Jurassic and late

Jurassic conceptual reservoirs may encounter an overpressure situation. The transformation ratio of five major source rocks indicate that the source rocks other than Cretaceous Verrill Canyon have more than 90% hydrocarbon transformations,

- Because of lower heat flow trends (based on newly measured data) of all three seismic lines in comparison to previous report (Mukhopadhyay, 2007), all conceptual reservoirs specially in the early Cretaceous and Palaeocene periods in the slope may contain more oil (C15+ and C6-C14 hydrocarbons; especially in seismic line 1400). However, in both seismic lines FGP 88-1a and NOVASPAN 1600, the liquid hydrocarbons (oil and condensates) are mostly associated with mainly dry and wet gas components (C1 and C2-C5 hydrocarbons).

A.3. Hydrocarbon Mass Balance

- The comparative mass balance of hydrocarbons (in Metric Tons) in three seismic lines (NOVSPAN 1400, FGP 88-1a and NOVSPAN 1600) illustrate that: (a) the seismic line 88-1a has the highest amount of hydrocarbons generated and expelled from four deeper source rocks, and accumulated in the Upper Jurassic and Triassic reservoirs; (b) the seismic line 88-1a accumulated at least five times more hydrocarbons in various reservoirs compared to lines NOVSPAN 1400 and NOVSPAN 1600; and (c) the main HC accumulations in lines 88-1a and NOVSPAN 1600 (in lower saturations) are concentrated in the late Triassic, late Jurassic, and early Cretaceous reservoirs while the main accumulation is restricted to the late Jurassic reservoir in the line NOVSPAN 1400.
- The major loss of expelled hydrocarbons was caused by major migration loss due to seal instability allowing outflow of hydrocarbons from the top of each individual reservoirs in all three lines. The other main hydrocarbon loss was connected to the lateral seal inadequacies possibly

caused by lower sediment compaction in this region. The lower heat flow could be another issue related to sediment compaction,

- **Seismic lines FGP 88-1a and NOVSPAN 1600** - The late Jurassic and Early Cretaceous reservoir hydrocarbons contains more than 80% dry gas (methane) and 20% condensate (C6-C14 HC components); **Seismic line NOVSPAN 1400** – Early Cretaceous and Palaeocene reservoir hydrocarbons contain greater than 60% liquid hydrocarbons (C15+ and C6 to C14).

Thermal & Petroleum System Modelling (Phase II) of seismic line NOVASPAN 1600 and the revision of 2D PS modelling of Seismic Lines NOVASPAN 1400 and FGP 88-1A, Scotian Basin, Offshore Nova Scotia based on new heat flow data of 2008

1. INTRODUCTION

1.1. Administrative Aspects

Global Geoenergy Research Limited (GGRL) of Halifax, Nova Scotia has finalized his contract obligation submitting the final research report for the 2D petroleum system modelling of three seismic lines (NOVASPAN 1400, FGP 88-1A, and NOVASPAN 1600) that was performed by GGRL between May 17 and December 31, 2009. The Phase II study of the research contract was designed to perform two-dimensional thermal and petroleum system modelling of seismic line NOVASPAN 1600 and the revision of seismic Lines NOVASPAN 1400 and FGP 88-1A based on the new heat flow data. In the summer of 2008, the new heat flow data was collected by Prof. Keith Loudon and his associates from the Dalhousie University. The final interpretation of the heat flow data was completed in 2009 (Table 1; Loudon et al., 2009).

This final report is an extension of the Phase I study of the OETR-Dalhousie contractual agreement that was completed in 2007 and the final report was submitted in January 2008 (Mukhopadhyay, 2008). Global Geoenergy Research Limited had performed the second phase of the 2D modelling work based on the guidelines specified in the proposal to OETR-Dalhousie that was submitted on May 2, 2009. A preliminary report (with interpretations) of the Phase II study has already been submitted to Prof. Keith Loudon in September 2009 (as power-point presentations; Mukhopadhyay, 2009).

The total contract price of the Phase II study for Global Geoenergy Research Limited (GGRL) has been finalized at \$35,000.00 + 13% HST. As Global Geoenergy Research Limited has already received a total sum of \$23,333.34

(two-third of the Phase II contract money of \$35,000.00) plus 13% HST in two instalments, a final invoice of \$11,666.66 + 13% HST was enclosed along with this report.

1.2. Objectives

The objectives of the proposed research are to document the following information using 2D Petroleum System Modelling of one new composite seismic line (NOVSPAN 1600) and on two revised composite seismic lines (NOVSPAN 1400 and FGP88-1a).

- ❑ Define the source rock maturity and the burial, heat flow, temperature, and pressure histories through geological time intervals using the measured heat flow data,
- ❑ Identify the hydrocarbon migration fairways: vertical and lateral migration and charge characteristics of each individual reservoir and seal stability
- ❑ Assess each individual reservoir saturation, hydrocarbon phase and fingerprinting of source rock input within various reservoir hydrocarbon composition
- ❑ Establish the mass balance of hydrocarbon generation, expulsion, reservoir preservation, and leakage comparing all three seismic lines (NOVSPAN Line 1400, FGP 88-1A, and NOVSPAN Line 1600).

2. PETROLEUM SYSTEM MODELLING: GEOLOGY, WELLS AND INPUT PARAMETERS

The Scotian Basin is one of the major passive margin Triassic-Quaternary epicentres in Eastern Canada. This basin, within Nova Scotia's provincial jurisdiction, extends from the Laurentian Subbasin in the east to the Yarmouth Arch on the United States-Canada border in the west. The aerial extent for exploration areas of the deepwater Scotian Basin is approximately 150, 000 square kilometres. The Scotian Basin contains Mesozoic-Cenozoic sedimentary

rocks, which are up to 16 km thick. It developed during the break-up of the Supercontinent Pangaea in the Late Triassic to Early Jurassic (~230-190 Ma) Period as North America separated from Africa (Jansa and Wade, 1975; Welsink et al., 1989; Wade and MacLean, 1990; Loudon 2002). In the Nova Scotia Margin, the extrusive volcanism in the southwest during the Bajocian age (example; Georges Bank) to the non-volcanic margin in the northeast (example: Sable Subbasin) as seen through the East Coast Magnetic Anomaly documents the boundary between the continental and the oceanic crust (Dehler et al, 2004; Funck et al., 2004; Loudon et al., 2005; Wu et al., in press).

Approximately 167 wells have been drilled in the Scotian Slope region. Only five wells (Acadia K-62, Albatross B-13, Shelburne G-29, Shubenacadie H-100, and Tantallon M-41; Figure 1a) were drilled in the Scotian Margin and no significant quantities of hydrocarbons could be detected in this region. In the second phase of petroleum exploration activity between 1999-2004, renewed interest in hydrocarbon exploration in the deepwater offshore Nova Scotia resulted in the drilling of six wells in the Scotian Margin (Annapolis B-24/G-24, Balvenie B-79, Crimson F-81, Newburn H-23, Torbrook C-15, and Weymouth A-45). However, only in the Annapolis G-24 well, Marathon Oil and its partners made a gas and condensate discovery in the Mississauga sands (Middle to Early Cretaceous). Approximately 30 meters of net pay had been encountered over two zones in the Mississauga (Cretaceous) sands.

This study will include the petroleum system development histories in sediments between the Late Triassic [Norian: 210 Ma] to Recent period in the area deepwater sediments of the Scotian Basin. The three seismic lines (FGP 88-1A, NOVSPAN 1600, and NOVSPAN 1400) of the Phase II research for the Dalhousie-OETR contract were carried out in the western part of the Sable Subbasin and the eastern portion of the Shelburne Subbasin (Figures A-1). The sediments within both seismic lines FGP 88-1a and NOVSPAN 1400 are

associated with salt diapirs (Figures 4a, 4b, and 4c). Line 1600 has also been connected with some rooted autochthonous Jurassic age base salt structures and includes some allochthonous salt tongues (Figure 4d). The Torbrook C-15 and Moheida P-15 wells have been projected on line NOVASPAN 1400 line (Figure 5a). The wells Acadia K-62 (in the shelf) and the Shubecadie H-100 wells could be projected on seismic line FGP 88-1A (Figure 5a). The Balvenie B-79 well lies close to seismic line NOVASPAN 1600. However, the Balvenie B-79 was not projected on the seismic line 1600. Three shelf wells (Como P-21, Panuke P-09 and Panuke H-08) have been projected within the seismic line 1600.

The 2D Petroleum System Modelling includes three parts of composite work schedule: (1) **Petrobuilder** – this part requires input parameters of geological, geophysical, and geochemical data; (2) **Simulator** – in this phase, the modeller has to define the time and quality of modelling parameters of a chosen seismic file. Moreover, the modeller has to assign the output parameters using various kinetics and calibration components; and (3) **Viewer 2D** – this section of the software illustrates the final output of the modelling data showing the calibration of heat flow, maturity, hydrocarbon expulsion, and reservoir saturation, etc.

2.1. Petrobuilder: Input Parameters

The input parameters are similar to that defined in the Phase I Report of the OETR-Dalhousie contract (Mukhopadhyay, 2008). For details on the input parameters of various geological, geophysical, and geochemical elements and their interpretation, refer to Kidston et al. (2002), Mukhopadhyay (2008; 2006), Eric Negulic (2007), Shimeld (2004), Young (2005), Wade and Mclean (1990), and Wade et al. (1995). The geological database includes the following (incorporated by Mukhopadhyay from various literatures):

- Formation boundaries,
- Possible lithology or lithology mixes for each stratigraphic unit,

- Defining the timing of erosion, paleowater depths, and paleotemperature (through time) from biostratigraphic analysis, and
- Designating the hydrocarbon reservoirs and their proper seals in relation to various play types, etc.

Various students and staff members from the Department of Oceanography and Department of Earth Sciences, Dalhousie University have incorporated the geophysical database on the target three seismic lines (1400, 88-1a, and 1600). GX Technology has provided the depth converted seismic images for both lines. In the Phase II study of the OETR-Dalhousie University Contract, the line 1600 and the revised lines of 88-1a and 1400 have been utilized for the petroleum system modelling.

The geochemical database has been provided by Dr. P. K. Mukhopadhyay.

This data includes the following:

- ❖ defining organic richness of various source rock intervals and hydrocarbon potential,
- ❖ present day maturity, temperatures, and heat flow
- ❖ multi-component kinetics of two major source rocks (Jurassic Verrill Canyon and Cretaceous Verrill Canyon; Mukhopadhyay, 2006; 2008)
- ❖ oil and gas properties for each individual source rock based on compositional analysis by pyrolysis-gas chromatography (Mukhopadhyay, 2006).

For the 2D modelling of three seismic lines, the formation boundaries and age of each stratigraphic and lithological boundary have been assigned from the well history reports for individual wells (see Mukhopadhyay, 2008). The assignment of various stratigraphic nomenclatures from each individual well has been established using earlier publications (Wade and MacLean, 1990; Wade et al., 1995; Mukhopadhyay, 2008). Similar to Mukhopadhyay (2008), published

biostratigraphic data from the Geological Survey of Canada Basin Database and recent data from various reports have been utilized for the age, paleo-water depths, paleo-temperature, and unconformities at various intervals. Moreover, this data has precisely been established after discussions with various biostratigraphers and geologists working in Halifax, Nova Scotia.

The lithology and other properties of twelve (11 from the Slope and one from the shelf; see Mukhopadhyay, 2006; 2008; Figures 5a and 5b) wells from the Scotian Basin were utilized for splitting various horizons and implementing mixed lithology. For details of the input for the (a) lithologies, unconformities, and faults; (b) play types and reservoirs; (c) source rocks and petroleum system elements; (d) movement and timing of salt structures and their relationship with the various play types and reservoirs, see Phase I report of Mukhopadhyay, 2008.

2.2. Heat Flow

The entire Phase II modeling is based on the input of heat flow data along various locations of all three seismic lines (Line 1400, 88-1A, and 1600) measured by Dr. Keith Loudon and his team at the Oceanography Department of the Dalhousie University. The following Table 1 lists the measured heat flows and their locations from each individual seismic line.

Station No.	Lat. (N)	Long. (W)	X	Y	Offset (m)	Shot Point	Depth (m)	Heat Flow (mW/m ²)
<i>Line 1 (1400 profile)</i>								
08-hf101	42°34.07	62°17.48	557731.47	4713136.40	100700	3177	1700.00	23.9
08-hf102	42°26.62	62°15.32	560933.71	4700057.71	114200	2908	2180.00	34.7
08-hf103	42°21.42	62°13.71	562881.08	4690215.09	124300	2708	2467.00	37.3
08-hf104	42°20.07	62°13.29	563876.25	4687289.61	127300	2646	2530.00	38.1
08-hf105	42°18.89	62°12.98	563678.13	4686122.53	128500	2626	2616.00	46.9
08-hf106	42°17.50	62°12.60	564565.41	4683077.27	131700	2563	2685.00	39.3
08-hf107	42°16.15	62°12.24	565420.07	4680149.96	134800	2500	2750.00	40.3
08-hf108	42°13.00	62°11.40	566488.09	4674153.31	140900	2378	2888.00	37.1
08-hf109	42°10.15	62°10.65	567341.83	4669073.51	146100	2276	3031.00	39.4

08-hf110	42°07.45	62°09.93	568113.59	4664439.62	150900	2182	3095.00	43.3
08-hf111	42°05.61	62°09.38	569409.65	4661258.96	154300	2114	3191.00	65.7
08-hf112	42°04.19	62°09.03	570250.24	4658122.33	157600	2050	3301.00	54.9
08-hf113	42°02.51	62°08.61	570317.60	4655408.38	160300	1995	3370.00	43.1
08-hf114	41°58.88	62°07.66	571647.14	4649142.90	166800	1868	3475.00	43.4
08-hf115	41°55.85	62°06.87	572606.96	4643508.66	172600	1753	3520.00	56.6
08-hf117	41°51.93	62°05.80	574221.49	4636377.85	180000	1606	3778.00	51.7
08-hf118	41°47.85	62°04.74	575833.58	4628743.21	187800	1451	3789.00	43.3
08-hf119	41°40.29	62°02.83	578541.73	4614105.16	201700	1178	3910.00	46

Station No.	Lat. (N)	Long. (W)	X	Y	Offset (m)	Shot Point	Depth (m)	Heat Flow (mW/m^2)
-------------	----------	-----------	---	---	------------	------------	-----------	--------------------

Line 2 (88-1a profile)

08-hf201	42°49.75	61°28.46	624265.79	4743901.45	34300	2492	1482.00	29.1
08-hf202	42°46.25	61°24.59	629556.52	4736882.50	43100	2602	1890.00	31.7
08-hf203	42°42.55	61°20.22	636002.1	4728696.165	53500	2731	2341	43.9
08-hf204	42°37.68	61°16.32	641390.7	4721797.612	62200	2841	2671	54.7
08-hf205	42°35.84	61°14.42	643952.2	4718624.638	66300	2893	2763	65.5
08-hf206	42°34.40	61°13.00	645449.1	4715442.52	70000	1605	2920	61.3
08-hf207	42°33.32	61°11.91	647061.2	4713378.41	72600	2970	3010	72.8
08-hf208	42°32.13	61°10.75	648830.9	4710985.725	75600	3007	3170	60.7
*08-hf209	42°30.36	61°09.11	651737.5	4708062.383			3249	
08-hf210	42°27.51	61°06.22	655833.1	4702850.292	86000	3139	3535	47.1
08-hf219	41°58.54	60°37.64	695968.9	4650443.79	152000	3964	4180	42.6
08-hf220	41°53.29	60°32.54	703388.4	4640612.751	164500	4120	4337	44.5
08-hf221	41°47.24	60°26.66	711751.5	4629585.37	178200	4292	4464	41.1

Line 3 (1600 profile)

08-hf309	42°49.85	60°13.60	726101.8	4746783.642	150400	2406	2915	47
08-hf310	42°45.70	60°12.05	728958.4	4739021.285	158700	2242	3085	48.3
08-hf311	42°41.52	60°10.51	730914.9	4731120.244	166800	2077	2356	51.4
08-hf312	42°37.46	60°09.03	733626.4	4723602.946	174800	1919	3539	41.4
08-hf313	42°34.77	60°08.05	735106.5	4719050.445	179500	1824	3650	34.4
*08-hf314	42°32.15	60°07.08	736643.6	4713450.953	185300	1708	3785	
08-hf315	42°30.07	60°06.32	737559	4709570.841	189300	1626	3890	43.1
08-hf316	42°24.60	60°04.31	740639.6	4700195.174	199200	1429	4065	43.1
08-hf317	42°18.54	60°02.10	744260.9	4689008.382	211000	1196	4220	41.4

The high heat flows (55-65 mW/m²) in all three seismic lines are connected to the top of the salt diapirs. The basement heat flux and the paleoheat flow values have been incorporated based on the measured vitrinite reflectance in the central Scotia Basin and heat flow generated by various basement structures.

2.3. Source Rocks

Based on earlier and current research on source rock evaluation of the sediments from the Scotian shelf and slope wells and the DSDP wells of the Moroccan Margin and Blake Bahama Basin (Legs 76 and 79), the following stratigraphic units could be projected as potential source rocks within the Scotian Slope (modified from Mukhopadhyay et al, 2000; Mukhopadhyay, 2002; Mukhopadhyay et al., 2003; Rullkotter and Mukhopadhyay, 1986, Rullkotter et al., 1984):

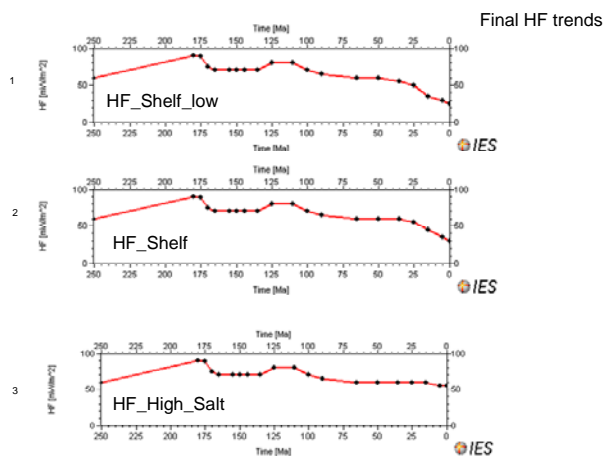
- Late Triassic/Early Jurassic lacustrine;
- Middle Jurassic marine;
- Late Jurassic marine (*Jurassic Verrill Canyon Formation*);
- Early Cretaceous marine (*Cretaceous Verrill Canyon Formation*);
- Mid-Cretaceous marine (Shortland Shale or Logan Canyon Formation);
- Early Tertiary marine (Banquereau Formation).

2.4. Assigned Petroleum Systems

Prior to the completion of the PS modelling, no sequence stratigraphic work was carried out. Therefore, selected conceptual reservoirs and seal rocks have been defined as the Petrobuilder input data similar to the Phase I studies on Line 1400 and 88-1a.

3. PETROLEUM SYSTEM MODELLING: RESULTS AND DISCUSSIONS

As the area of investigation lies within the eastern portion of the Shelburne Subbasin and the western part of the Sable Subbasin, the seismic line NOVASPAN Line 1400 with three major salt diapiric structures starts at the beginning of all three lines (Figure 1a). Figures 1, 2, 3 illustrate the details of petroleum system modelling in Petrobuilder and Simulation results for the seismic lines NOVASPAN 1400, 88-1A, and NOVASPAN 1600 lines respectively. As discussed earlier, all the above three seismic lines have similar horizon assignments, lithology mix, petroleum system element names, and similar geochemical properties (Figures 1b-i; 2b-i to 2b-v; and 3b-i to 3b-iii). However, the positions of the reservoir units in each seismic line are different. Based on several simulation runs of each seismic line and correlating the measured heat flow data (present day), the lateral heat flow variability for each seismic lines has been assigned in the Petrobuilder portion of the modelling. The following figure shows some examples of parts of heat flow assigned to all three seismic lines.



Figures 1b-ii, 2a-vi, and 3b-iv show the assigned heat flow for each of the three seismic lines (NOVASPAN 1400, 88-1A, and NOVASPAN 1600). These three

figures illustrate the extreme variability of heat flow between the shelf region, areas around a major salt diaper, and ultra-deep slope regions.

3.1. Seismic Line NOVSPAN 1400

Based on the seismic stratigraphy, the assigned conceptual reservoir units in line NOVSPAN 1400 lie mainly in the deeper slope region (around the three diapiric salts; Figure 1c-i). The correlation of measured and modelled heat flow values in this line indicates that some minor variability between these two parameters will still remain (Figures 1c-ii to 1c-vii). This minor variability between these two parameters was possibly caused by a lack of calibration of basement heat flow anomalies. In 2D petroleum system modelling, it is extremely difficult to incorporate the change of basement flow values in geological time. However, this variability is minor compared to the 2007 modelling work when no measured heat flow data was available. However, the 2007 modelling data shows better heat flow correlation on top of some diapiric salt structures (Mukhopadhyay, 2008; Figure 1c-vii).

The present day temperature and maturity profiles illustrate a higher temperature and maturity on top of the salt diapirs compared to the flank region (Figure 1c-viii and Figure 1c-ix). A similar effect could be documented for the generation of oil and gas as the oil zone could be observed in the stratigraphically higher zones, which are associated with the diapiric salts (Figure 1c-x). The pore pressure profile illustrates that deeper Late Jurassic reservoirs may encounter an overpressure condition (Figure 1c-xi).

The onset of hydrocarbon expulsion data indicates that only the Late Triassic, Middle and Late Jurassic, and Early Cretaceous source rocks are currently lying within the hydrocarbon expulsion phase (Figure 1d-i). All other source rocks above the Early Cretaceous source rocks are currently immature for hydrocarbon expulsion (Figures 1d-i and 1d-ii). Most of conceptual late

Jurassic reservoirs are fully saturated with both liquid and gaseous hydrocarbons.

The flash calculation and source rock fingerprinting of a selected late Jurassic conceptual reservoir 41834 was mainly saturated with liquid hydrocarbons (24.8% with C15+ and 32.8% C6-C14 hydrocarbons) with an API of 59.3 and mainly derived from the Kimmeridgian to Oxfordian marine Type II source rock (Figures 1e-ia, 1e-ib, 1e-ic, 1e-id, and 1e-e). Minor contributions of hydrocarbons come from the Misaine and Top Jurassic source rocks (Figure 1e-ic). The hydrocarbons in the reservoir were fully charged only during the last 10 Ma although most of reservoir hydrocarbons were partially saturated before 100 Ma.

Some contrasting source rock input could be observed in two early Cretaceous reservoirs (numbers 41889 and 41869). The Early Cretaceous reservoir (41869) that is situated in the middle section of the seismic section contains mainly liquid hydrocarbons (56% is C15+ oil) originated from the Jurassic Verrill canyon source rock (Figures 1e-iiia and 1e-iiib). Similar early Cretaceous reservoir in the ultra-deep water (41889; 54.9 API; Figure 1e-iiia) consists of only 40% liquid hydrocarbons (both C15+ and C6-C14 components) and the rest are gas (methane and C2-C5 components; Figure 1e-iiib). On the other hand, the Palaeocene reservoir (42010; Figure 1e-iva) hydrocarbons (mainly liquid in vapour phase) was derived from mixed source rock contributions (Misaine and Jurassic or Cretaceous Verrill Canyon) and has a mixture of both oil and gas components (Figure 1e-ivb, Figure 1e-ivc, and Figure 1e-ivd).

The mass balance of all reservoir hydrocarbons indicates that reservoir hydrocarbons in all reservoirs have the following source rock contributions: 17% from late Triassic; 28% from Jurassic Verrill Canyon; 30% comes from the Misaine formations; and the rest comes from some unknown source rocks (Figure 1f-i). The composite mass balance calculation also suggests that 150

MTons of hydrocarbons slowly accumulated during the last 100 Ma although most of the reservoir hydrocarbon accumulation occurred between 135 and 110 Ma (Figures 1f-ii and 1f-iii).

3.2. Seismic Line FGP 88-1A

In contrast to line NOVASPAN 1400, the correlation of measured and modelled heat flow values in line FGP-88-1a indicates that there is only minor variability between these two parameters (Figures 2b-i, 2b-ii and 2b-iii). The minor variability as noticed near the major salt diapir may indicate that during seismic modelling the proper shape of the salt diapir has not been defined precisely. Therefore, we can notice a slight abnormality around the salt diapir region (Figure 2b-iii).

Similar to Line 1400, the present day temperature and the maturity profiles illustrate a higher temperature and maturity on top of the salt diapirs compared to the flank region (Figures 2c-i, 2c-ii and 2c-iv). Because of lower heat flow history in this line, the maturity calibration data indicates that even the late Triassic source rocks could lie within the main dry gas generation zone. The pore pressure profile illustrates that all conceptual reservoirs (late Triassic, late Jurassic, and early Cretaceous) will definitely encounter an overpressure situation (Figure 2c-iii). The transformation ratio of five major source rocks indicates that all source rocks below Cretaceous Verrill Canyon have more than 90% kerogen transformation to hydrocarbons (Figure 2c-v).

In the Shubenacadie I-100 well, the one-dimensional extraction data suggests that the measured (vitrinite reflectance) and calculated maturity and temperature lines correlated quite well establishing the accuracy of low heat flow values in this section (Figures 2d-ii and 2d-iii). Similarly, the pressure profiles of the Shubenacadie I-100 well coincide quite nicely with the well data (Figure 2d-iv).

The onset of hydrocarbon (HC) expulsion on line 88-1a indicates that the HC expulsion begins in the Triassic source rock around 175 Ma and is still expelling HCs at a slow pace (Figure 2e). On the other hand, the Early Cretaceous source rock starts expelling HCs since 110 (Figure 2e).

The conceptual late Triassic reservoirs in the ultra-deep waters of line 88-1a indicates that these reservoirs are currently fully charged mostly with dry gas although some reservoirs contain liquid hydrocarbons (Figures 2f-i, 2f-ii, and 2f-iii). The source rock fingerprinting of hydrocarbons within one selected late Triassic reservoir (number 27339) shows that the HCs are all dry gas (methane) and were derived from the late Triassic lacustrine Type I or II source rocks (Figures 2f-iv and 2f-v). One dimensional extraction of one selected late Triassic reservoir (number 27339) indicates that this reservoir lies in a major overpressure state so the current reservoir temperature would be between 150°C to 200°C, and has a maturity around 3.5% R_o (Figures 2f-vi, 2f-vii, and 2f-viii). Similarly, another late Triassic reservoir (number 27340), HC was derived from similar late Triassic source rocks (Figure 2f-ix and 2f-x). The hydrocarbons in those late Triassic reservoirs may generate condensate at the surface pressure and temperature conditions.

An illustration of hydrocarbon (liquid and vapour) expulsion vectors from the late Triassic, late Jurassic and early Cretaceous source rocks through various geological time indicates that the late Triassic reservoirs in the distal part of the seismic line 88-1a were saturated with liquid hydrocarbons between 144 and 65 Ma (Figures 2f-xi, 2f-xii, 2f-xiii, and 2f-xiv). After 65 Ma, most of the reservoir hydrocarbons in the late Triassic reservoirs have been transformed or cracked to dry gas and converted to the vapour phase. In the shelf and upper slope side of the line 88-1a, the migration of hydrocarbon vectors indicates that there is a massive loss of hydrocarbons (both laterally and vertically) from three other conceptual HC-saturated reservoirs of the late Jurassic, Early

Cretaceous, and Miocene periods (Figures 2f-xiii, 2f-xiv, 2f-xv, and 2f-xvi). It is quite surprising to see that hydrocarbons were preserved within similar reservoirs in the deep and ultra-deep water regions of the seismic line 88-1a (Figure 2f-xvi).

Contrary to line 1400, both late Jurassic reservoirs (numbers 27394 and 27398) the main hydrocarbon component in the reservoir would be methane (>50%). The liquid portion (mainly C6-C14 hydrocarbons) of the reservoir hydrocarbons would be an associated component (Figures 2g-i, 2g-ii, 2g-iii, 2g-iv, and 2g-v). These hydrocarbons in the late Jurassic reservoirs were derived from an input of three different source rock components (late Triassic, Misaine, and Jurassic Verrill Canyon; Figures 2g-ii and 2g-iv). Similarly, the hydrocarbons in the early Cretaceous reservoirs (numbers 27448) in the distal part of the line also contains a mixture of oil/condensate and methane (>50%) and were originated from a mixture of late Triassic, Jurassic Verrill Canyon, and Cretaceous Verrill Canyon source rocks (figures 2h-i, 2h-ii, and 2h-iii).

The mass balance of hydrocarbons in all reservoirs suggests that all reservoir hydrocarbons will be a composite mixture of oil (C15+)/condensates (C6-C14), wet gas (C2-C5), and dry gas (C1 or methane) (Figure 2j-i). Figures 2j-ii and 2j-iii illustrate the hydrocarbon inflow and outflow, generation balance, and total convertible kerogen, liquid and vapour for all reservoir hydrocarbons within this seismic line. Compared to line 1400, line 88-1a contains nearly double the amount of hydrocarbons accumulated (about 2000 MTons) within various reservoirs (Figure 2j-v).

3.3. Seismic Line NOVSPAN 1600

As discussed earlier, the seismic line NOVSPAN 1600 includes two rooted diapiric salt structures that have extended tongues and separate allochthonous

salt bodies (Figure 3a). This line also contains three projected wells (Como P-21 and Panuke wells).

Similar to earlier PS modelling of seismic lines (NOVSPAN 1400 and FGP 88-1a), the correlation of measured and modelled heat flow values in line NOVSPAN 1600 indicates that there is only minor variability between these two parameters (Figures 3c-ii, 3c-ii, 3c-iv, and 3c-v). This variability may indicate the low density of measured heat flow data. Moreover, no measured heat flow data was available in the shelf and shallower part of the slope region. Therefore, the correlation of measured and modelled heat flow could not be achieved.

The present day temperature and maturity profiles illustrate a higher temperature and maturity on top of the salt diapirs (Figures 3c-vi and 3c-vii). Slightly higher temperatures and maturity could also be observed on top of the allochthonous salt bodies. Because of higher basement structures, the shelf region is comparatively hotter compared to the slope areas except in the region surrounding the autochthonous or allochthonous salt bodies. Because of lower heat flow history of this line, the maturity calibration data indicates that even the basement rocks in the shelf and early Jurassic sediments in the ultra-deep slope could lie within the main dry gas generation zone (Figures 3c-vi and 3c-vii). The pore pressure profile illustrates that only the conceptual late Jurassic and lower reservoirs would have encountered an overpressure (Figure 3c-viii). The transformation ratio of five major source rocks indicates that with the exception of the Cretaceous Verrill Canyon source rock in the ultra-deep water region on the line, all other lower source rocks in the slope have more than 90% hydrocarbon transformations (Figure 3c-ix). This data also suggests that the Triassic lacustrine source rock (if present) could be one of the main hydrocarbon source rocks that has contributed oil and gas within the possible conceptual reservoirs within the Shelf area.

The combination of hydrocarbon zones and reservoir liquid or vapour accumulations indicates that (Figures 3c-x): (a) there are several smaller accumulations of deep gas reservoirs (especially in the shelf break areas) and liquid accumulation in the shelf (close to the Como P21 well). As such, the modelling results clearly indicate the primary reason the reservoir accumulation barely missed the Como P-21 well as the reservoir is a km away from the drilled well location. The maturity and temperature data of the 1D line extraction of the Como P-21 well indicates: (a) the Mohican Formation in that well could encounter 2.0% Ro and about 175°C temperature (Figure 3c-xi); and (b) the Jurassic reservoir should encounter a major overpressure (Figure 3c-xii).

The onset of hydrocarbon expulsion data indicates that since 100 Ma, all five source rocks have started expelling hydrocarbons (Figure 3d-i). As discussed earlier, there are several liquid and vapour accumulations that can be encountered in both shelf and slope areas in this line (Figure 3d-ii). However, the size of the reservoir would be smaller than line 88-1a.

Hydrocarbon fingerprinting of early Cretaceous reservoirs in the shelf region (reservoir numbers 67486 and 67540; Figures 3e-ia and 3e-iiia) has established that: (a) the reservoir fluids are a combination of major gas and minor condensate derived from a mixture of various source rocks but mainly from the Cretaceous Verrill Canyon (Figures 3e-ib, 3e-ic, 3e-iib, and 3e-ii-c); and (b) the fluid may have an API of 69.7. On the other hand, the characterization of reservoir fluids from the shelf-break late Jurassic reservoir (number 61383) indicates that although the reservoir fluid may have an API of 51.5, but more than 90% of hydrocarbon components are dry gas (methane) methane at the reservoir temperature and pressure. The methane and liquid hydrocarbons in the reservoir are derived from the Misaine and Jurassic Verrill Canyon source rocks (Figures 3e-iiia, 3e-iiib, and 3e-iiic).

A documentation of hydrocarbon migration vectors through the geological ages clearly indicate that most of the reservoir hydrocarbons have been continuously leaking on the surface since 90 Ma (Figures 3f-i, 3f-ii, 3f-iii, 3f-iv, and 3f-v). This situation has persisted throughout the geological time periods from 90 Ma to the present day. In comparison to the seismic line NOVSPAN 1600, the vertical hydrocarbon leakage from the seismic line 88-1a is much less although both lines have similar lithology and petroleum system elements.

Hydrocarbon generation from three major source rocks (late Triassic, Jurassic Verrill Canyon, and Cretaceous Verrill Canyon) illustrated that these source rocks have generated 4.0 to 9.5, 1.6 to 5.2, and 1.4 to 2.2 metric tons of hydrocarbons per sq. km, respectively along the seismic line 1600 from west to east (Figure 3g-i; Figure 3g-ii; Figure 3g-iii). The mass balance hydrocarbons in all reservoirs suggest that methane from the late Triassic and Jurassic Verrill Canyon source rocks would be the main contributors for all reservoir hydrocarbons (Figure 3h-i). The mass balance of source rock input and reservoir accumulations illustrate: (a) total hydrocarbon generated and expelled from the source rocks through geological time and accumulated in various reservoirs (Figure 3h-ii); (b) complete generation balance, amount of convertible kerogen, and the amount of liquid and vapour accumulated in various reservoirs through geological time (Figure 3h-iii); (c) timing of primary or secondary cracking and the amount of liquid and vapour accumulated in various reservoirs through geological time (Figure 3h-iv); and (d) petroleum system events chart with histograms showing the timing of total generated and total expelled hydrocarbons (Figure 3h-v).

4. PETROLEUM SYSTEM MASS BALANCE CALCULATIONS

The comparative mass balance of hydrocarbon generated from various source rocks and accumulated (in Metric Tons) in various reservoirs for seismic lines NOVSPAN 1400 and FGP 88-1a established that (Figure 4a): (a) The

hydrocarbon generation from various source rocks and accumulated in various reservoirs in line 88-1a indicated that the reservoirs in Line 88-1a contain almost 10 times more hydrocarbons than the seismic line 1400; (b) In line 88-1a, the Jurassic and Cretaceous Verrill Canyon source rocks have generated the highest amount of hydrocarbons, while in seismic line NOVASPAN 1400, the early Jurassic, Misaine (Callovia), and Jurassic Verrill Canyon source rocks contributed maximum; and (c) the main HC accumulation in line 88-1a is within the Early Cretaceous and late Jurassic reservoirs while the reservoir accumulation in seismic line 1400 mainly concentrated in the late Jurassic reservoir. On the other hand, in seismic line NOVASPAN 1600, the Cretaceous Verrill Canyon source rock generated the highest amount of HCs while all late Triassic, Late Jurassic and Early Cretaceous reservoirs accumulated hydrocarbons but in lower reservoir saturations (Figure 4b).

The overall comparative mass balance of hydrocarbons derived from 2D petroleum system modelling for all three seismic lines (NOVASPAN 1400, FGP 88-1a, NOVASPAN 1600) established that (Figure 4c): (a) all three lines have major hydrocarbon loss from the reservoirs; (b) line 88-1a has the highest amount of hydrocarbons generated, expelled, and accumulated; and (c) comparatively, lines 1400 and 1600 have at least five times less accumulated hydrocarbons in various reservoirs compared to line 88-1a.

5. CONCLUSIONS

The final interpretation of the thermal properties and hydrocarbon accumulation potential of three seismic lines (NOVASPAN 1400, FGP 88-1a, and NOVASPAN 1600) have been evaluated in the Phase II study of the 2D Petroleum System Modelling using the 2008 measured heat flow data along all three seismic lines. The current Phase II research established the following conclusions:

5.1. Seismic Line NOVSPAN 1400

- The modelled (used transient heat flow since the rifting) and measured heat flow values suggest that with the exception of two heat flow values (heat flow lines 110 and 111), all measured values are closely correlated. These two heat flow values are situated on top of the salt diapirs. This may indicate that (a) either the seismic interpretation on the outline of the salt diapir is not correct or (b) the calibration with the problem with the basement heat for any 2D seismic line,
- The heat flow values on top of the salt diapirs indicate that they are comparatively hotter than the heat flow values on the flanks (mini-basins) of the salt. However, the amount of heat flow variations depend on the thickness of individual salt structures and proximity of the salt diapirs to the sediment water interface locations,
- Because of lower heat flow trends (based on newly measured data) of this seismic line, all conceptual reservoirs (late Jurassic and early Cretaceous, and Paleocene) in the slope contain more than 50% oil (C15+ and C6-C14 hydrocarbons) compared to earlier report (Mukhopadhyay, 2007). The liquid hydrocarbons (oil and condensates) are mostly associated with dry and wet gas (C1 and C2-C5 hydrocarbons).
- The Mass Balance of hydrocarbons between the source rock generation, expulsion, and reservoir accumulation indicate that the (a) majority of the hydrocarbons show a migration loss due to seal instability; (b) Jurassic Verrill Canyon and Misaine source rocks are the main contributors for the accumulated hydrocarbons in various reservoirs.

5.2. Seismic Line FGP 88-1a

- Using the transient heat flow trends, the modelled and measured heat flow values have been calibrated. With the exception of three heat flow values (heat flow lines 206, 207, and 208), all measured flow values are closely calibrated. These three heat flow values are connected to the top of the diapiric salt. This anomaly between the measured and modelled heat flow could be caused by (a) an outline of the salt in the upper part of the section may not have been correctly drawn during the seismic interpretations, or (b) problems in attaining a well-defined basement heat flow along the 2-D seismic section. Similar to seismic line NOVSPAN 1400, both the temperature and maturity values on top of the salt diapirs are higher compared to the flank of the salt. However, the variation in heat flow values depends on the thickness of the salt diapirs and nearness to the surface,
- Because the revised model is calibrated with lower heat trends, both the Late Jurassic and Early Cretaceous conceptual reservoirs in the slope contain some additional liquid hydrocarbons (C15+ - oil and C6-C14 – condensate and light oil) within various reservoirs especially within Tertiary and Upper Cretaceous sections. In general, all early Cretaceous and late Jurassic reservoirs usually contain more than 75% methane and wet gas (C2-C5 hydrocarbons),
- Although the late Triassic conceptual reservoir contains mainly dry gas (methane), the reservoir temperature and pressure is much lower compared to our Phase I report (Mukhopadhyay, 2008). This could be useful for exploring the ultra-deep water reservoirs (if any) along this line. Moreover, lower heat flow within this area will also give an opportunity to drill the early Cretaceous and late Jurassic plays that could contain partially liquid hydrocarbons,
- Based on the composite mass balance of hydrocarbons generated and expelled from four major source rocks and accumulation within various

reservoirs suggest that even though more than 50% of the migrated hydrocarbons have been lost during the transit from reservoir and seal leakages, this seismic line has accumulated the highest amount of reservoir fluids (5 times more than seismic line NOVSPAN 1400 and NOVSPAN 1600).

- Eighty percent of the reservoir hydrocarbons in this line was methane and wet gas. The Jurassic and Cretaceous Verrill Canyon source rocks have generated the highest amount of hydrocarbons although the early Cretaceous and late Jurassic reservoirs have accumulated the highest amount of reservoir hydrocarbons

5.3. Seismic Line NOVSPAN 1600

- The modelled and measured heat flow values have been calibrated as closely as possible thus changing the transient heat flow trends. With the exception of one value (heat flow line 313), all measured flow values are closely fitting one other. However, this line needs much more measured heat flow data to achieve a better correlation between the measured and modelled heat flow values. Higher heat flow, temperature, and maturity could be documented on top of various salt diapirs. This feature is quite persistent similar to the other seismic lines. However, the variations in heat flow values depend on the thickness of the salt diapir and proximity to the surface
- Because the revised model is calibrated with lower heat trends, both the late Jurassic and early Cretaceous reservoirs in the slope contain a mixture of methane (>75%) and 25% condensate/light oil type of hydrocarbons
- Similar to line NOVSPAN 1400, the majority of the hydrocarbons expelled from four different source rocks from the late Triassic to early

Cretaceous reveal a major loss of reservoir hydrocarbons in various geological time periods from a migration loss and leakage in seal rock. This type of hydrocarbon leakage is quite vigorous in the early Cretaceous and younger reservoirs; (b) Jurassic and Cretaceous Verrill Canyon and source rocks are the main contributors of the accumulated hydrocarbons in both Jurassic and Cretaceous reservoirs.

6. ACKNOWLEDGMENTS

The author acknowledges the contribution and collaboration of Dr. Keith Loudon and from the Department of Oceanography, Dalhousie University for many fruitful discussions on various aspects of seismic interpretation. I acknowledge Dr. Mladen Nedimovic, Department of Earth Sciences, Dalhousie University for his laboratory facilities and other assistance. I acknowledge OETR for the overall contract and Financial Services, Dalhousie University for the contract payments. I acknowledge and thank Eric Negulic and other students from Dalhousie University for their assistance with the seismic interpretation and other matters. I gratefully acknowledge the help of various computer personnel, geoscientists and Managing Directors of IES Inc. (currently of Schlumberger Inc.), Aachen, Germany for their assistance and fruitful discussion during my stay in Aachen, Germany in both April and August 2009.

7. REFERENCES AND BIBLIOGRAPHY

Funck, T., Jackson, R.H., Loudon, K.E., Dehler, S.A. and Wu, Y. 2004. Crustal structure of northern Nova Scotia rifted continental margin (eastern Canada). *Jour. Geophys. Res.*, v. 109, B09102-1 to 19.

Gradstein, F. M., Ogg, J. G. et al. 2004. *A Geological Time Scale 2004*. Cambridge University Press, 500 p.

Hogg, J. R., Dolph, D. A., MacKidd, D. and Michael, K. 2001. 2001. Petroleum Systems of the Deep Water Scotian salt Province, Offshore Nova Scotia, Canada. In "Petroleum Systems of the Deep-Water Basins", GCSSEPM

Foundation 21st Annual Perkins Research Conference, Houston, Texas, p. 23-34.

Louden, K., Mukhopadhyay, P., Negulic, E., and Nedimovic, M. 2009. Heat flow calibration and hydrocarbon prospects as defined by petroleum system modelling within the western Sable Subbasin, Scotian Basin. Abstract 2009 OTANS Conference, Halifax, Nova Scotia. October 2009.

Louden, K., Helen, L, Funck, T. and Wu, J. 2005. Large-scale structural variations across the eastern Canadian Continental Margins: Documenting the Rift-to-Drift Transition. 25th Annual Annual GCS-SEPM Bob. F. Perkins Research Conference: Petroleum Systems of the Divergent Continental Margin Basins, p. 1-12 (CD-ROM)

Mukhopadhyay, P.K. 2009. Phase II Thermal & Petroleum System Modelling of seismic line NOVASPAN 1600 and the revision of modelling of Seismic Lines NOVASPAN 1400 and FGP 88-1A, Scotian Basin, Offshore Nova Scotia. Preliminary Report with interpretations. Submitted to Keith Louden, Dalhousie University, September 2009.

Mukhopadhyay, 2008. Thermal and petroleum system modelling of two composite seismic lines FGP 88-1A AND NOVASPAN 1400, Scotian Basin, Offshore Nova Scotia. *Final Report of Phase I Study for Dalhousie-OETR Contract*. 75 p. With figures and tables.

Mukhopadhyay, P. K., P. J. Harvey, and K. Kendell, 2006, Genetic relationship between salt mobilization and petroleum system parameters: Possible solution of finding commercial oil and gas within offshore Nova Scotia, Canada during the next phase of deep-water exploration: Gulf Coast Association of Geological Societies Transactions, v. 56, p. 627-638.

Mukhopadhyay, P. K. 2006. Evaluation of the petroleum systems by 1D and 2D numerical modeling and geochemical analysis in the area of most recent exploration wells on the Deepwater Scotian Slope, Offshore Nova Scotia. Report for Nova Scotia Department of Energy, *Contract Number 6012740*. 145 pages, 250 figures and tables

Mukhopadhyay, P. K., Wade, J. A. and Kruge, M. A. 2000. Petroleum Systems of the Scotian Basin, Offshore Eastern Canada and its Implications for Future Prospects in the Shelf Break and Slope Areas. AAPG Annual Convention Extended Abstract, New Orleans, Louisiana

Mukhopadhyay, P. K., Wade, J. A., Kruge, M. A., Samoun, A. and Harvey, P. J. 2002. Deepwater petroleum system of Jurassic-Tertiary sediments of the

Scotian Basin, offshore Nova Scotia, eastern Canada. AAPG Annual Meeting Abstract, March 10-13, 2002, Houston, Texas.

Mukhopadhyay, P. K., Wade, J. A. and Kruge, M. A. 1995. Organic facies and maturation of Jurassic/Cretaceous rocks, possible oil-source rock correlation based on pyrolysis of asphaltenes, Scotian Basin, Canada. *Org. Geochem.* 22 (1), p. 85-104.

Negelic, Eric. 2007. Interpretation of 2D Seismic Lines in the Slope Diapiric Province of the Scotian Basin for Petroleum System Modeling and Comparison with Analogue Modeling Sections. Shell Canada Funded Summer Student Report, Department of Earth Sciences, Dalhousie University, 27 p.

Rullkotter, J. and Mukhopadhyay, P. K. 1986. "Comparison of Mesozoic carbonaceous claystones in the western and eastern North Atlantic (DSDP Legs 76, 79, and 93)": In (Summerhayes, C. P. and Shackleton, N. J. (Eds.) *North Atlantic Paleoceanography*. Geological Society of London Special Publication, v. **22**, p. 377-387.

Rullkotter, J., Mukhopadhyay, P. K., Disko, U., Schaefer, R. G., and Welte, D. H. 1986. „Facies and diagenesis of organic matter in deep sea sediments from Blake Outer Ridge and Blake Bahama Basin, western North Atlantic": In Degens, E. T. et al. (Eds), *Biogeochemistry of Black Shales*, University of Hamburg Special Publication, v. **60**, p. 179-203.

Rullkotter, J., Mukhopadhyay, P. K., Schaefer, R. G., and Welte, D. H. 1984. "Geochemistry and petrography of organic matter in sediments from Deep Sea Drilling Project Sites 545 and 547, Mazagan Escarpment", In Hinz, K. et al. (Eds) *Initial Report of DSDP Leg 79*, p. 775-806.

Shimeld, J. W. 2004. A comparison of Salt Tectonic Subprovinces beneath the Scotian Slope and Laurentian Fan. 24th Annual GCS-SEPM Foundation Bob F. Perkins Research Conference, Houston, pp 502-532, CD-ROM.

Shimeld, J. W. 2004, A comparison of Salt Tectonic Subprovinces beneath the Scotian Slope and Laurentian Fan. 24th Annual GCS-SEPM Foundation Bob F. Perkins Research Conference, Houston, pp 502-532, CD-ROM.

Wade, J. A., MacLean, B.C. and Williams, G.L. 1995. Mesozoic and Cenozoic stratigraphy, eastern Scotian Shelf: new interpretation. *Can. Jour. Earth Sc.* v. 32, p. 1462-1473.

Wade, J. A. and MacLean, B.C. 1990. Aspects of the geology of the Scotian Basin from recent seismic and well data. In Keen, M. J. and Williams, G. L.

(Eds.). Geology of the Continental Margin of Eastern Canada, Geology of Canada, Part 2, p. 167- 238.

Wade, J. A., Campbell, G.R., Procter, R.M., and Taylor, G.C. 1989. Petroleum Resources of the Scotian Shelf. Geological Survey of Canada Paper 88-10, 26p, English version.

Wu, Y. 2007. Crustal structure of the ventral Nova Scotia margin and the transition from volcanic to non-volcanic rifting off eastern Canada. Ph.D. thesis, Dalhousie University, 341 pp.

Wu, Y., Loudon, K.E., Funck, T., Jackson, H.R., and Dehler, S.A., Crustal structure of the central Nova Scotia margin off Eastern Canada, Geophy. J. Int., in press.

Petroleum System Modelling – Scotian Basin

General Figures

Study Area: Seismic Lines 89-11 (line 2), 1400, 1600 and 88-1A

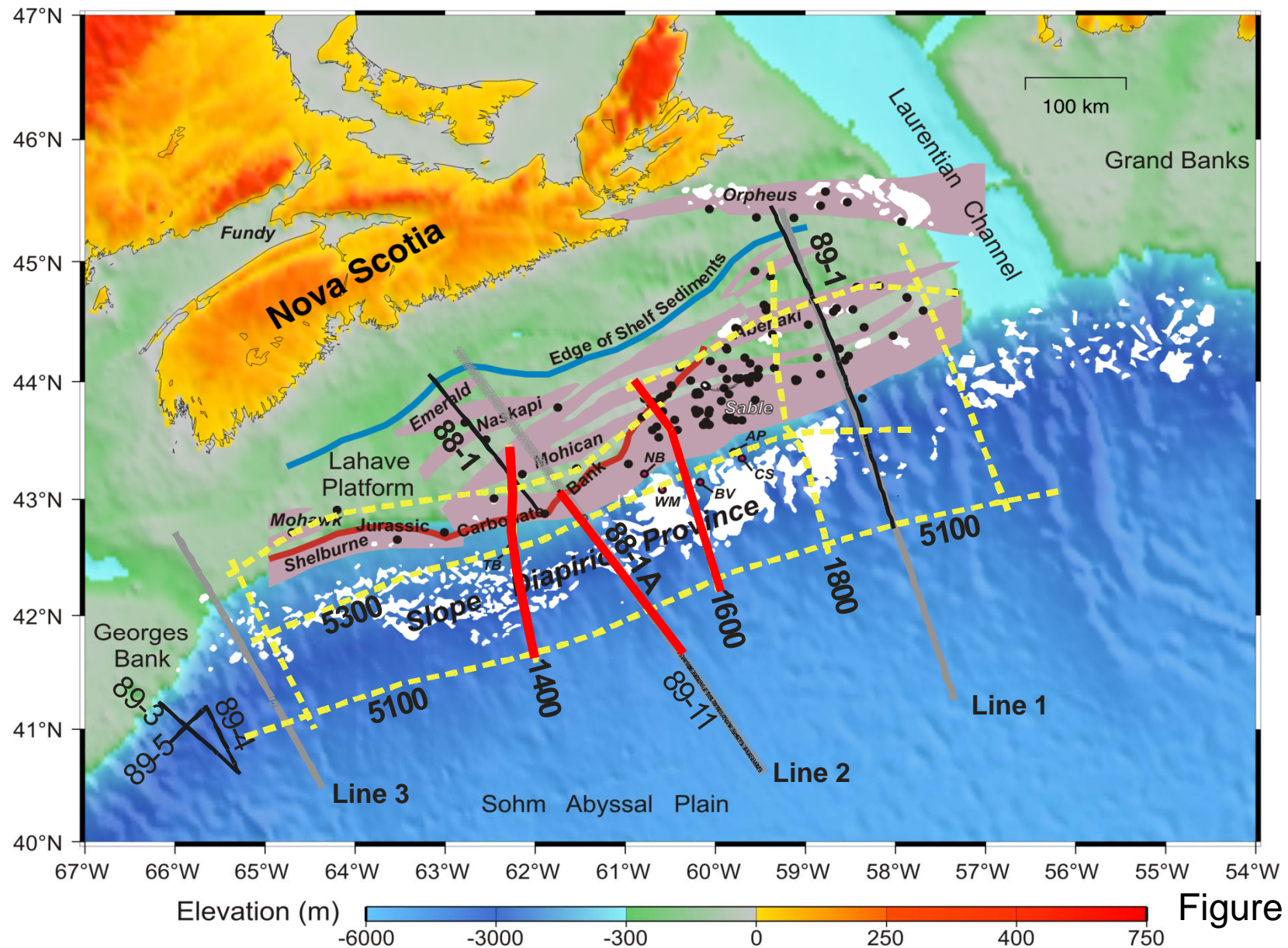


Figure A-1

Crustal Structure: Line 2

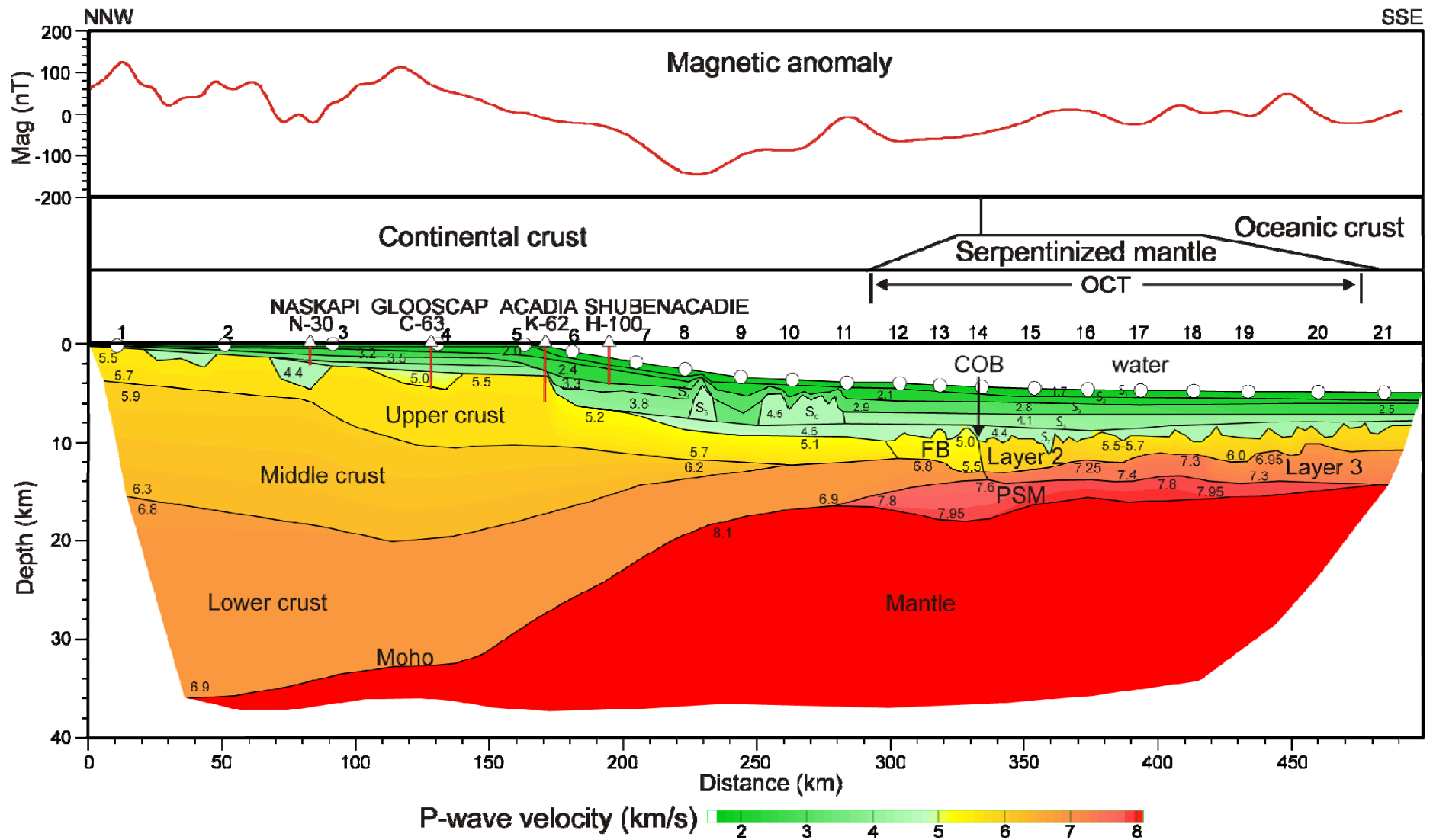
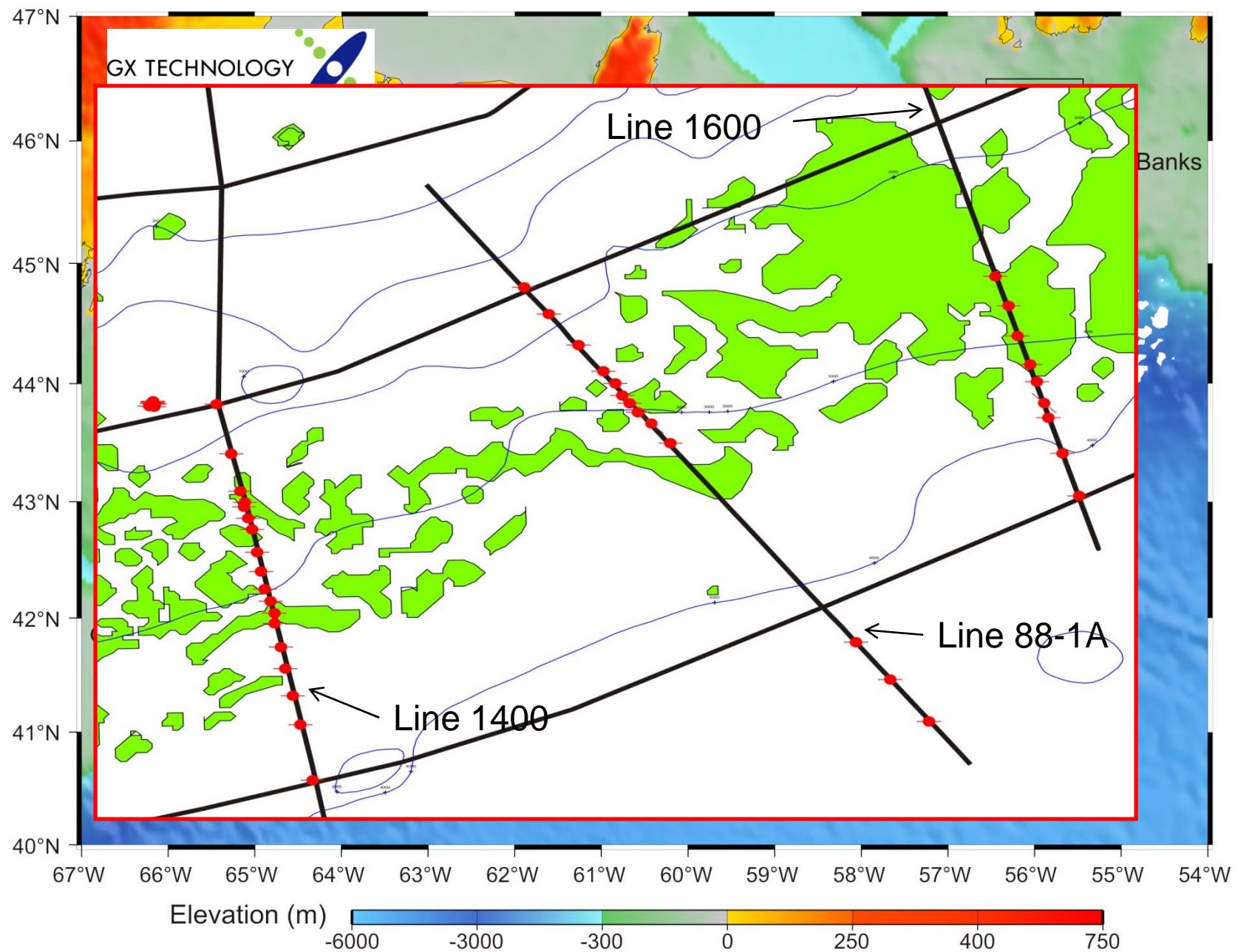


Figure A-2

2008 Heat Flow Survey

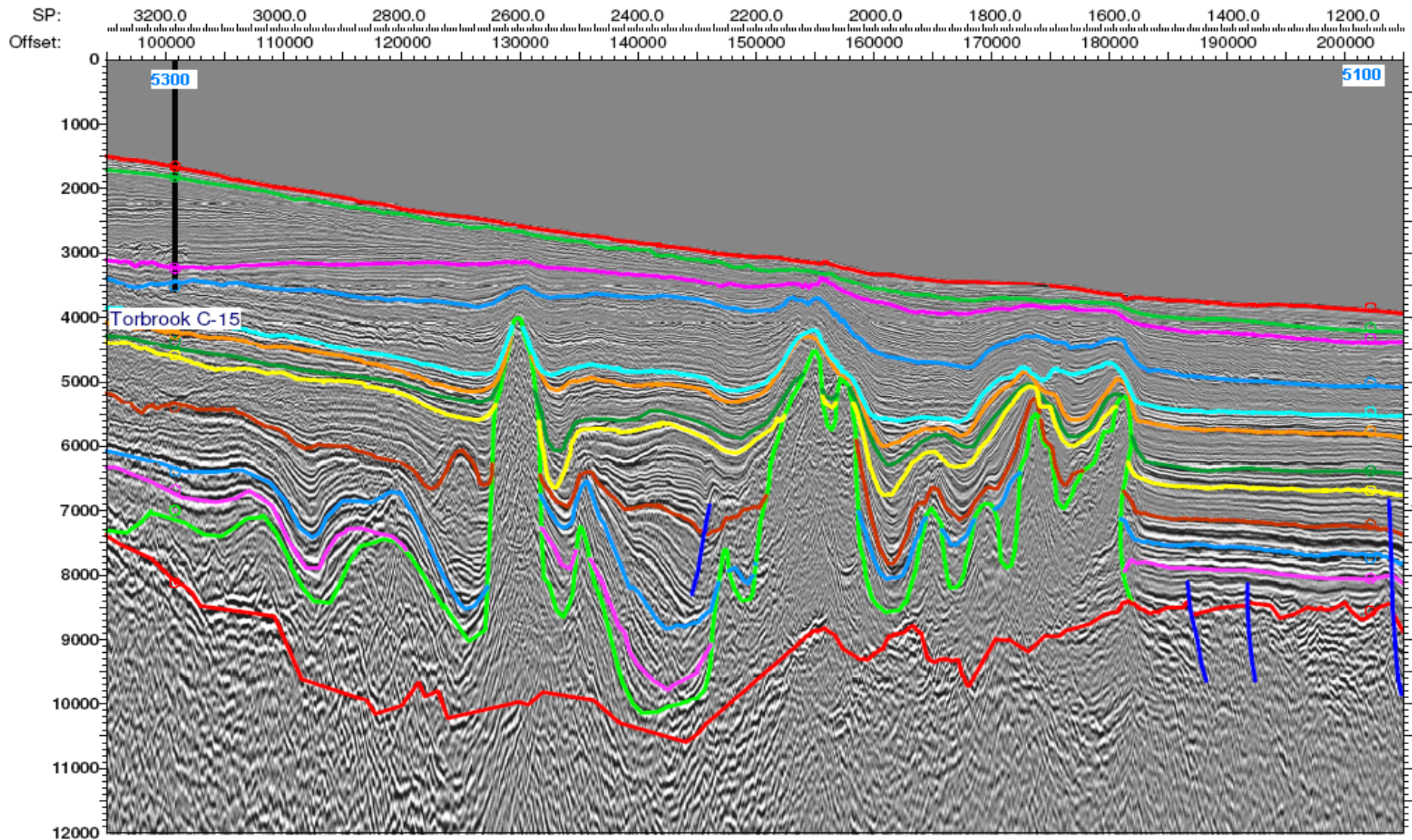
Figure A-3



Seismic Interpretation: Line 1400

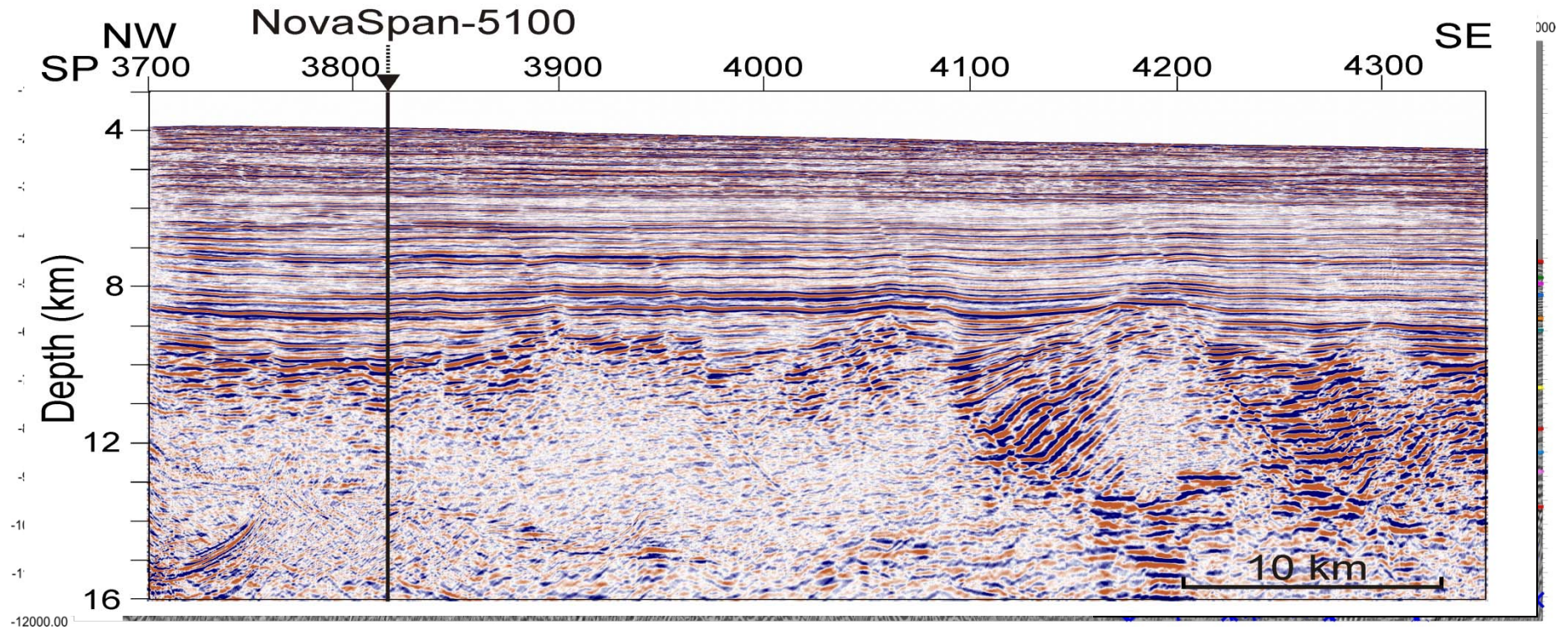
Figure A-4a

- Large vertical salt diapirs



Seismic Interpretation: Line 88-1a

Figure A-4b



Line 88-1A (bottom) & Seafloor Heat Flow Comparison

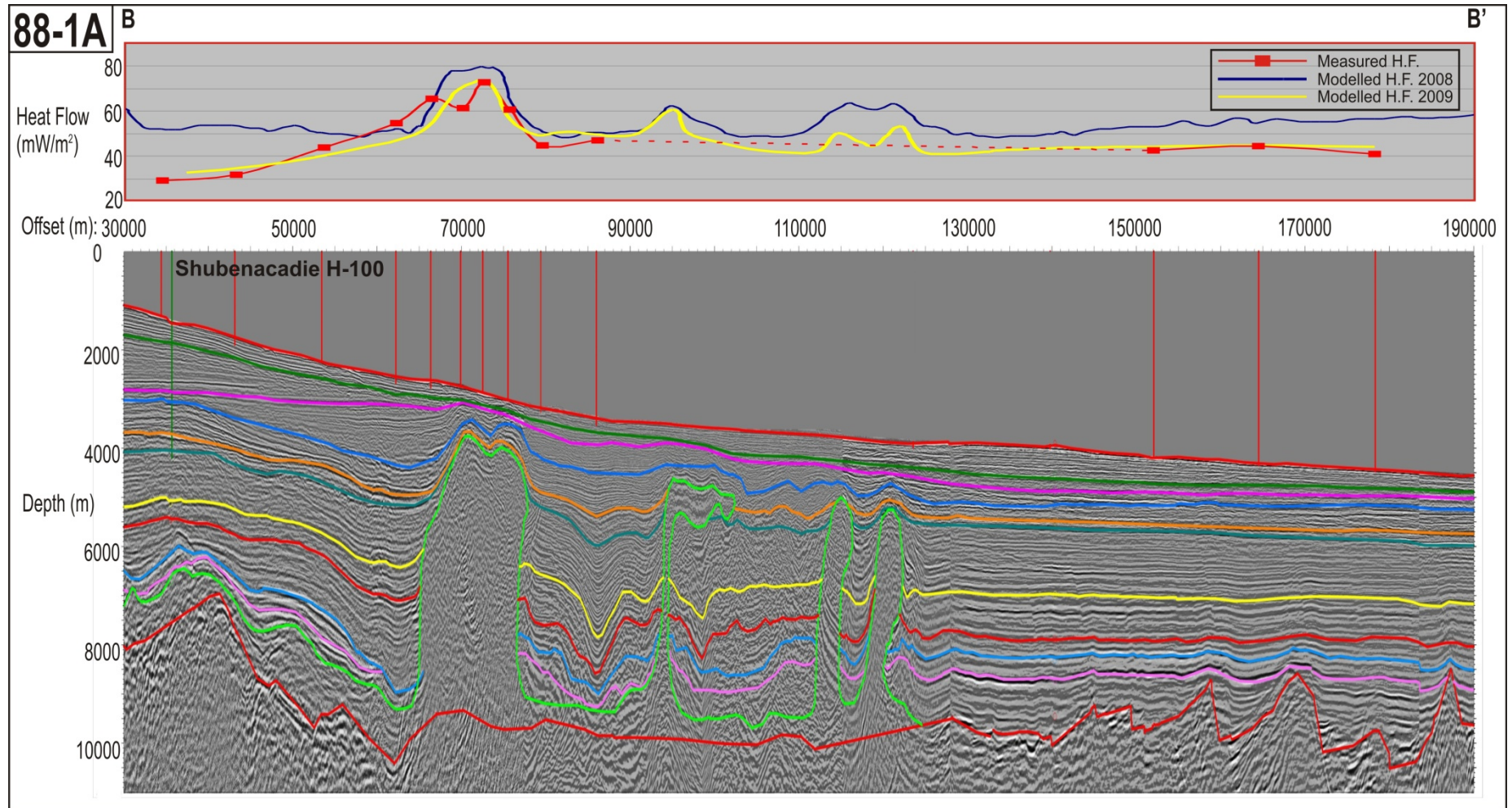


Figure A-4c

Seismic Interpretation: Line 1600

Figure A-4d

- Salt diapirs and canopies

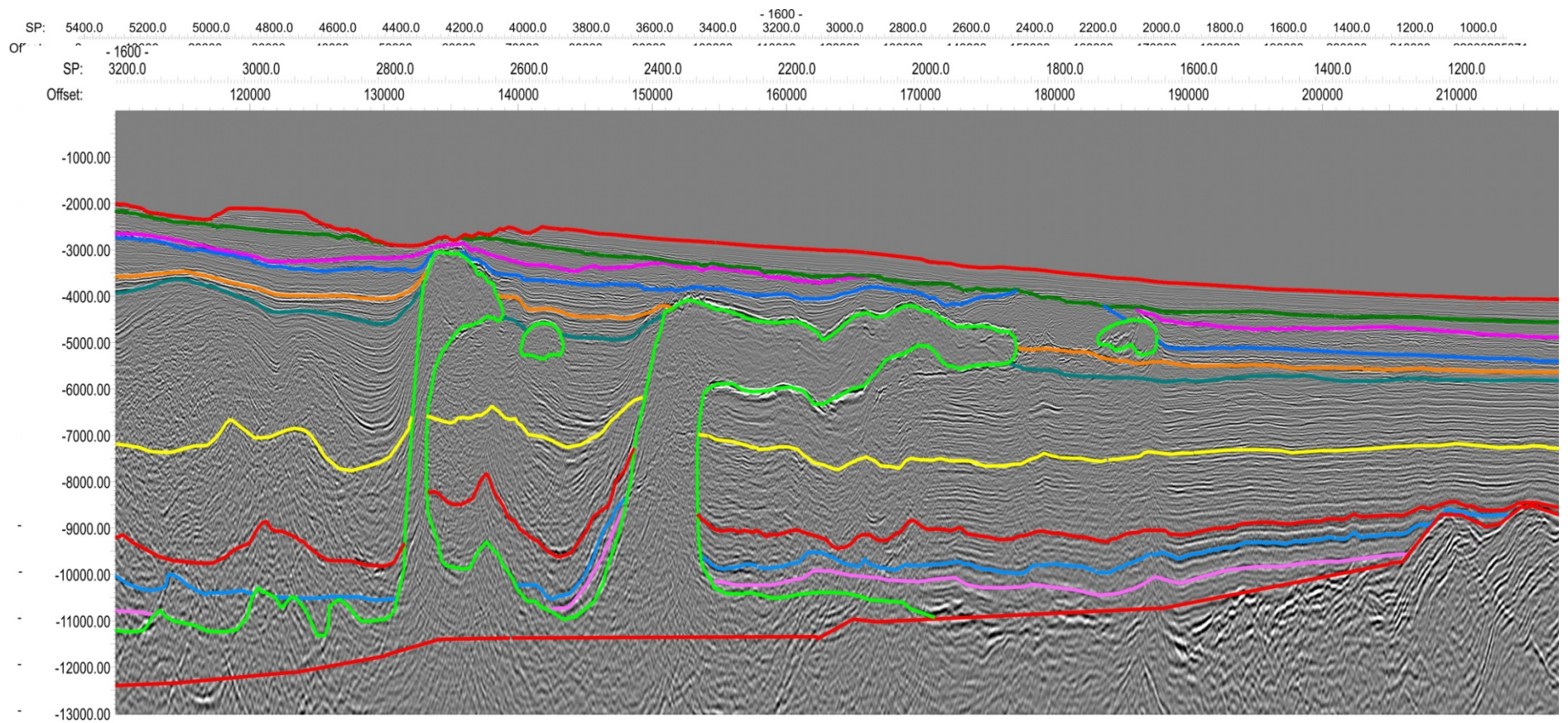
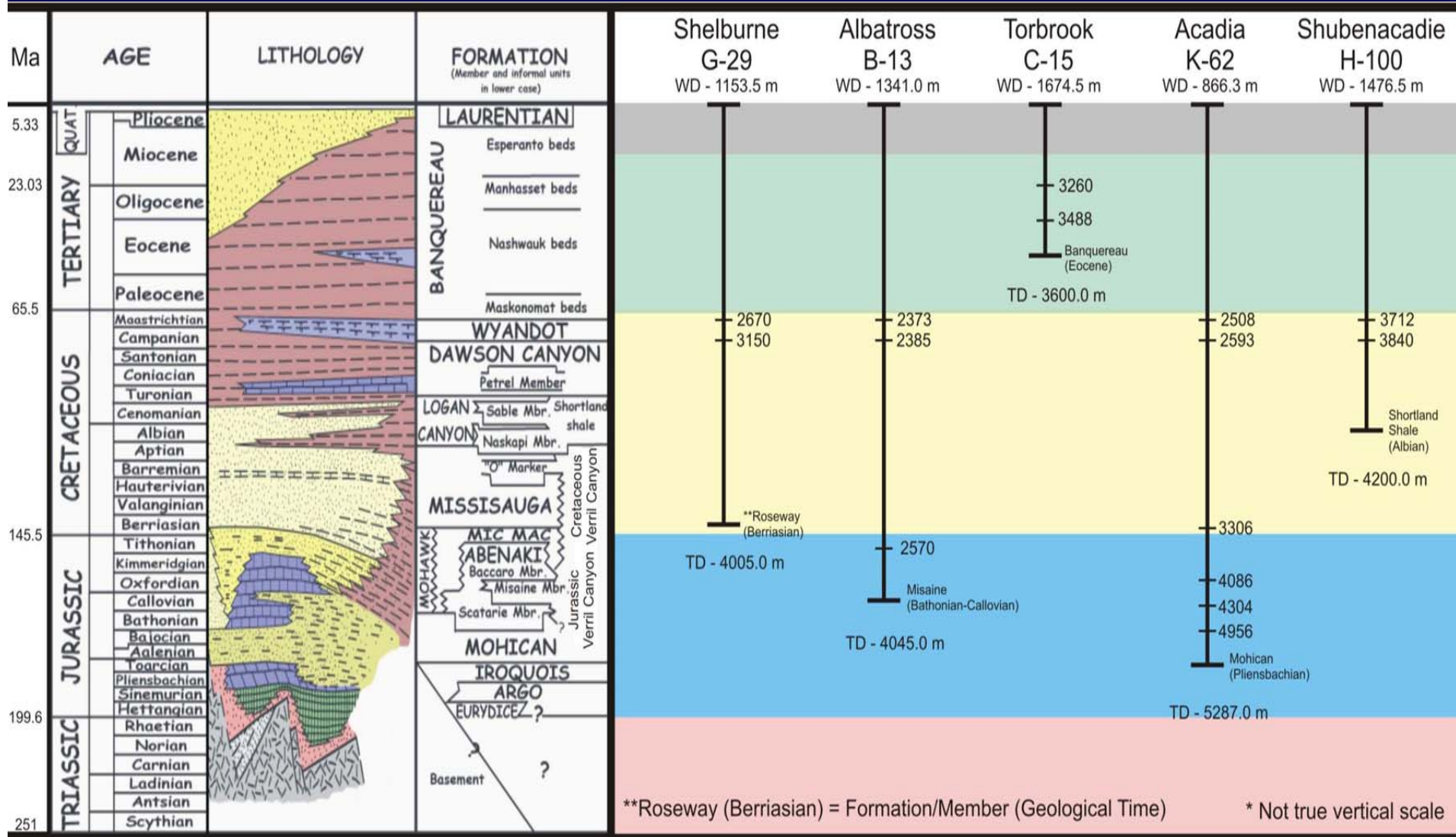


Figure A-5a

Western Sable Subbasin & Eastern Shelburne Subbasin



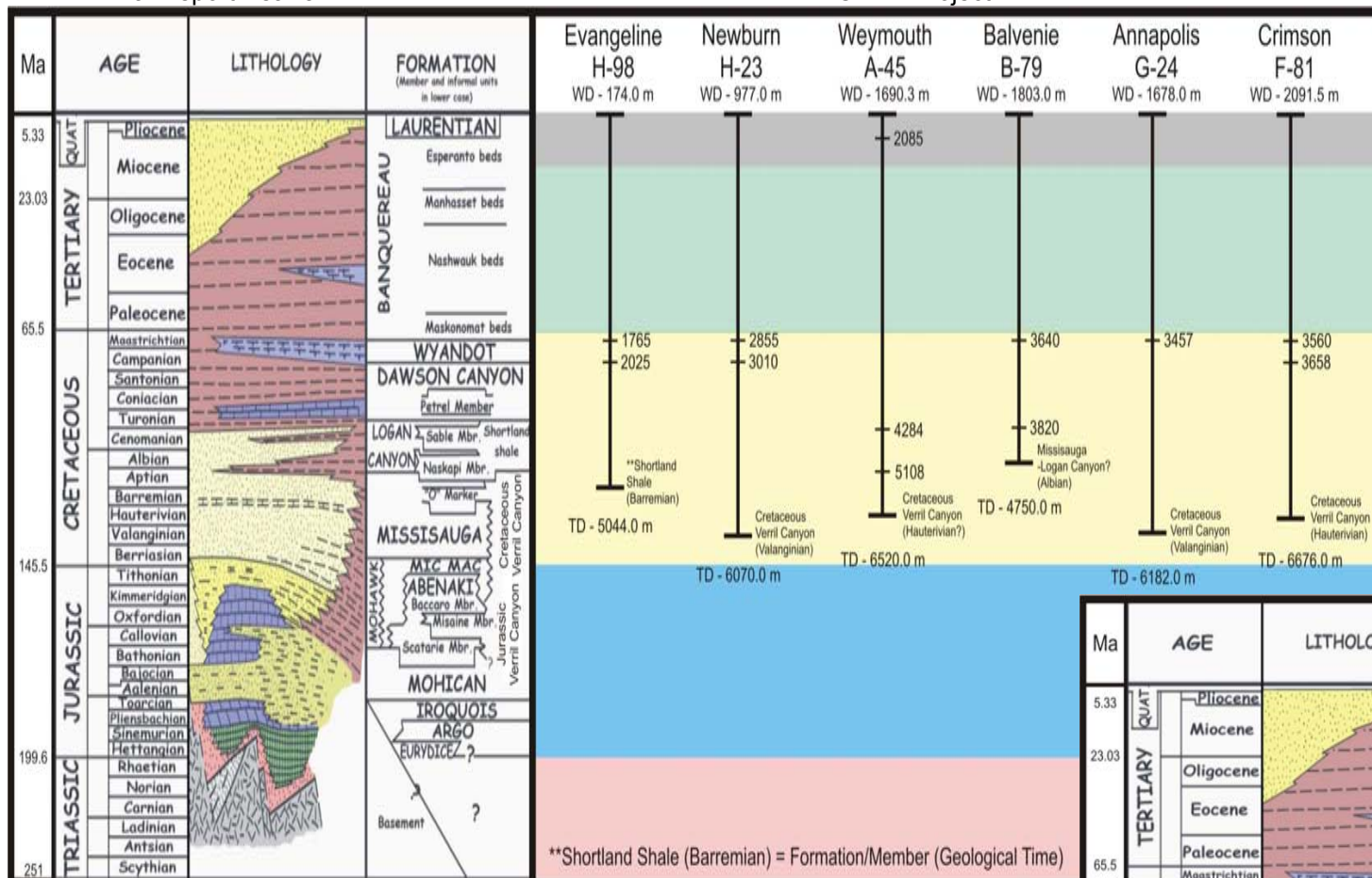
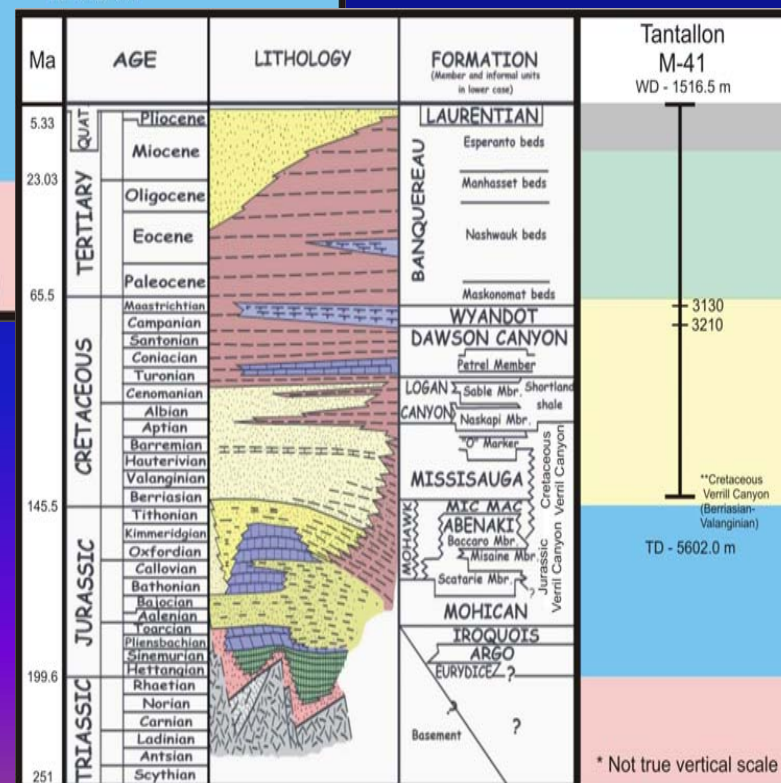


Figure A-5b

Eastern Sable Subbasin



Western Laurentian Subbasin

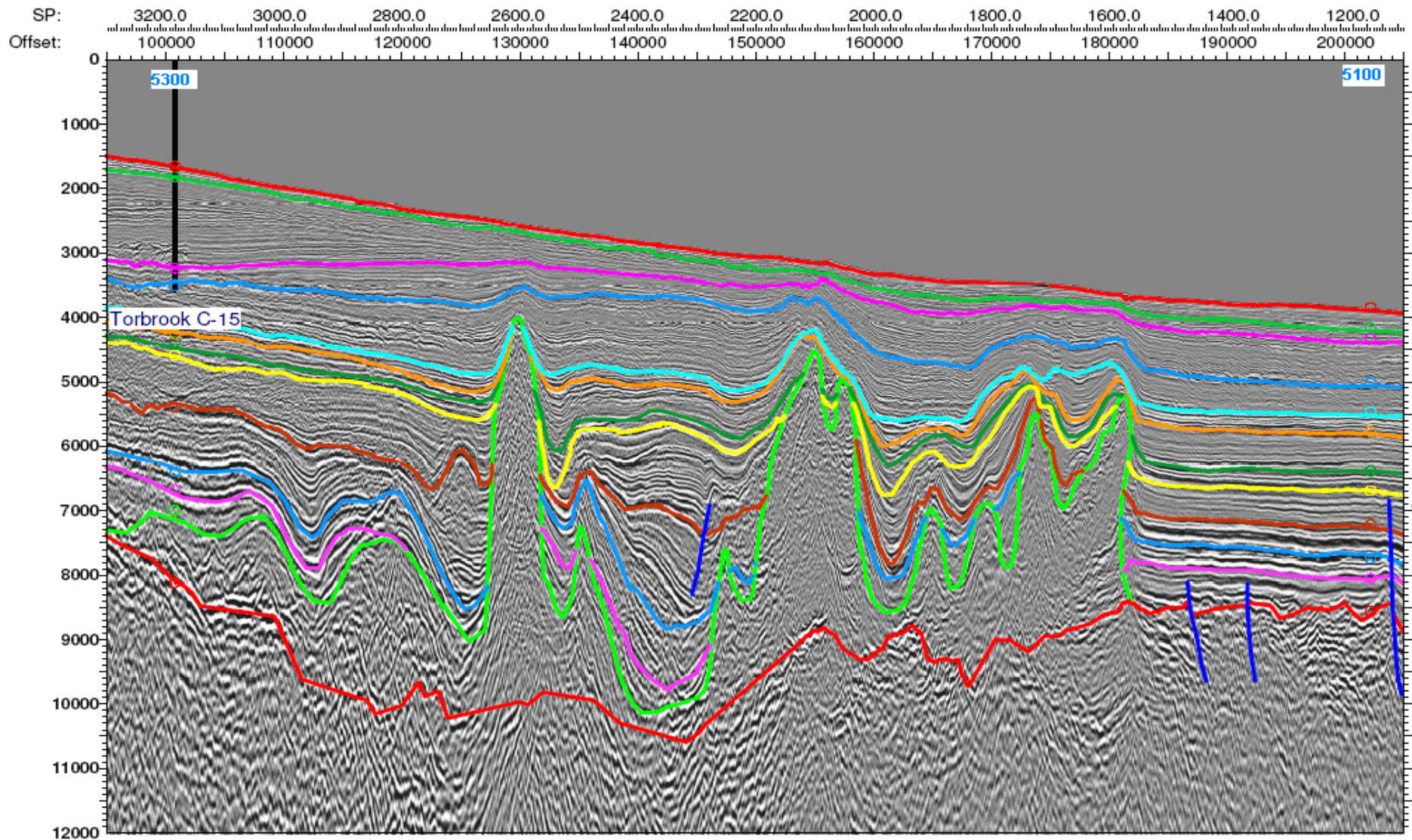
**Cretaceous Verrill Canyon (Berriasian-Valanginian) = Formation/Member (Geological Time)

2D Petroleum System Modelling

Seismic Line NOVASPAN 1400

Figure 1a

- Large vertical salt diapirs

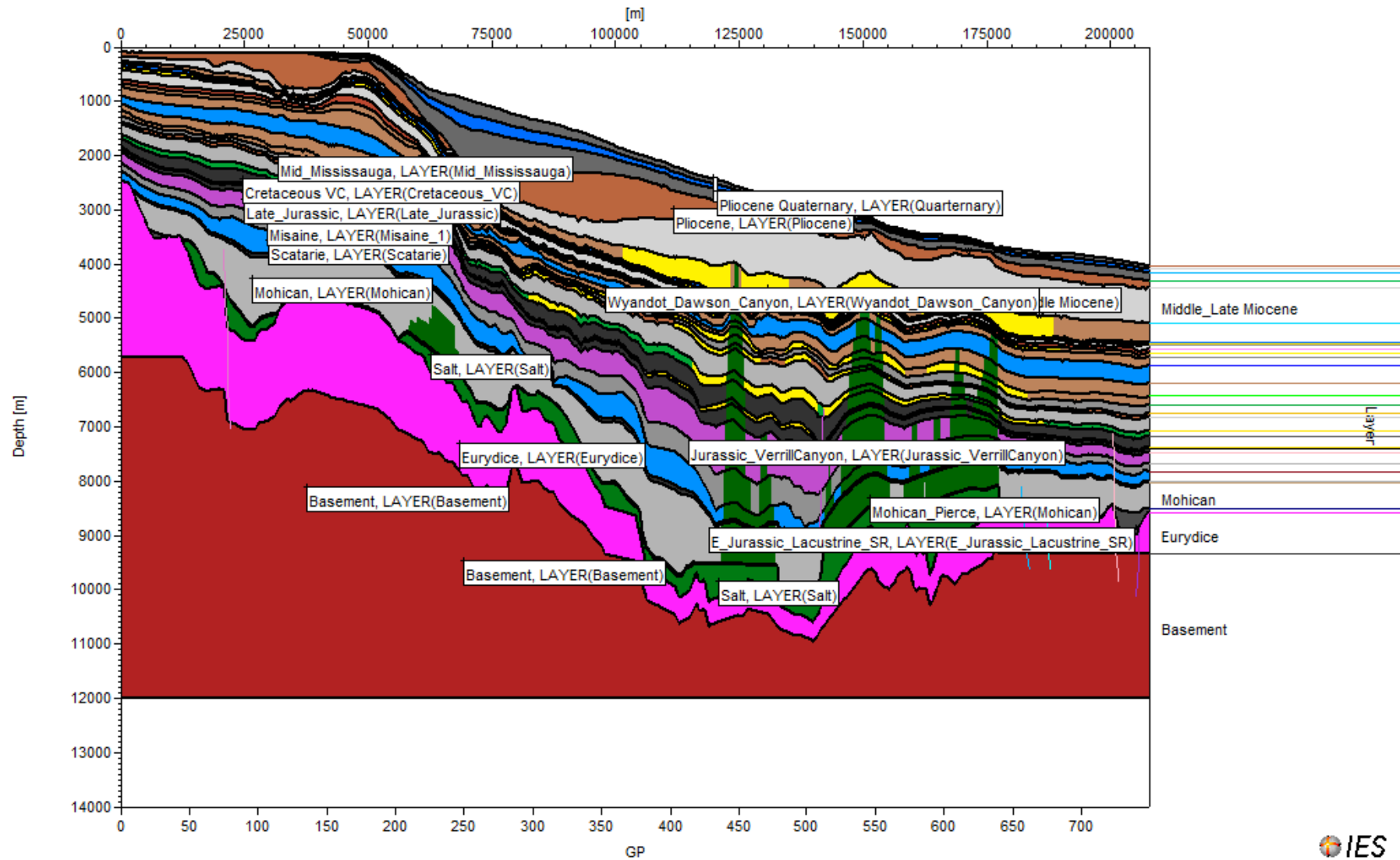


Seismic Line NOVASpan 1400

Petroleum System Modelling
PetroBuilder

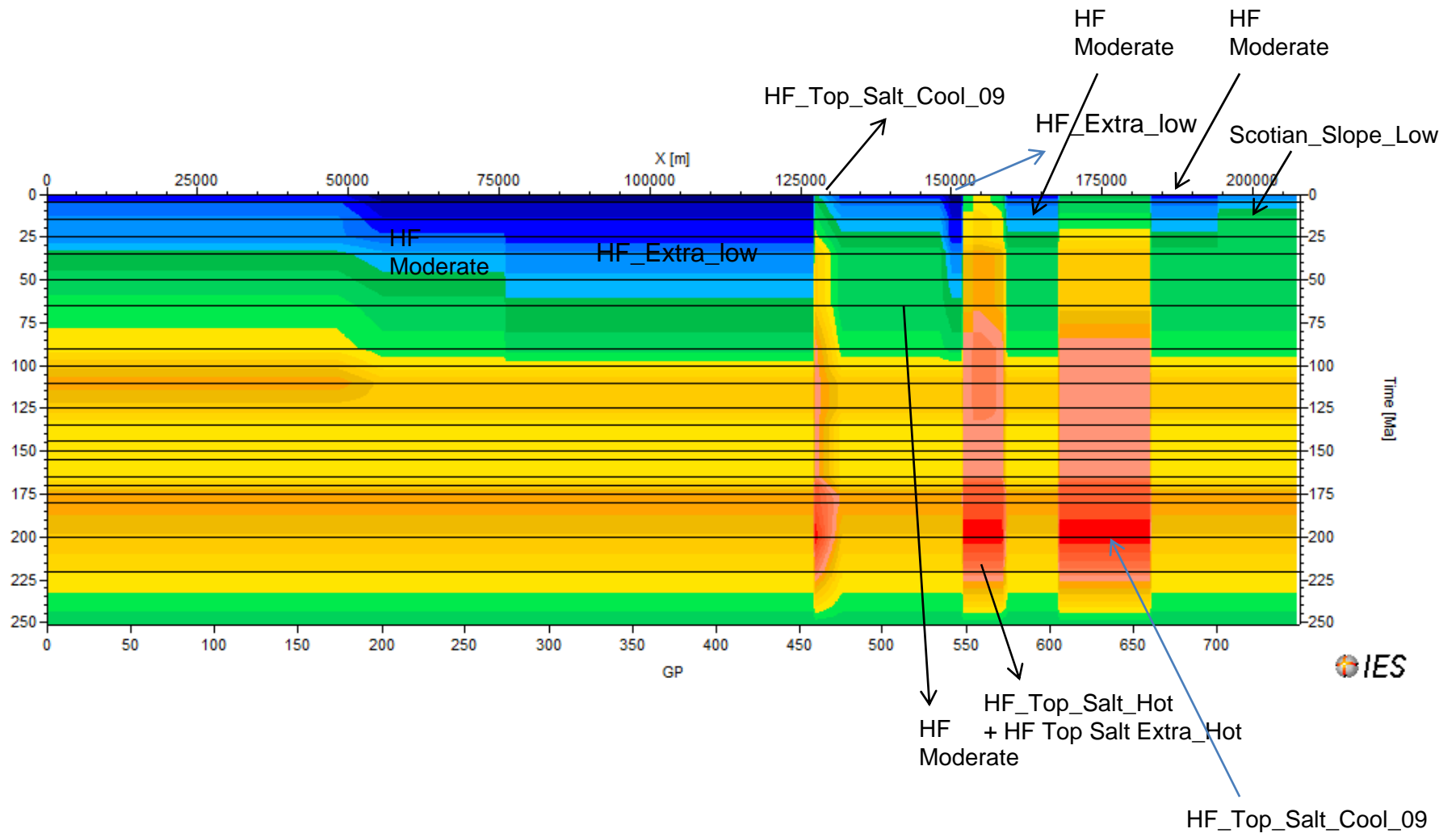
Line 1400 Final: Petrobuilder Horizon Assignment

Figure 1b-i



Line Novaspan1400: Assigned Heat Flow Trends for the entire seismic line

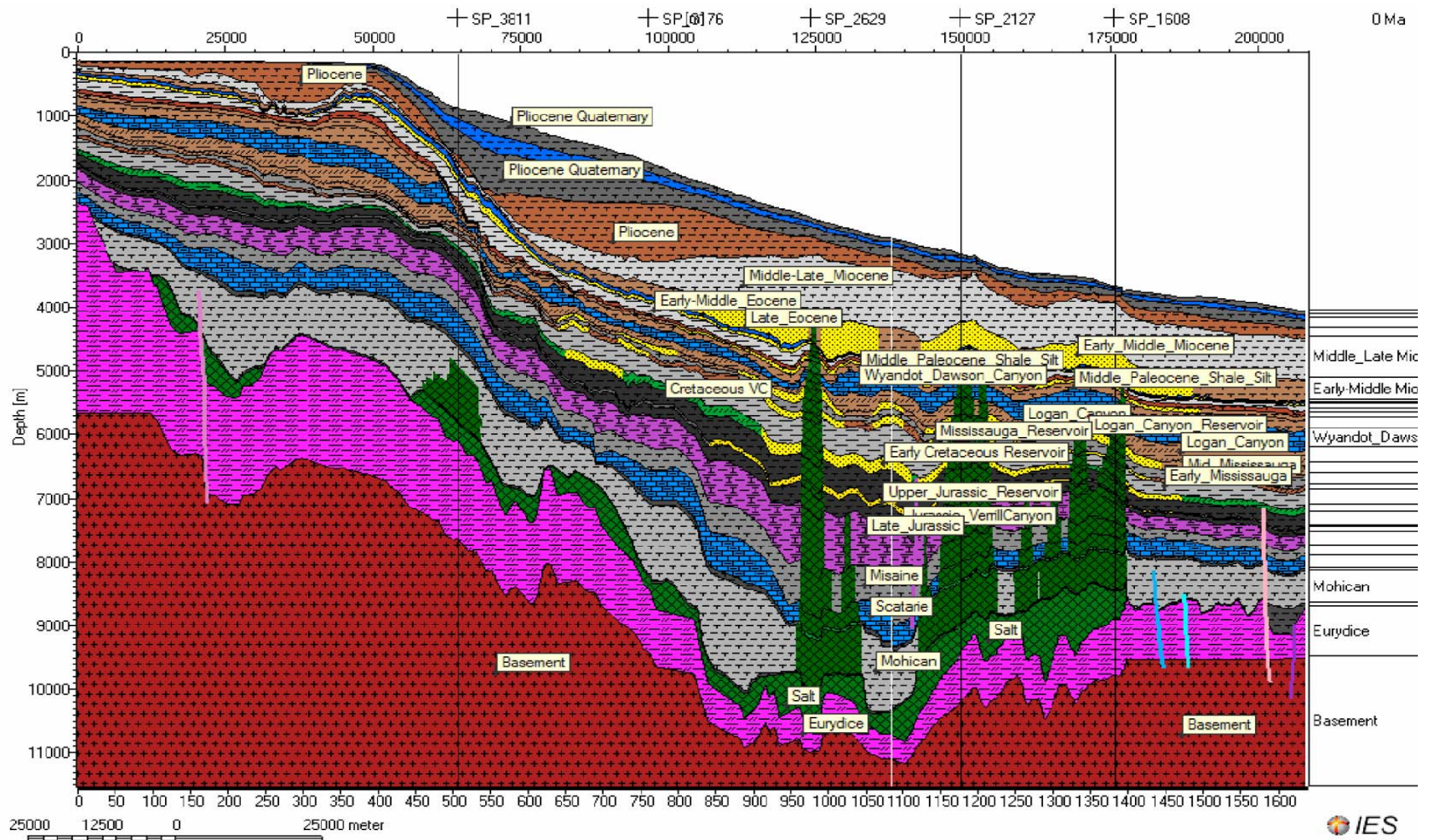
Figure 1b-ii



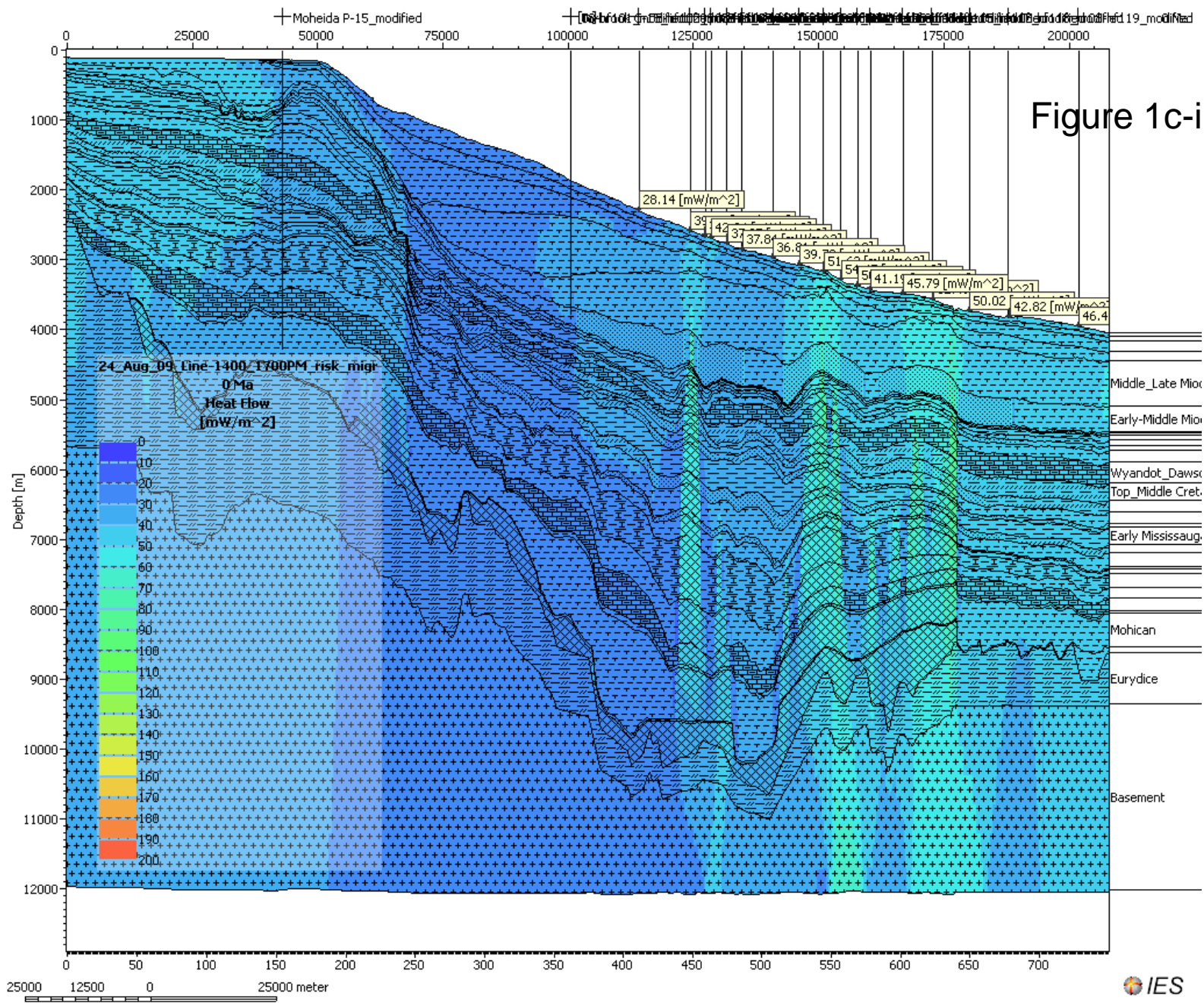
Seismic Line NOVSPAN 1400

Petroleum System Modelling After Simulation – Viewer 2D

Figure 1c-i



Line 1400 Final: Modelled heat flow values on the entire seismic section



Line 1400 Final: Modelled Heat Flow values on the entire seismic section

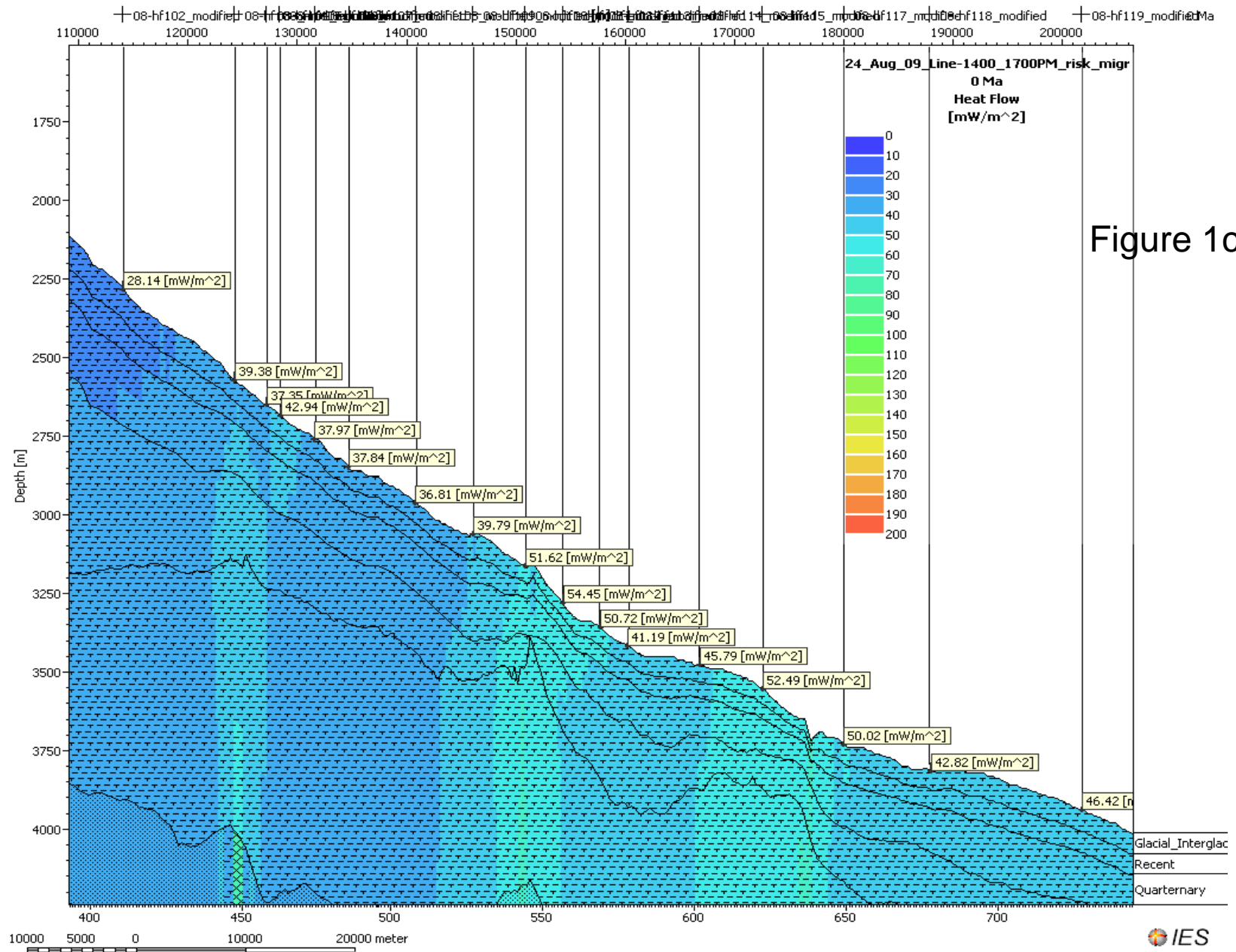
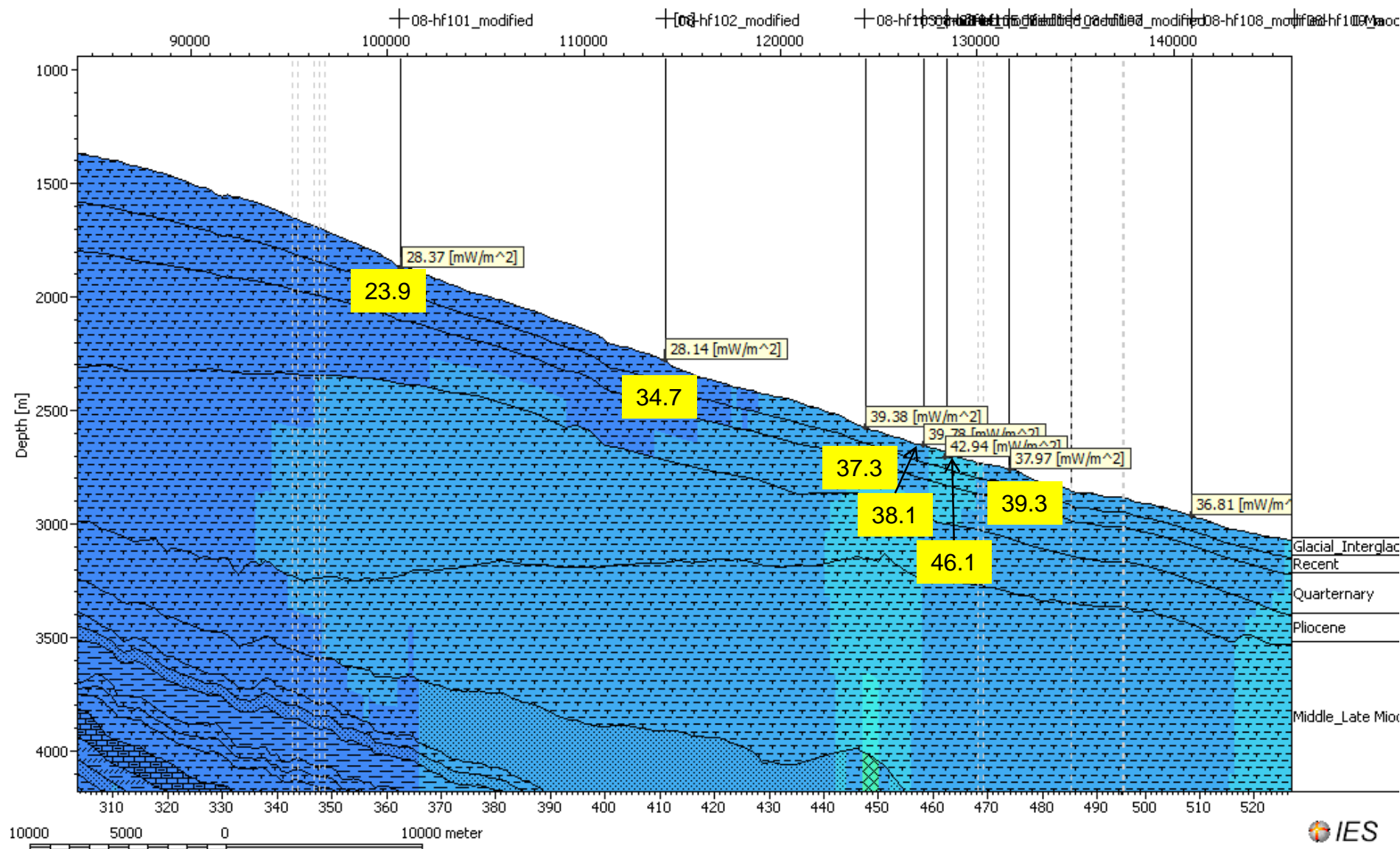


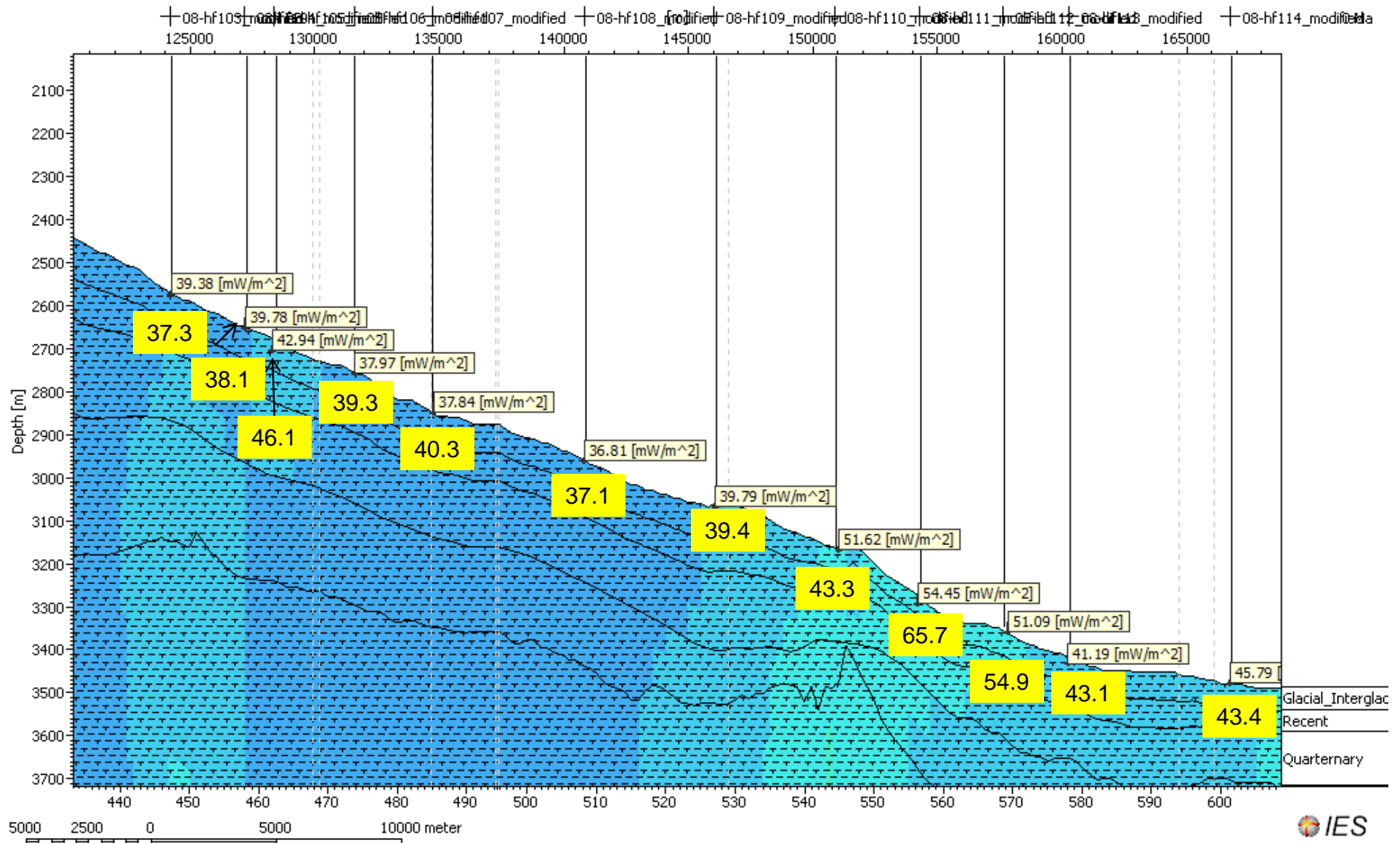
Figure 1c-iii

Line Novaspan 1400 after simulation : Calibration of modelled and measured heat flow values on top of selected measured heat flow lines

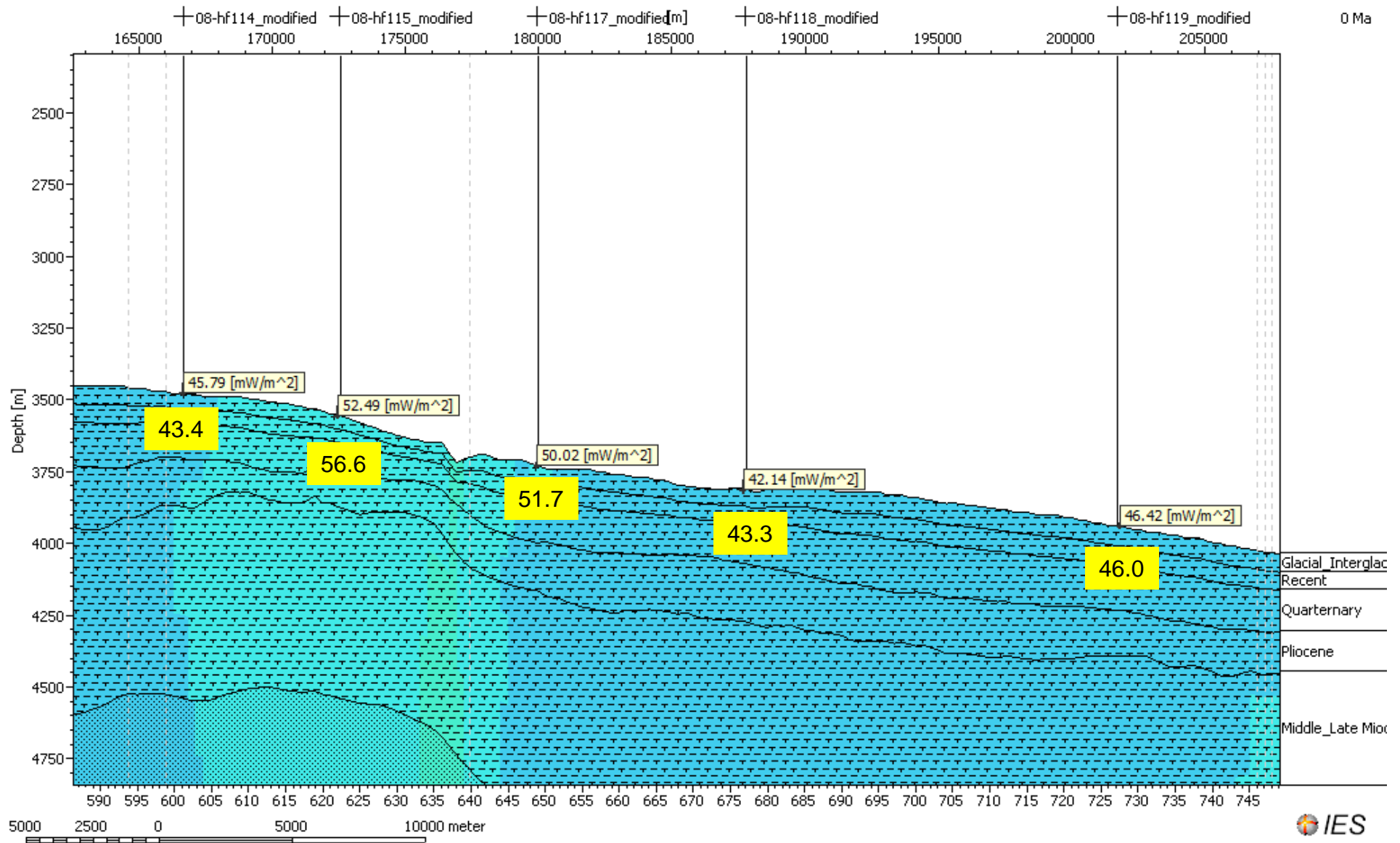
Figure 1c-iv



Line Novaspan 1400 after simulation : Calibration of modelled and measured heat flow values on top of selected measured heat flow lines Figure 10



Line Novaspan 1400 after simulation : Calibration of modelled and measured heat flow values on top of selected measured heat flow lines Figure 1c-vi



Seafloor Heat Flow: Measured vs. Modelled (Line 1400)

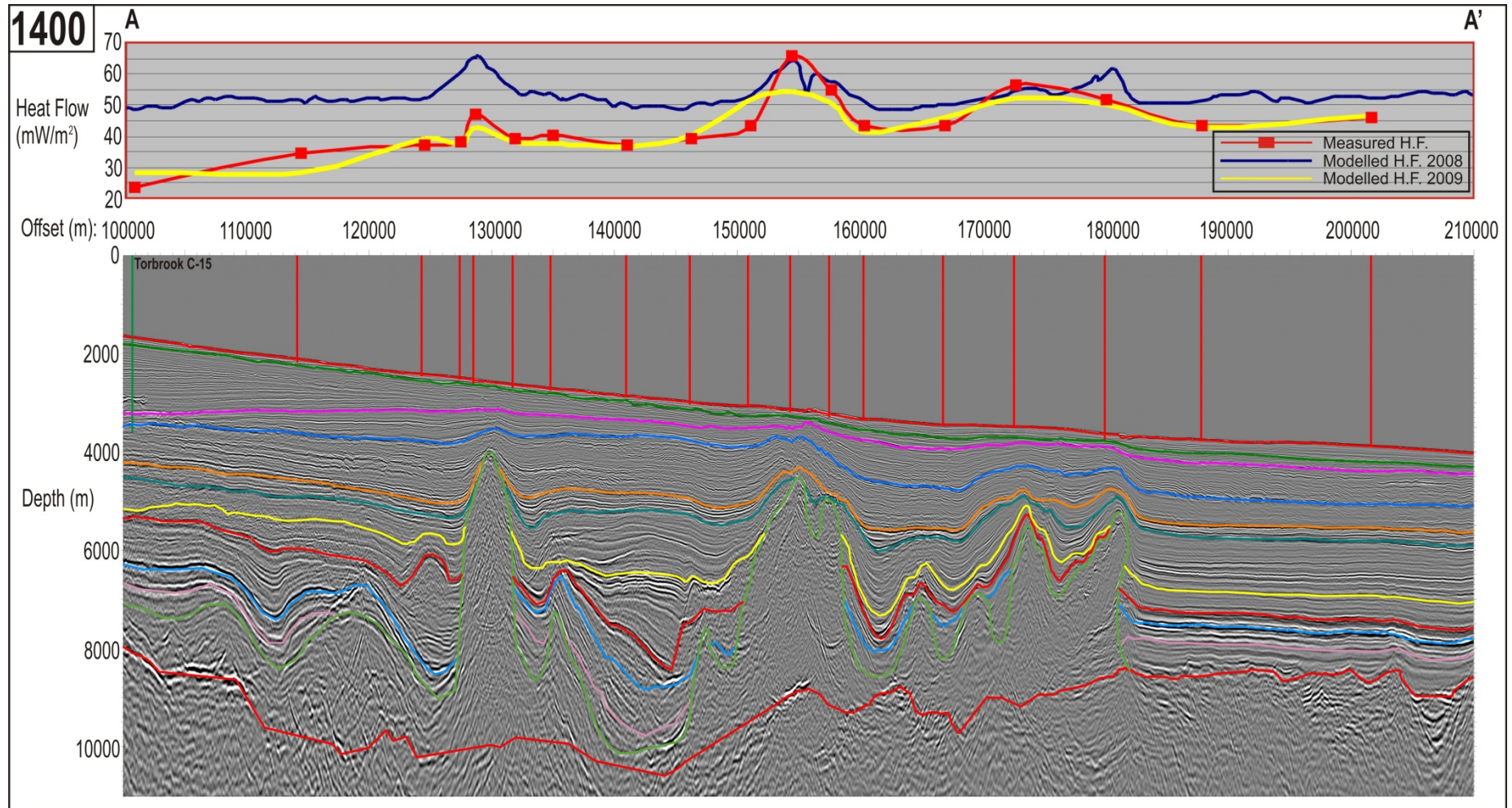
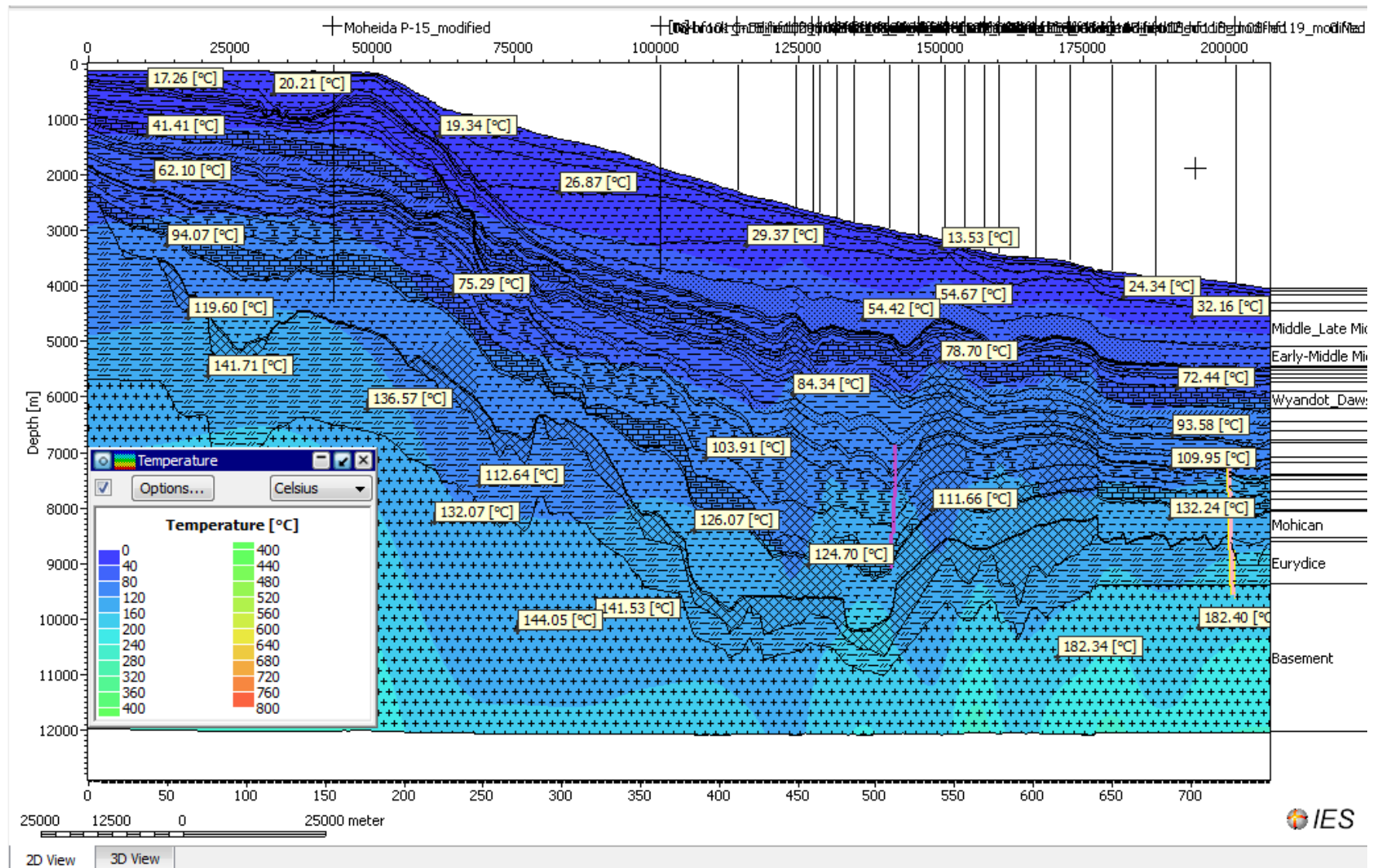


Figure 1c-vii

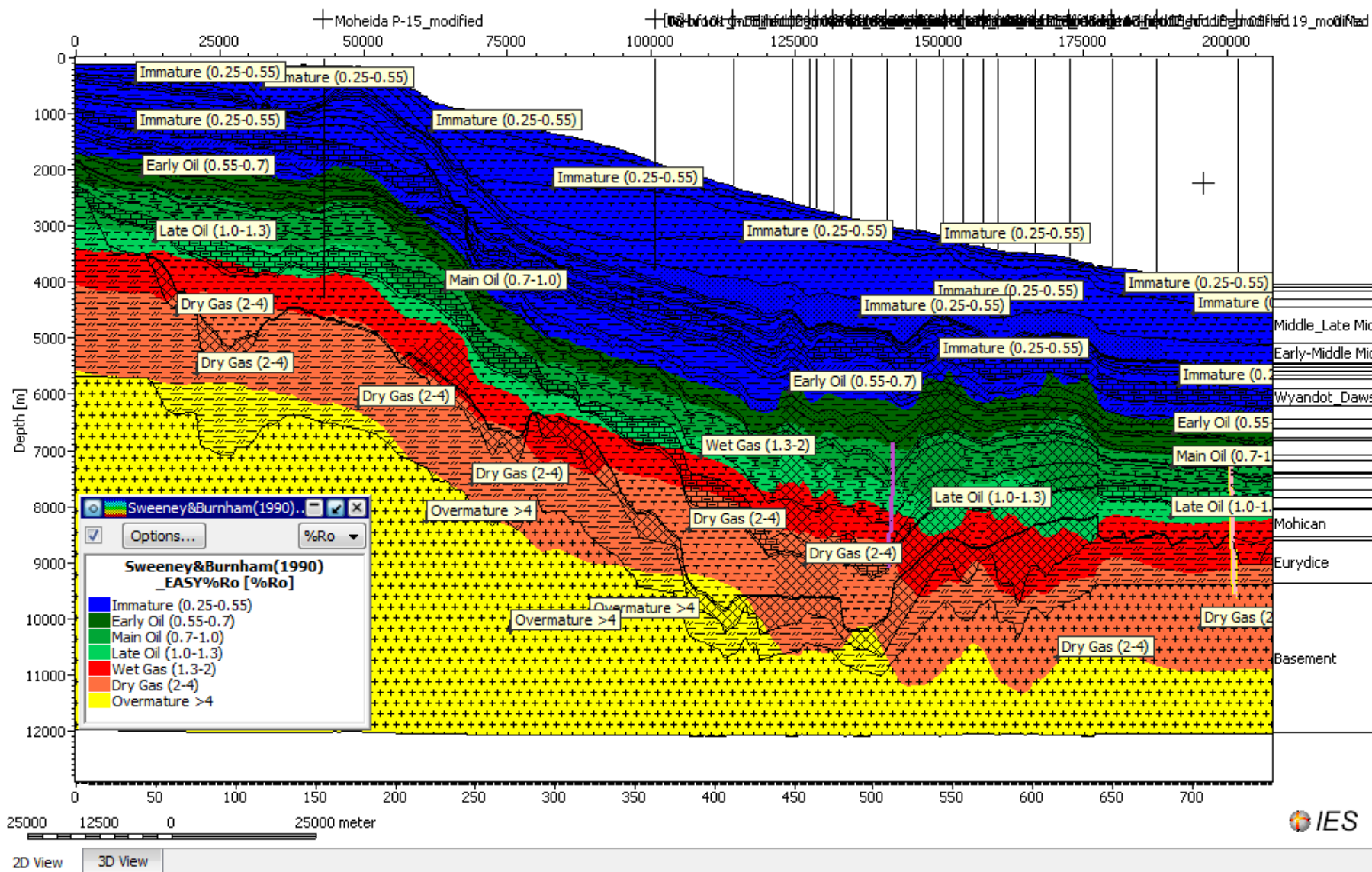
Line 1400: Temperature along the 2-D seismic section

Figure 1c-viii



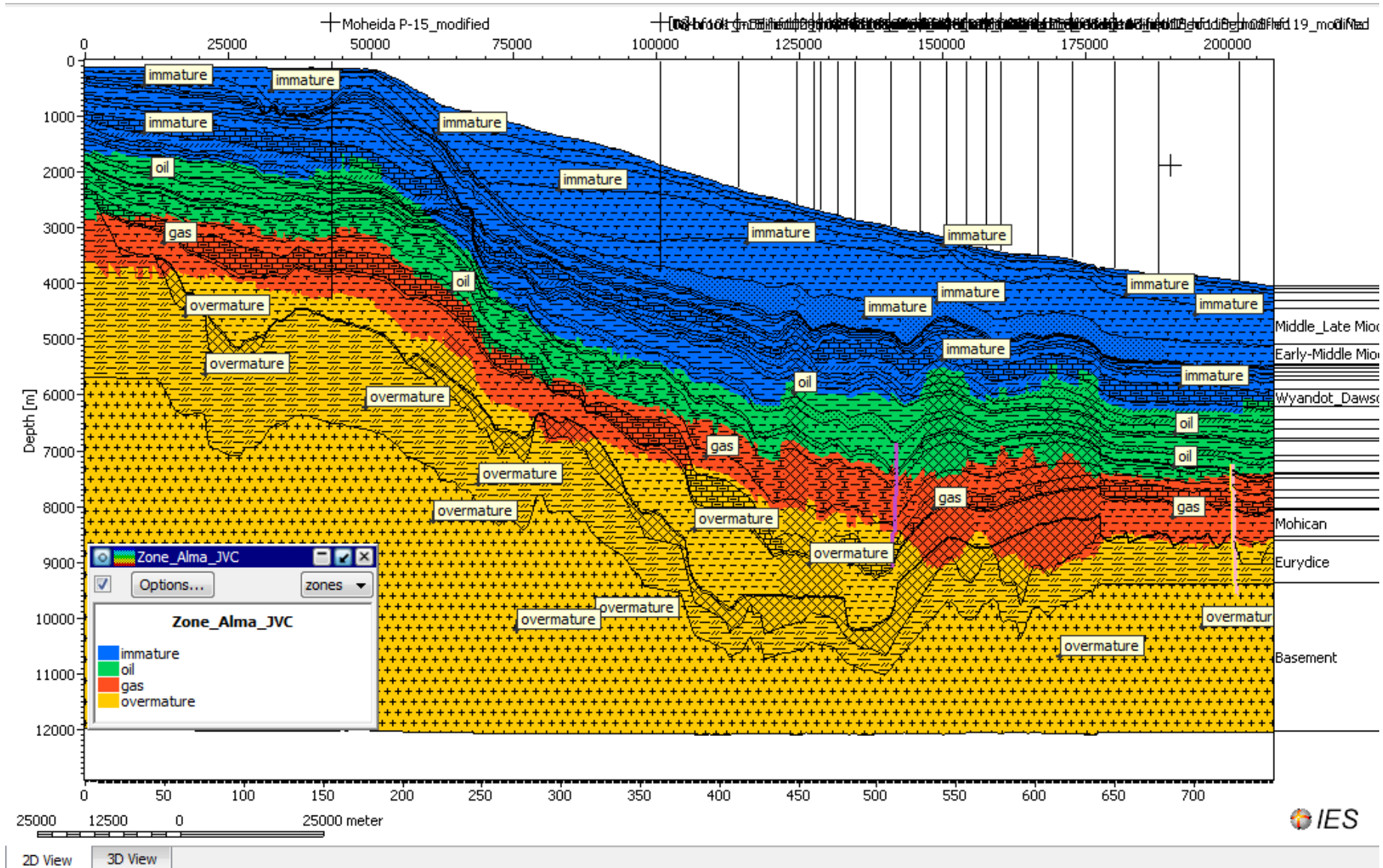
Line 1400: Maturity along the 2-D seismic section

Figure 1c-ix



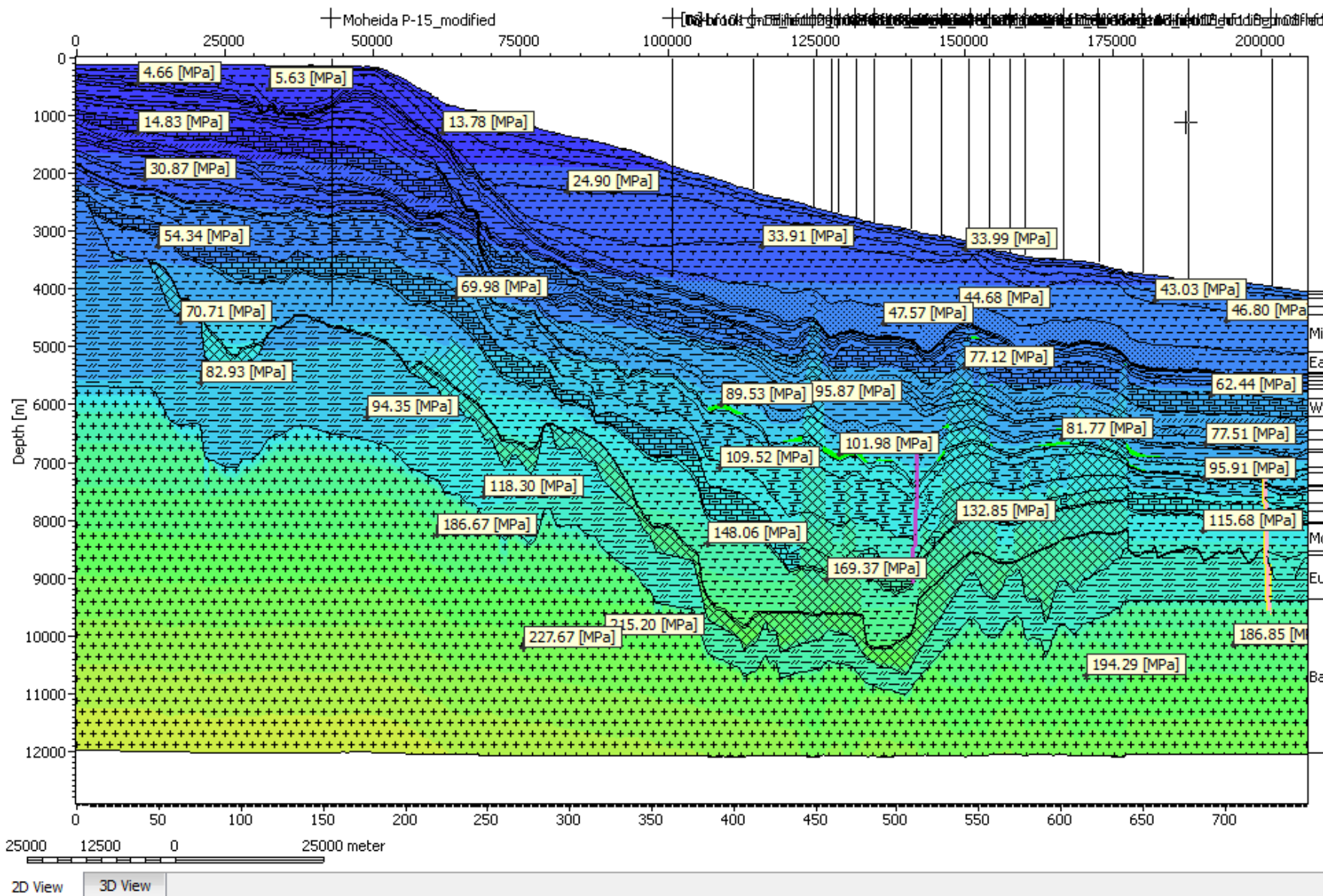
Line 1400: Hydrocarbon zones along the 2-D seismic section

Figure 1c-x



Line 1400: Pore Pressure along the 2-D seismic section

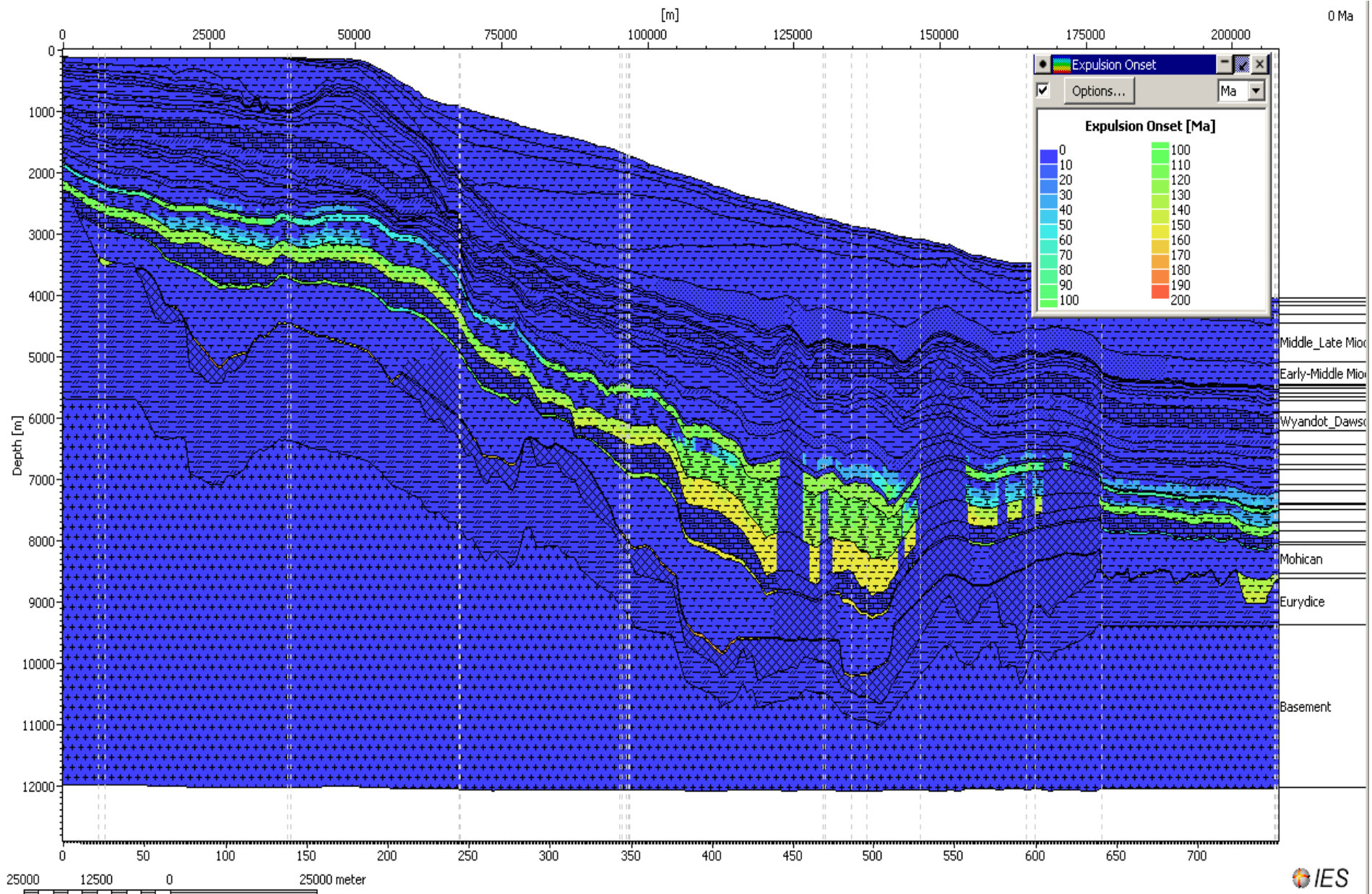
Figure 1c-xi



**SEISMIC LINE NOVASPAN 1400
ONSET OF HYDROCARBON
EXPULSION
AND RESERVOIR HYDROCARBON
FINGERPRINTING**

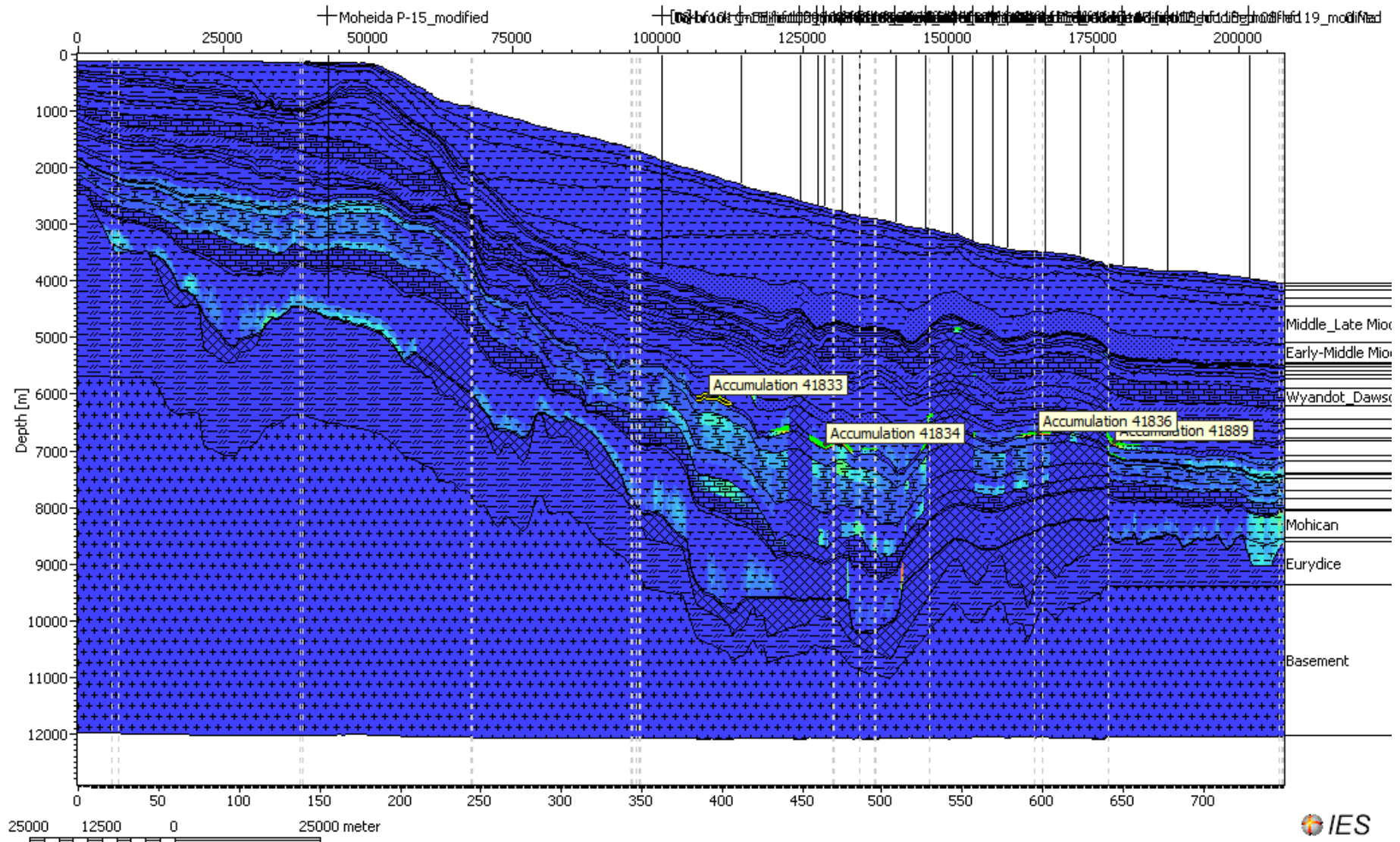
Onset of Expulsion: Line 1400

Figure 1d-i



Line Novaspan 1400 after simulation: Hydrocarbon saturation of various reservoirs

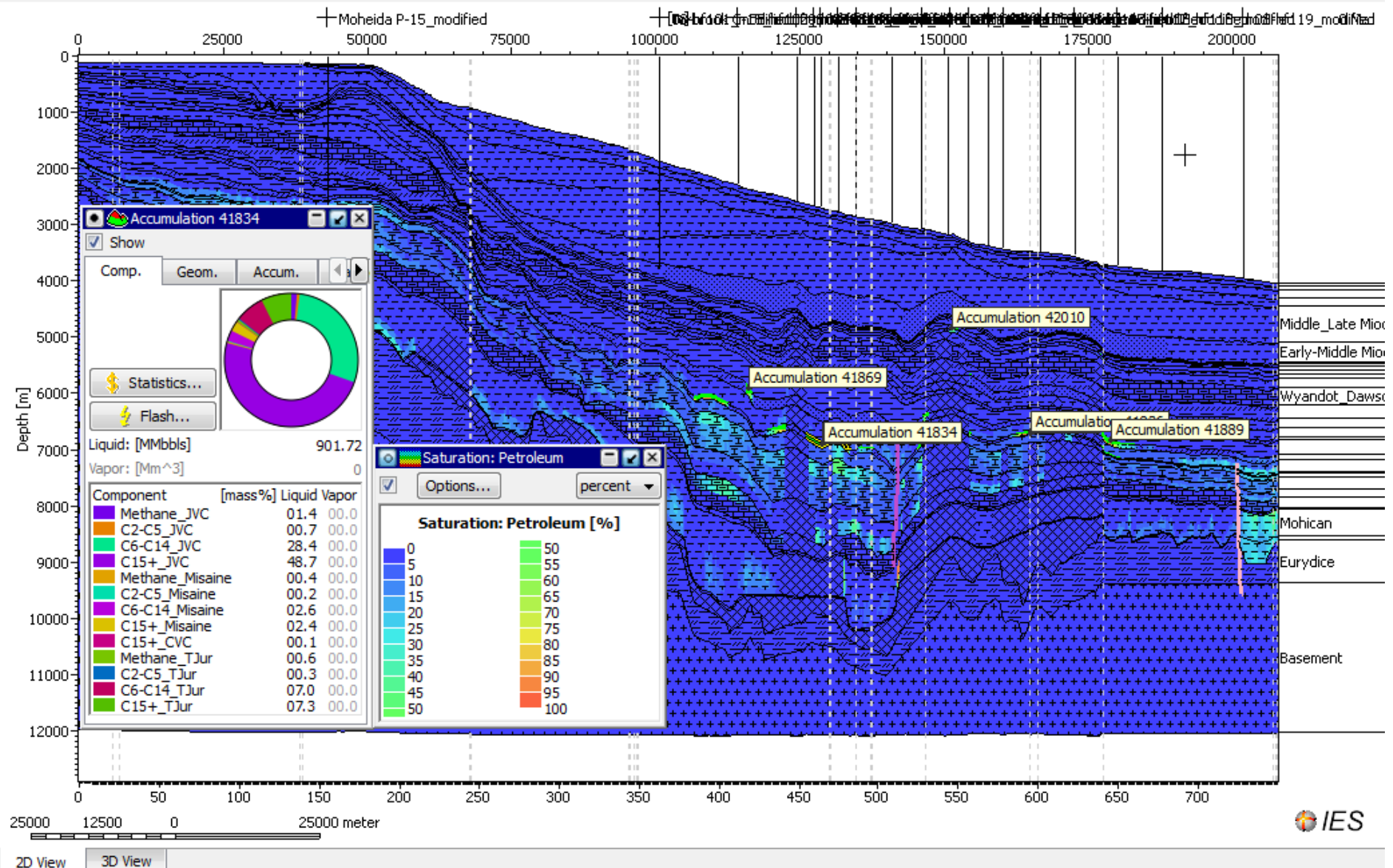
Figure 1d-ii



LATE JURASSIC RESERVOIR SATURATIONS: LINE NOVASPAN 1400

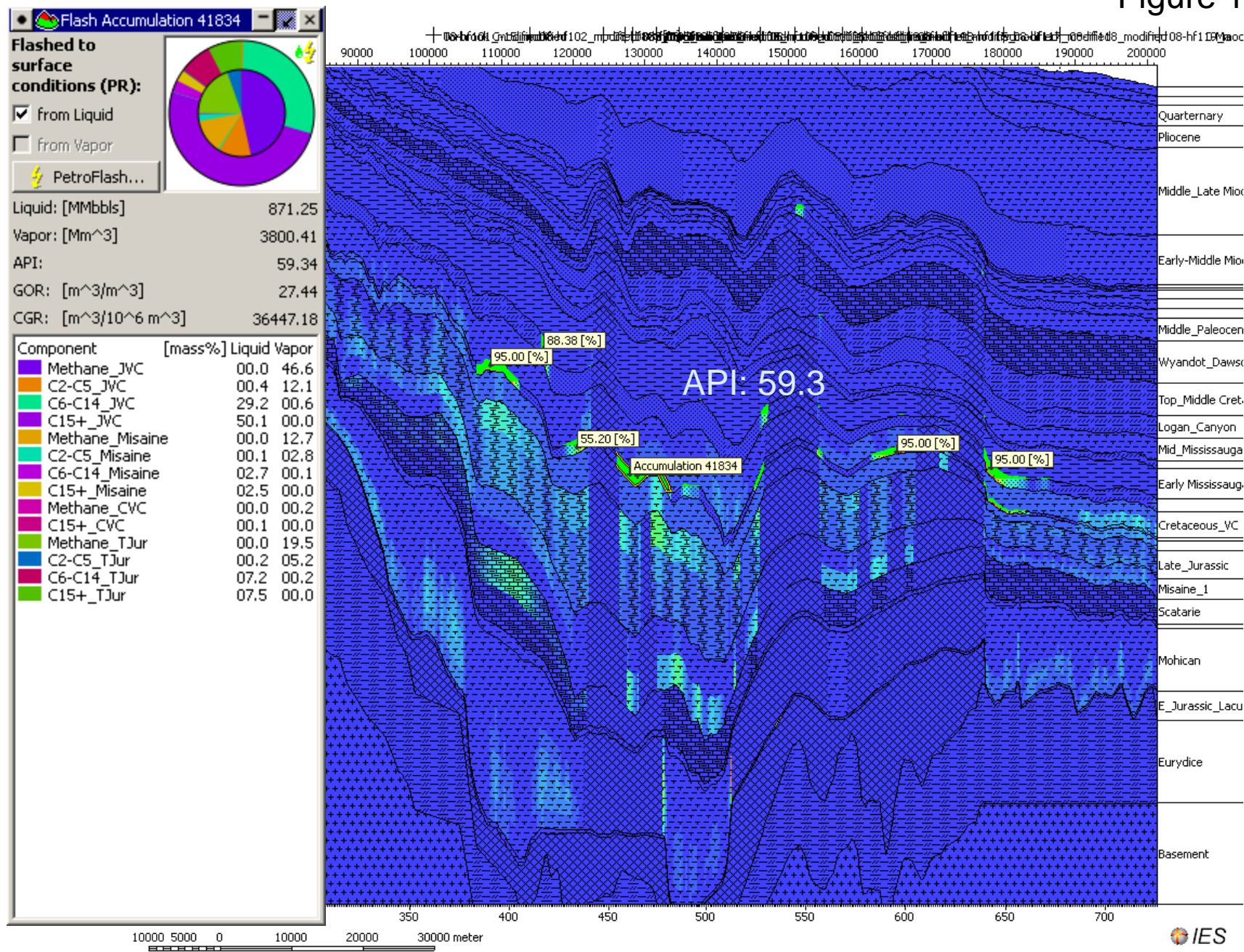
Line 1400: Late Jurassic Reservoir 41834: Percentages of reservoir hydrocarbons

Figure 1e-ia



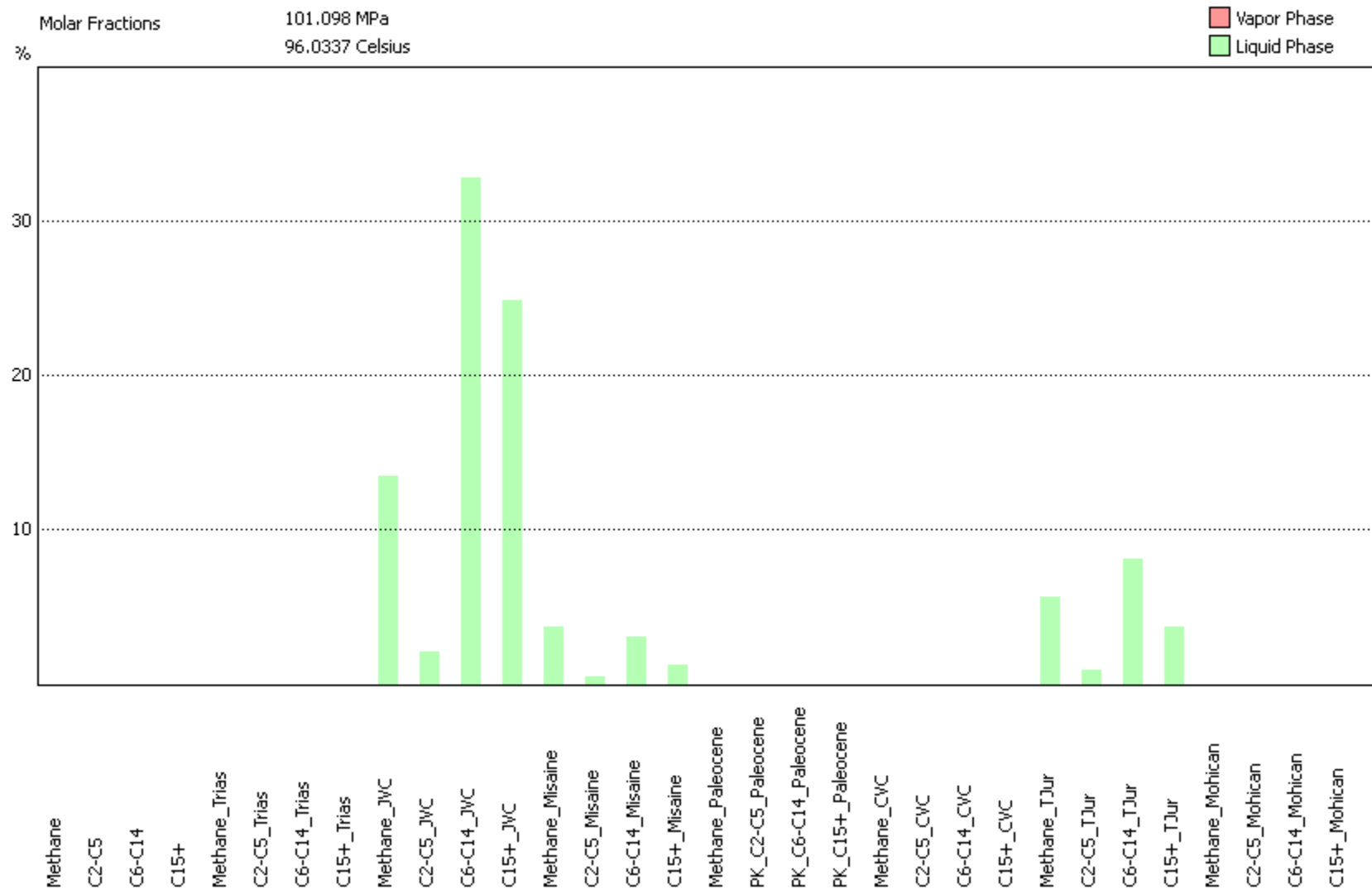
Line Novaspan1400: Upper Jurassic Reservoir (Accumulation 41834)

Figure 1e-ib



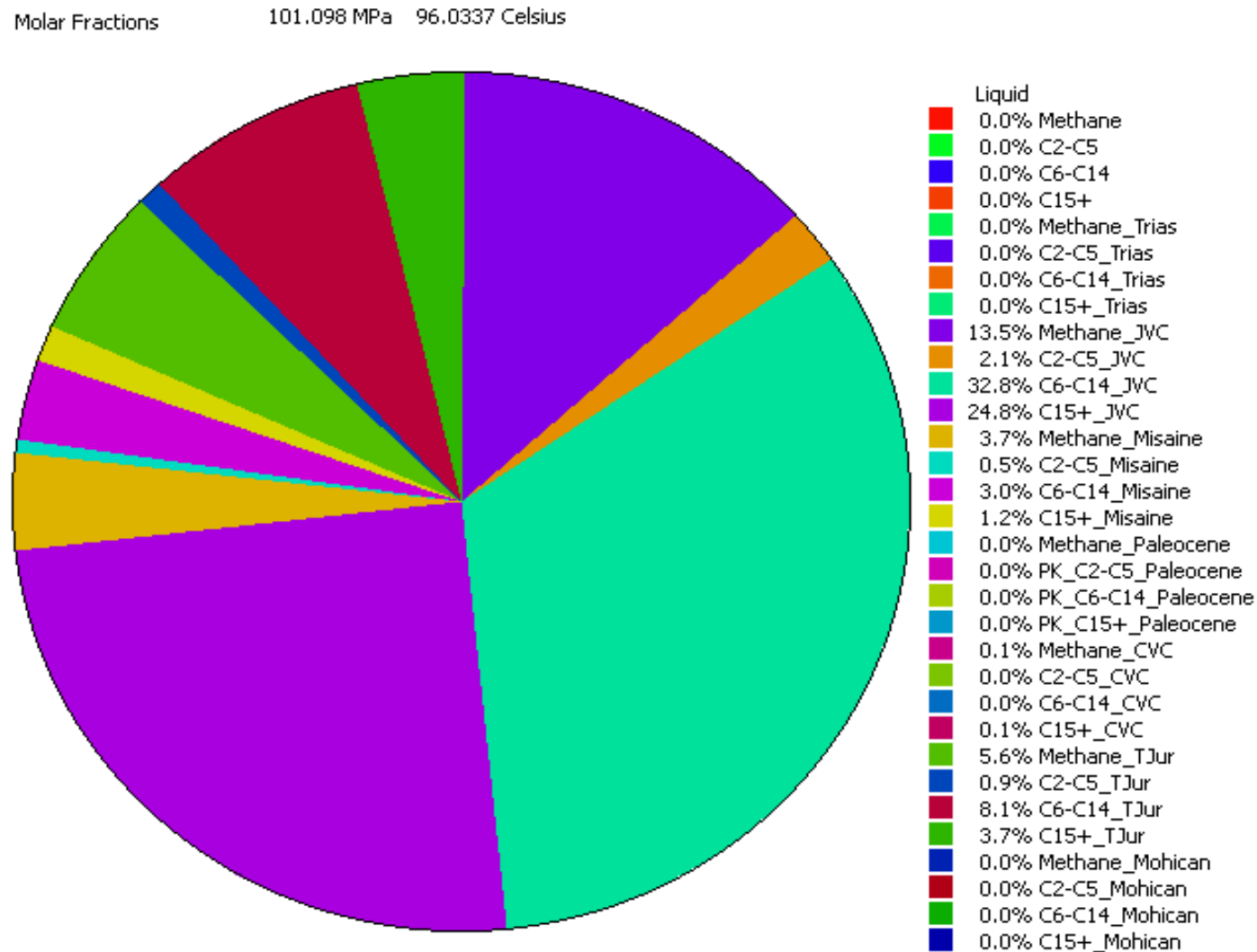
Line 1400: Upper Jurassic Reservoir (Accumulation 41834): Source Rock Fingerprinting

Figure 1e-ic



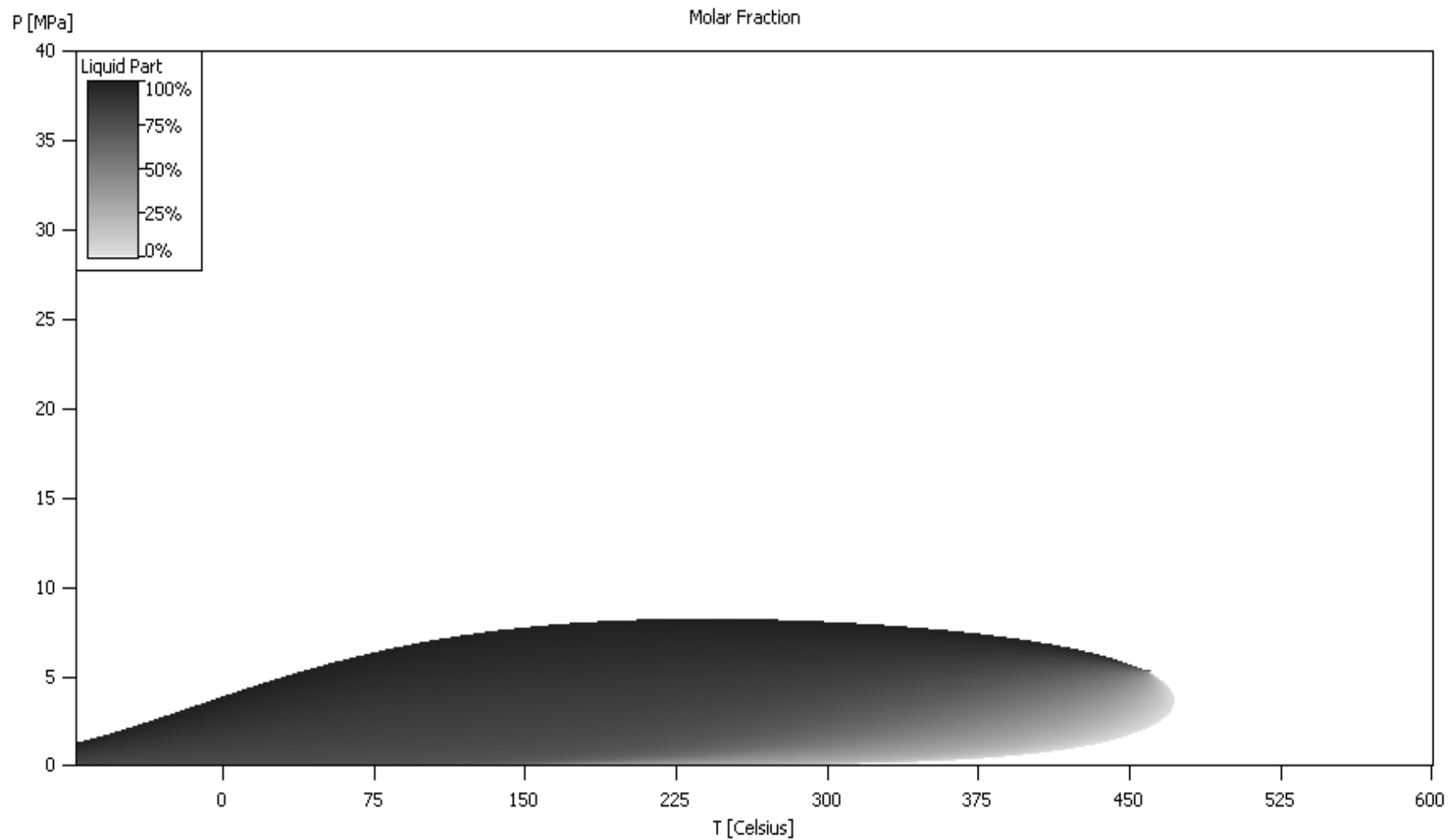
Line 1400: Upper Jurassic Reservoir (Accumulation 41834): Source Rock Fingerprinting and mass balance

Figure 1e-id



Line 1400: Upper Jurassic Reservoir (Accumulation 41834): P-T diagram

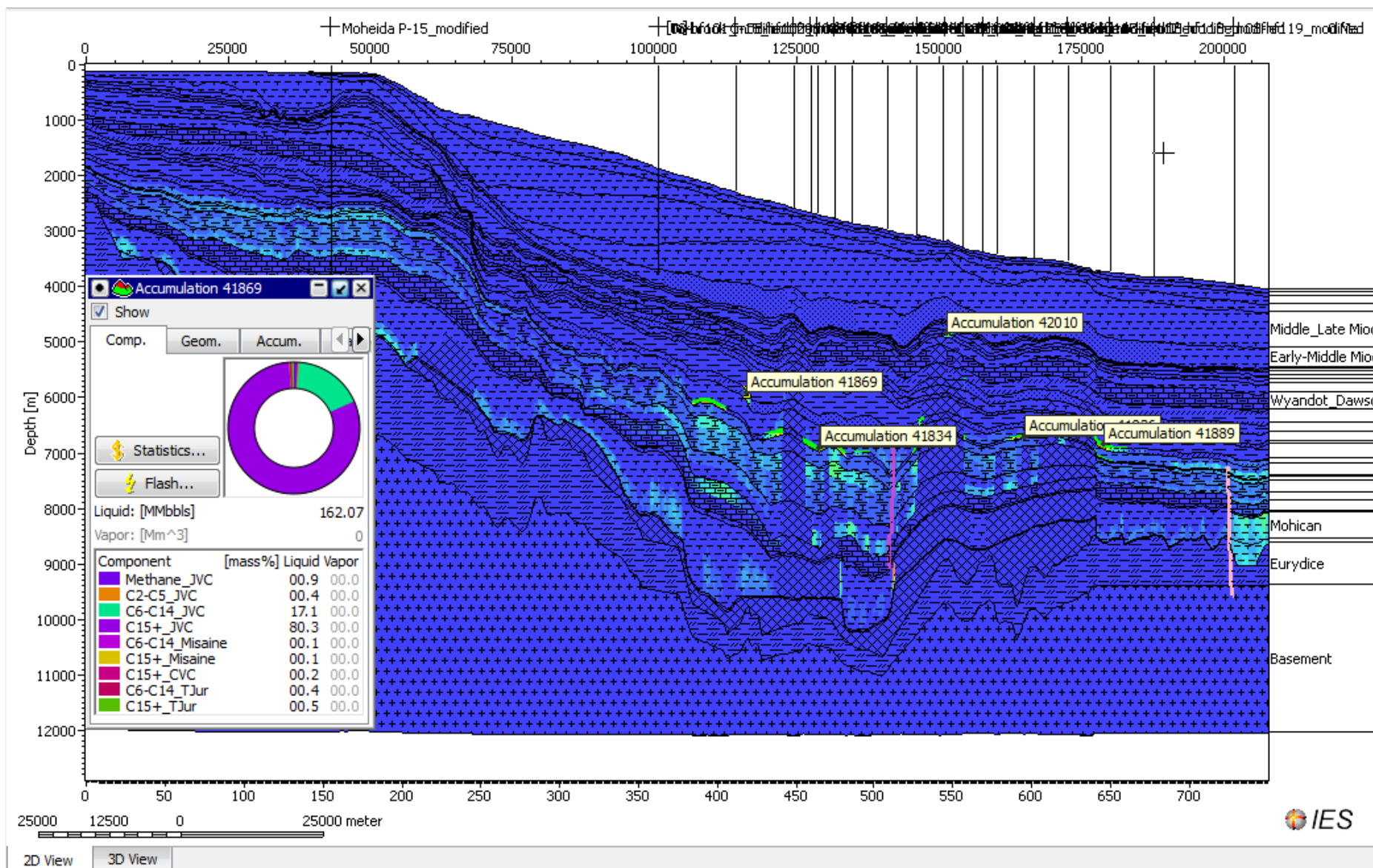
Figure 1e-ie



**EARLY CRETACEOUS RESERVOIR
FINGERPRINTING: LINE NOVASPACE
1400**

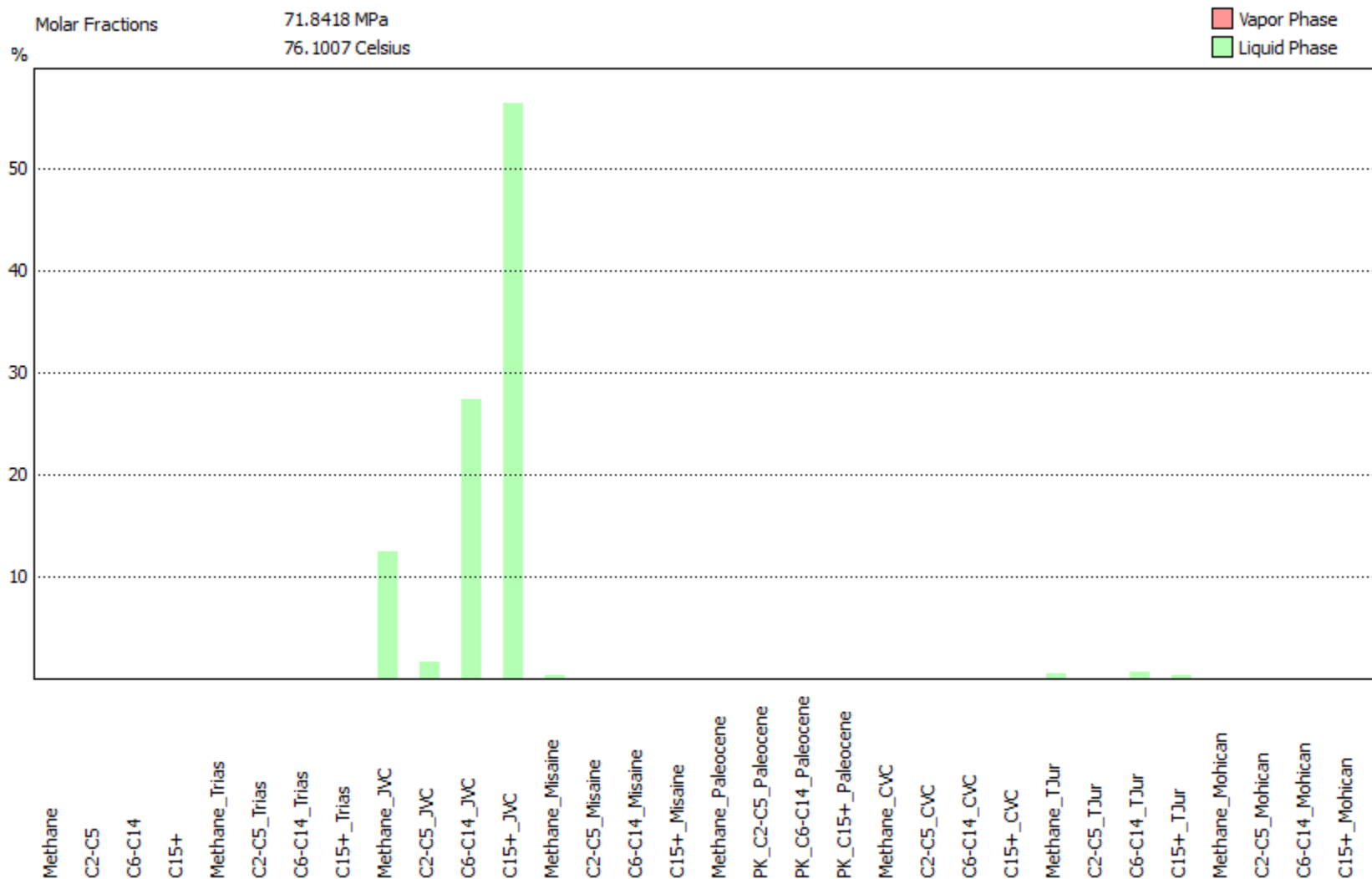
Line 1400: Early Cretaceous Reservoir 41869: Percentages of reservoir hydrocarbons

Figure 1e-ii-a



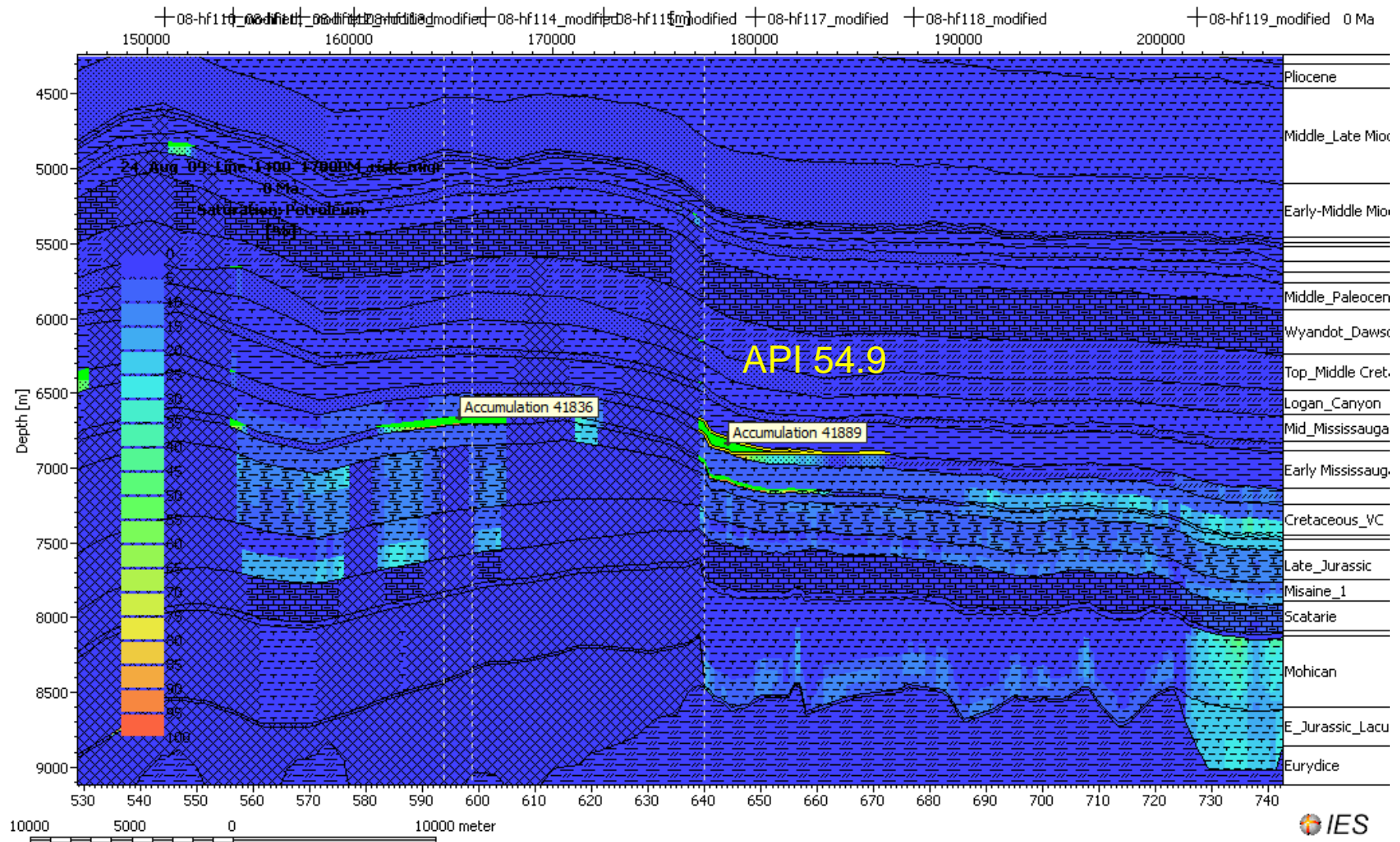
Line 1400: Early Cretaceous Reservoir 41869: Source Rock Fingerprinting of reservoir hydrocarbons

Figure 1e-iiB



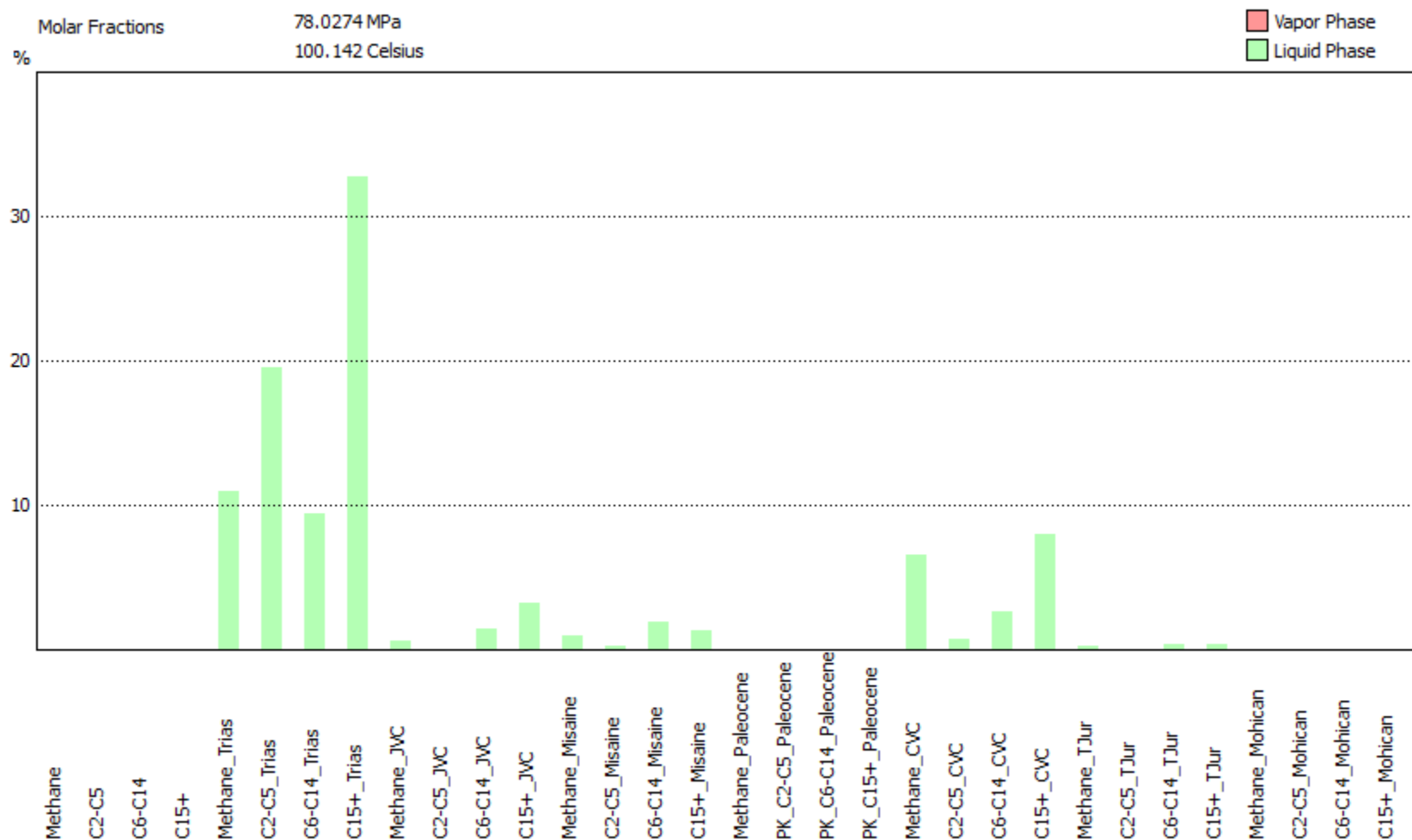
Line Novaspan1400: Focussing on early Cretaceous Reservoir showing the distributions of HC saturation (Accumulation 41889)

Figure 1e-iiia



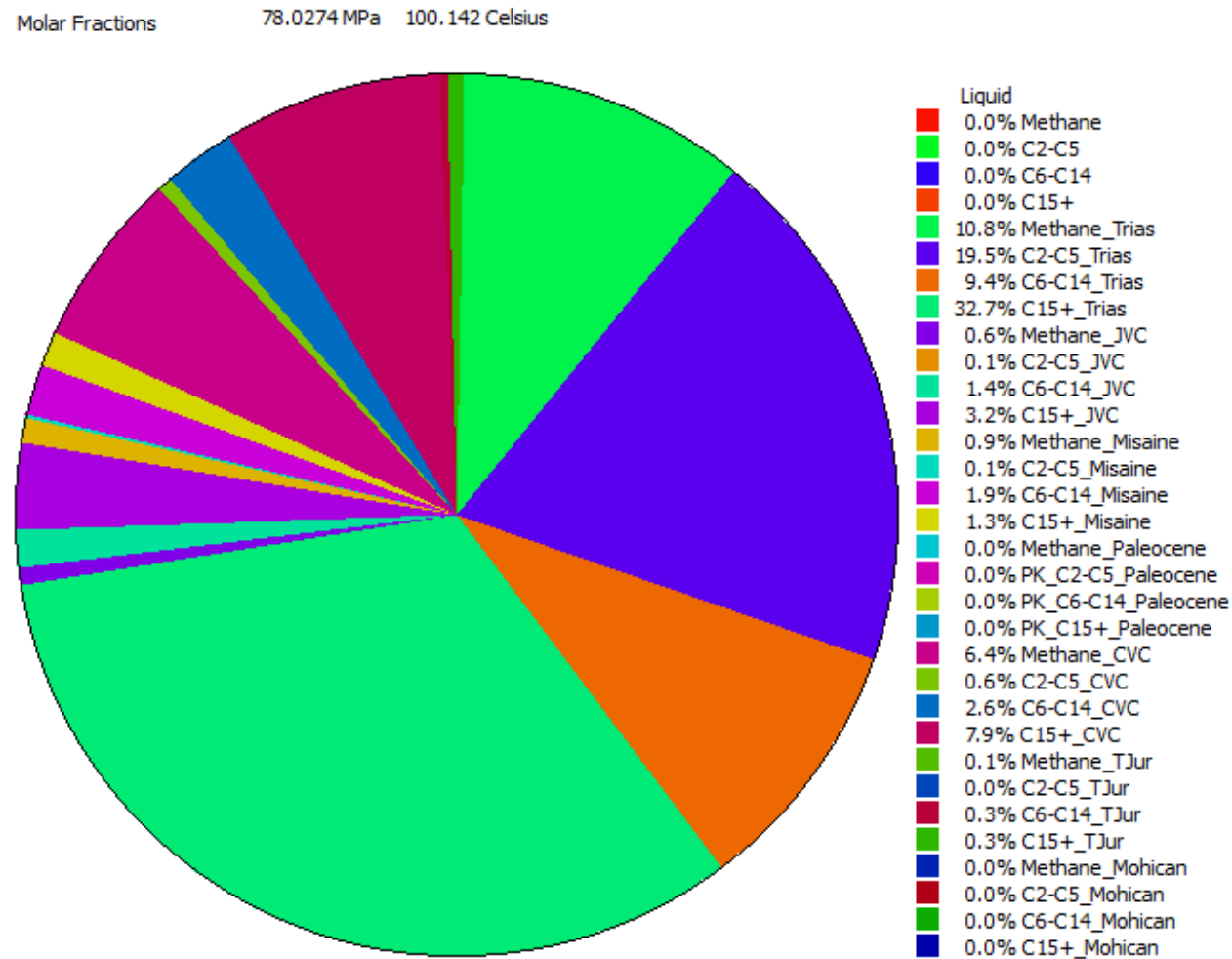
Line Novaspan1400: Focussing on early Cretaceous Reservoir showing the source rock fingerprinting (Accumulation 41889)

Figure 1e-iiib



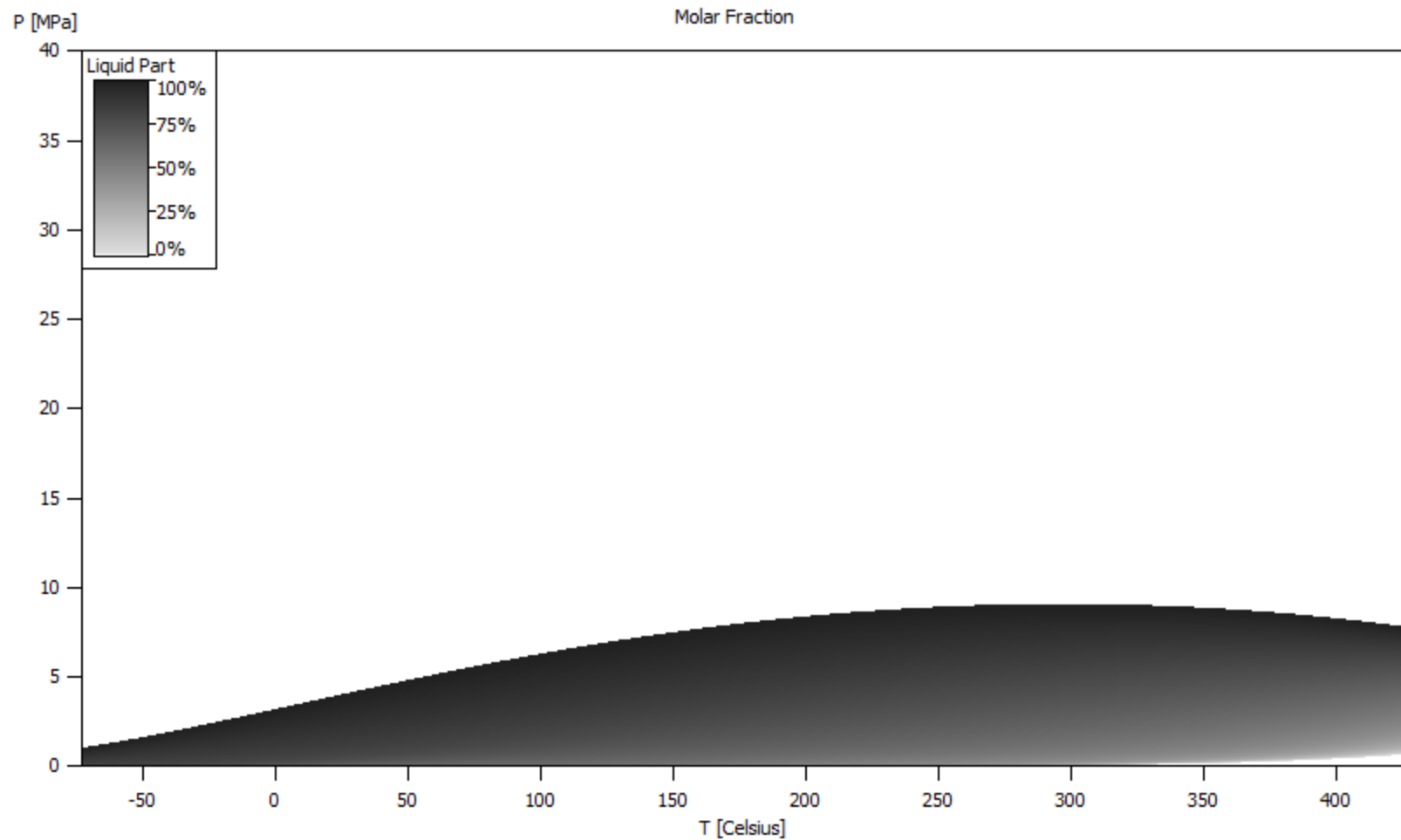
**Line Novaspan1400: Focussing on early Cretaceous Reservoir showing
the hydrocarbon distribution & source rock fingerprinting
(Accumulation 41889)**

Figure 1e-iiic



**Line Novaspan1400: Focussing on early Cretaceous Reservoir showing
the distributions of HC pressure-temperature digram
(Accumulation 41889)**

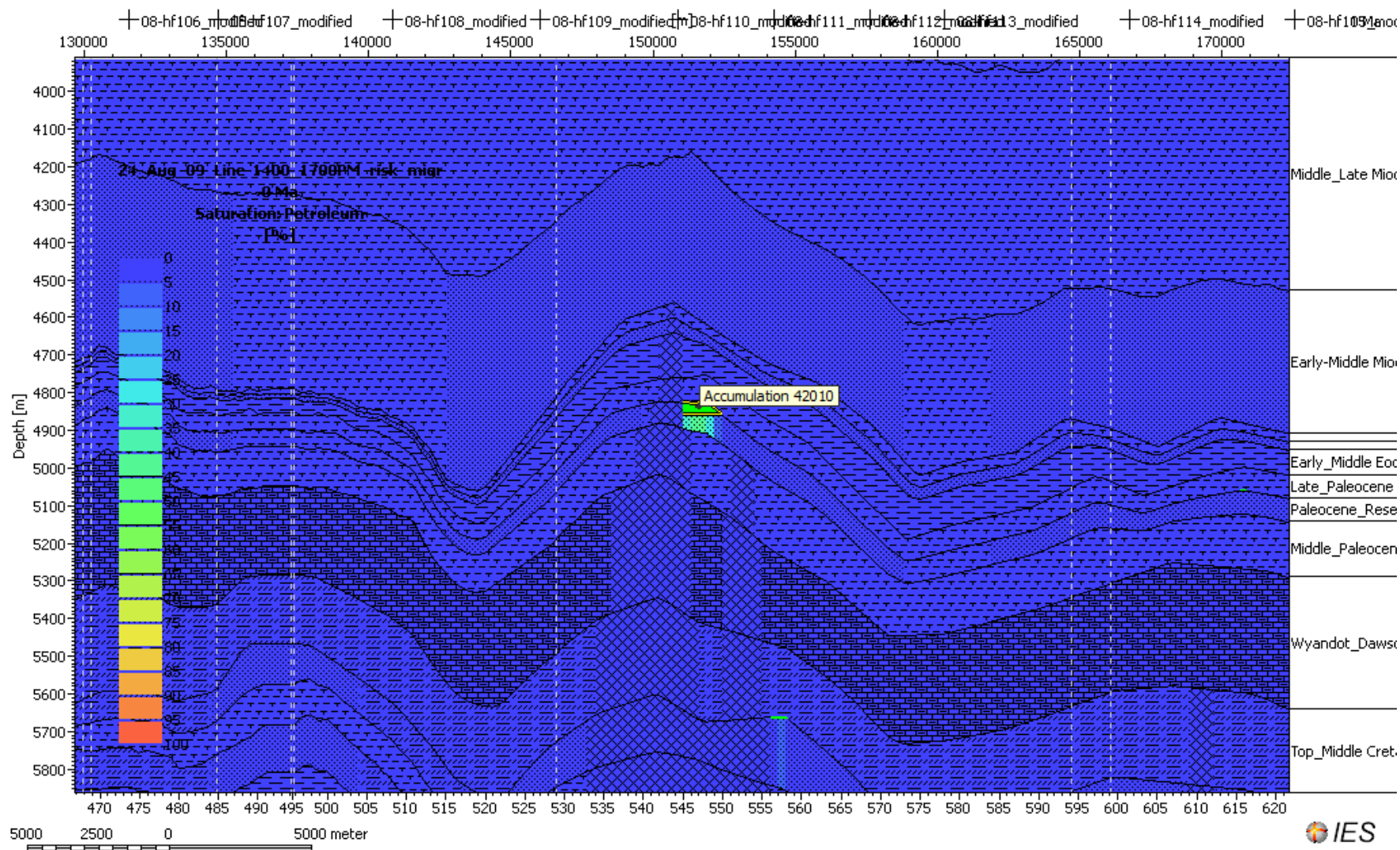
Figure 1e-iiid



**TERTIARY RESERVOIR
FINGERPRINTING: LINE NOVASPAN
1400**

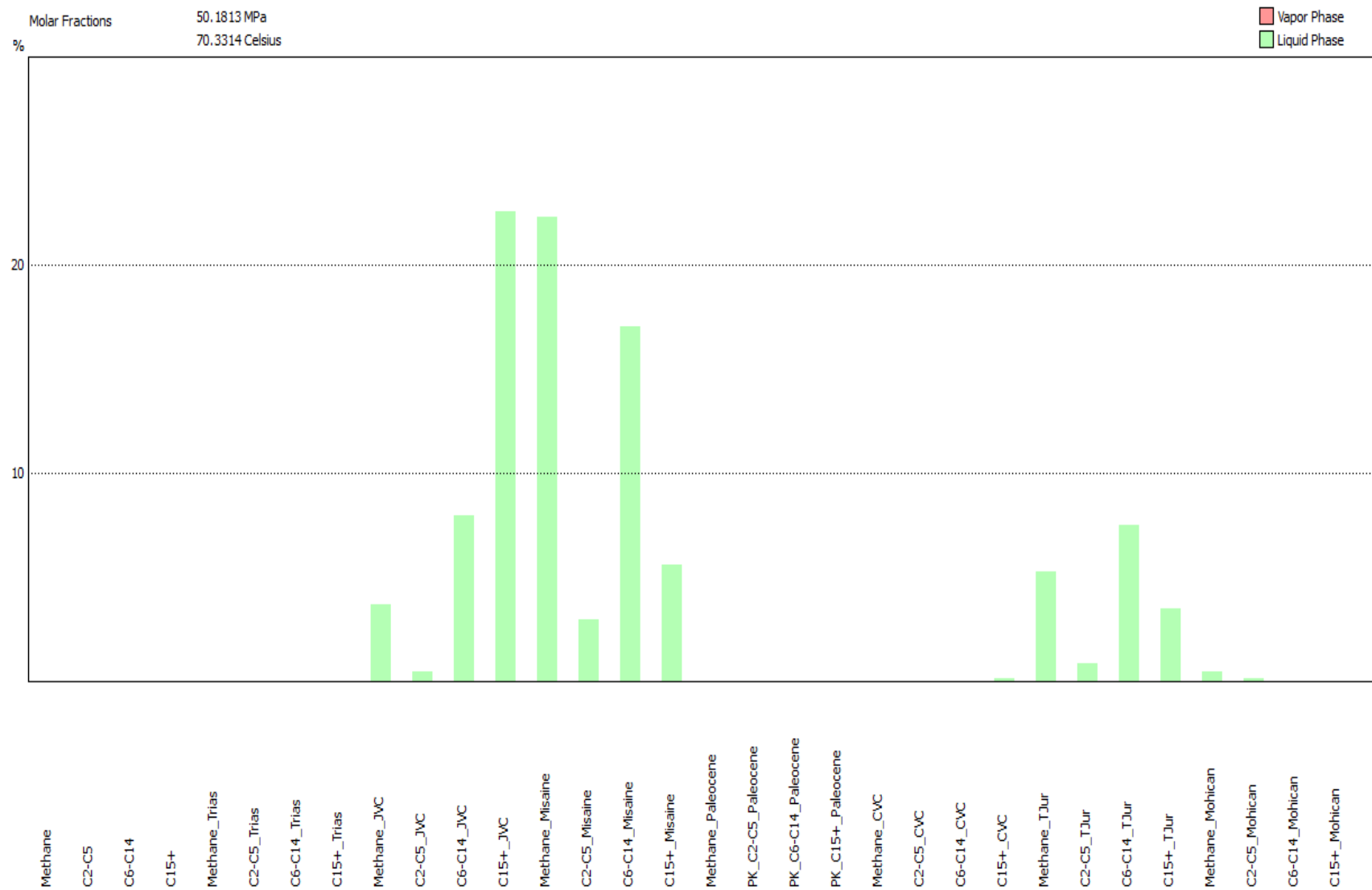
Line Novaspan1400: Focussing on Paleocene Reservoir with hydrocarbon saturation (Accumulation 42010)

Figure 1e-iva



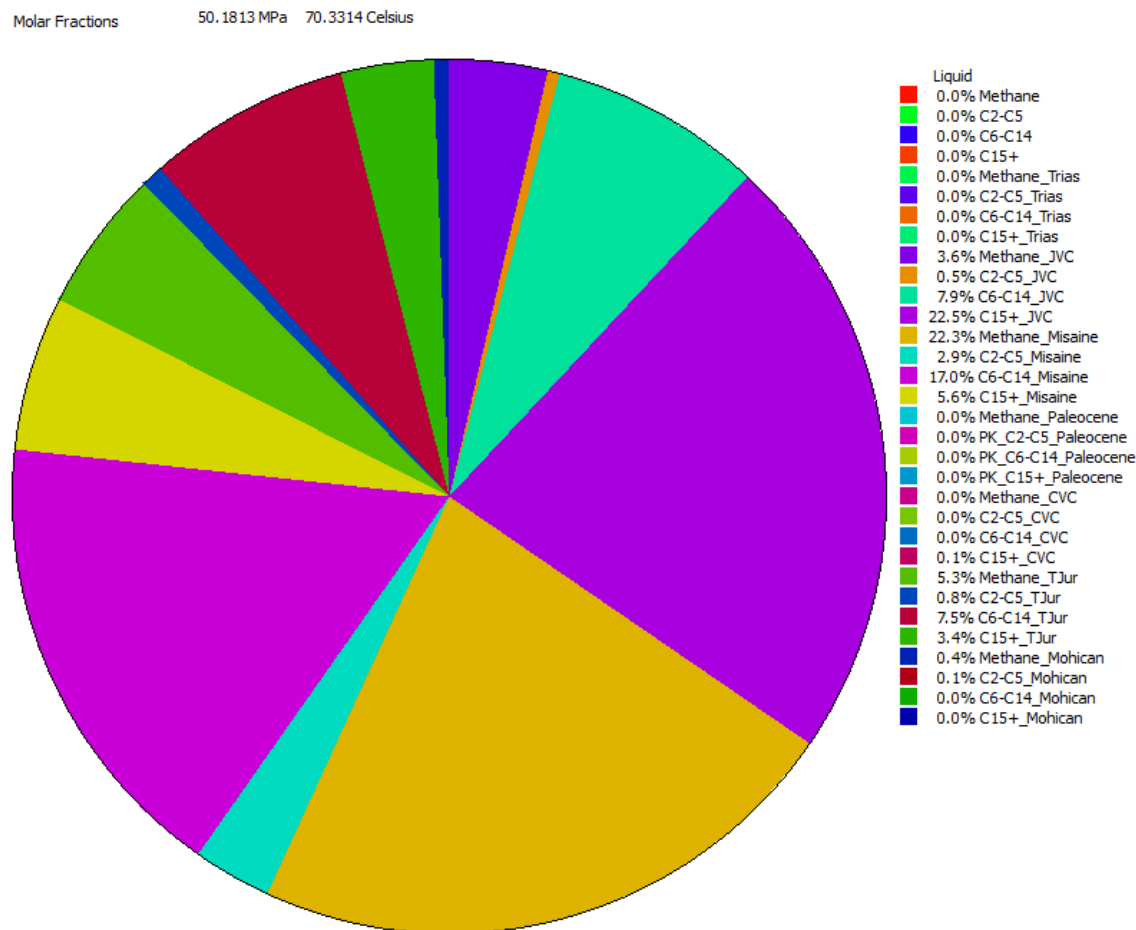
Line Novaspan1400: Focussing on Paleocene Reservoir with source rock fingerprinting (Accumulation 42010)

Figure 1e-ivb



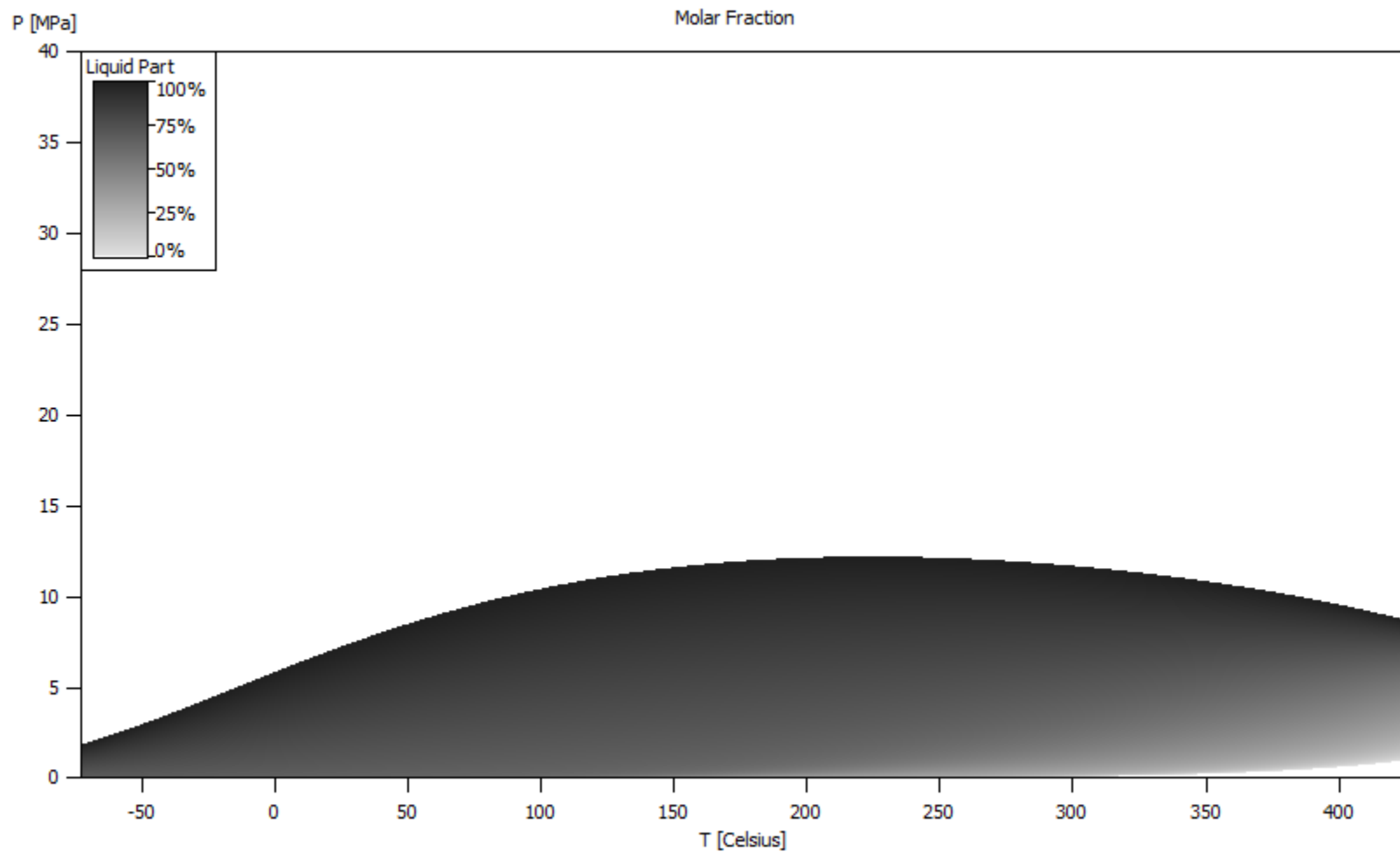
**Line Novaspan1400: Focussing on Paleocene Reservoir with source rock
fingerprinting and showing the hydrocarbon component distributions
(Accumulation 42010)**

Figure 1e-ivc



Line Novaspan1400: Focussing on Paleocene Reservoir with pressure-temperature diagram of the reservoir hydrocarbons (Accumulation 42010)

Figure 1e-ivd

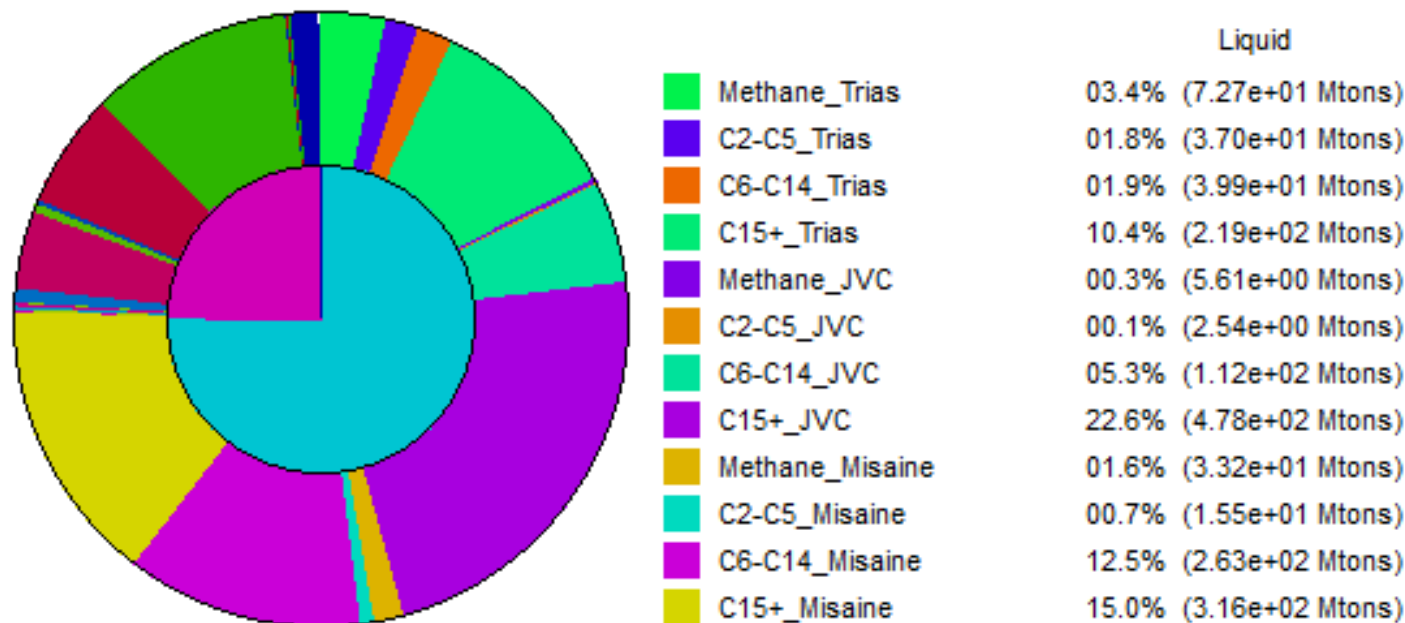


MASS BALANCE OF HYDROCARBON IN LINE NOVASPAN 1400

Line 1400: Mass Balance of Reservoir Hydrocarbons

Figure 1f-i

Info: Only percentages are rounded. Values < 0.005% are displayed as 0.00%!
 Volumes/masses calculated for a width of 1 km



The curve showing cumulative total generated, total expelled, and total accumulated in geological time since 170 Ma – Line 1400

Figure 1f-ii

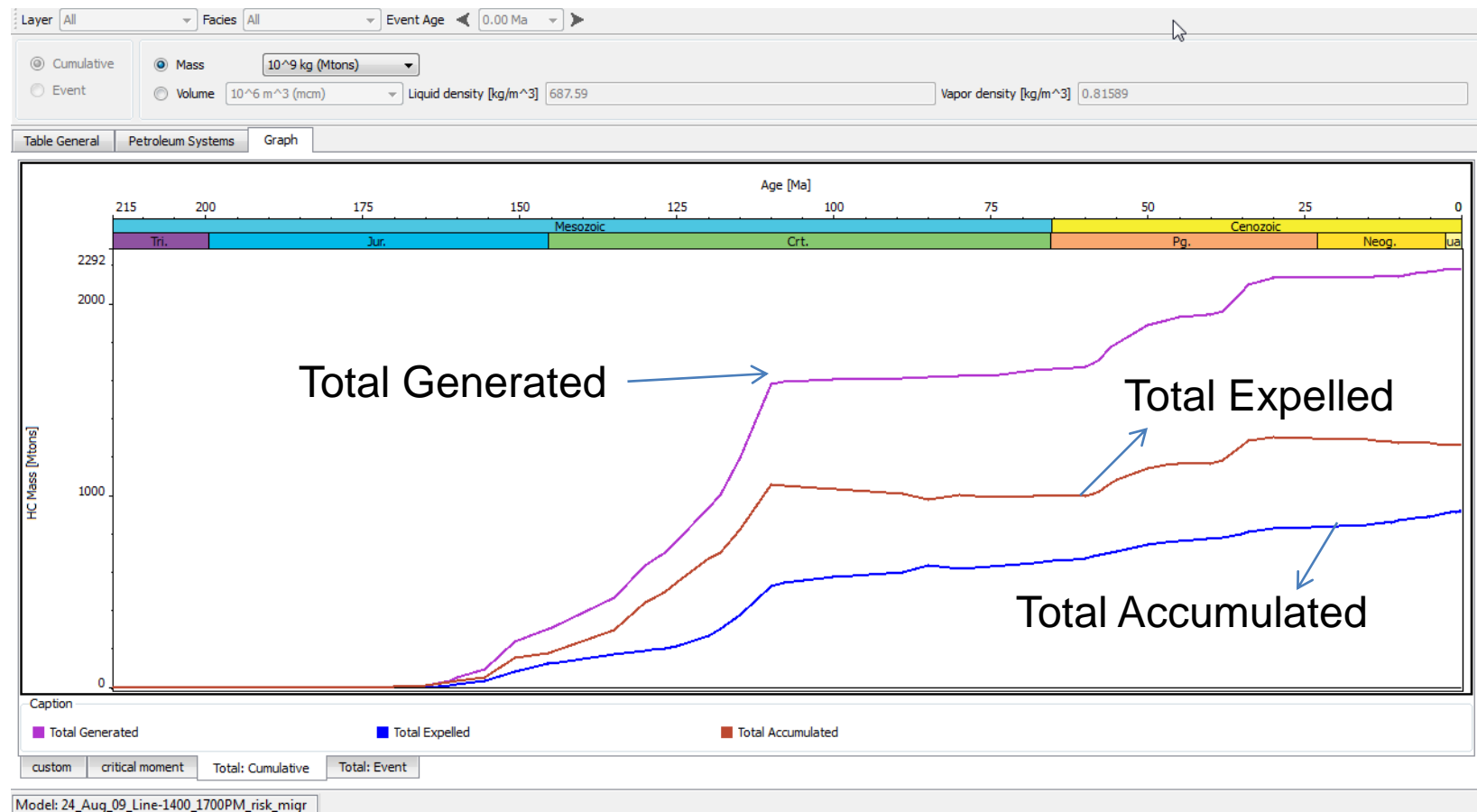
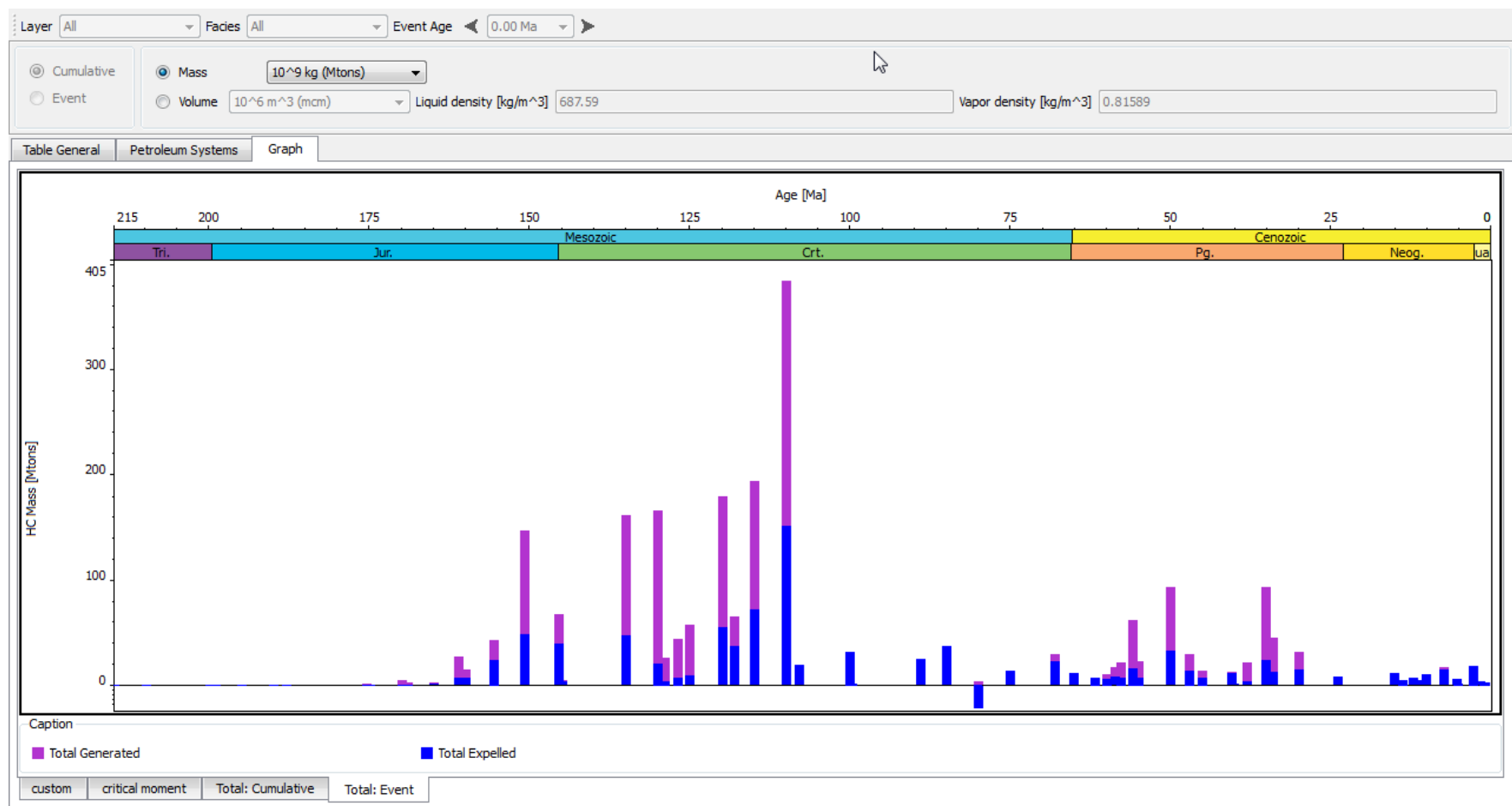


Figure 1f-iii

Line 1400: Timing of total HC generated and total expelled



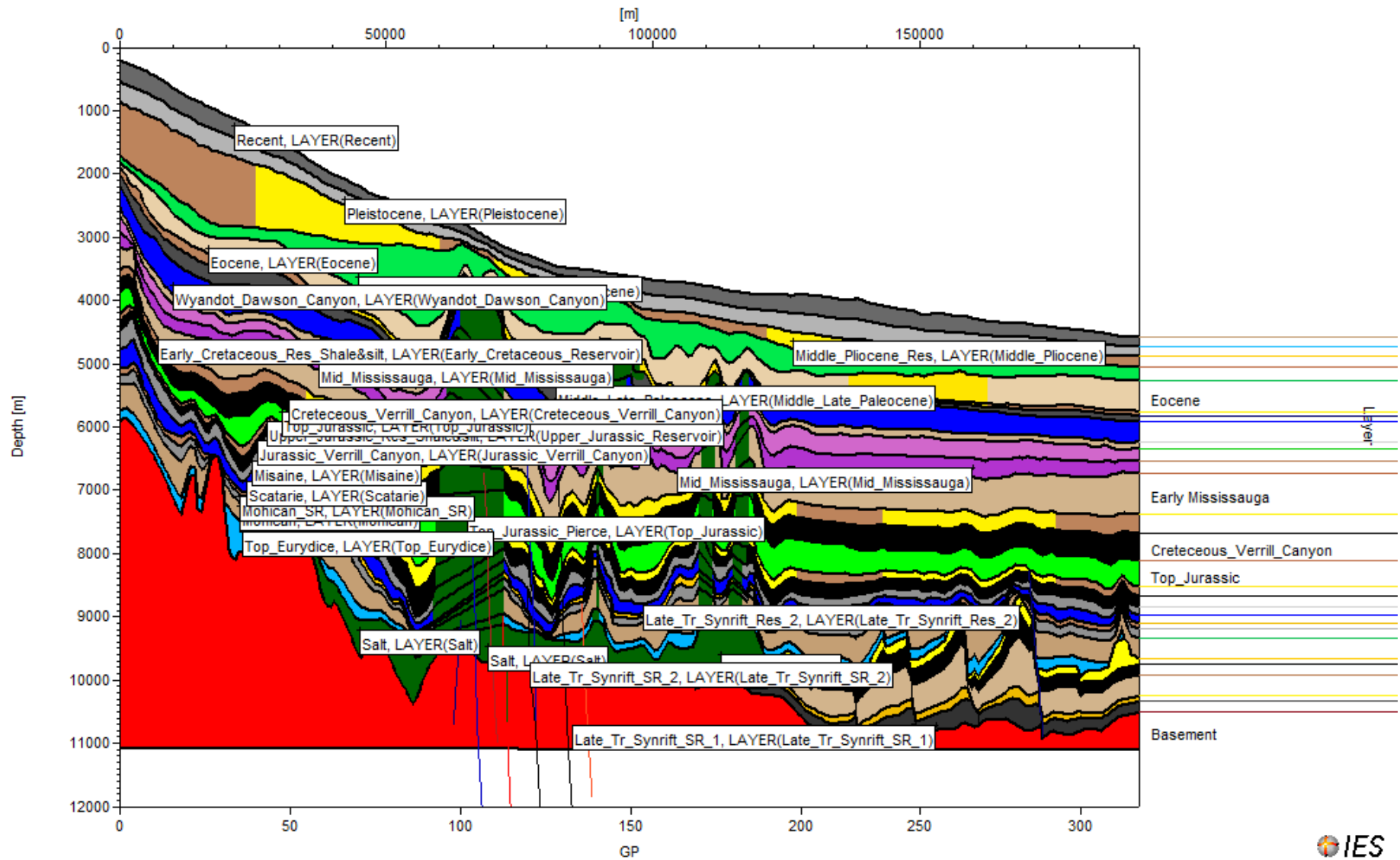
Conclusion: Seismic Line Nova Span 1400

- Using the transient heat flow trends, the modelled and measured heat flow values have been calibrated . With the exception of two heat flow values (heat flow lines 110 and 111), all measured flow values are closely calibrated. These two heat flow values are connected close to the diapiric salt. Therefore, it is be possible that seismic interpretation on the outline of the salt (in upper section) has to be modified to calibrate the measured values
- Because the revised model is calibrated with lower heat trends, both Late Jurassic and Early Cretaceous conceptual reservoirs in the slope contain more oil (C15+ and condensates), which is associated with methane and wet gas. The Paleocene conceptual reservoir has mainly oil (C15+ and C6-C14 components)
- The heat flow values on top of the salt diapir is much hotter compared to the flank of the salt. However, the variation in heat flow values depends on the thickness of the salt diapir and nearness to the surface

LINE 88-1A: PETROLEUM SYSTEM MODELLING PETROBUILDER

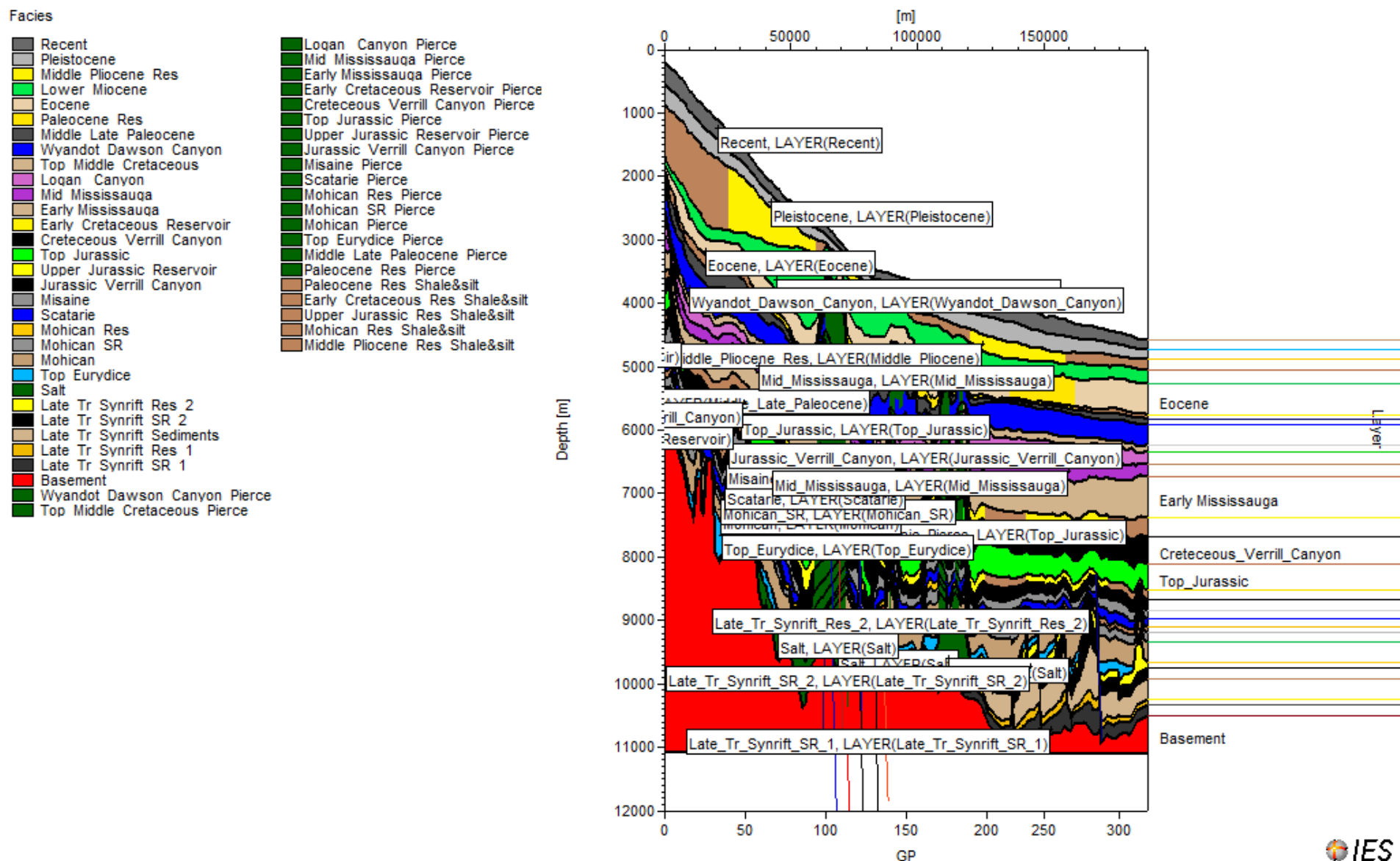
Line 88-1A: General Stratigraphy with Horizons as assigned within PetroBuilder

Figure 2a-i



Line 88-1A: General Stratigraphy with Horizons and legends as assigned within PetroBuilder

Figure 2a-ii

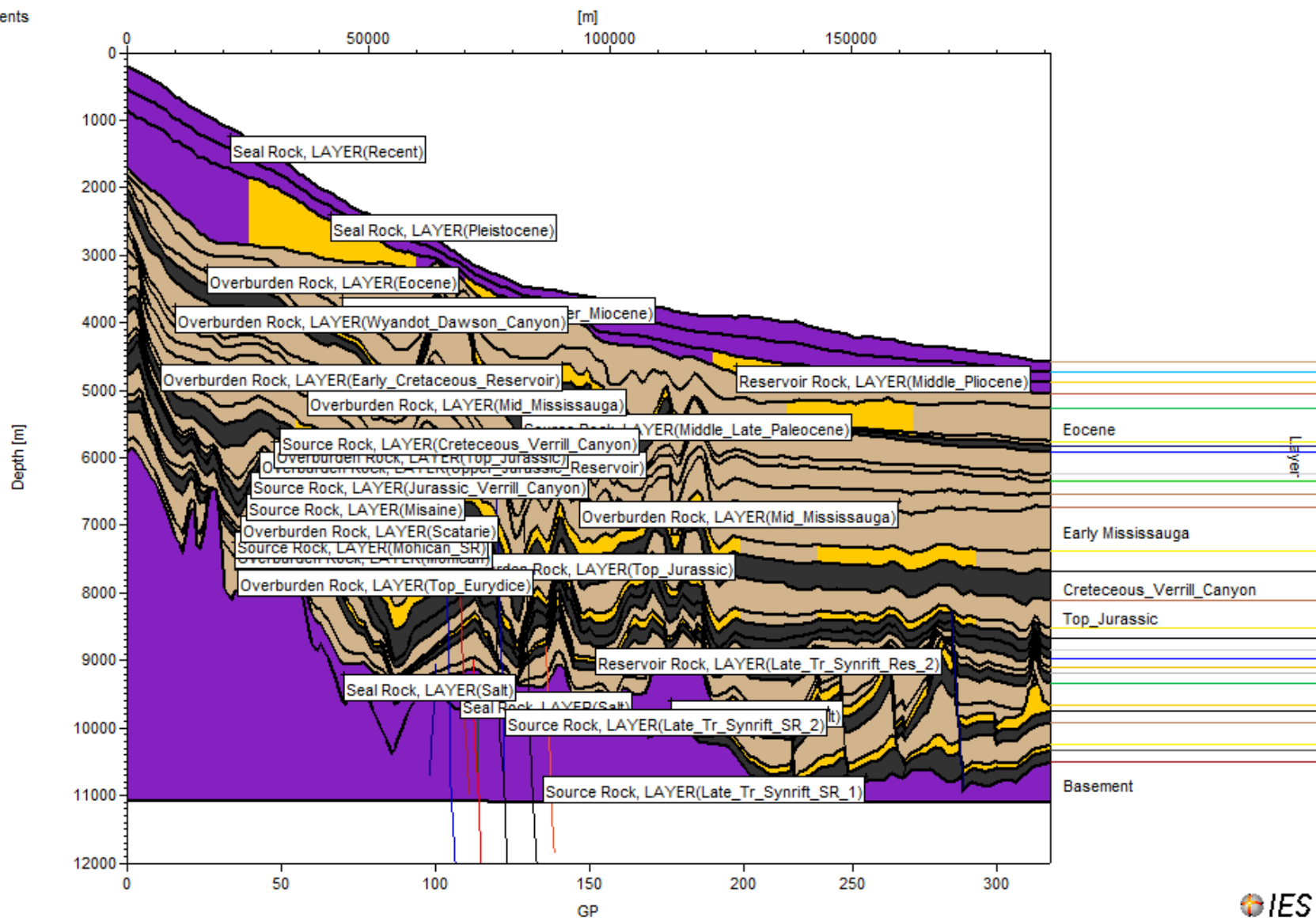


Line 88-1A: General Stratigraphy with Horizons and petroleum system elements as assigned within PetroBuilder

Figure 2a-iii

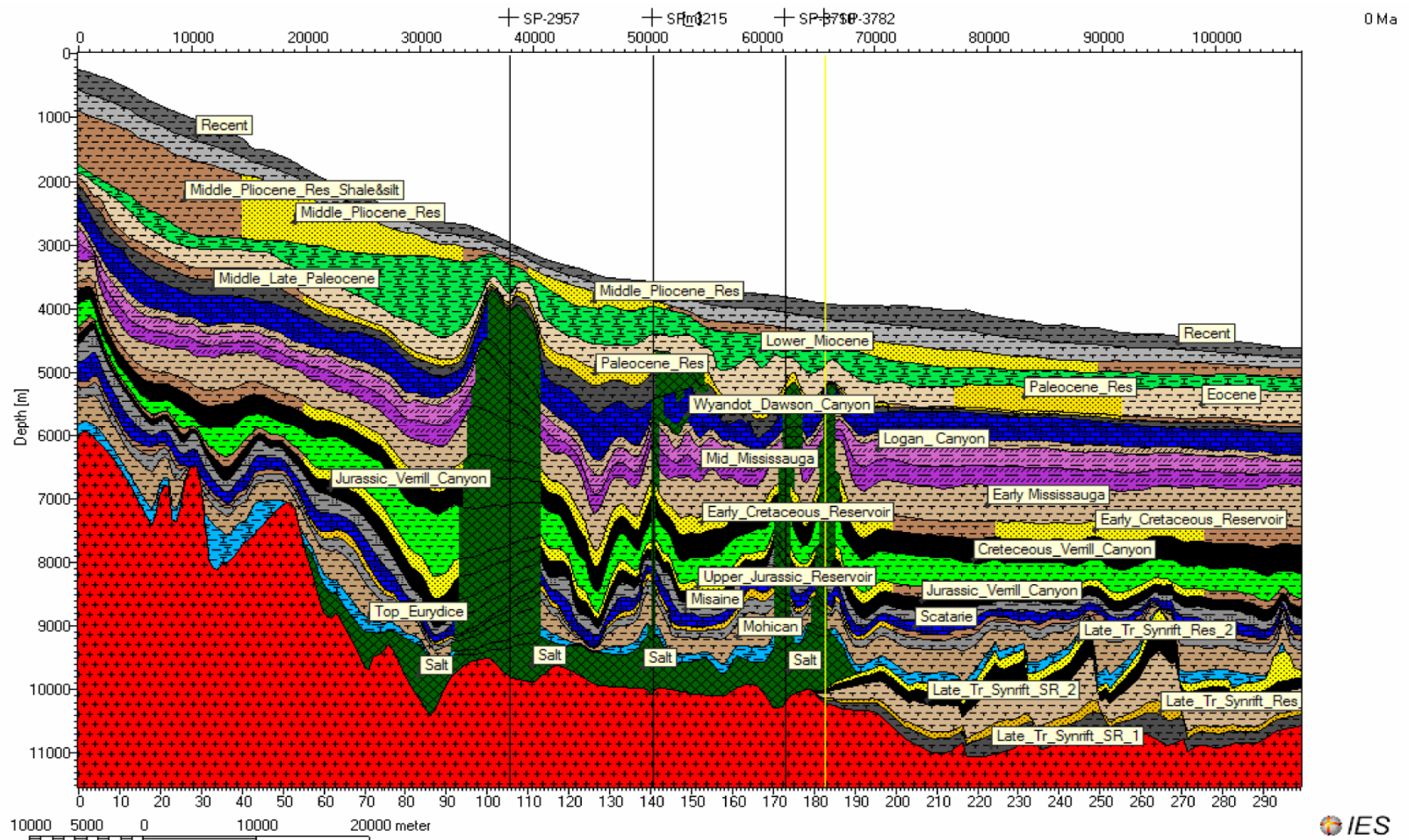
Petroleum System Elements

- Seal Rock
- Reservoir Rock
- Overburden Rock
- Source Rock



Model Lithology Distribution: Line 88-1A

Figure 2a-iv



Line 88-1A – Morphology of diapiric and allochthonous salt

Figure 2a-v

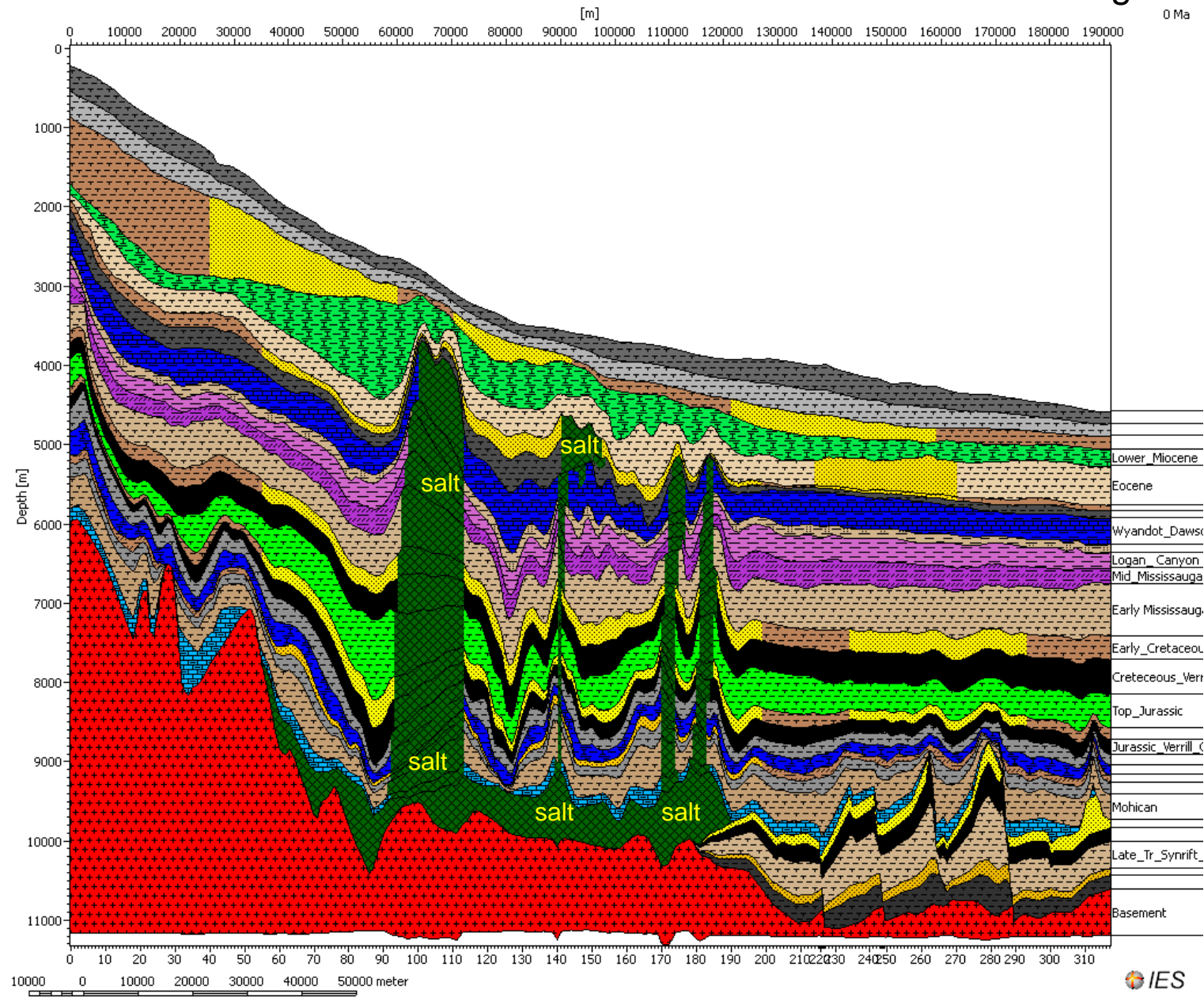
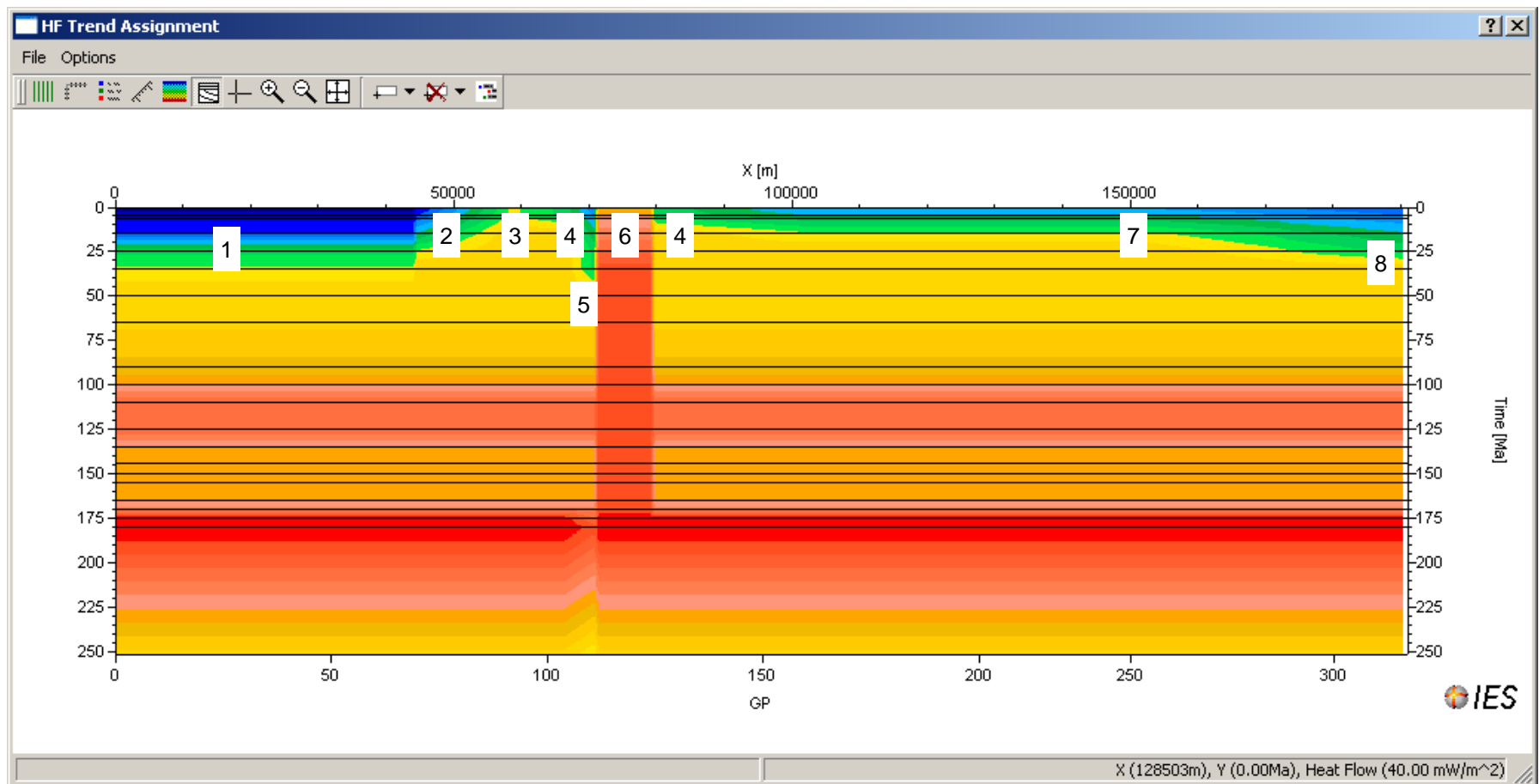


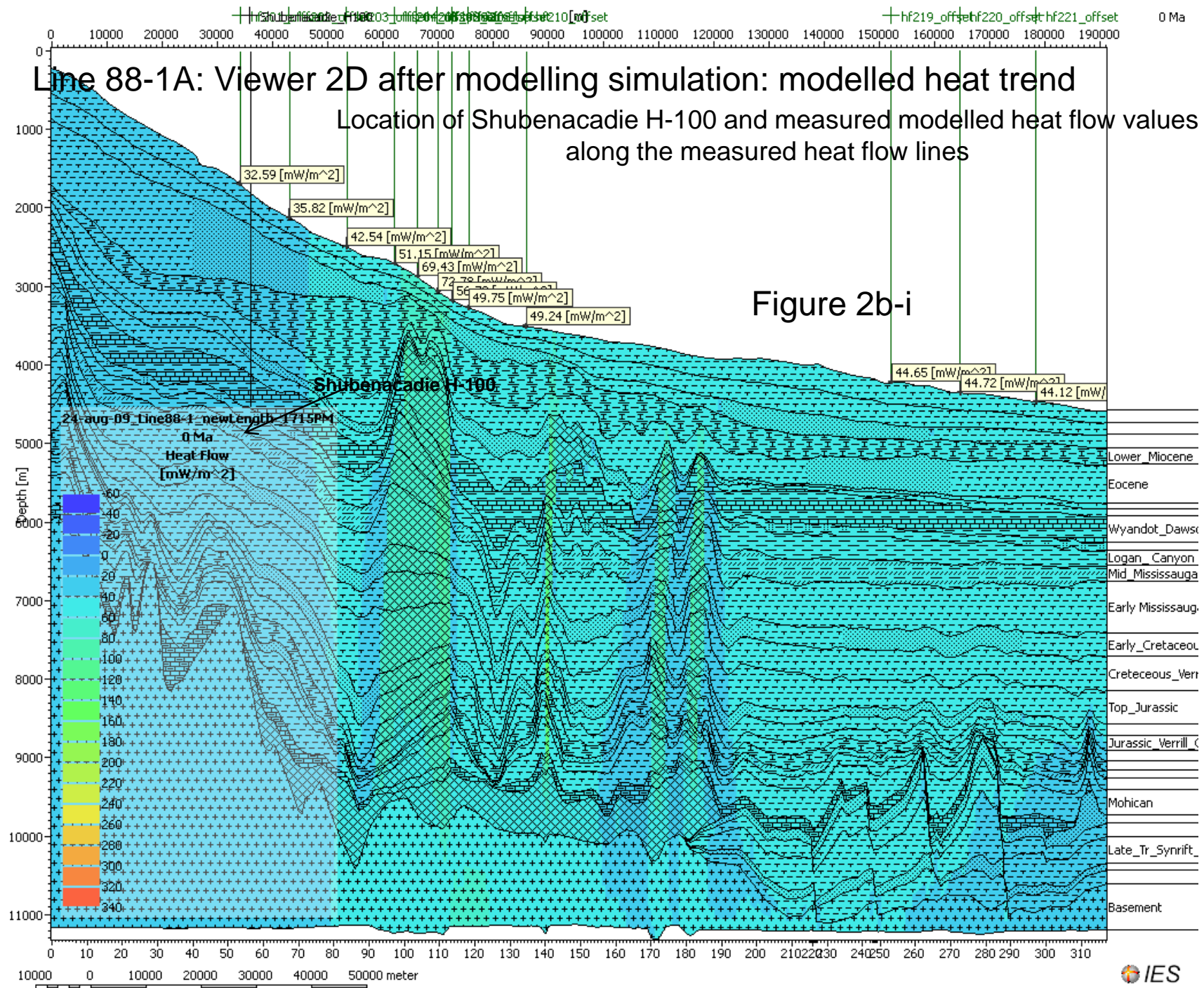
Figure 2a-vi

Heat flow trend used for line 88-1A (final): before modelling simulation in PetroBuilder



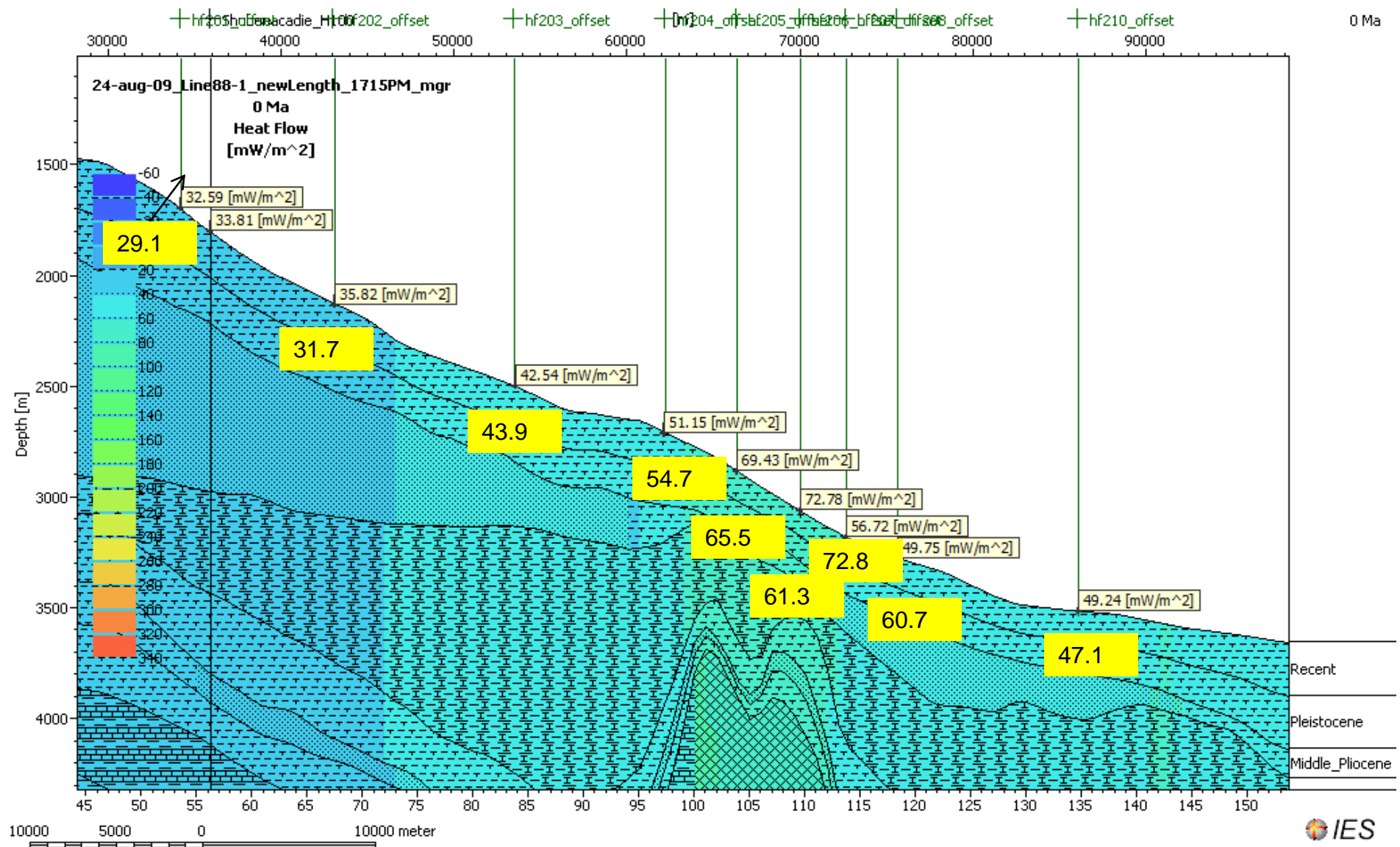
1:HF_Shelf_low; 2:HF_Shelf; 3: HF_High_Salt; 4: HF_Salt; 5: Scotian1600_Cooler; 6: HF_VH_Salt; 7: HF_Slope; 8: HF_Slope_lower

**LINE 88-1A:
PETROLEUM SYSTEM MODELLING
AFTER SIMULATION – VIEWER 2D**



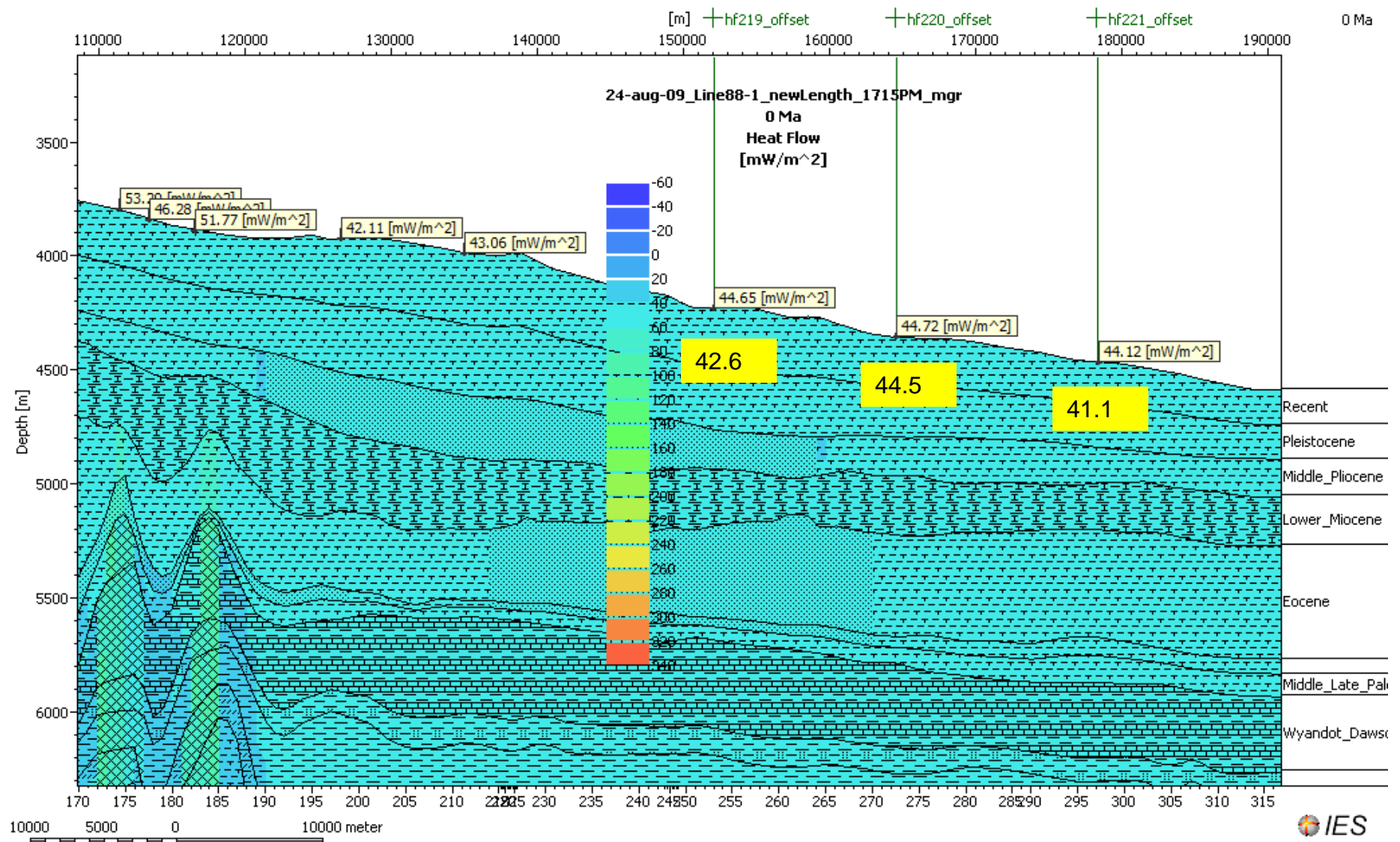
Heat flow trend for line 88-1A (final): Modelled heat values on each heat flow measured points based on calibration of measured heat flow values (Shelf to Mid Section of the Seismic Line 88-1A)

Figure 2b-ii



Heat flow trend for line 88-1A (final): modelled heat values
on each heat flow points based on calibration of
measured values (Mid Section to end of the section in the slope)

Figure 2b-iii



Seafloor Heat Flow: Measured vs. Modelled (Line 88-1A)

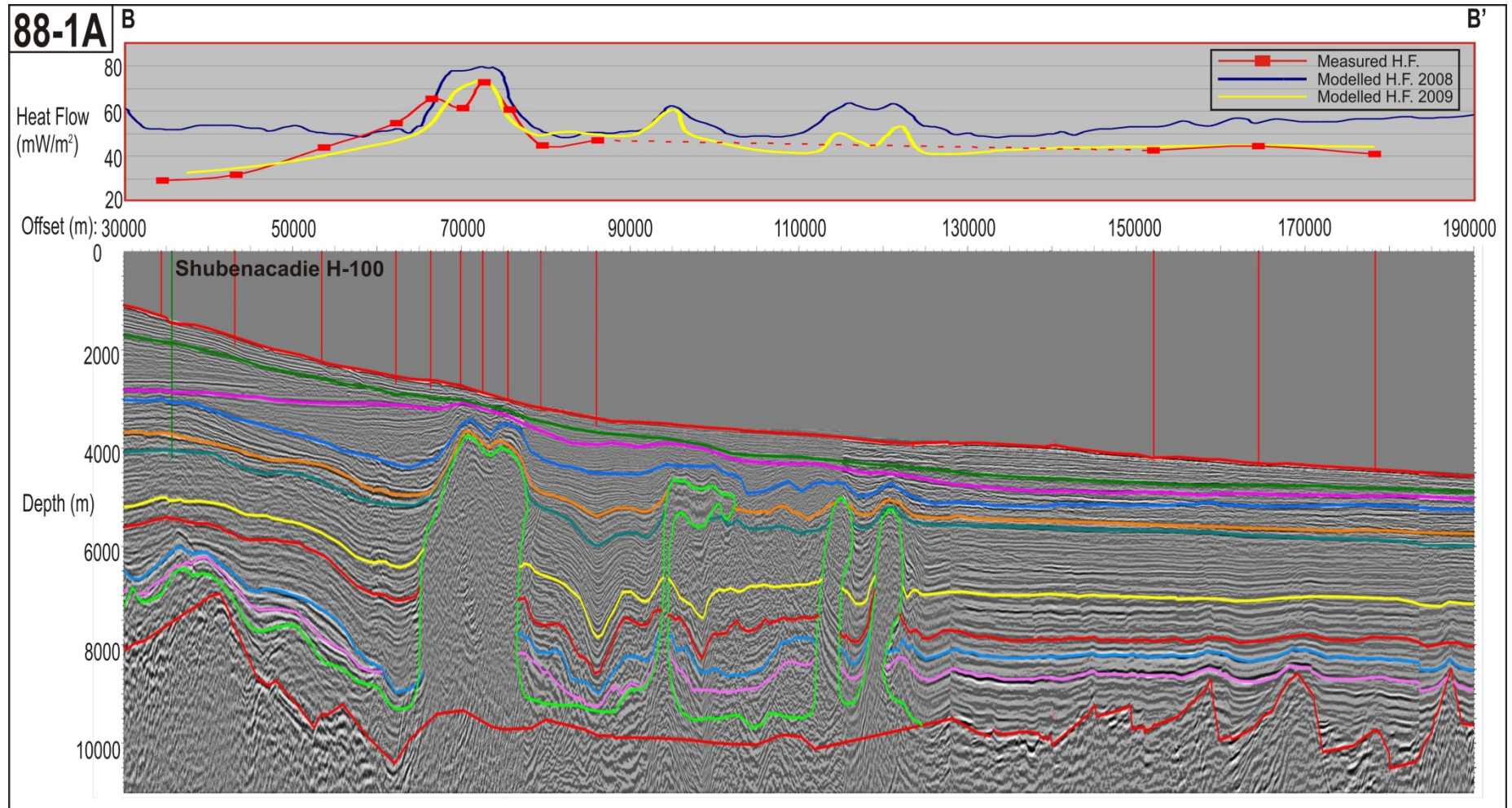
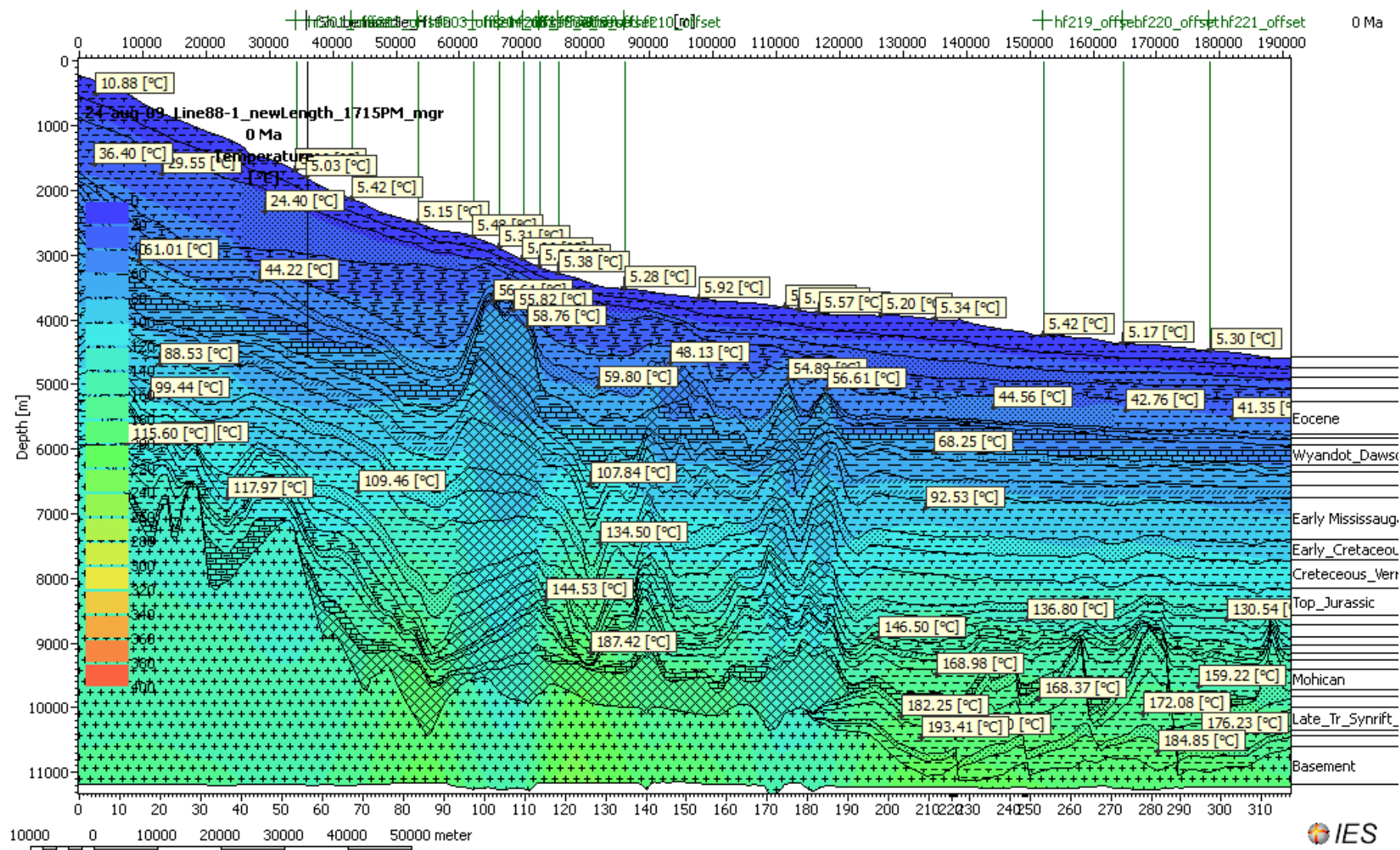


Figure 2b-iii

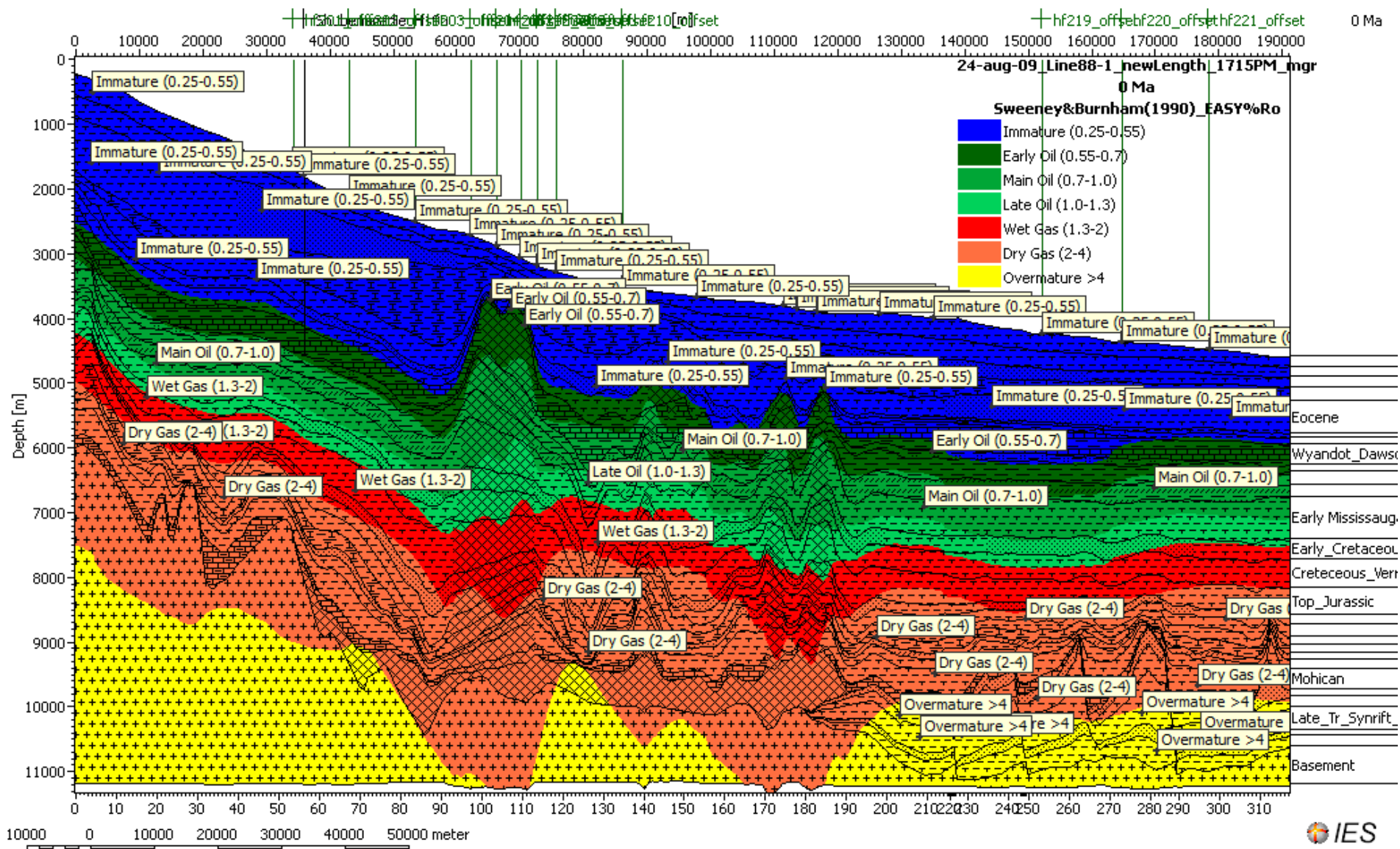
Line 88-1A (final): modelled temperature profile along the section
(depth-wise and length-wise)

Figure 2c-i



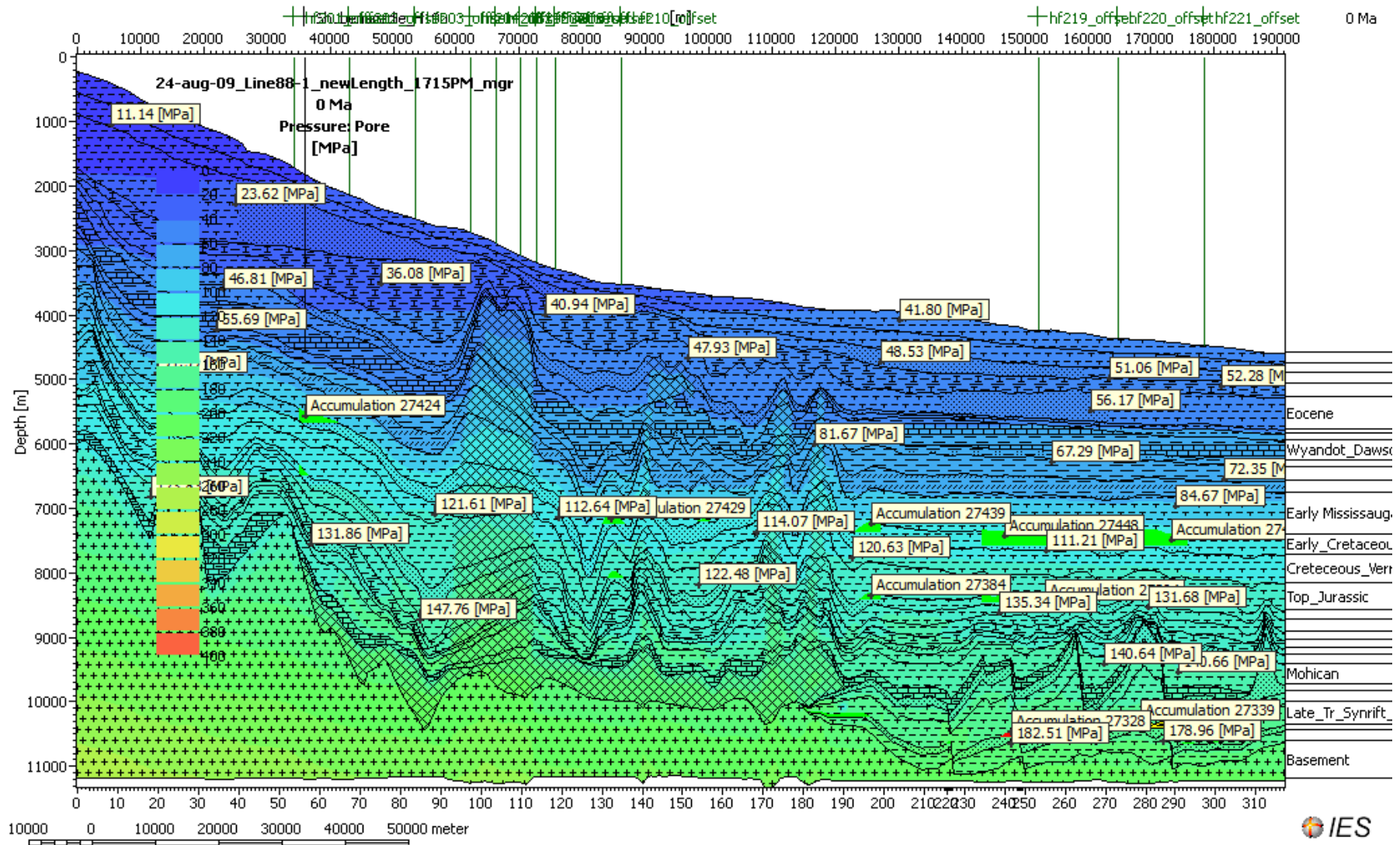
Line 88-1A: Modelled Maturity Calibration based on Sweeney and Burnham (1990)

Figure 2c-ii



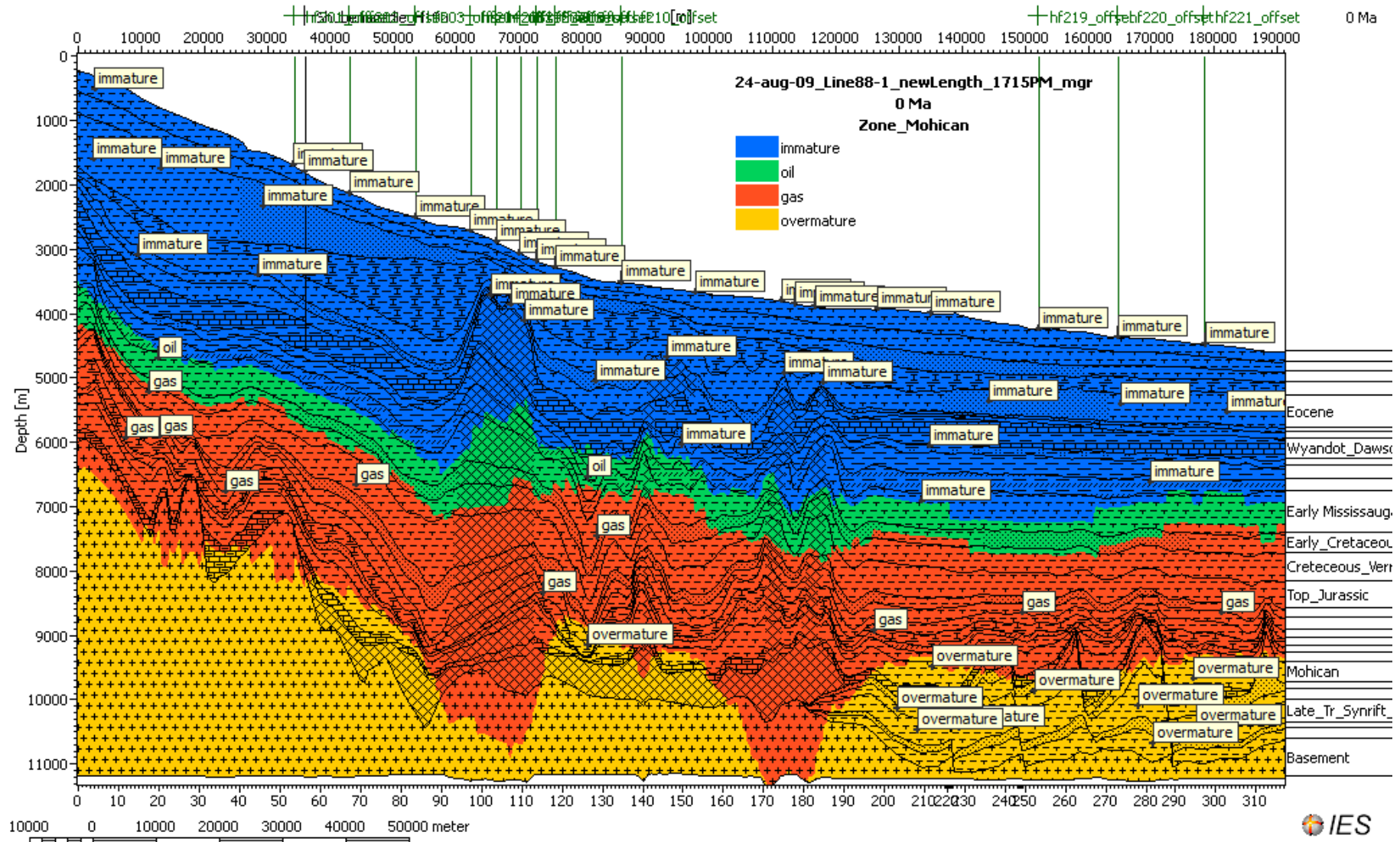
Line 88-1A: Modelled Pore Pressure Calibration

Figure 2c-iii



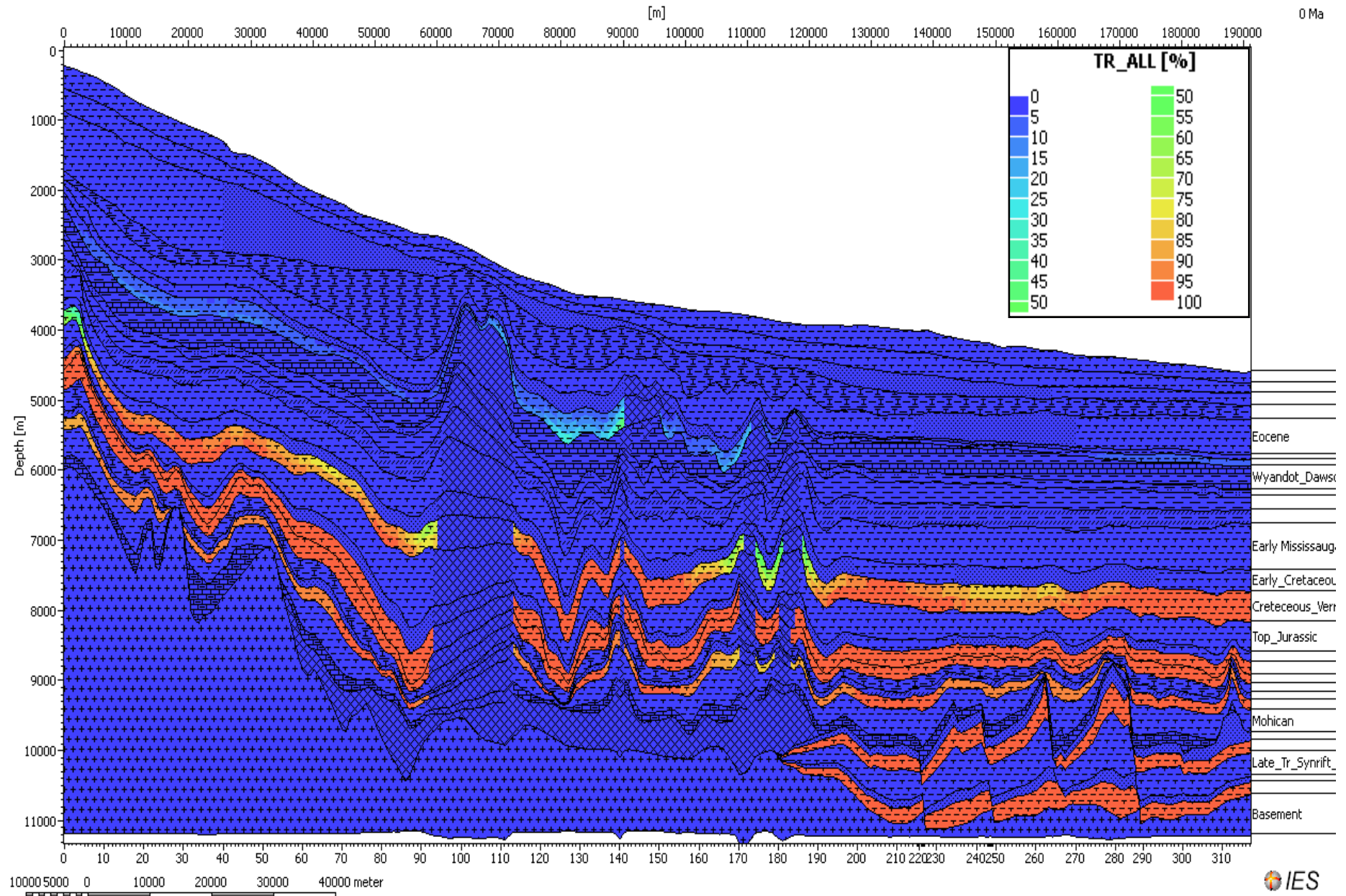
Line 88-1A (final): Modelled Hydrocarbon Zones

Figure 2c-iv



Transformation Ratio: Line 88-1a

Figure 2c-v

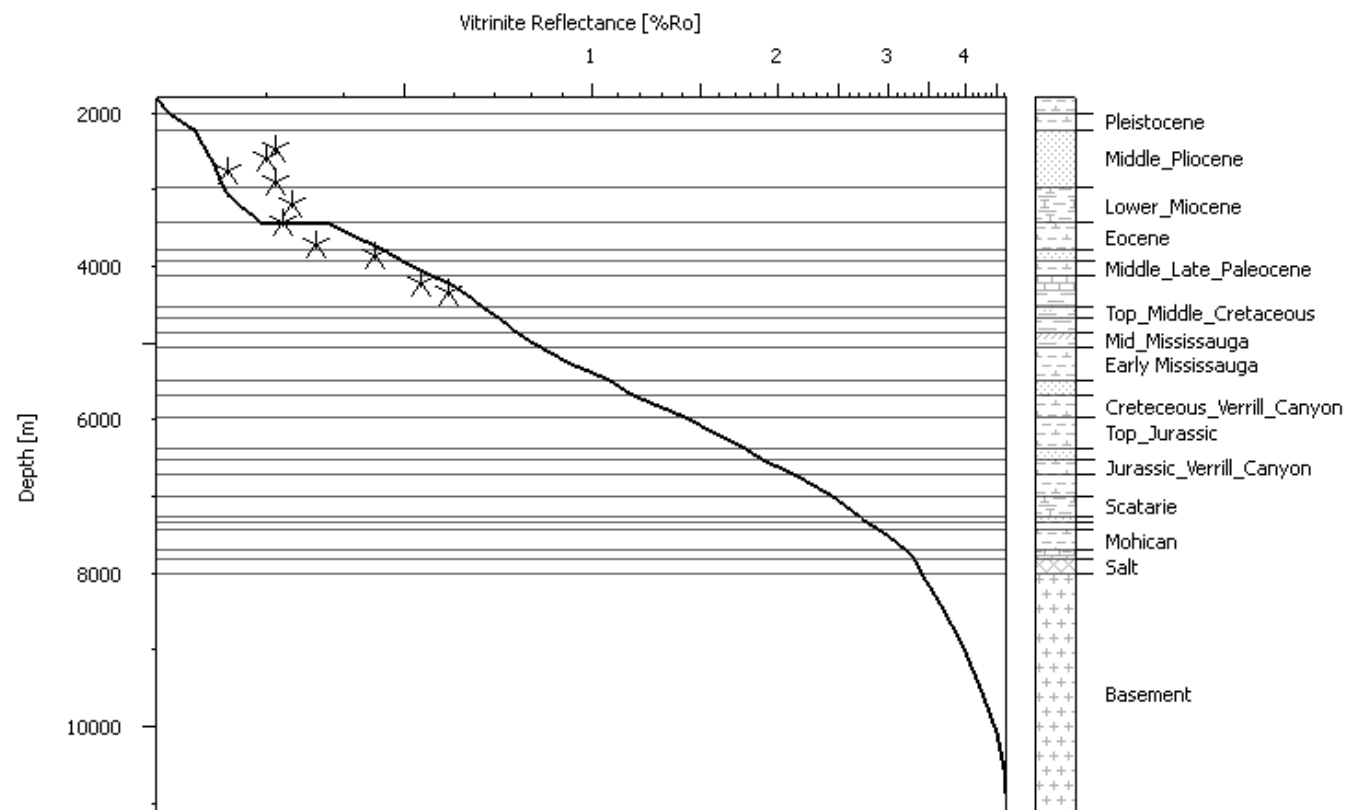


Line 88-1A: ID Extraction of Shubenacadie H-100 well: Vitrinite Reflectance profile

Shubenacadie_H100
— Sweeney&Burnham(1990)_EASY%Ro [%Ro] for 20-aug-09_Line88-1_newLength_1335PM_final_mgratShubenacadie_H100 (projected 36000.0m) at 0

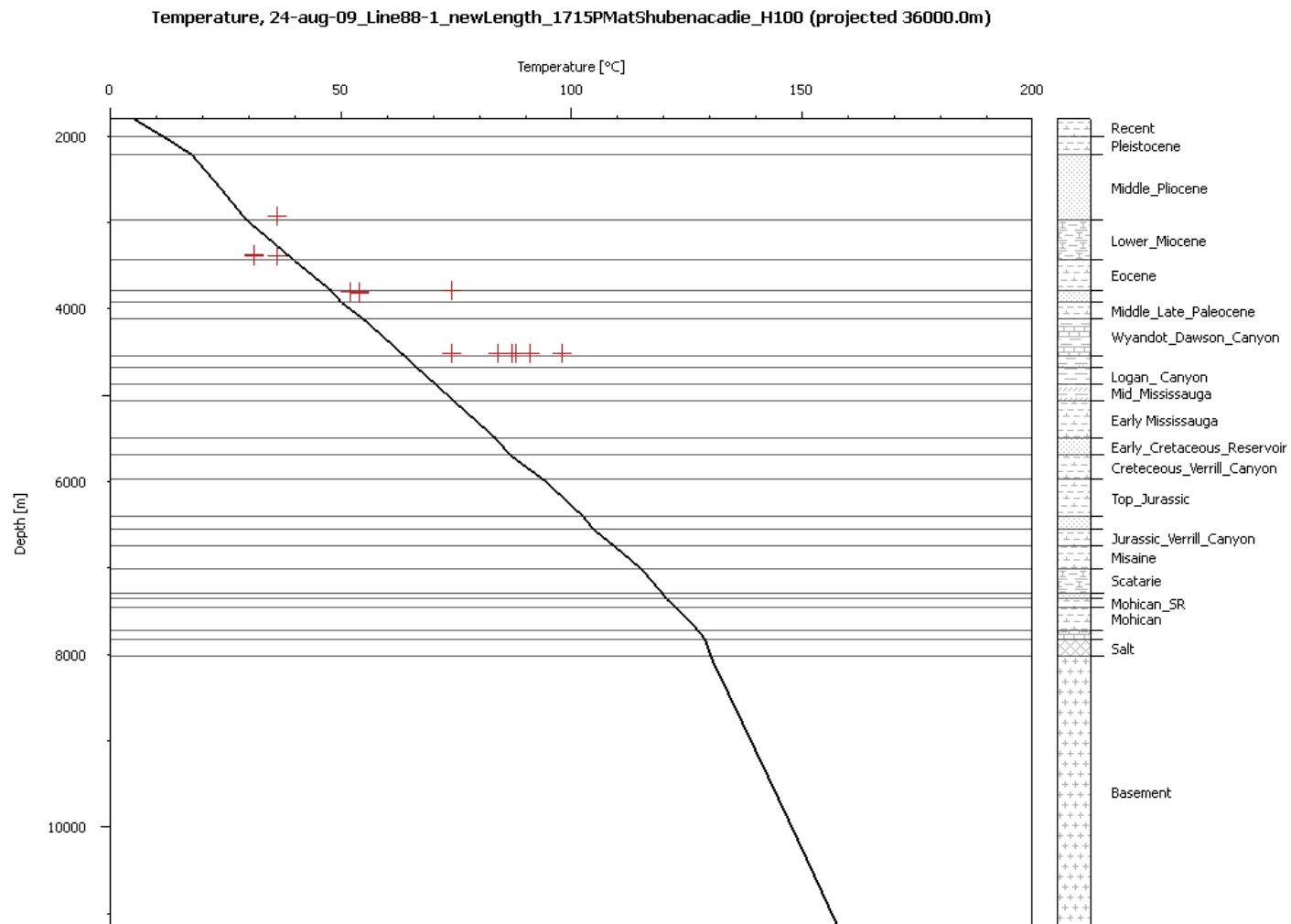
Figure 2d-ii

aturity, 20-aug-09_Line88-1_newLength_1335PM_final_mgratShubenacadie_H100 (projected 36000.0m)



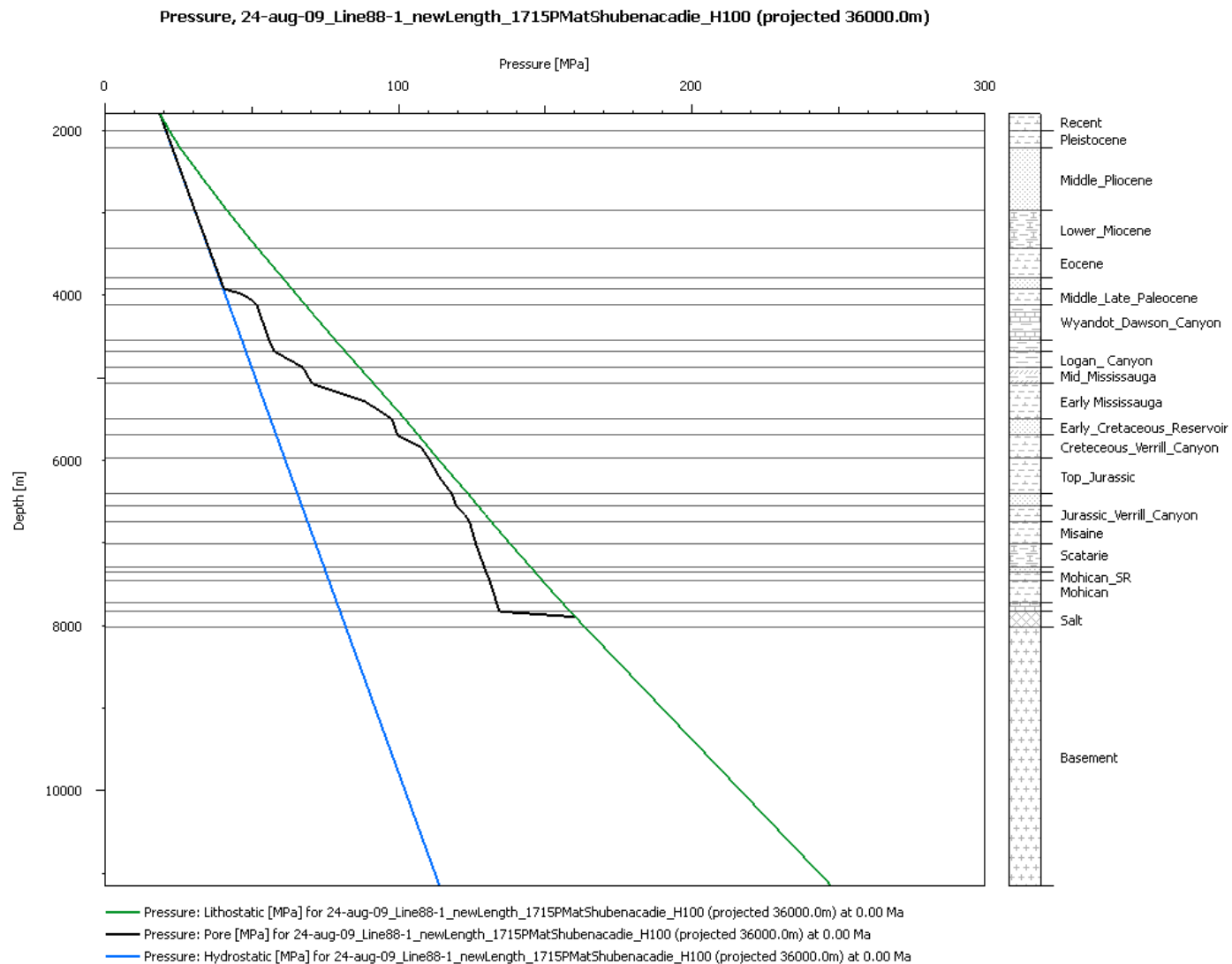
Line 88-1A: ID Extraction of Shubenacadie H-100 well: temperature vs. depth profile

Figure 2d-iii



Line 88-1A: ID Extraction of Shubenacadie H-100 well: pressure vs. depth profile

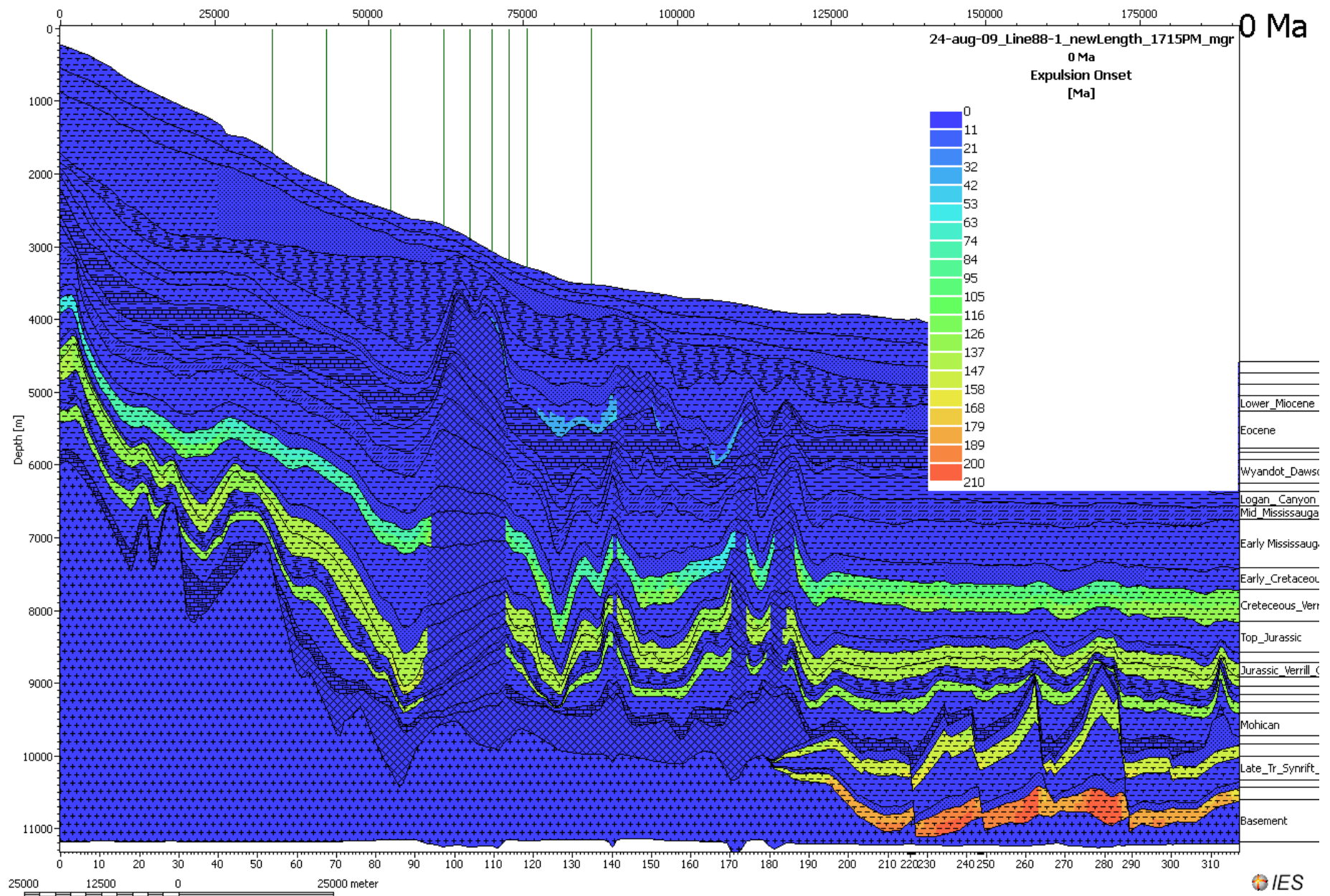
Figure 2d-iv



**LINE 88-1A: ONSET OF
HYDROCARBON EXPULSION
AND RESERVOIR HYDROCARBON
FINGERPRINTING**

Onset of Expulsion: Line 88-1a

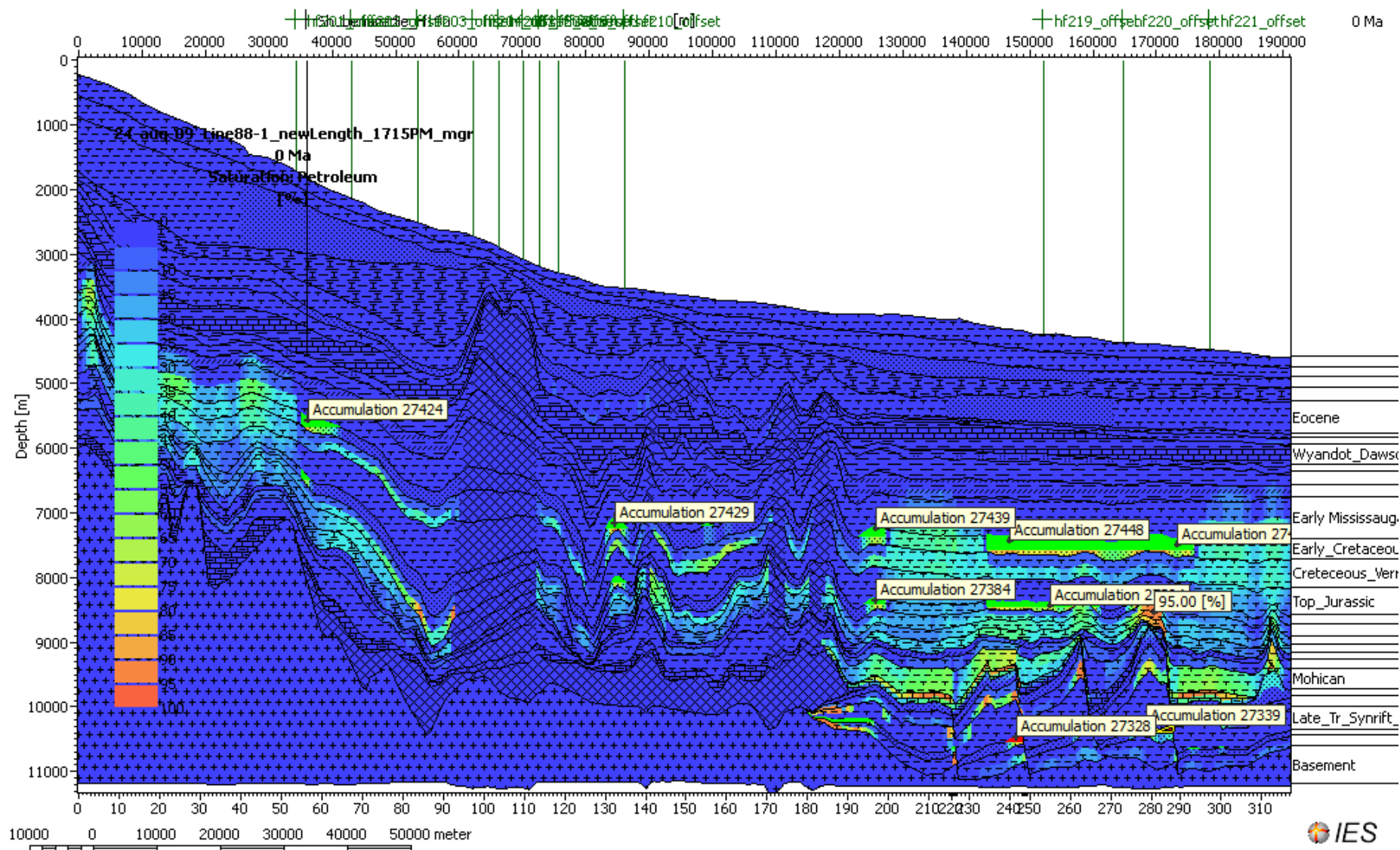
Figure 2e



LATE TRIASSIC RESERVOIRS: LINE 88-1A

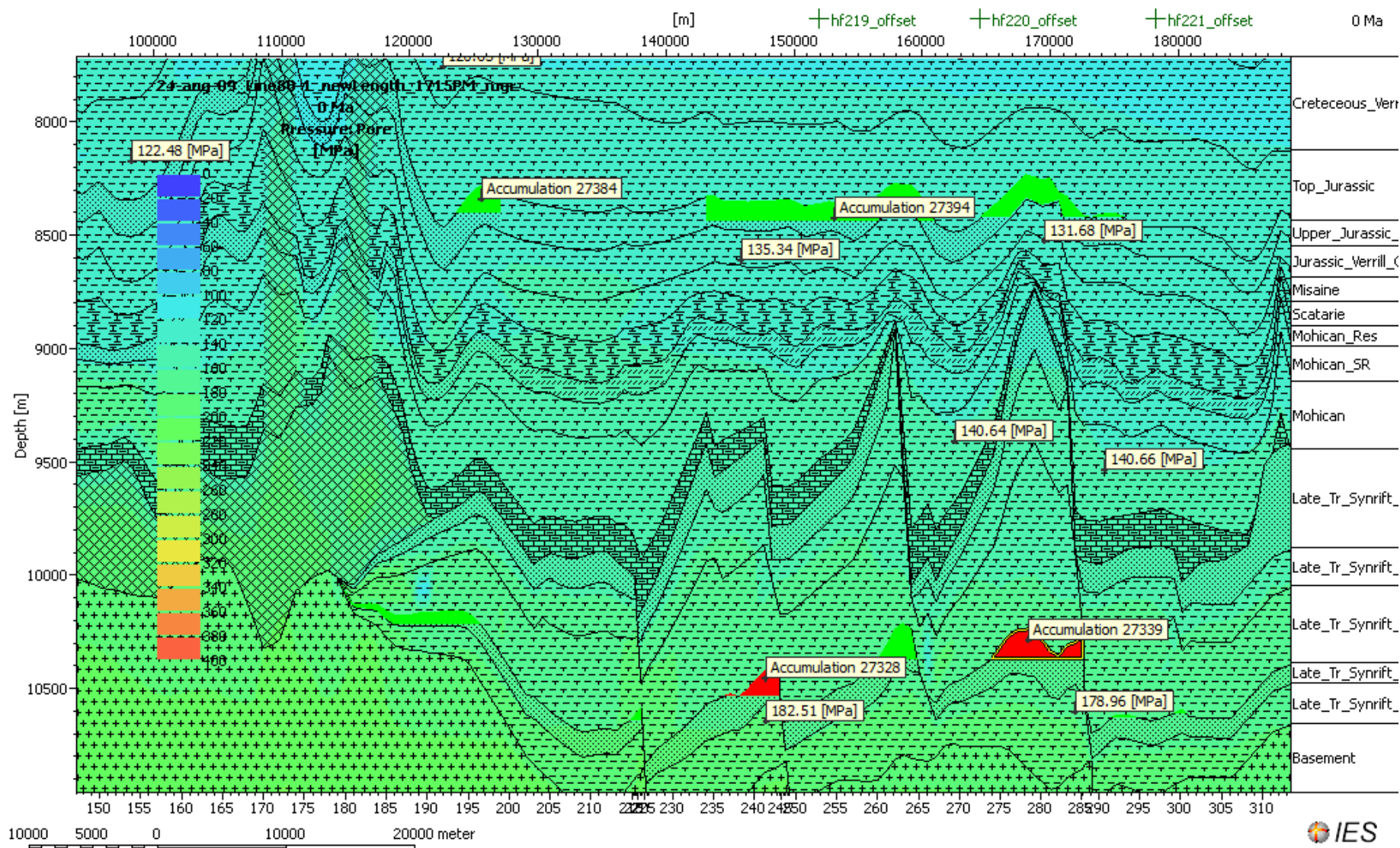
Line 88-1A: Late Triassic Reservoir 27339 – ultradeep section beyond salt diapirs

Figure 2f-i



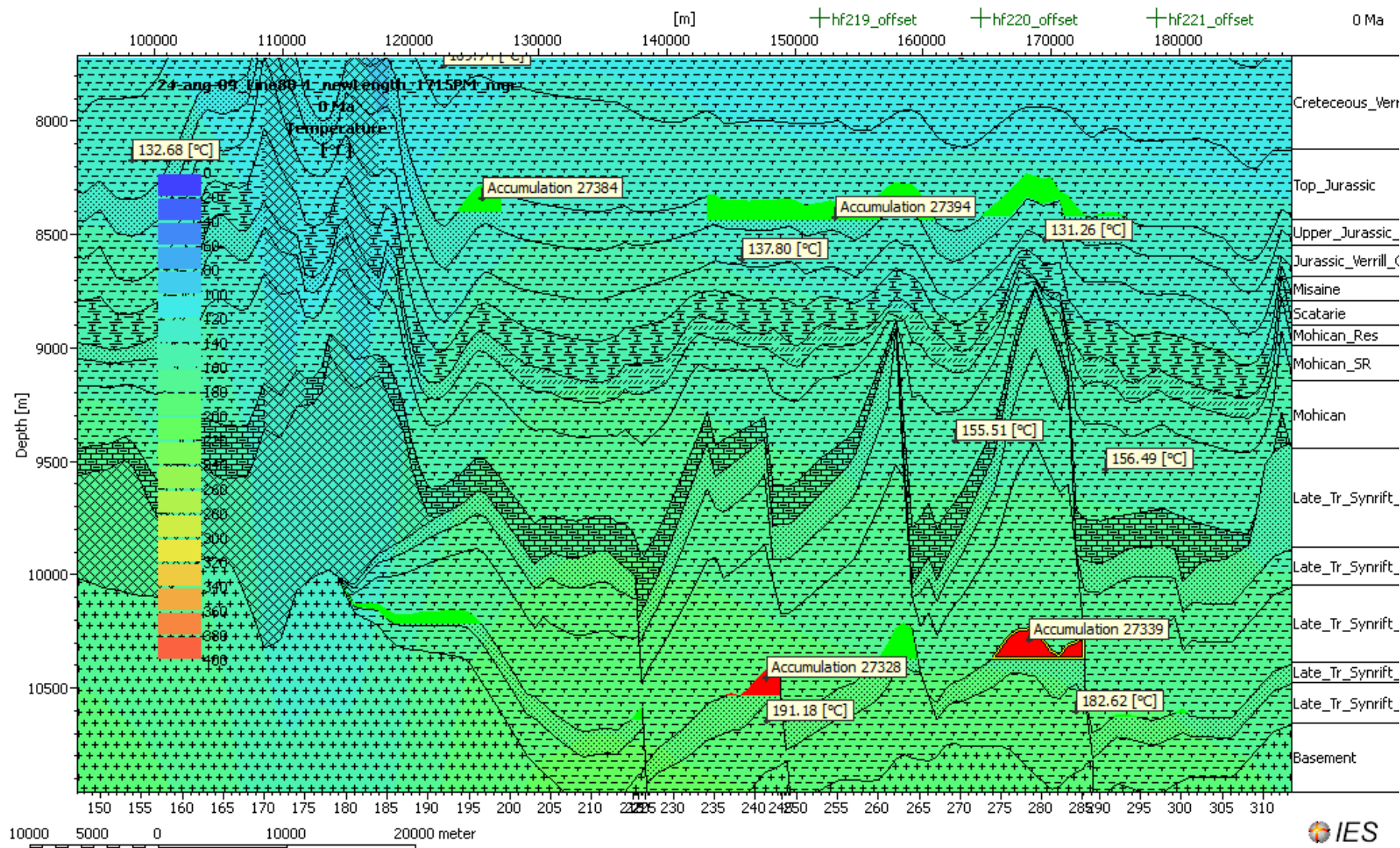
Line 88-1A: Ultradeep section beyond salt diapirs
pore pressure distribution surrounding the Late Triassic Reservoir 27339

Figure 2f-ii



Line 88-1A: Ultradeep section beyond salt diapirs
temperature distribution surrounding the Late Triassic Reservoir 27339

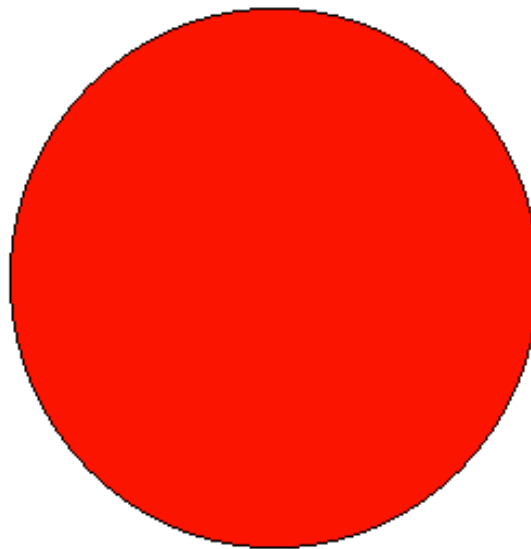
Figure 2f-iii



Line 88-1A: Late Triassic Reservoir 27339 – ultradeep section beyond salt diapirs: source rock fingerprinting

Molar Fractions

173.011 MPa 178.215 Celsius

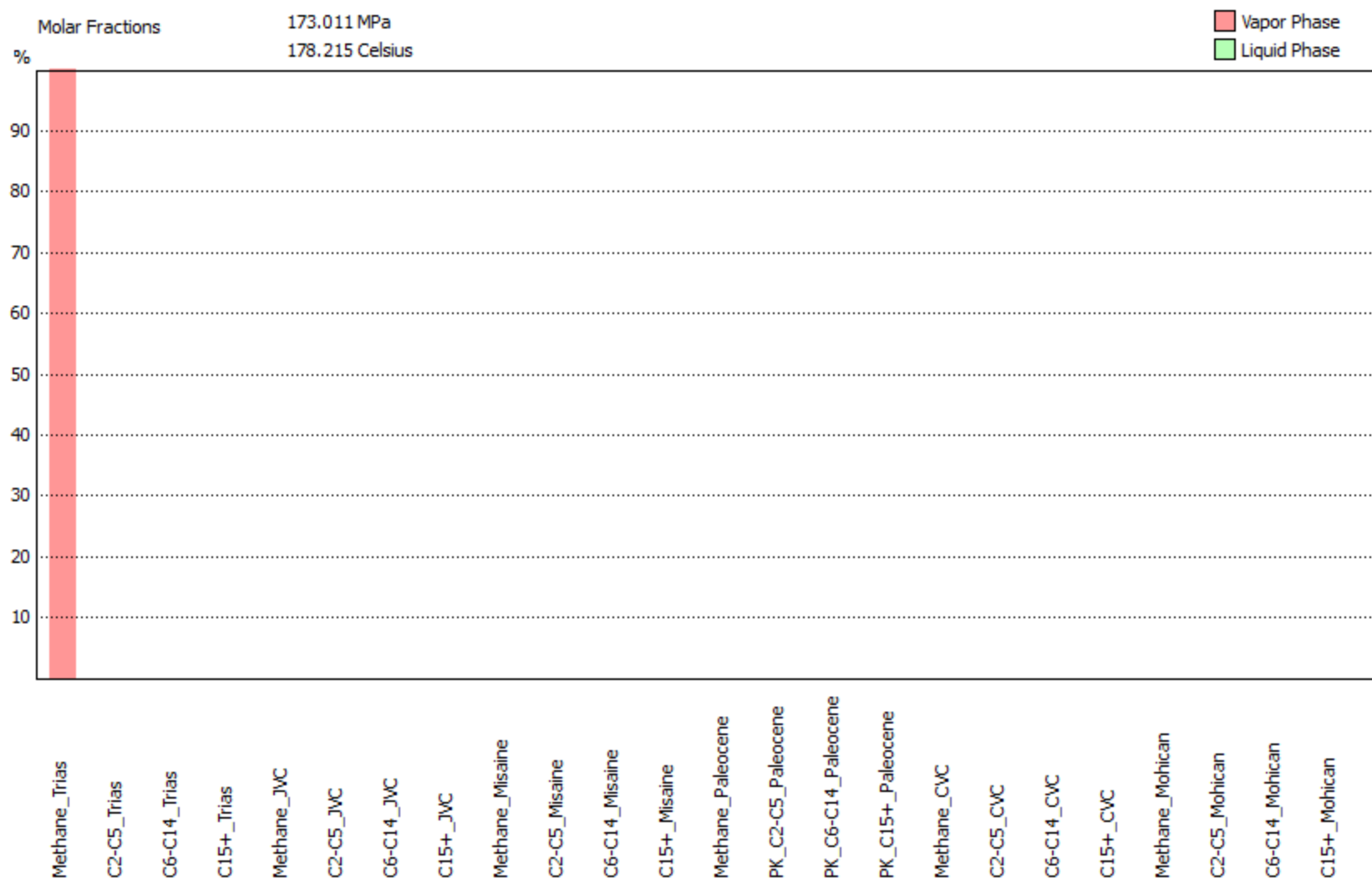


Vapor
100.0% Methane_Trias
0.0% C2-C5_Trias
0.0% C6-C14_Trias
0.0% C15+_Trias
0.0% Methane_JVC
0.0% C2-C5_JVC
0.0% C6-C14_JVC
0.0% C15+_JVC
0.0% Methane_Misaine
0.0% C2-C5_Misaine
0.0% C6-C14_Misaine
0.0% C15+_Misaine
0.0% Methane_Paleocene
0.0% PK_C2-C5_Paleocene
0.0% PK_C6-C14_Paleocene
0.0% PK_C15+_Paleocene
0.0% Methane_CVC
0.0% C2-C5_CVC
0.0% C6-C14_CVC
0.0% C15+_CVC
0.0% Methane_Mohican
0.0% C2-C5_Mohican
0.0% C6-C14_Mohican
0.0% C15+_Mohican

Figure 2f-iv

Line 88-1A: Late Triassic Reservoir 27339 – ultradeep section
beyond salt diapirs: source rock fingerprinting : methane from
Late Triassic lacustrine source rock

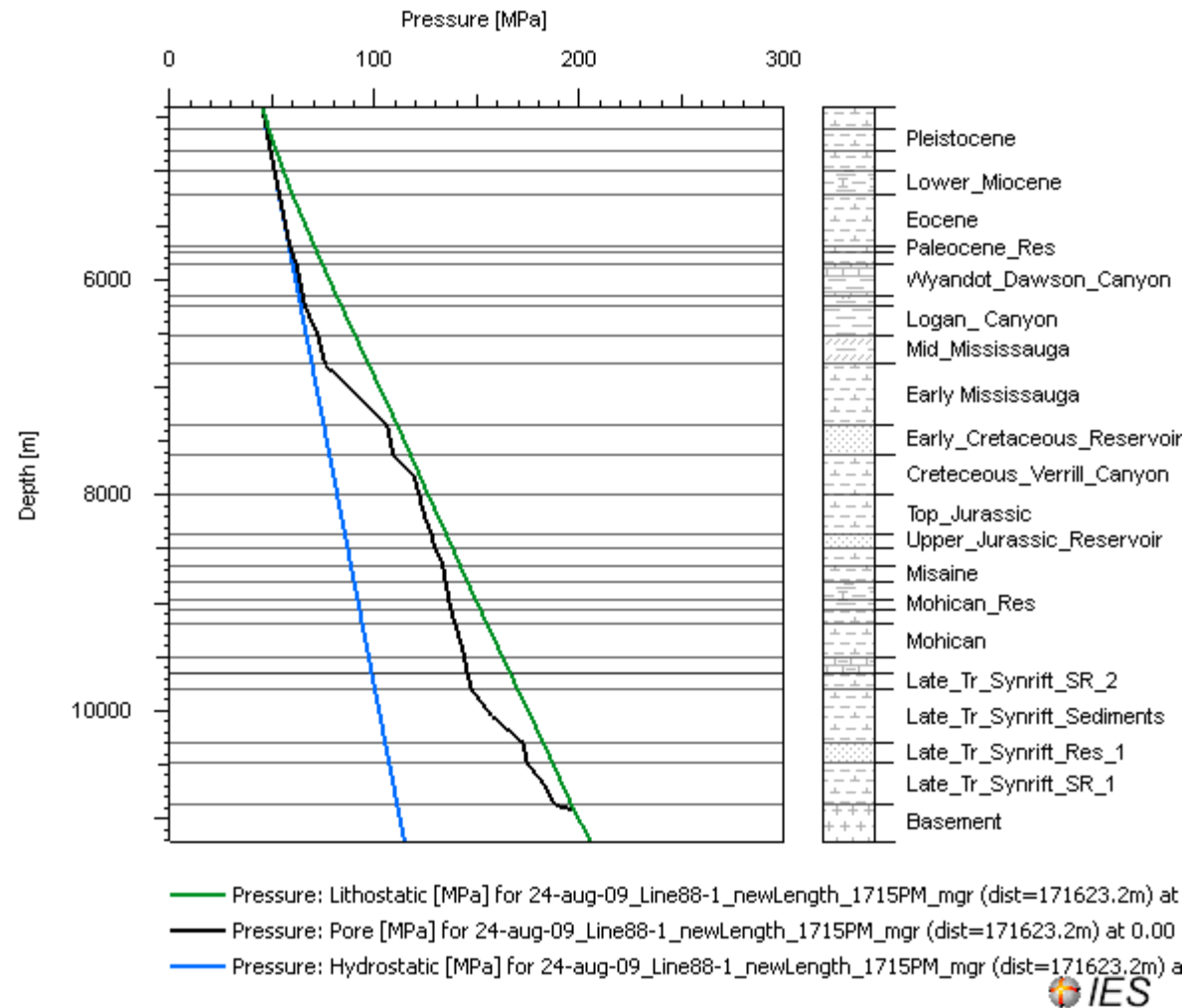
Figure 2f-v



Line 88-1A: Ultradeep section beyond salt diapirs – 1D Extraction pore pressure versus depth on the Late Triassic Reservoir 27339

Figure 2f-vi

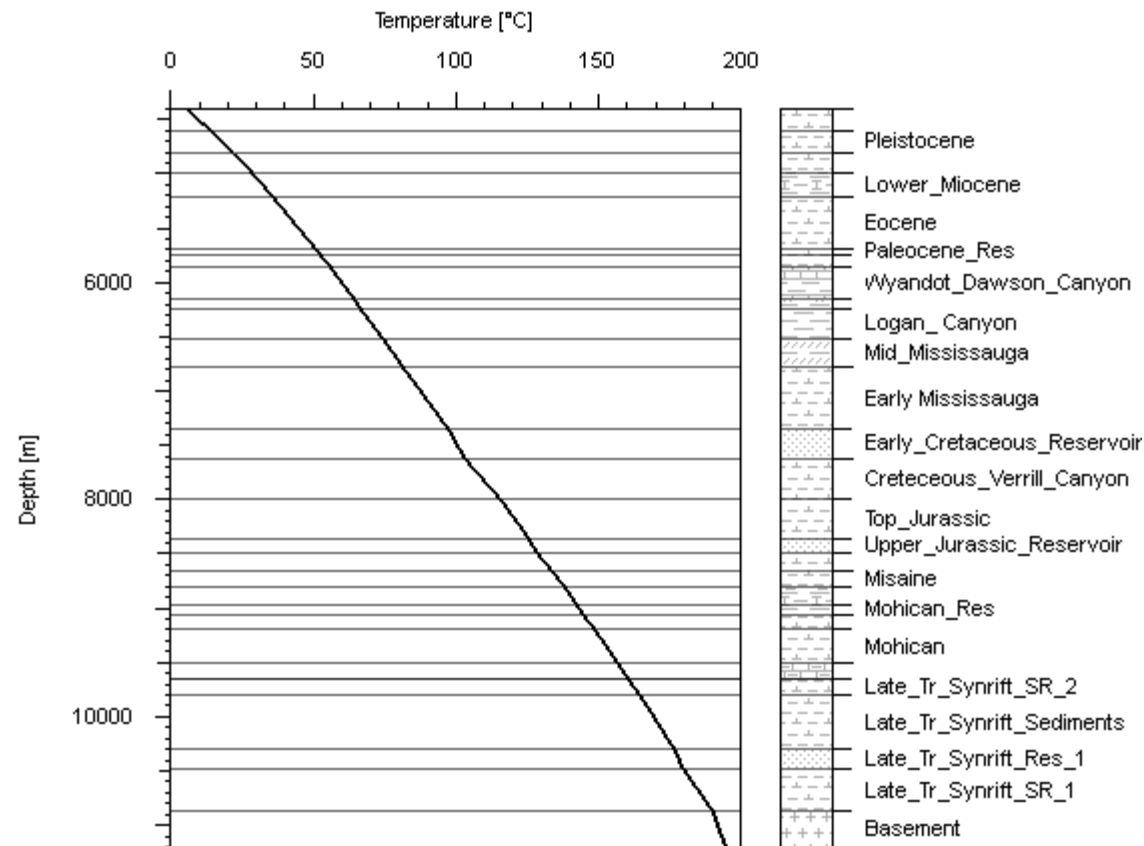
Pressure, 24-aug-09_Line88-1_newLength_1715PM_mgr (dist=171623.2m)



Line 88-1A: Ultradeep section beyond salt diapirs – 1D Extraction Temperature versus depth on the Late Triassic Reservoir 27339

Figure 2f-vii

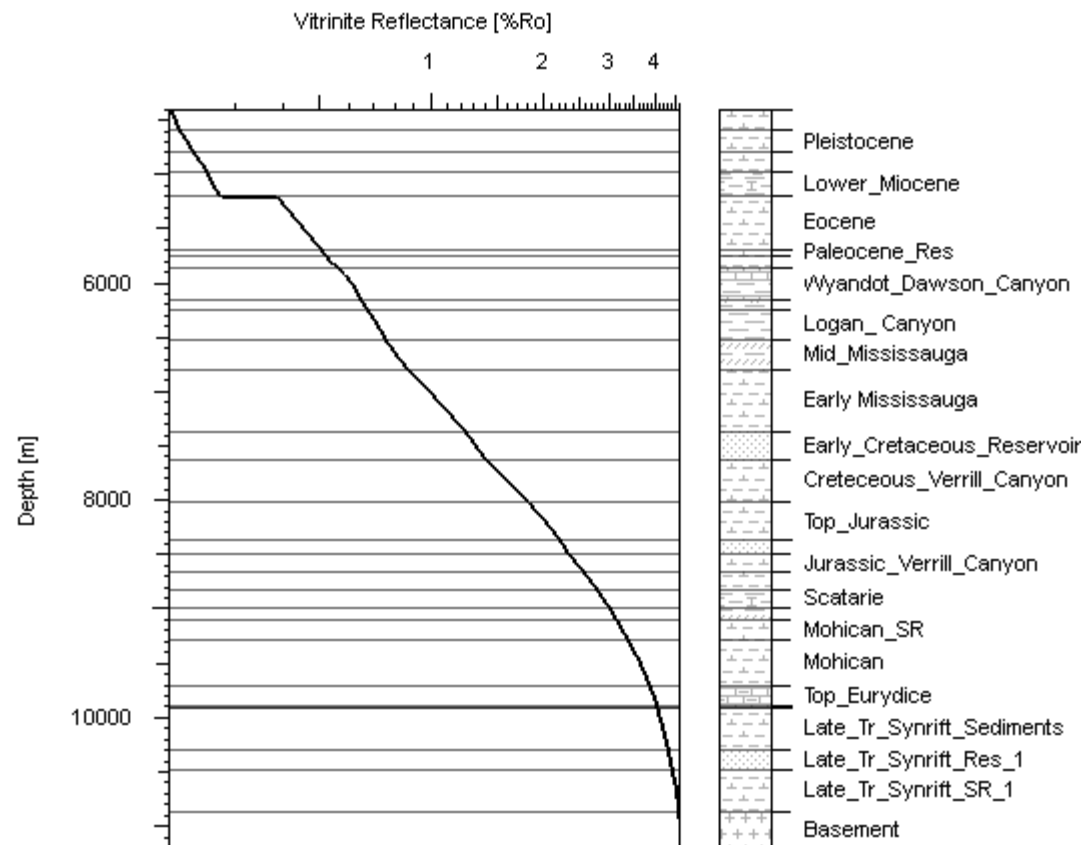
Temperature, 24-aug-09_Line88-1_newLength_1715PM_mgr (dist=171623.2m)



Line 88-1A: Ultradeep section beyond salt diapirs – 1D Extraction
Temperature versus depth on the Late Triassic Reservoir 27339

Figure 2f-viii

Maturity, 24-aug-09_Line88-1_newLength_1715PM_mgr (dist=171836.1m)



Line 88-1A: Target Late Triassic target reservoir 27340: 99.7% coming from Late Triassic source rock

Figure 2f-ix

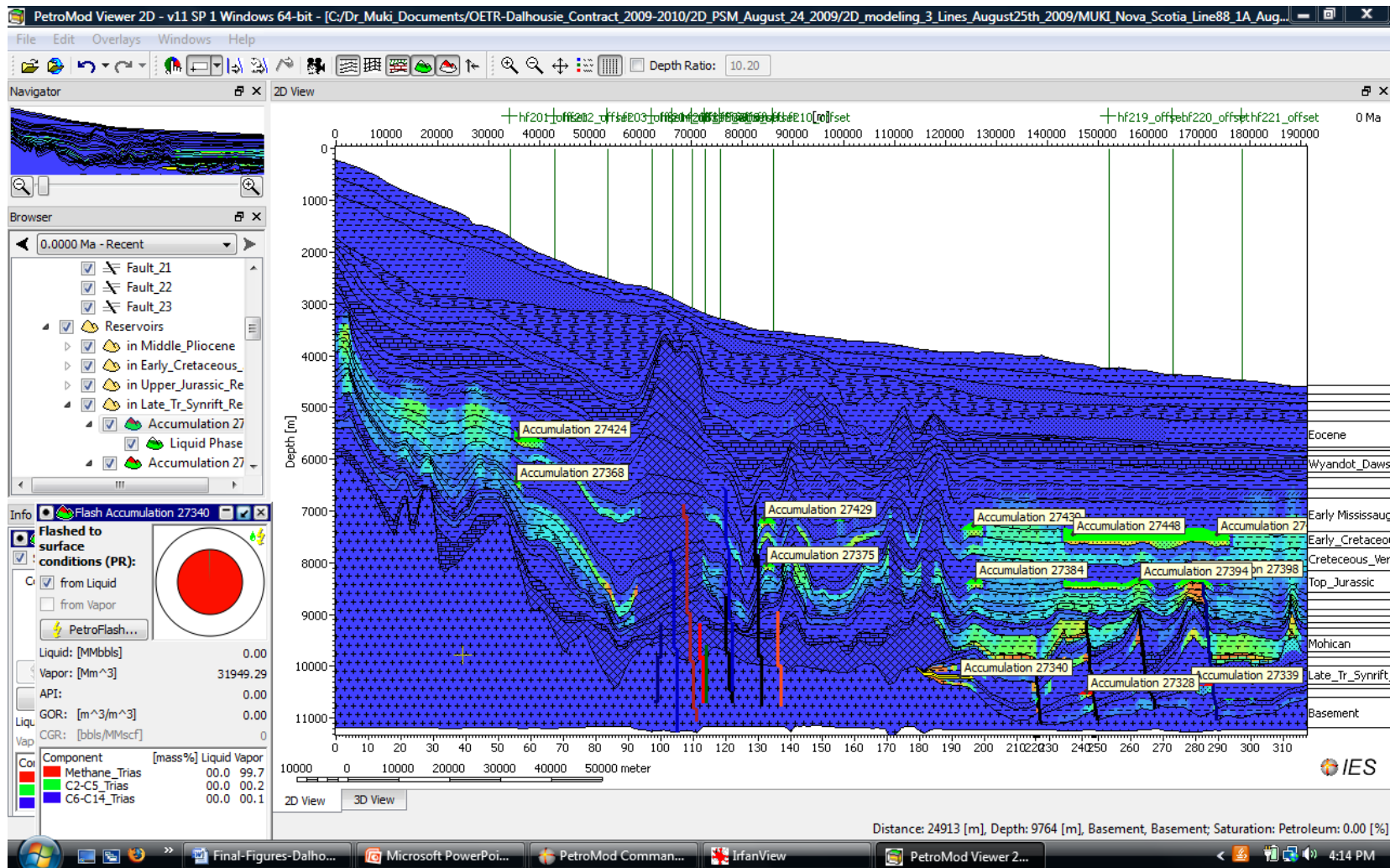
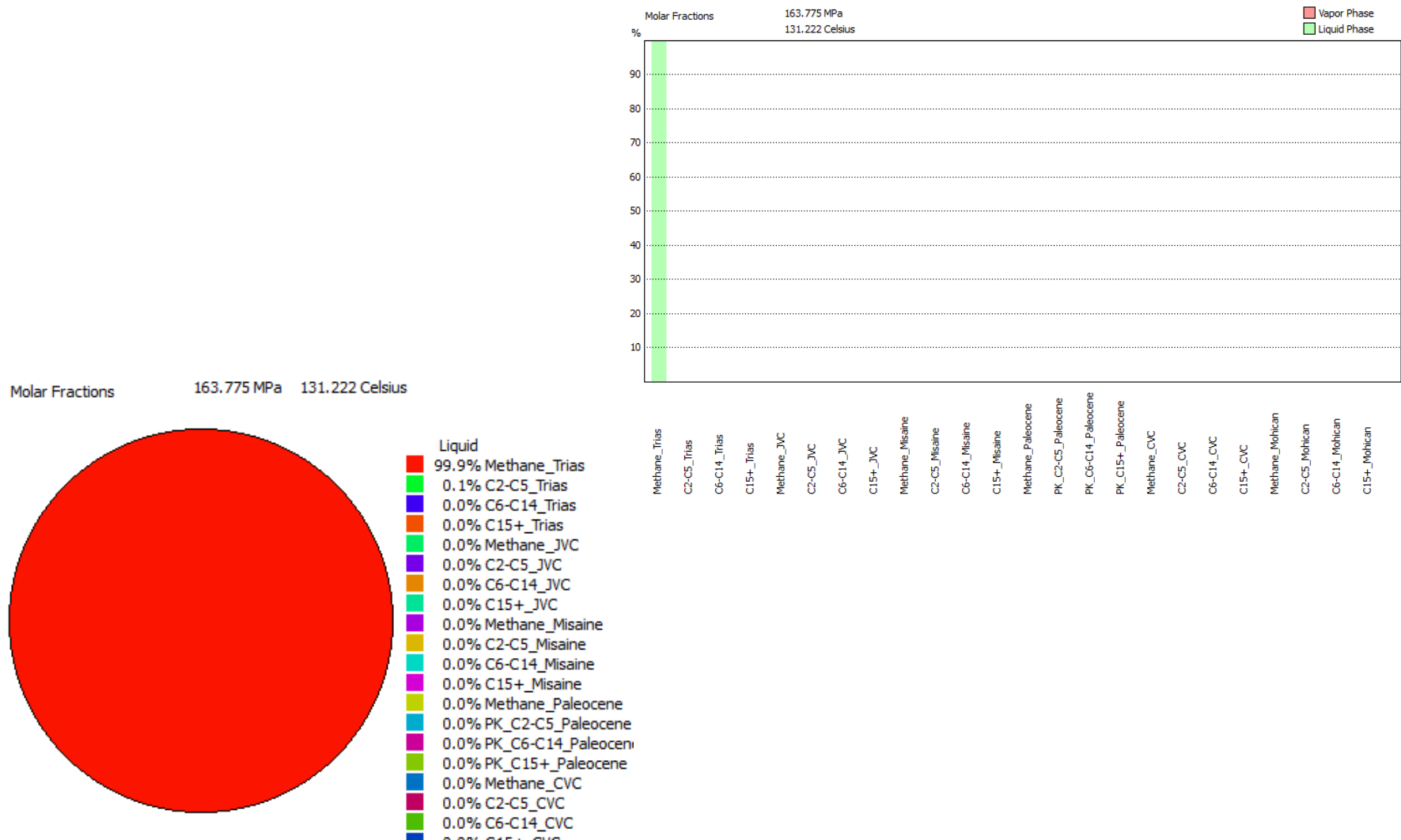


Figure 2f-x

Line 88-1A: Target Late Triassic target reservoir 27340: It is in a liquid phase in the reservoir



Line 88-1A: Target Late Triassic target reservoir 27340 (4051) at 144 Ma with hydrocarbon migration vectors showing no leakage

Figure 2f-xi

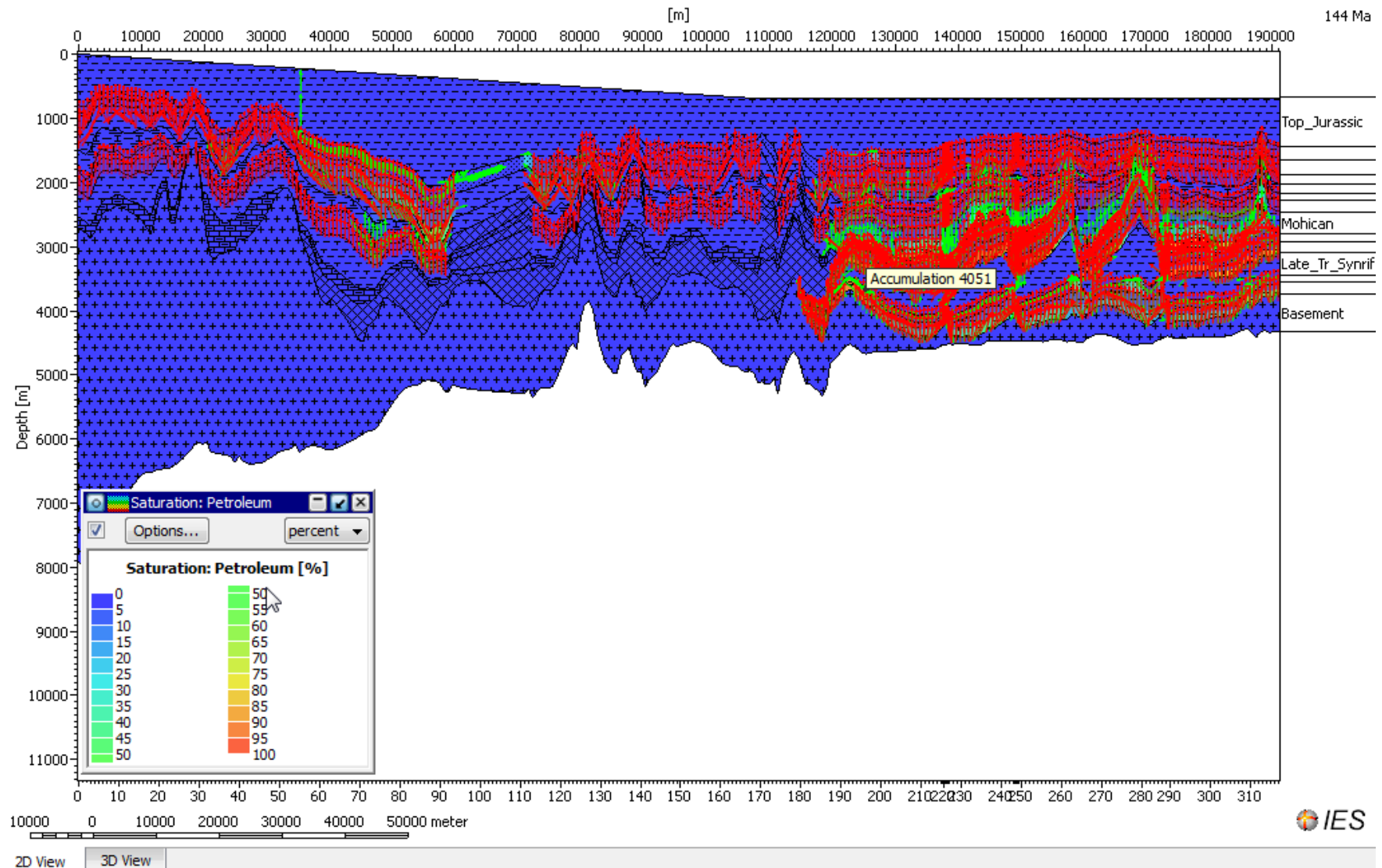
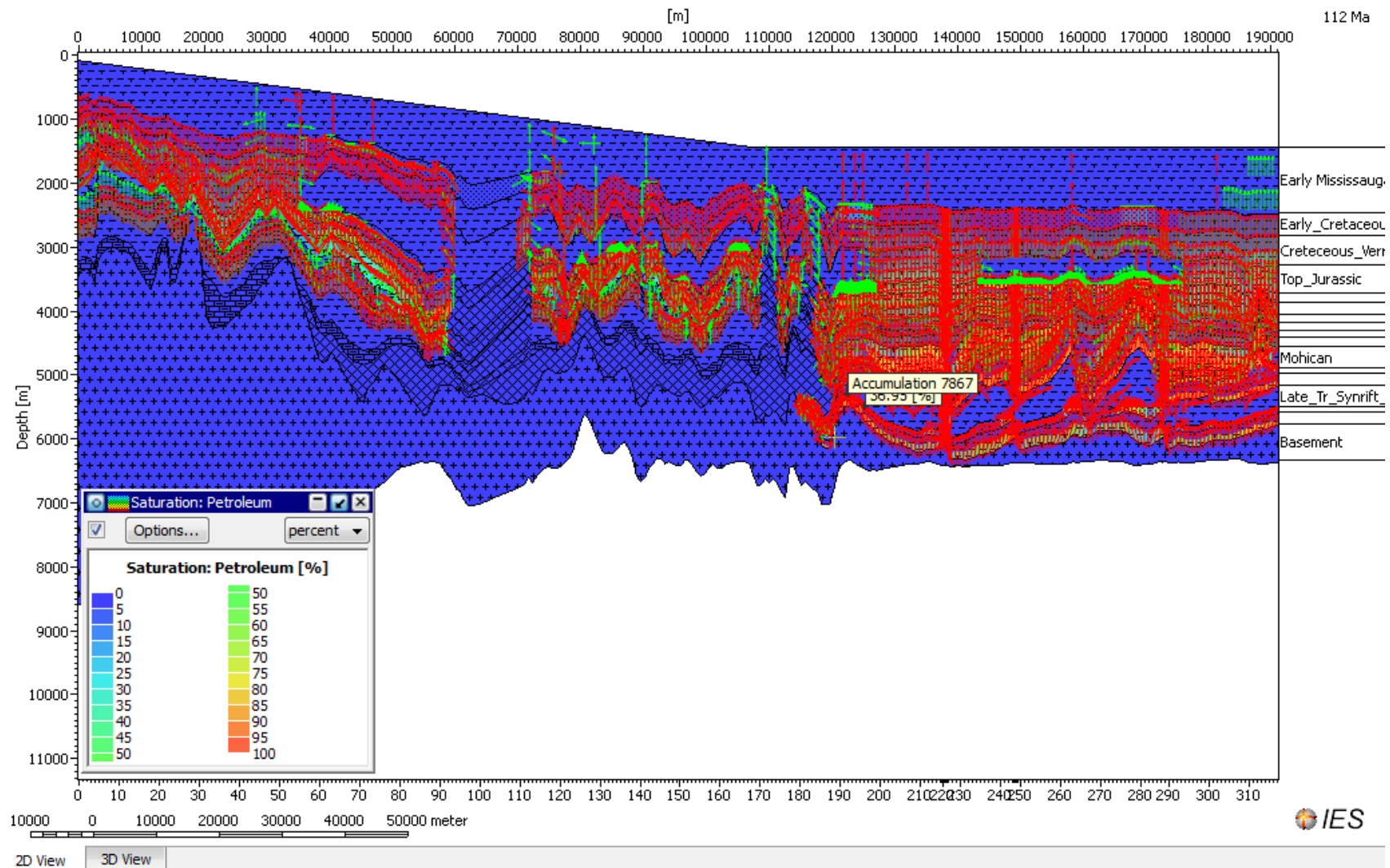


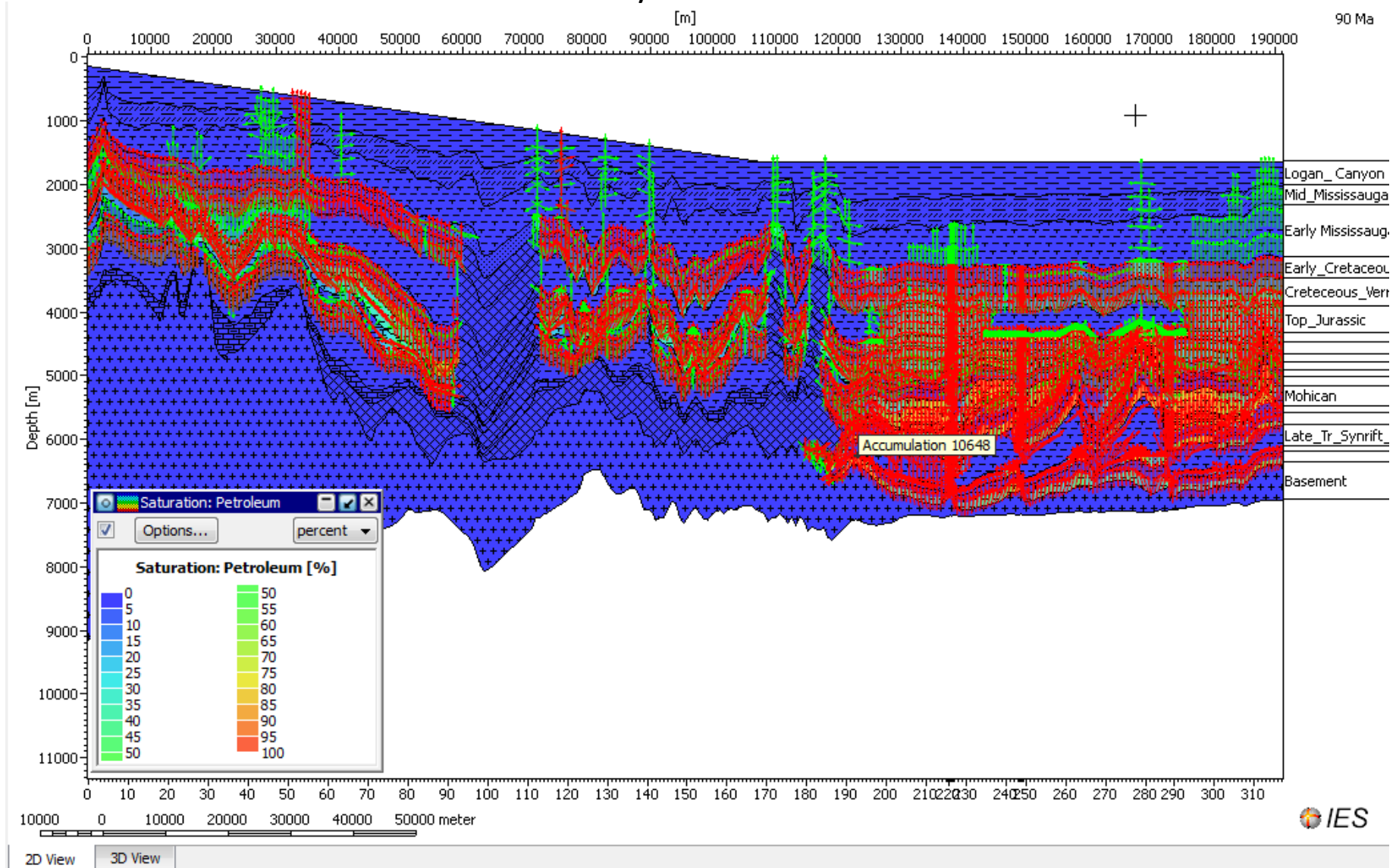
Figure 2f-xii

Line 88-1A: Target Late Triassic target reservoir 27340 (7867) at 112 Ma with Hydrocarbon migration vectors showing leakage from the Jurassic and Cretaceous reservoirs

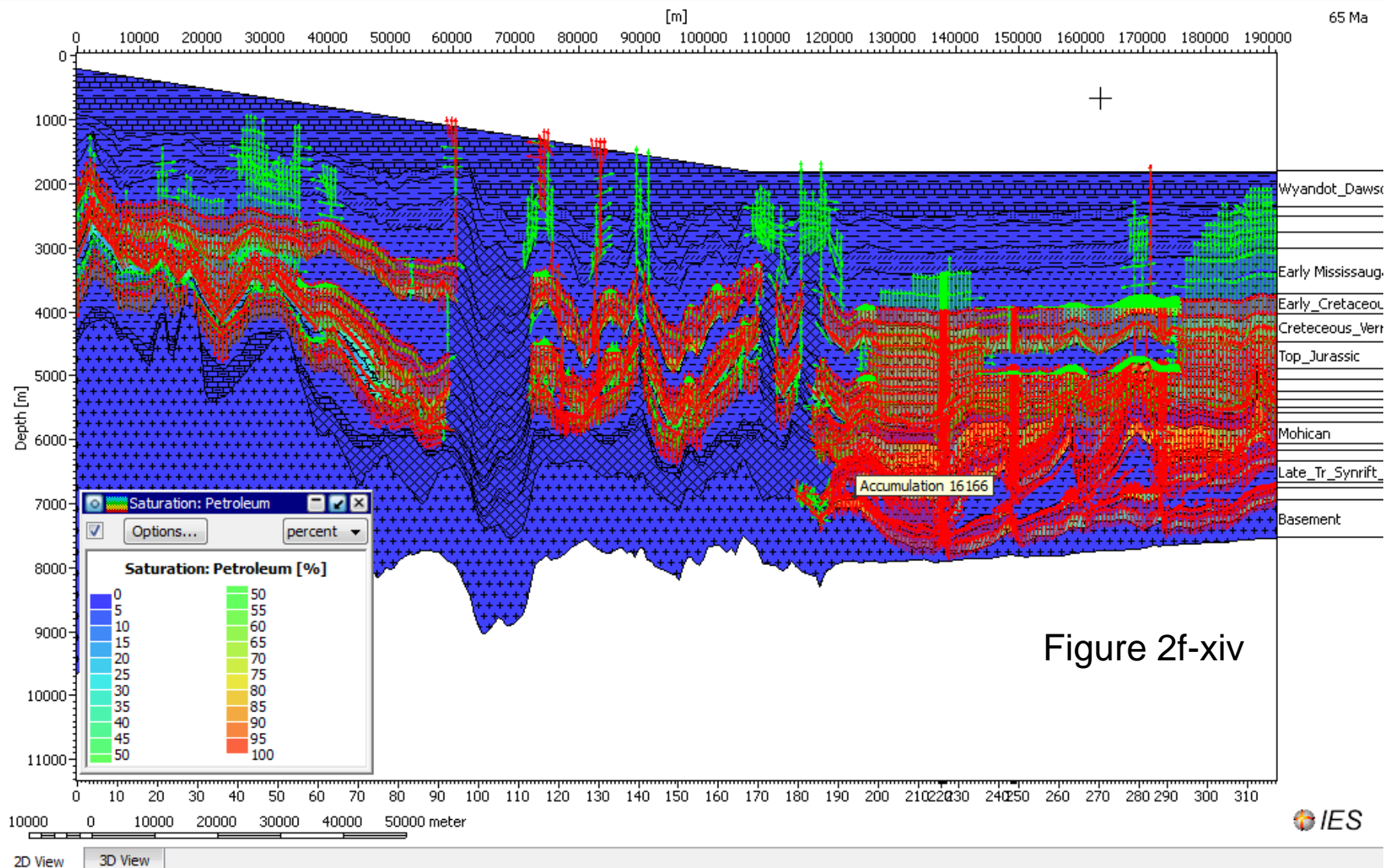


Line 88-1A: Target Late Triassic target reservoir 27340 (10648) at 90 Ma with Hydrocarbon migration vectors showing leakage from late Jurassic and early Cretaceous reservoirs

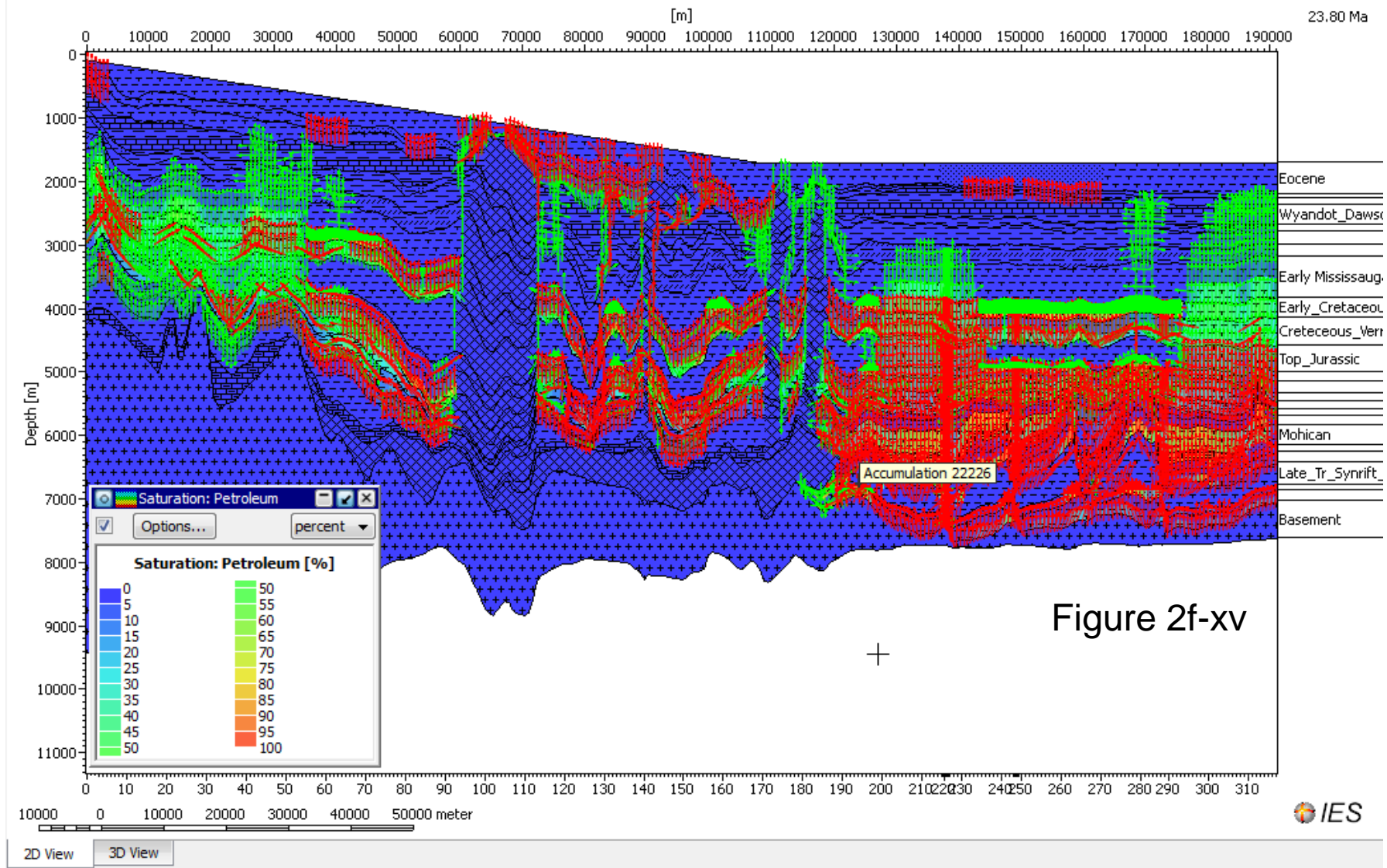
Figure 2f-xiii



Line 88-1A: Target Late Triassic target reservoir 27340 (16156) at 65 Ma
with Hydrocarbon migration vectors showing leakage from late Jurassic
and early Cretaceous reservoirs

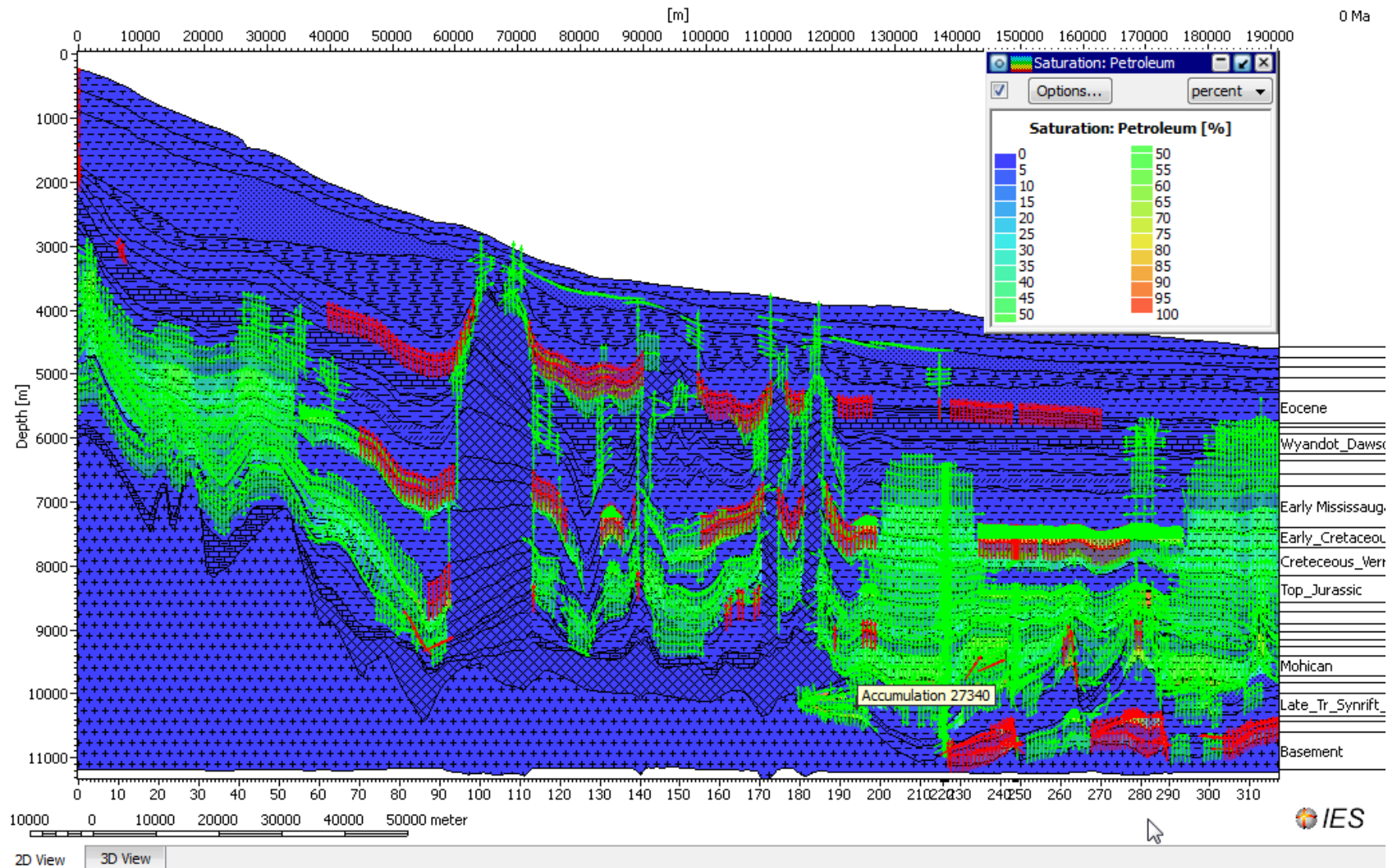


Line 88-1A: Target Late Triassic target reservoir 27340 (22226) at 23.8 Ma with Hydrocarbon migration vectors showing leakage from late Jurassic and early Cretaceous reservoirs



Line 88-1A: Target Late Triassic target reservoir 27340 at the present time with Hydrocarbon migration vectors showing leakage from late Jurassic, Cretaceous, and Tertiary reservoirs

Figure 2f-xvi



LATE JURASSIC RESERVOIR SATURATIONS: LINE 88-1A

Line 88-1A: Late Jurassic target reservoir 27394: 36% of liquid HC is of C6-C14 & C15+ and comes from Jurassic Verrill Canyon Source Rock

Figure 2g-i

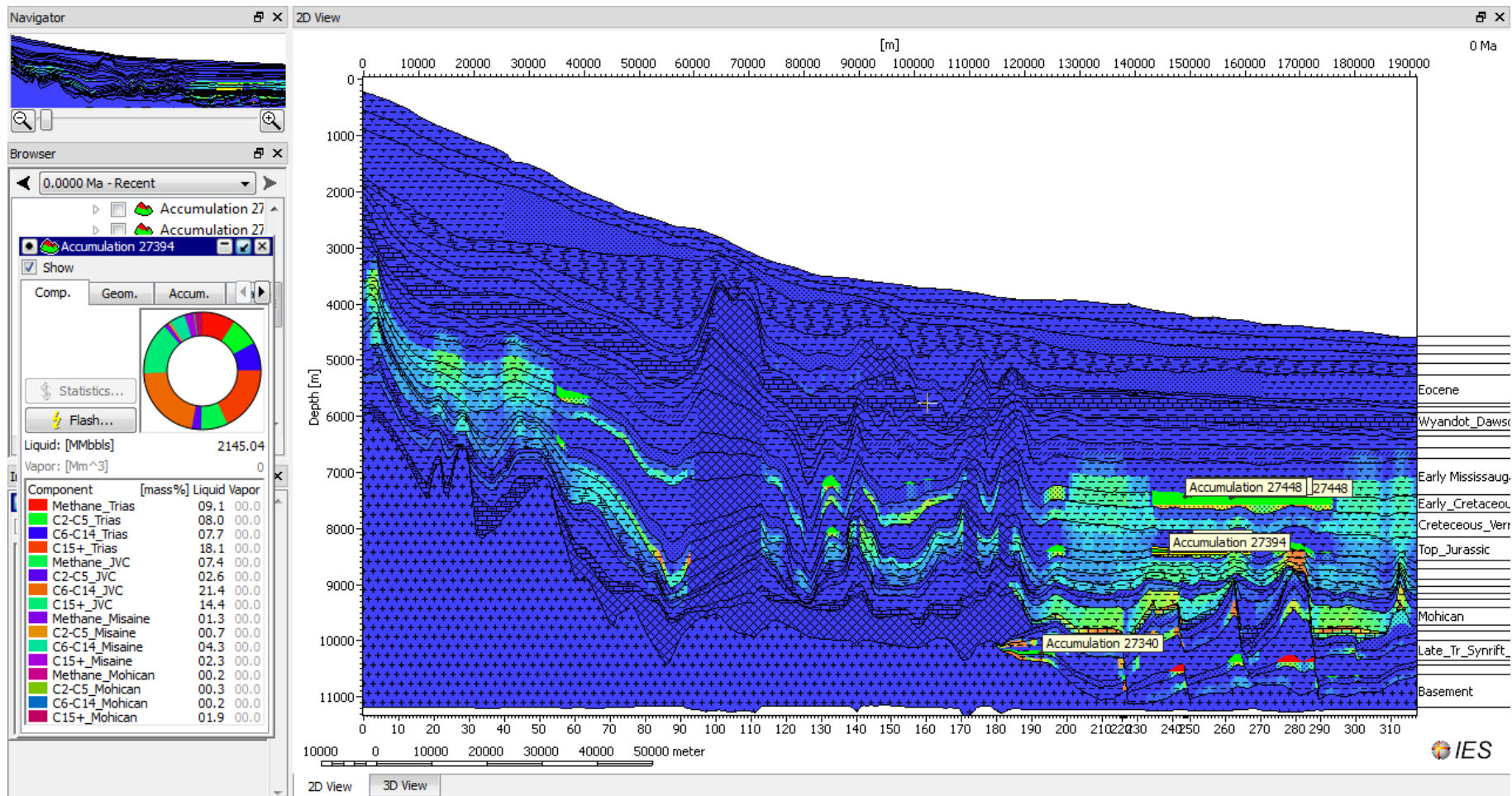
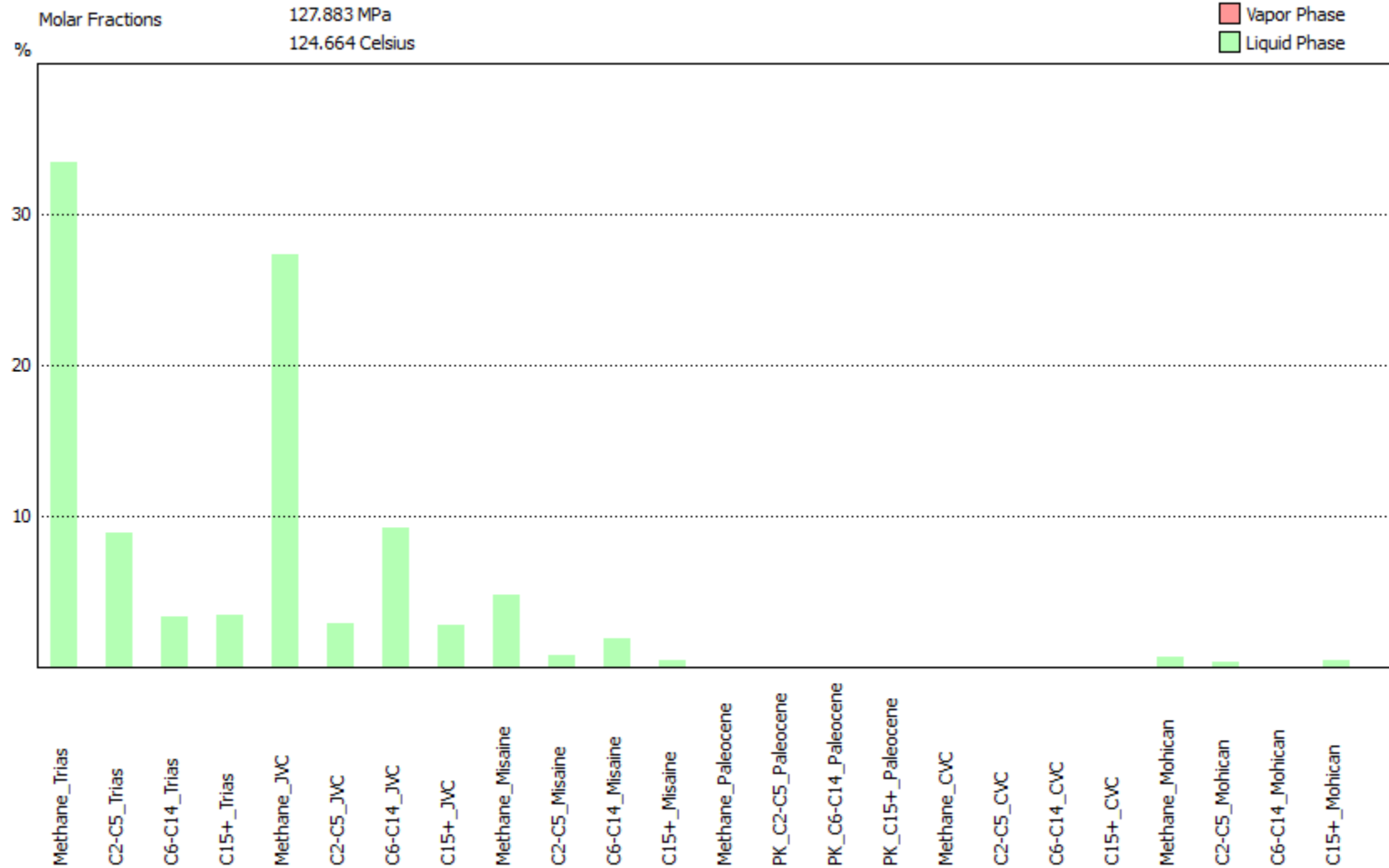
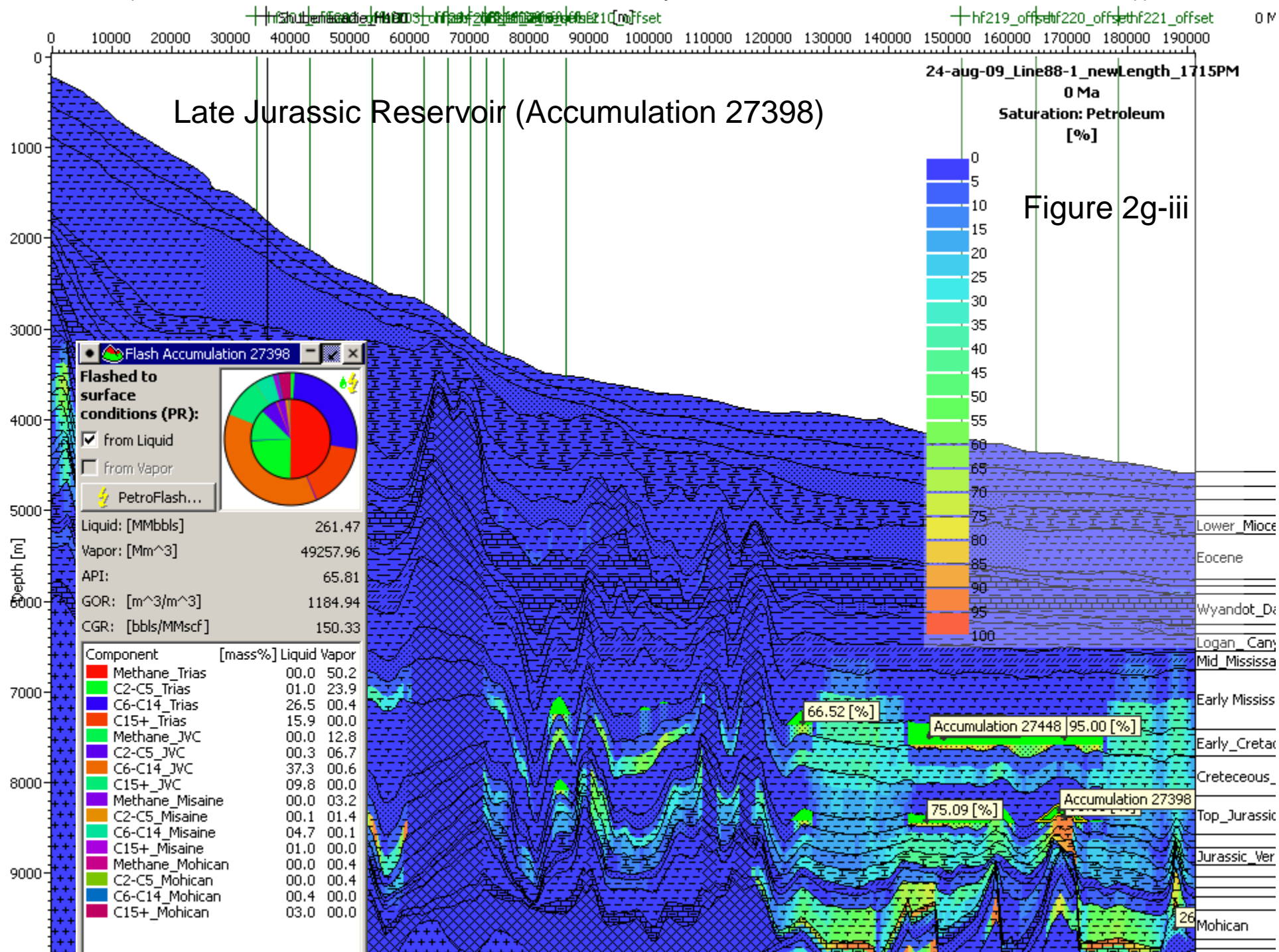


Figure 2g-ii

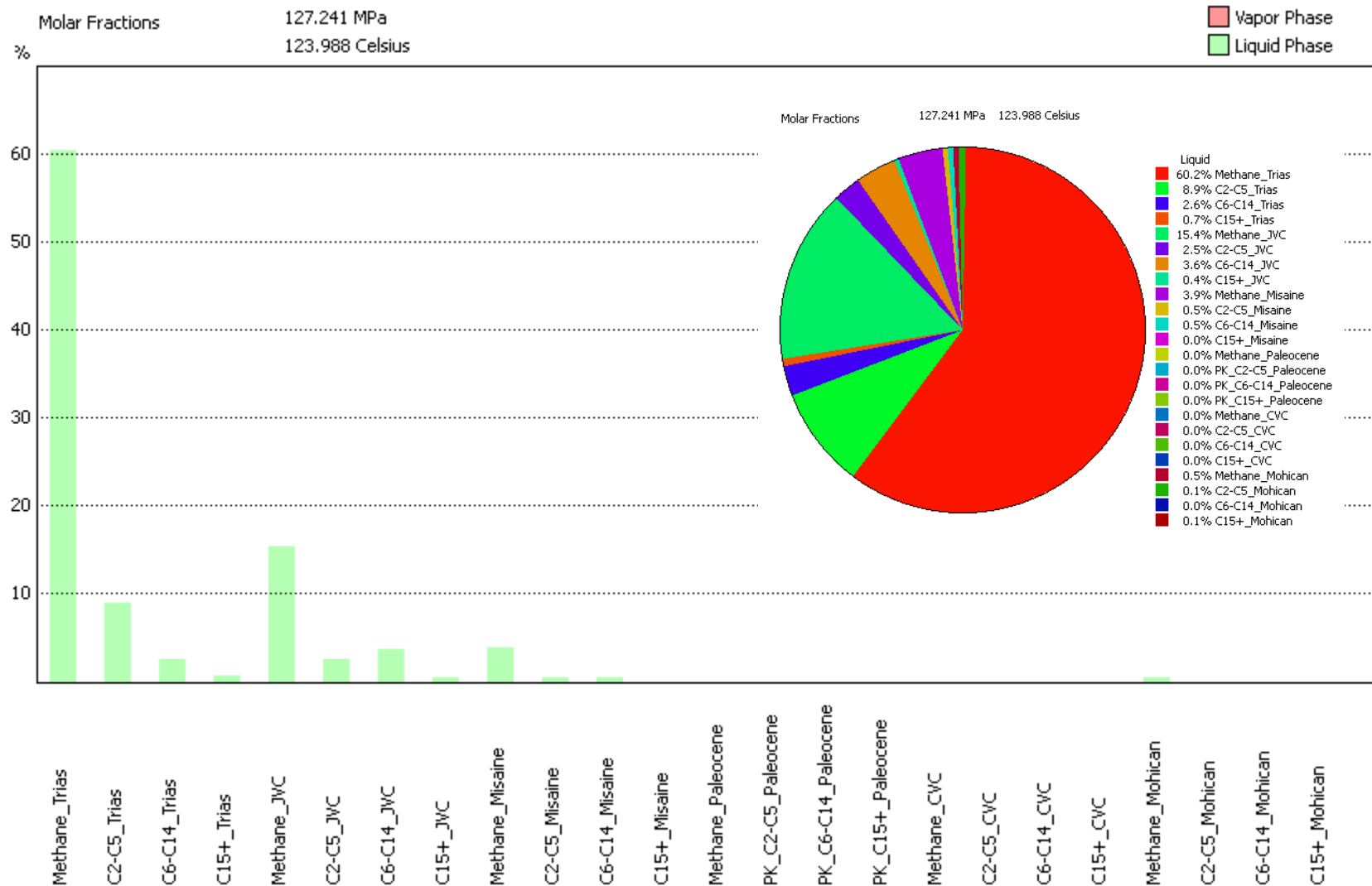
Line 88-1A: Late Jurassic target reservoir 27394: Source Rock
Fingerprinting of Late Jurassic reservoir 27394 to various sources





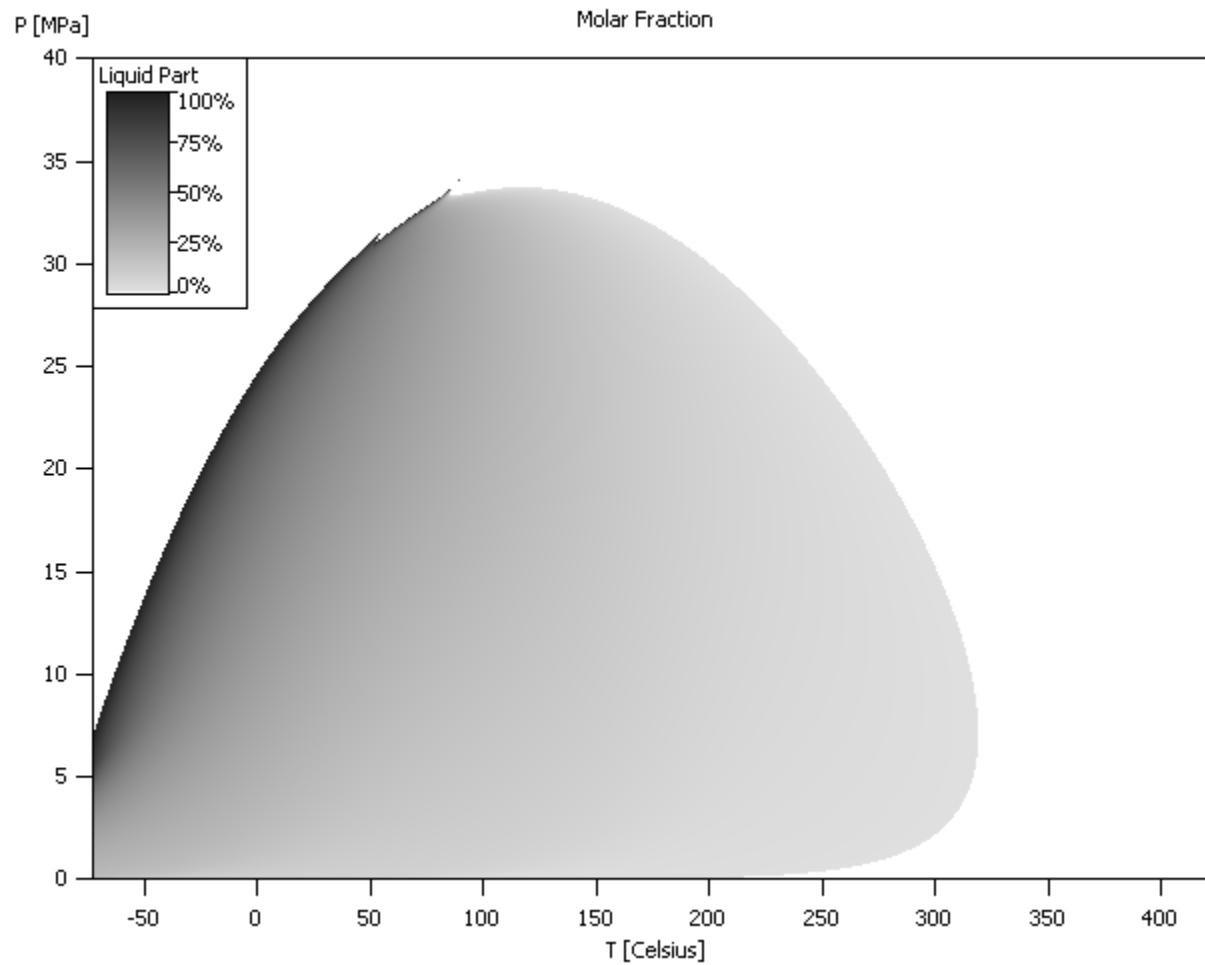
Line 88-1A: Compositional mass balance and source rock fingerprinting Late Jurassic Reservoir (Accumulation 27398)

Figure 2g-iv

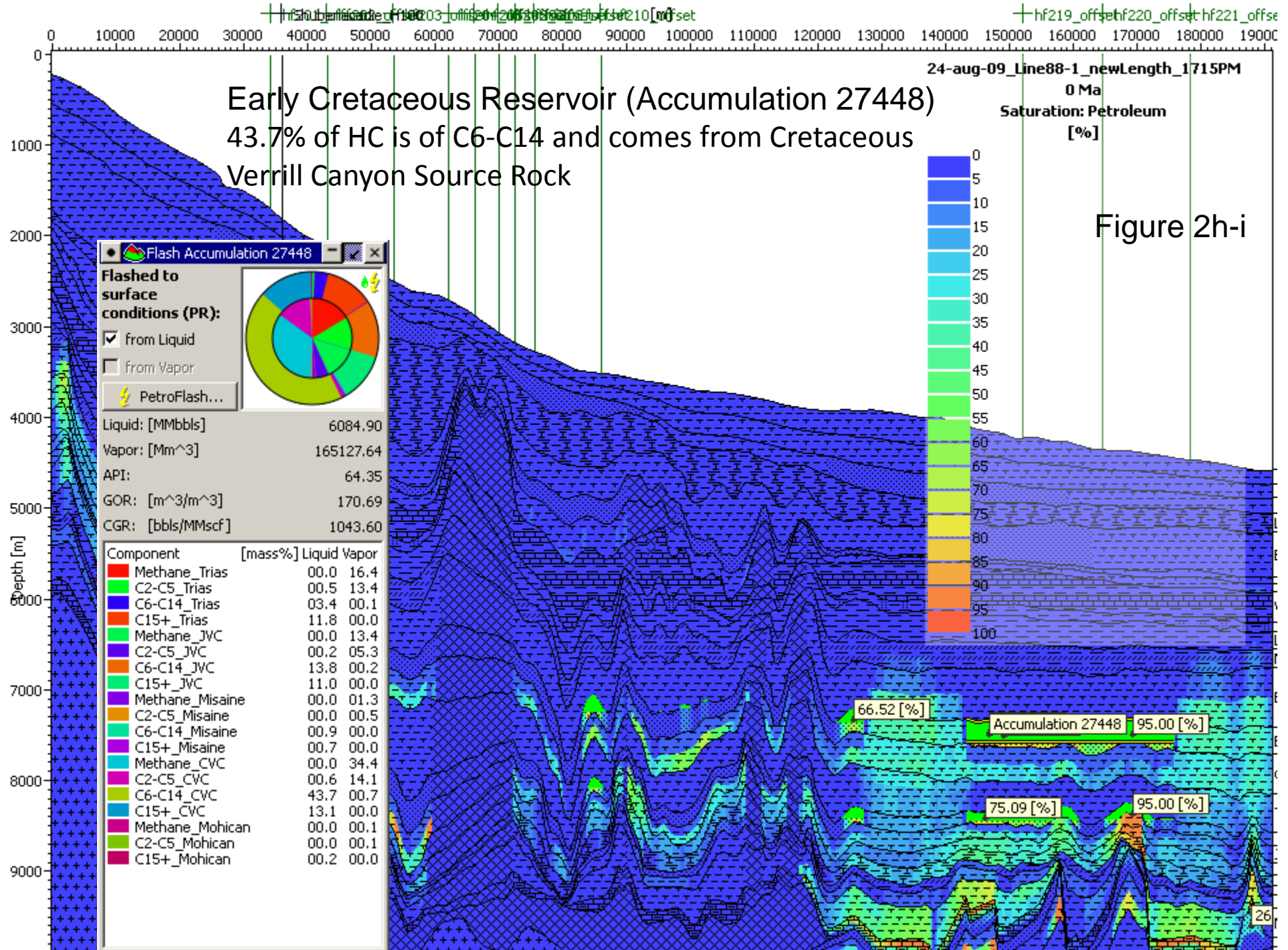


Line 88-1A: Bubble Point Curve of Late Jurassic Reservoir (Accumulation 27398)

Figure 2g-v



EARLY CRETACEOUS RESERVOIR SECTIONS: LINE 88-1A



Early Cretaceous Reservoir (Accumulation 27448)

Figure 2h-ii

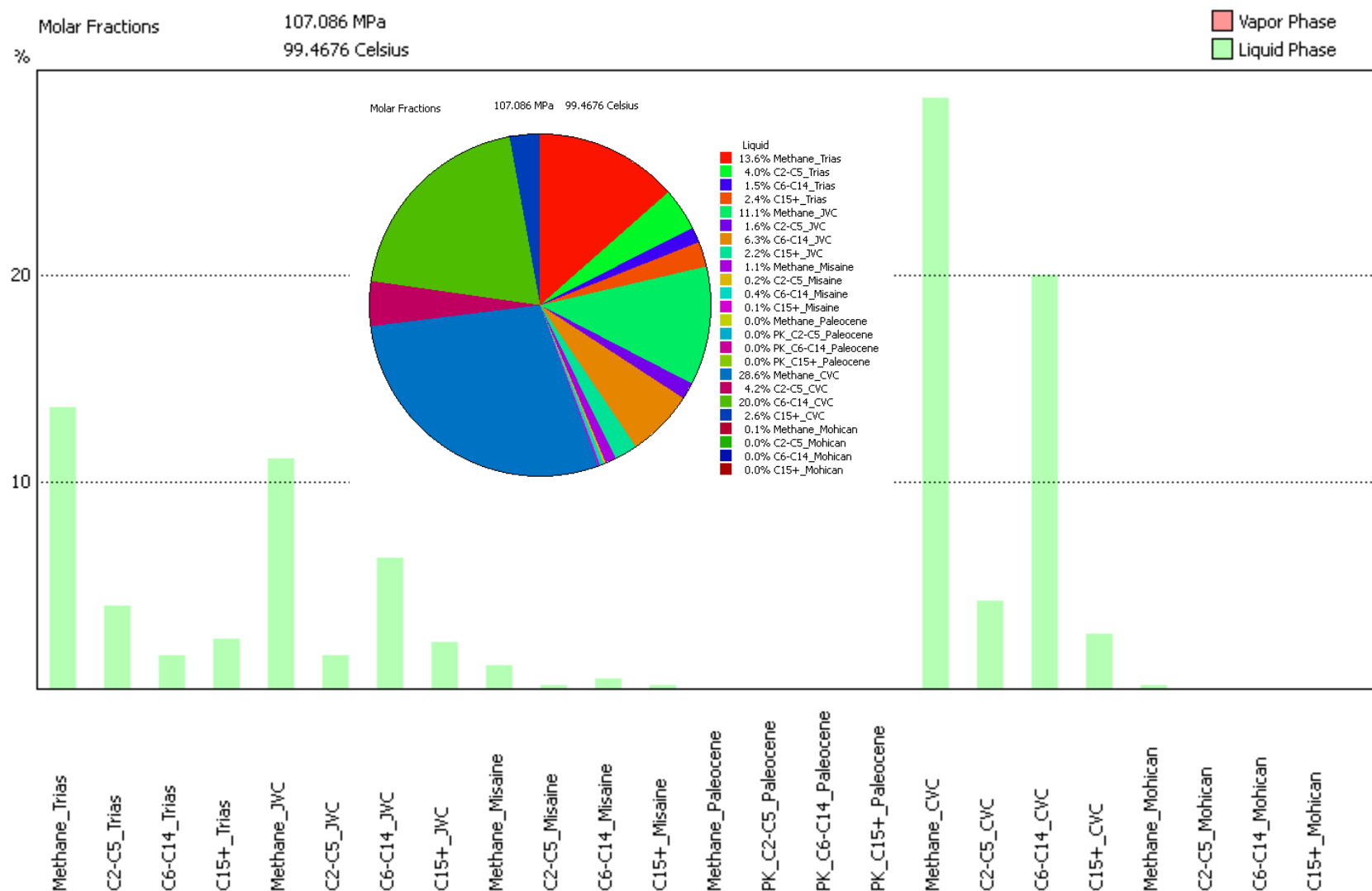
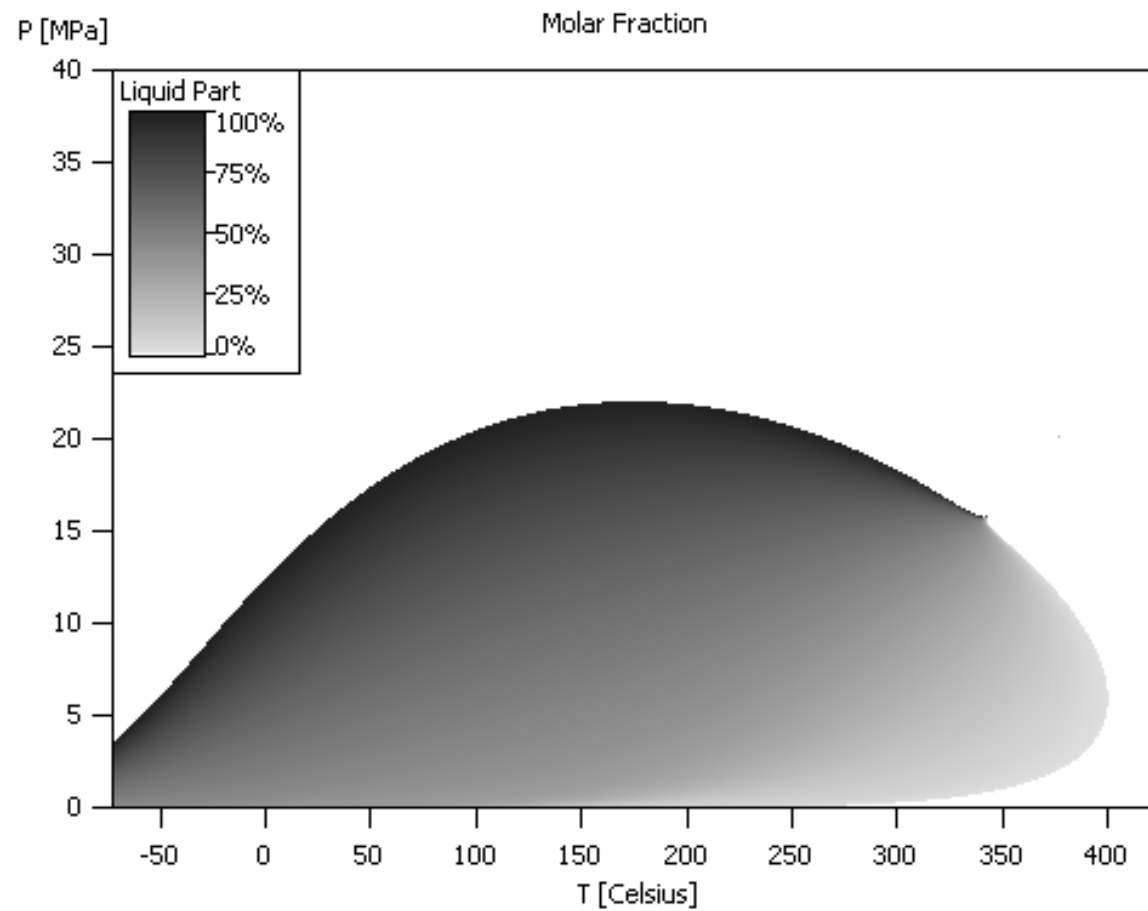


Figure 2h-iii

Line 88-1A: Early Cretaceous Reservoir Bubble Point Curve
(Accumulation 27448)



MASS BALANCE CALCULATION: LINE 88-1A

Info: Only percentages are rounded. Values < 0.005% are displayed as 0.00%!
 Volumes/masses calculated for a width of 1 km

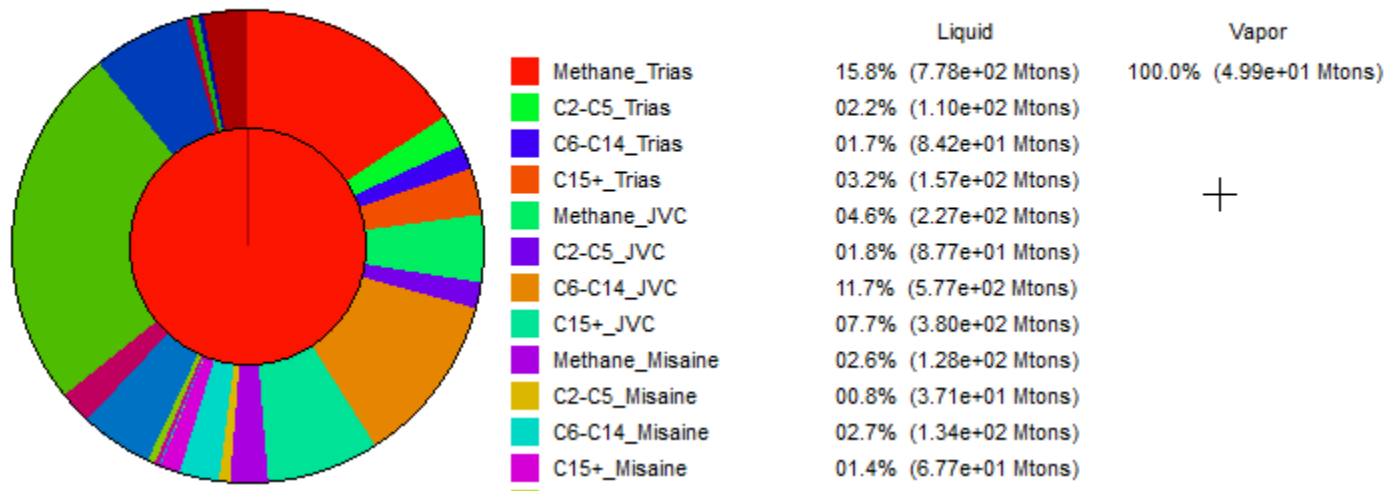
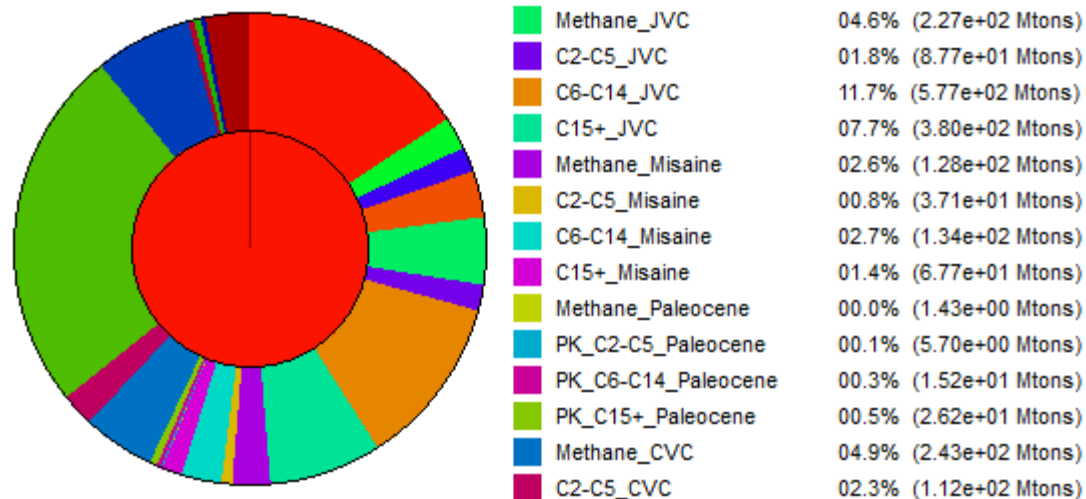


Figure 2j-i

Complete Mass Balance of HC Volumes present in various reservoirs in percentages Line 88-1A

Info: Only percentages are rounded. Values < 0.005% are displayed as 0.00%!
 Volumes/masses calculated for a width of 1 km



Generation Balance, Inflow, and Outflow of HC in all Reservoirs- Line 88-1A

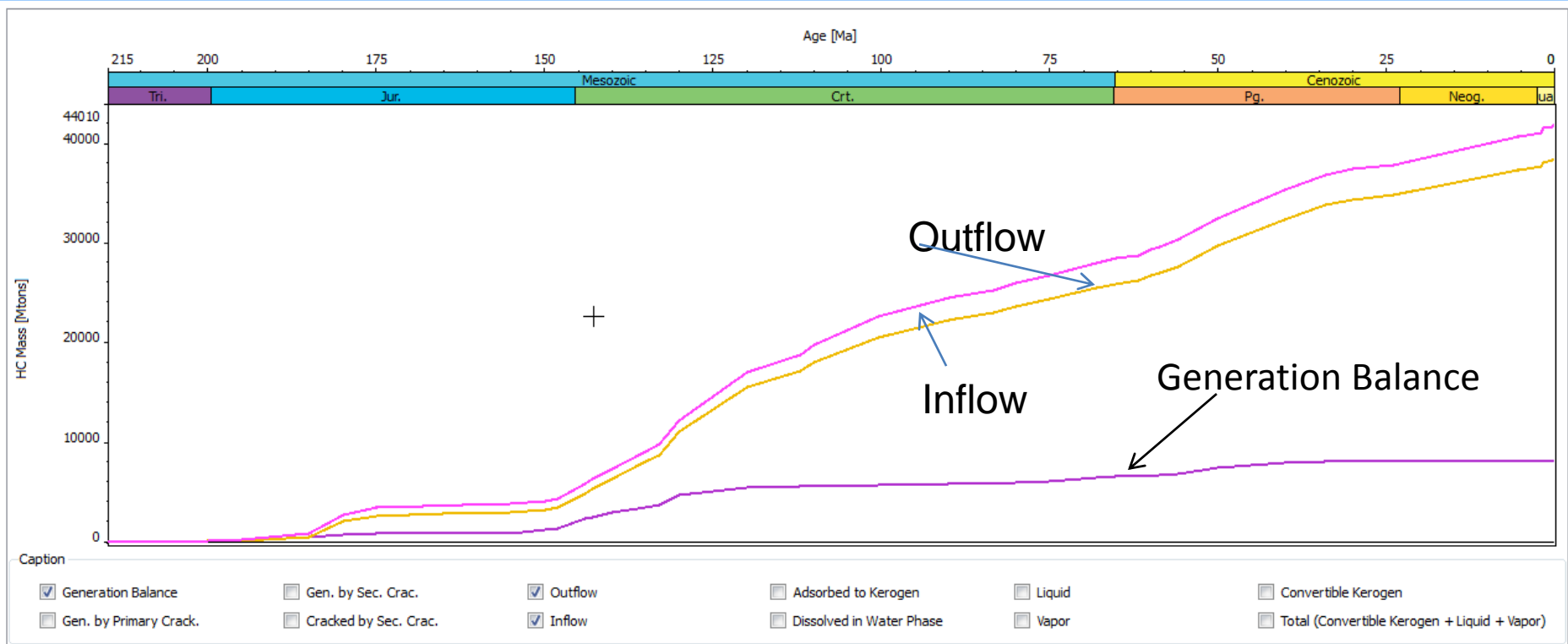


Figure 2j-ii

Figure 2j-iii

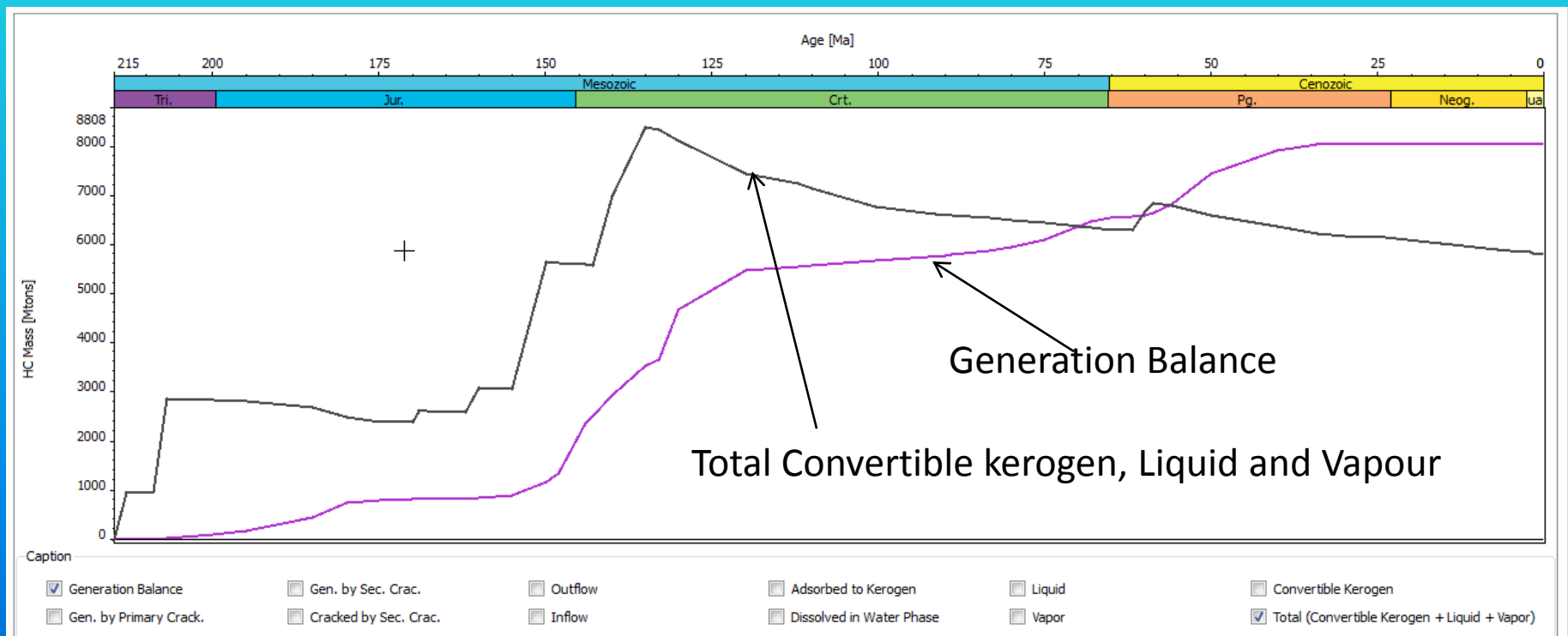
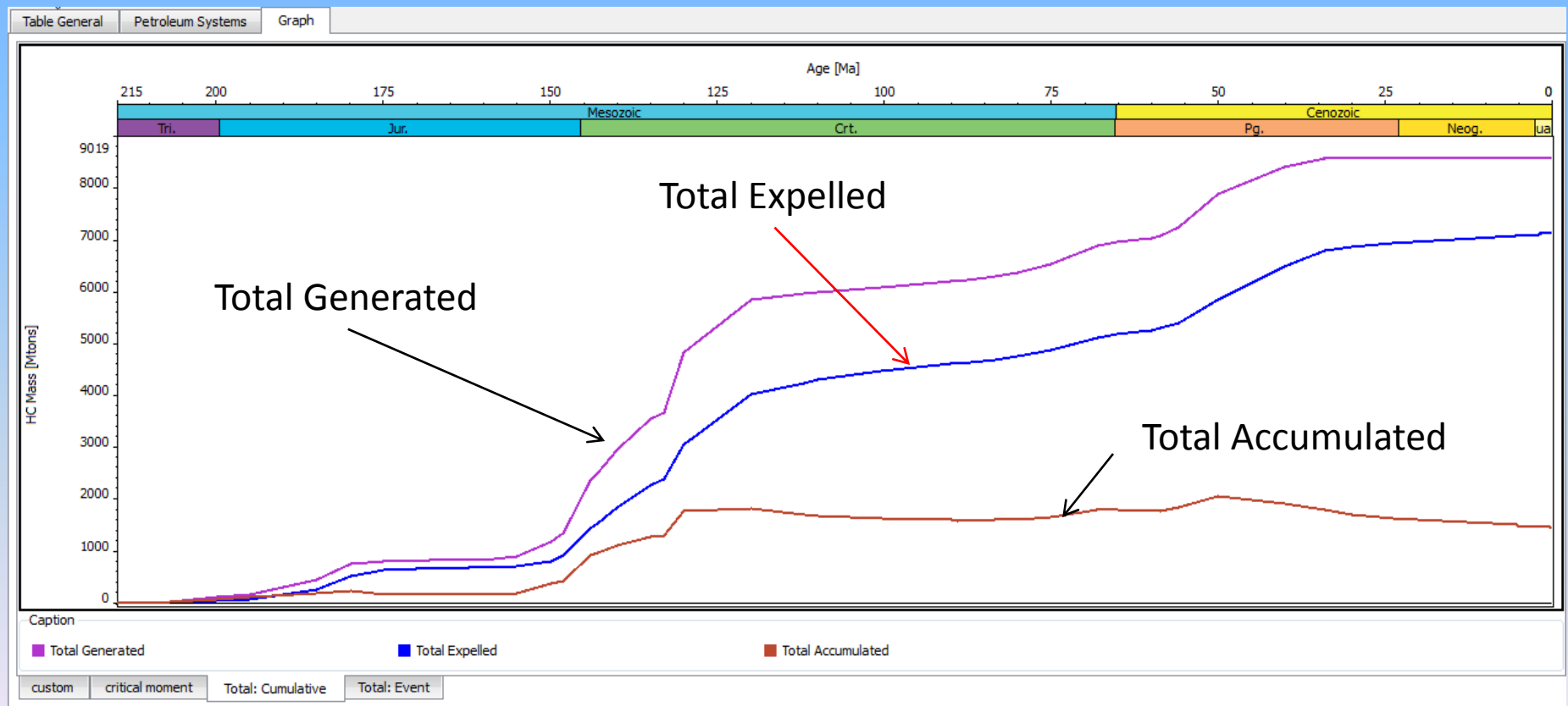
Generation Balance and Total Convertible Kerogen, Liquid, and Vapour: Line 88-1A

Figure 2j-v

Total Cumulative of Generated, Expelled and Accumulated: Line 88-1A

Seismic Line 88-1A: Conclusion

- Using the transient heat flow trends, the modelled and measured heat flow values have been calibrated . With the exception of three heat flow values (heat flow lines 206, 207, and 208), all measured flow values are closely calibrated. These three heat flow values are connected close to the diapiric salt. Therefore, it is obvious that outline of the salt in the upper part of the section has to be modified to calibrate the measured values
- Because the revised model is calibrated with lower heat trends, both Late Jurassic and Early Cretaceous conceptual reservoirs in the slope contain more oil (C15+ and condensates), which is associated with methane and wet gas
- Although the late Triassic conceptual reservoir contain mainly dry gas (methane), the reservoir temperature and pressure is much lower compared to our Phase I model
- The heat flow values on top of the salt diapir is much hotter compared to the flank of the salt. However, the variation in heat flow values depends on the thickness of the salt diapir and nearness to the surface

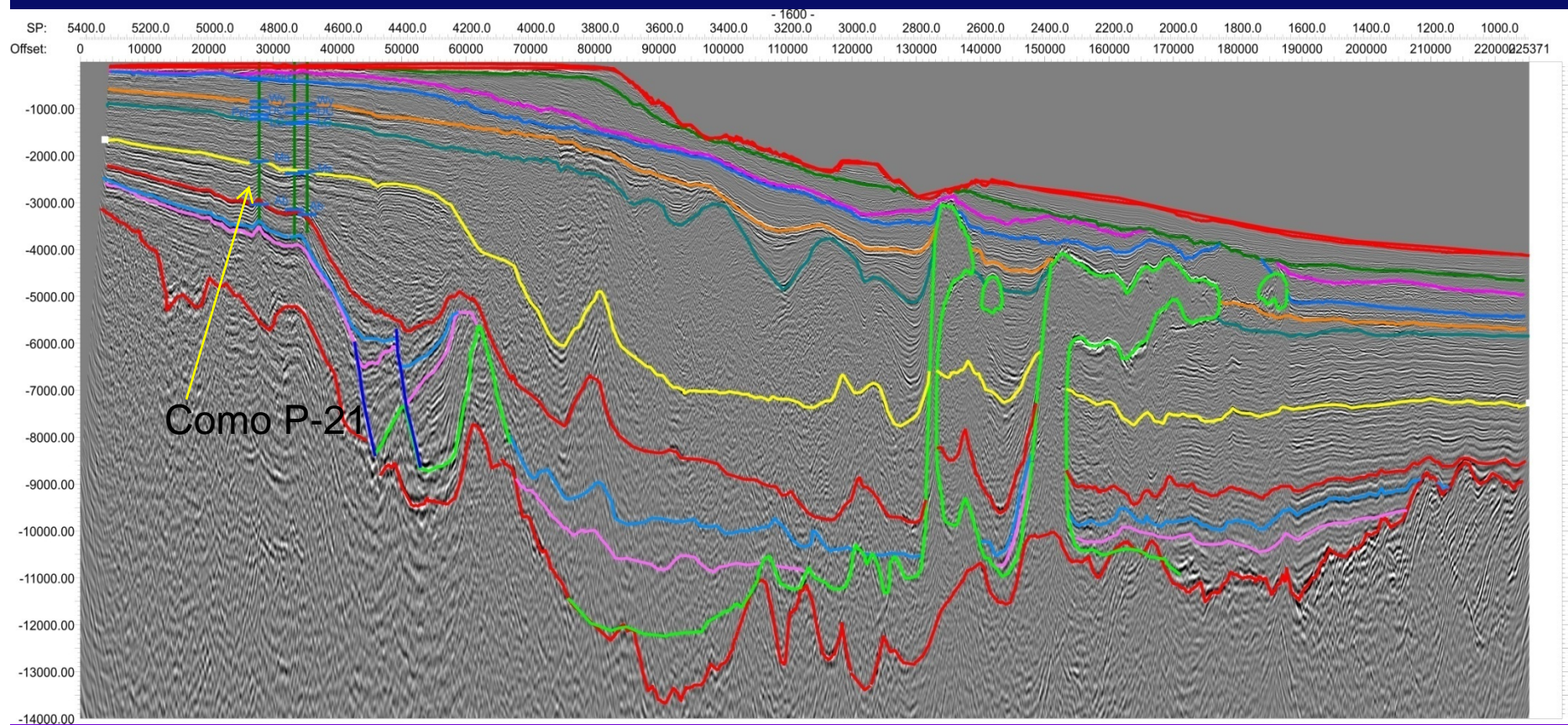
2D Petroleum Systems Modelling

Seismic Line NOVASPAN 1600

Seismic Interpretation: Line 1600

Figure 3a

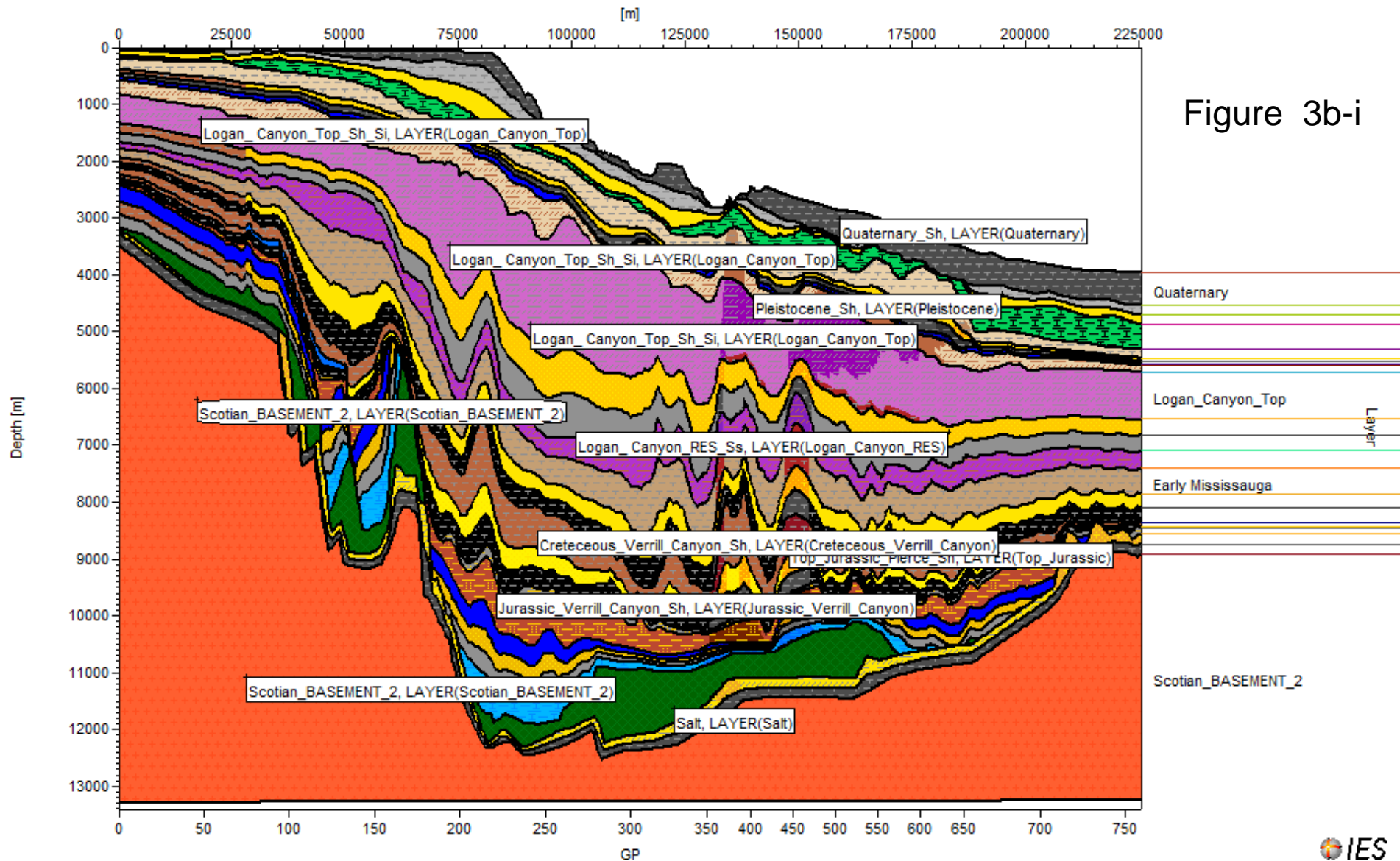
- Salt diapirs and canopies



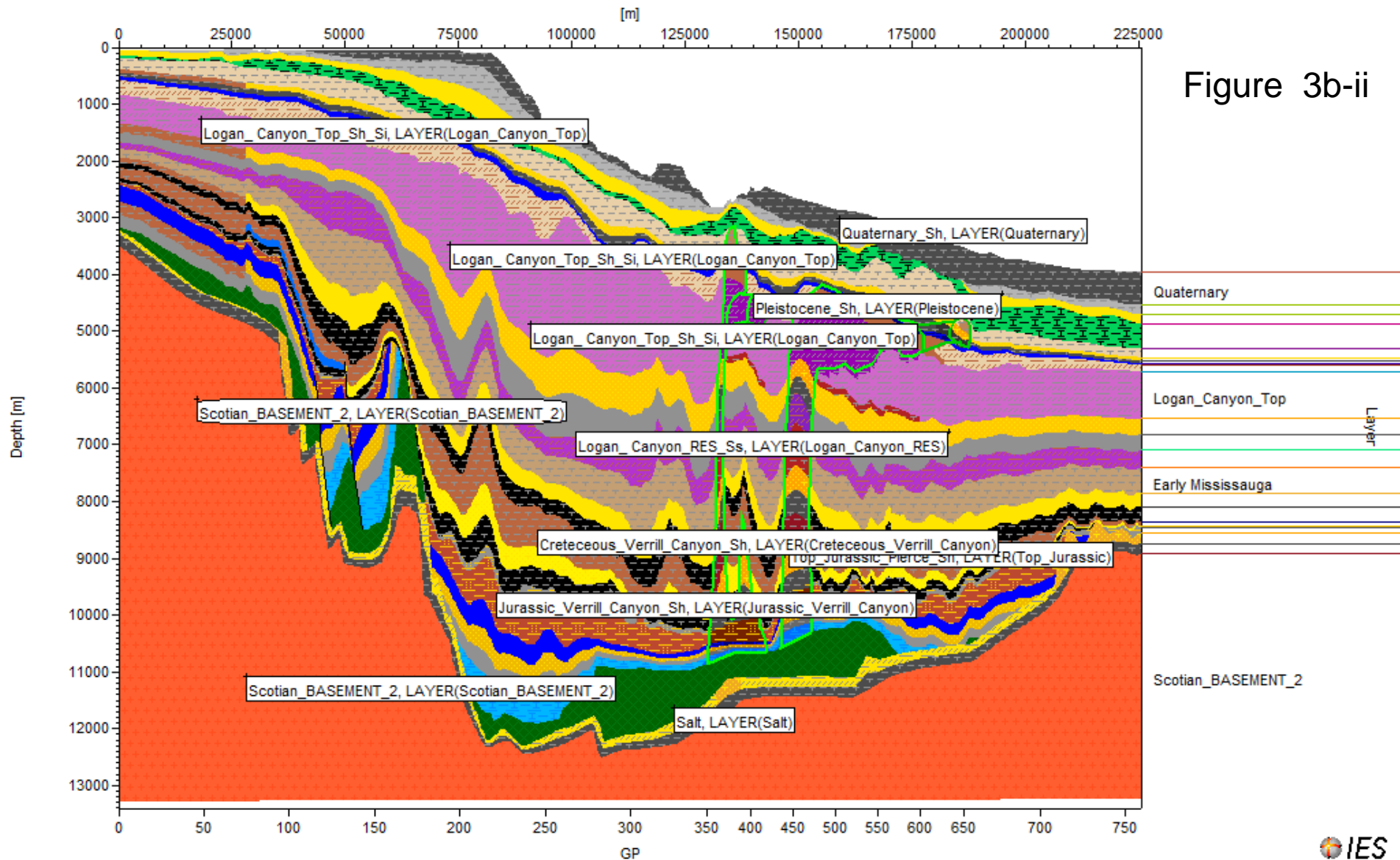
Seismic Line NOVASpan 1600

Petroleum System Modelling
PetroBuilder

Line NOVASPAN 1600: PetroBuilder Assignment of Horizons with lithology patterns



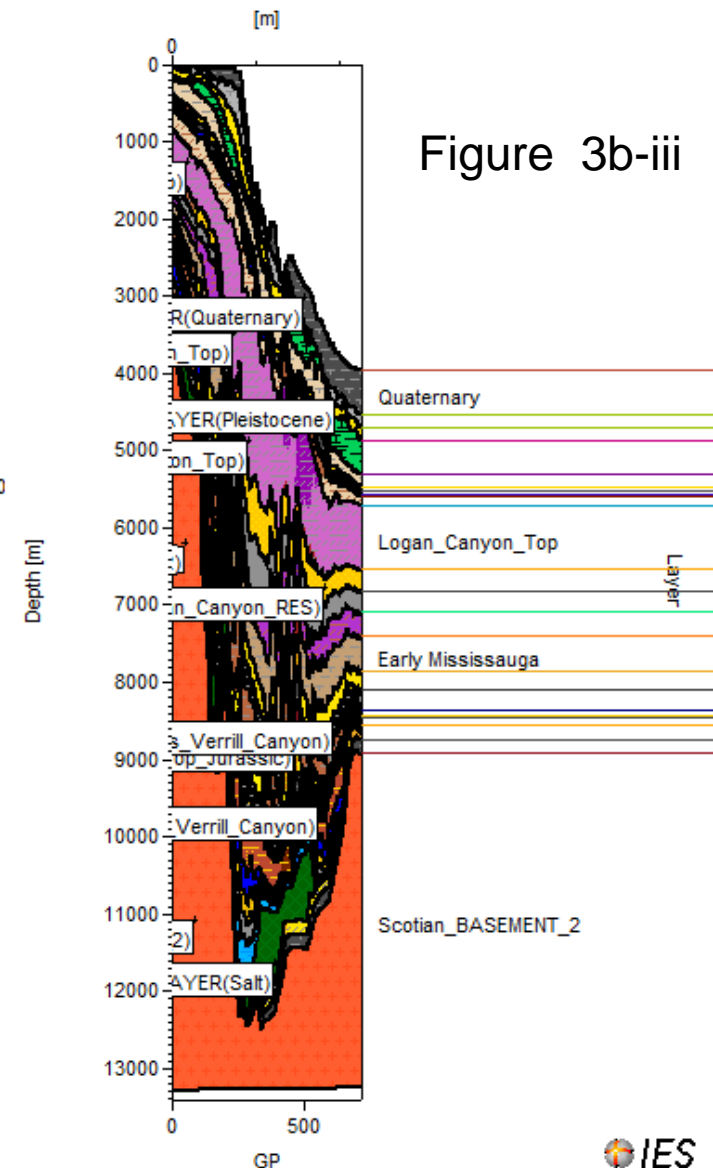
Line NOVASPAN 1600: PetroBuilder Assignment of Horizons with lithology patterns and facies polygons



Line NOVASPAN 1600: Legends for PetroBuilder Assignment of Horizons

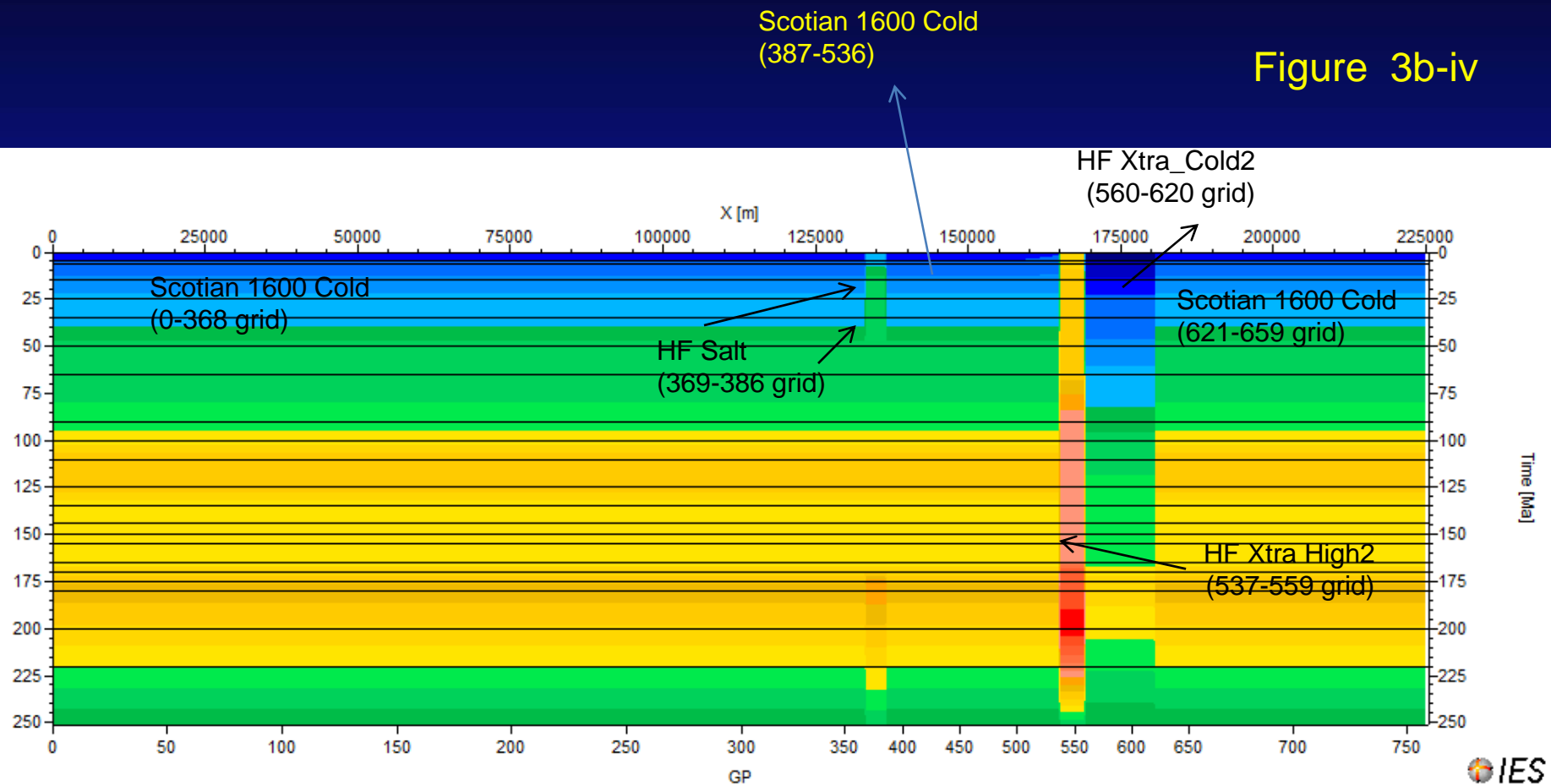
Facies

Quaternary Sh	Scatarie Li60 Sh20 Ch20
Pleistocene Sh	Mohican RES Pierce Ss
Middle Pliocene Ss	Mohican RES Ss
Miocene Sh50 St20 Ss10 L10 Ma10	Mohican SR Pierce Sh
Eocene Sh	Mohican SR Sh
Paleocene Res Pierce Ss	Eurydice Pierce Sh60 Si15 Do15 An5 Li5
Paleocene Res Ss	Eurydice Sh60 Si15 Do15 An5 Li5
Middle Late Paleocene Pierce Sh	Salt
Middle Late Paleocene	Late Tr Synrift Res 1
Wyandot Dawson C Pierce Si70 Sh20 Ma10	Late Tr Synrift SR 1
Wyandot Dawson C S170 Sh20 Ma10	Scotian BASEMENT 2
Top Middle Cretaceous Pierce Sh50 Si40 S10	Eocene Sh Pierce
Top Middle Cretaceous Sh50 Si40 S10	Loqan Canyon RES Pierce Ss
Loqan Canyon Top Pierce Sh Si	Loqan Canyon RES Ss
Loqan Canyon Top Sh Si	Loqan Canyon SR Pierce Sh
Mid Missi Pierce Sh50 Si40 Ma10	Loqan Canyon SR Sh
Mid Missi Sh50 Si40 Ma10	Misaine
Early Mississauga Pierce Sh	Misaine Pierce
Early Mississauga Sh	Loqan Canyon Top Pierce Merged Sh Si
Early Cretaceous RES Pierce Ss	Merged Middle Late Paleocene Pierce Sh
Early Cretaceous RES Ss	Merged Wyandot Dawson C Pierce Si70 Sh20 Ma10
Cretaceous Verrill Canyon Pierce Sh	Merged Top Middle Cretaceous Pierce 2nd Sh50 Si40 S10
Cretaceous Verrill Canyon Sh	General Carrierbed
Top Jurassic Pierce Sh	General Seal
Top Jurassic Sh	Loqan Canyon Seal
Upper Jurassic Reservoir Pierce Ss	Abenaki Carbonate Reservoir
Upper Jurassic Reservoir Ss	
Jurassic Verrill Canyon Pierce Sh	
Jurassic Verrill Canyon Sh	
Misaine SR Pierce Sh75 Si10 Ss15	
Misaine Sh75 Si10 Ss15	
Scatarie Pierce Li60 Sh20 Ch20	



Line NOVASPAN 1600: Heat Flow Trends used for the calibration
Of measured heat flow values in the following slides

Figure 3b-iv



Seismic Line NOVSPAN 1600

Petroleum System Modelling After Simulation – Viewer 2D

Figure 3c-i

Line NOVASPAN 1600: General Stratigraphy without overlays after simulation

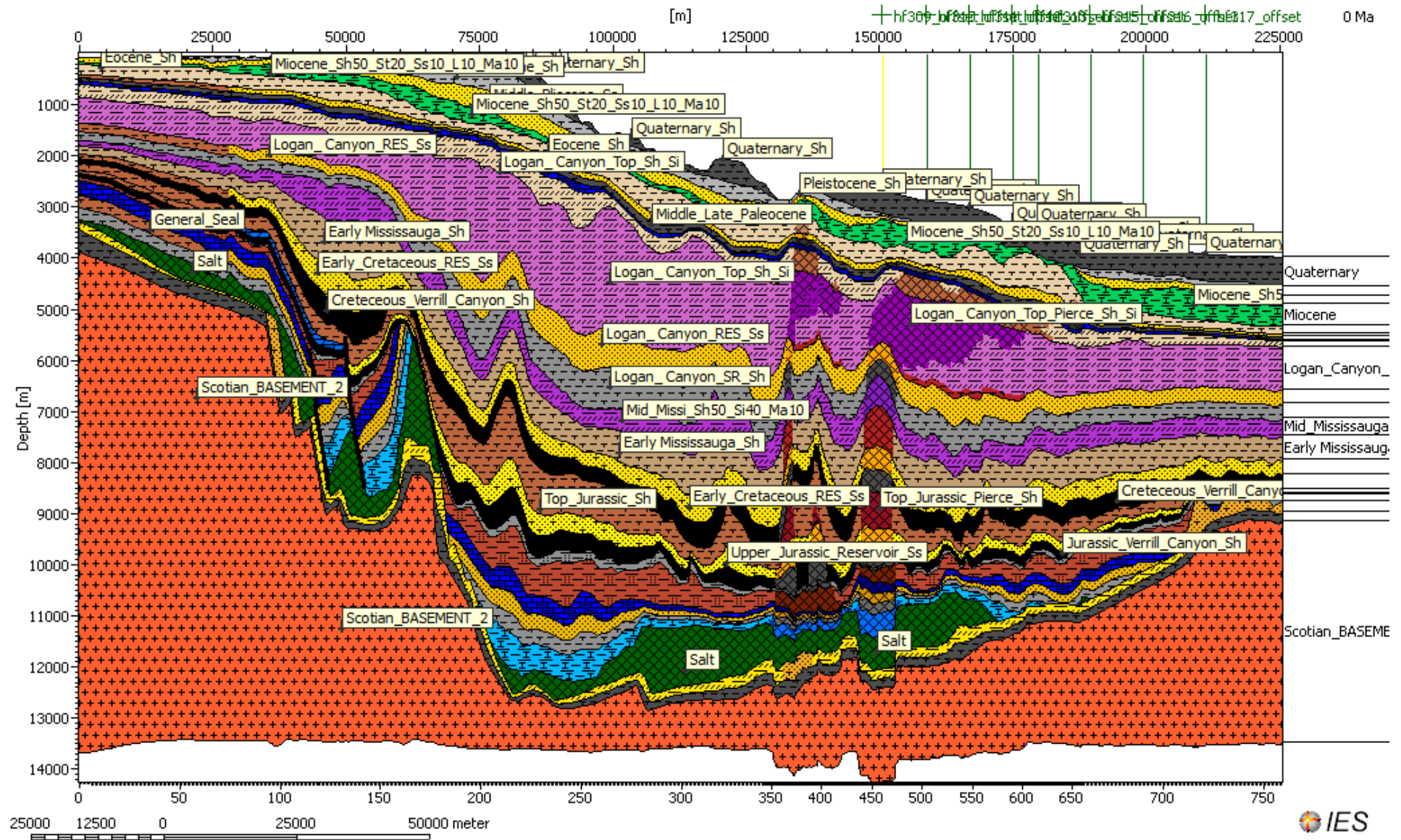
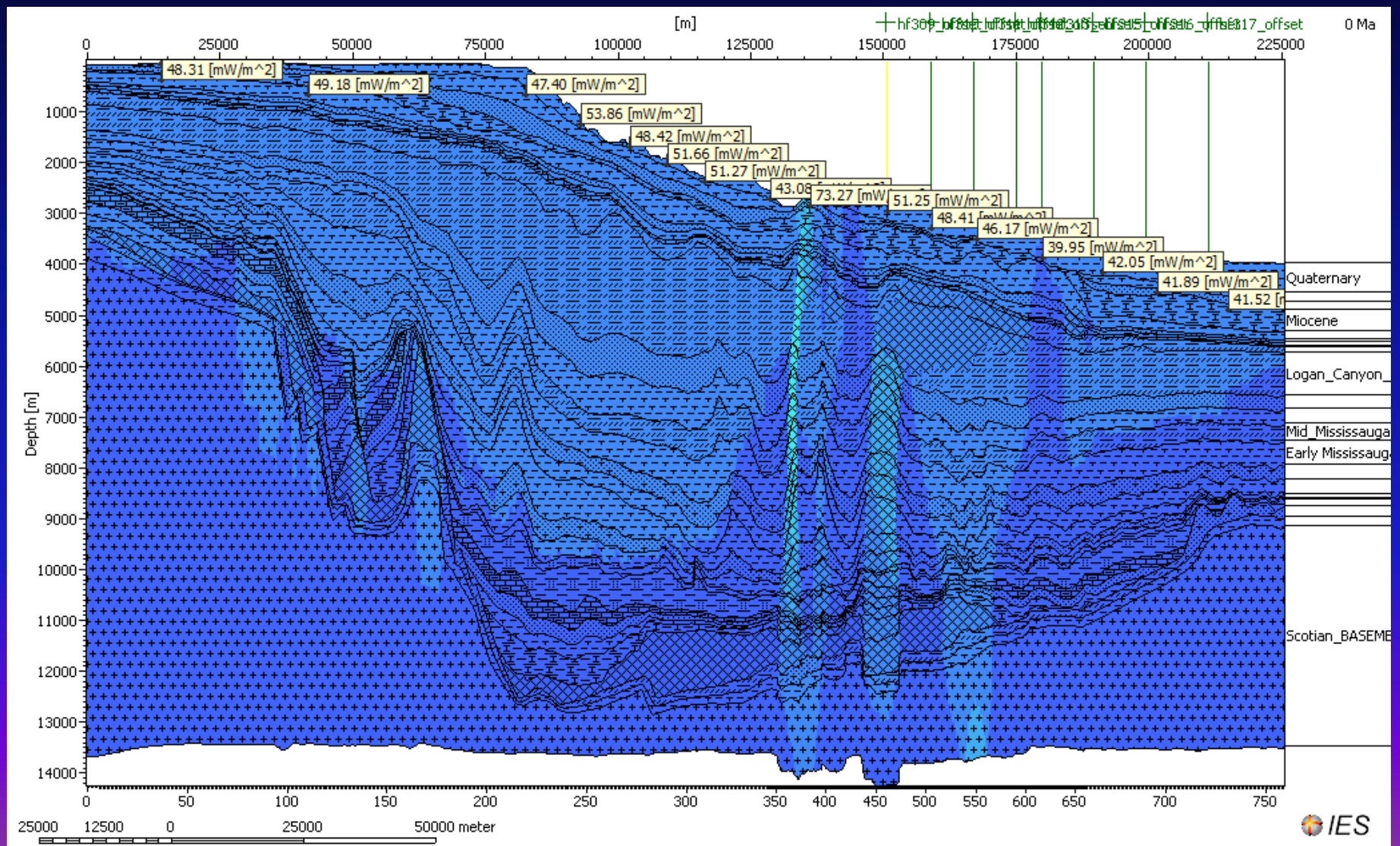


Figure 3c-ii



Line NOVASPAN 1600: modelled heat flow values on top of the measured heat flow data points
and associated areas on top of the salt diapir

Figure 3c-iii

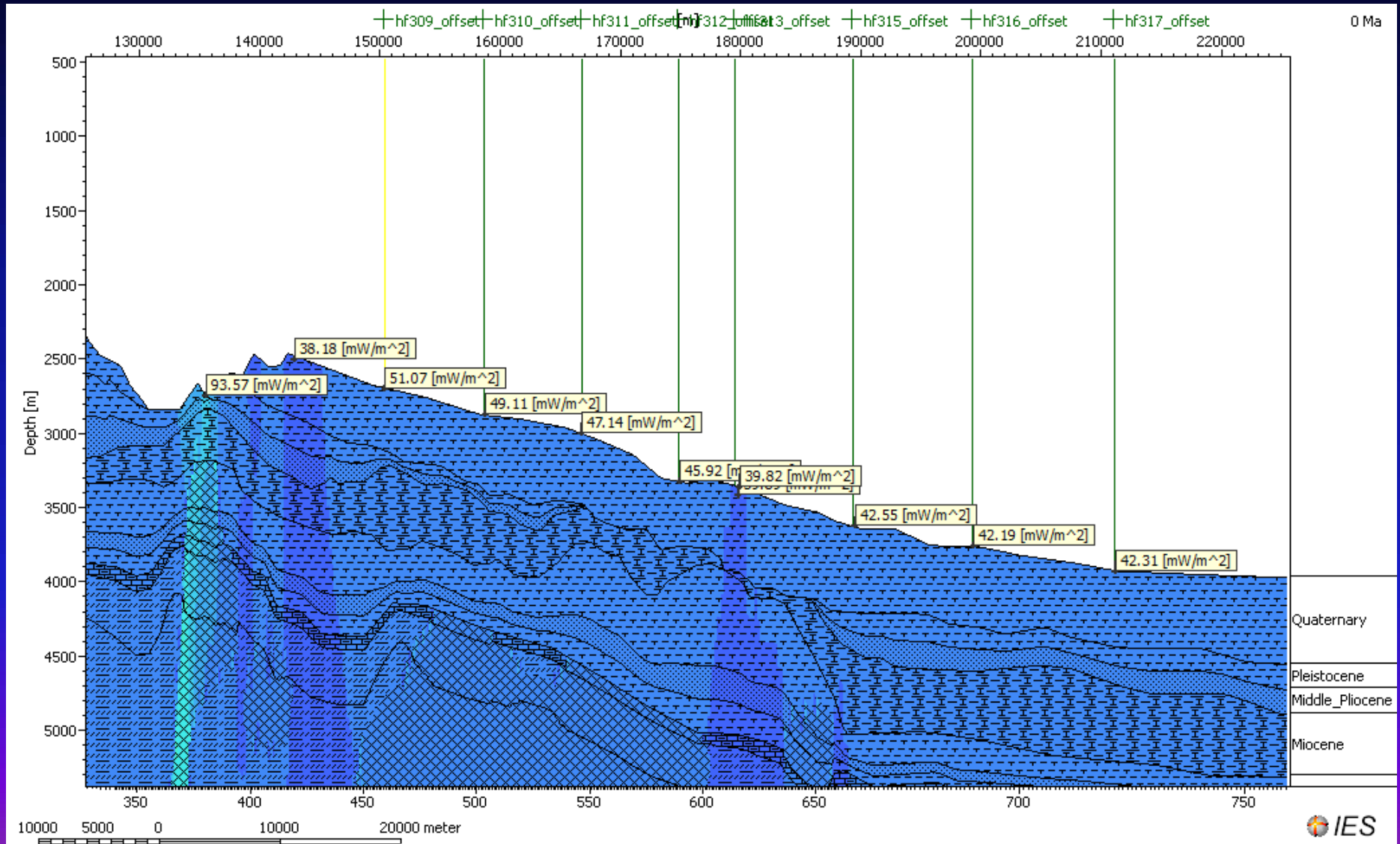


Figure 3c-iv

Line NOVASPAN 1600: calibration of measured and calculated heat flow values

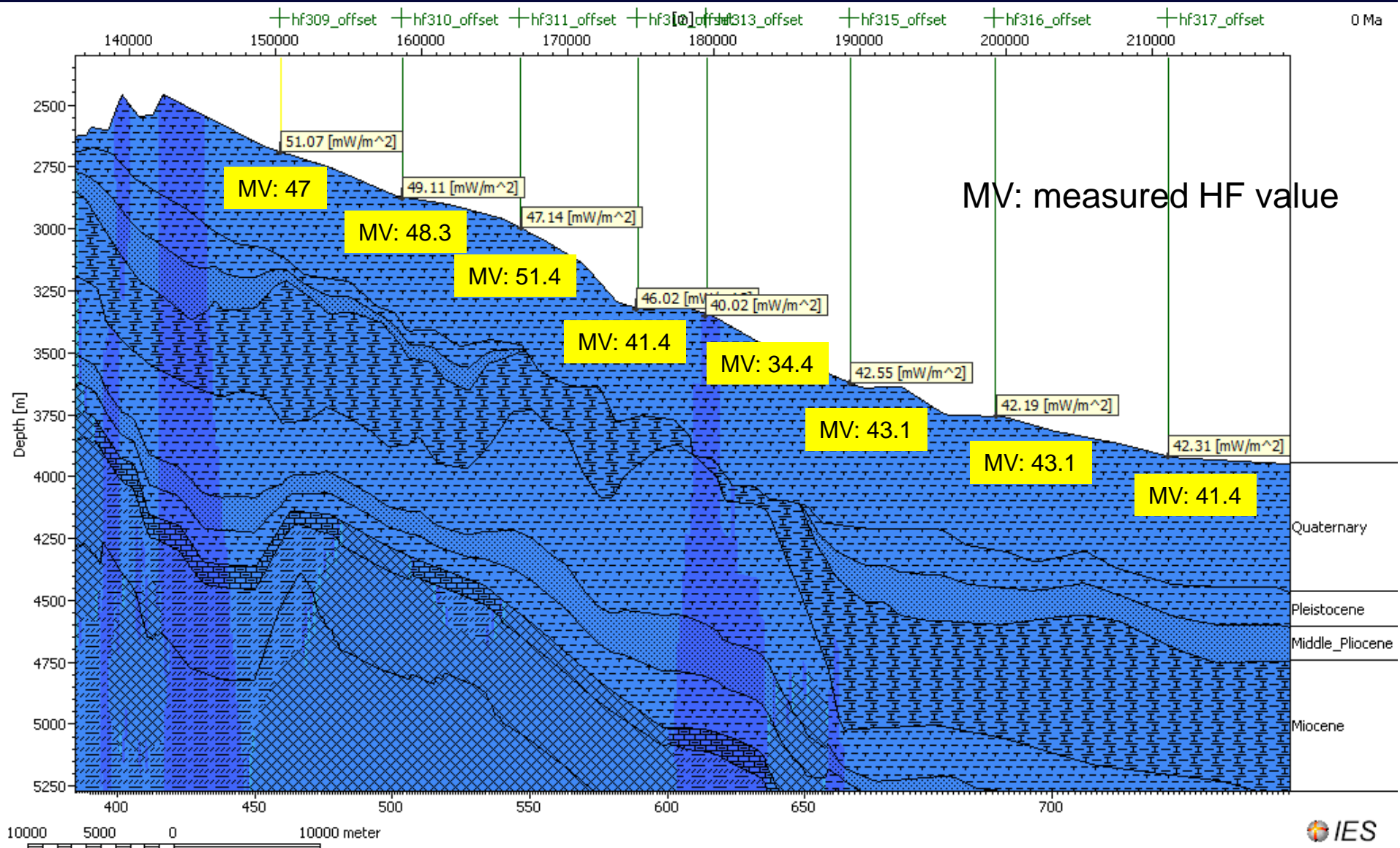
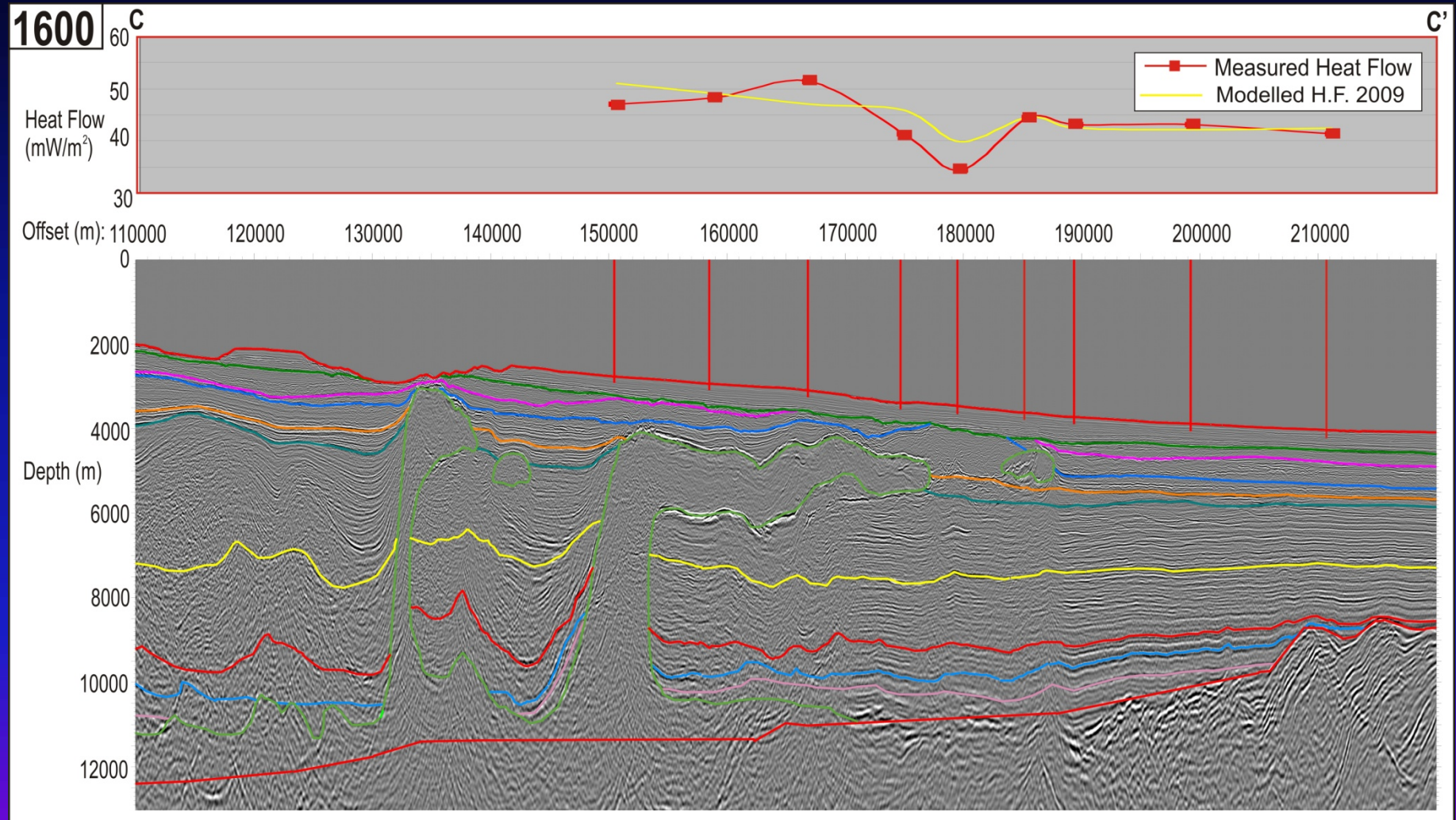


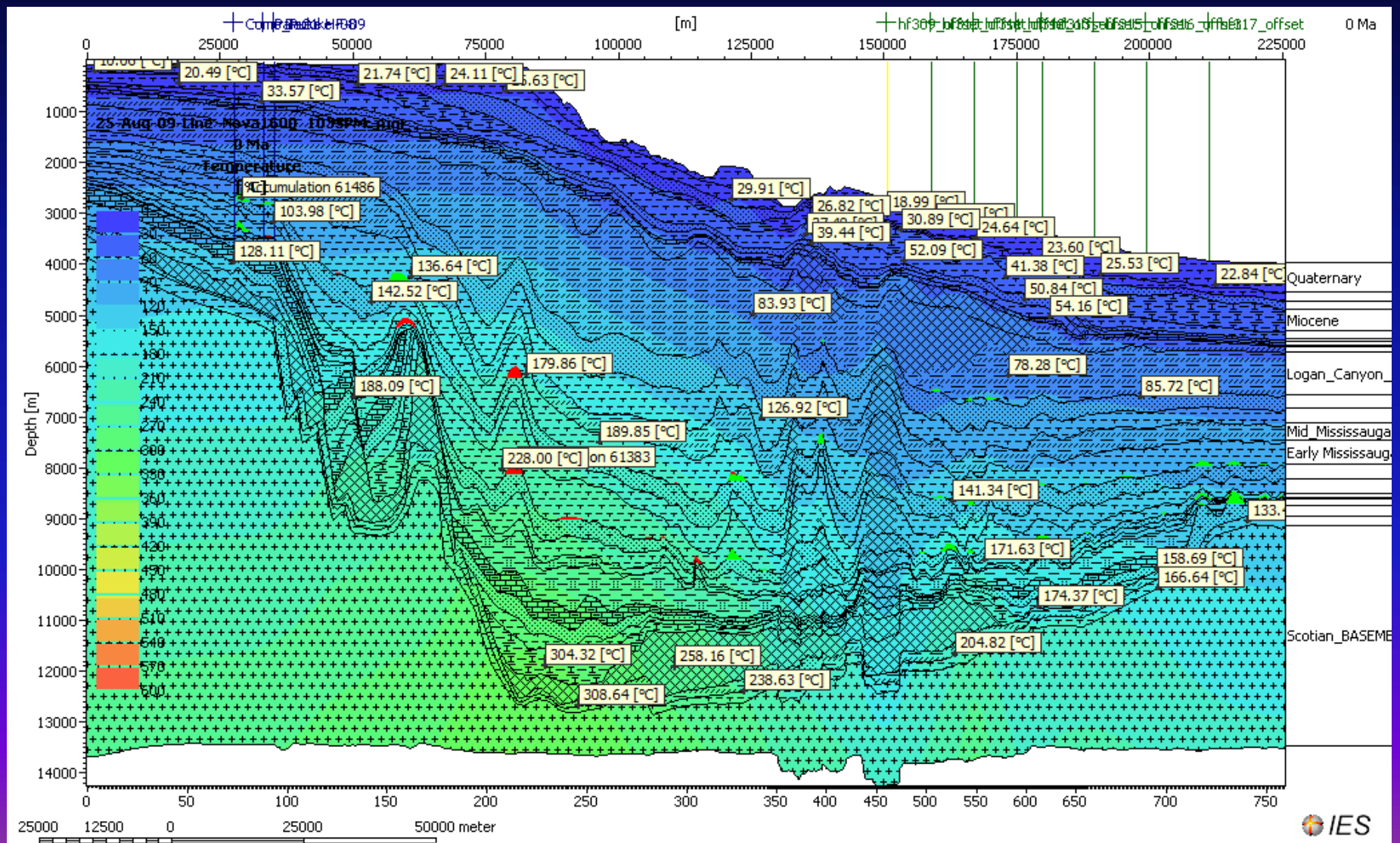
Figure 3c-v

Seafloor Heat Flow: Measured vs. Modelled (Line 1600)



Line NOVASPAN 1600: Illustrates the modelled temperatures and three wells in the shelf and the temperature surrounding the heat flow lines.

Figure 3c-vi



Line 1600: Shows the maturation calibration based on Sweeney and Burnham (1990) .

Figure 3c-vii

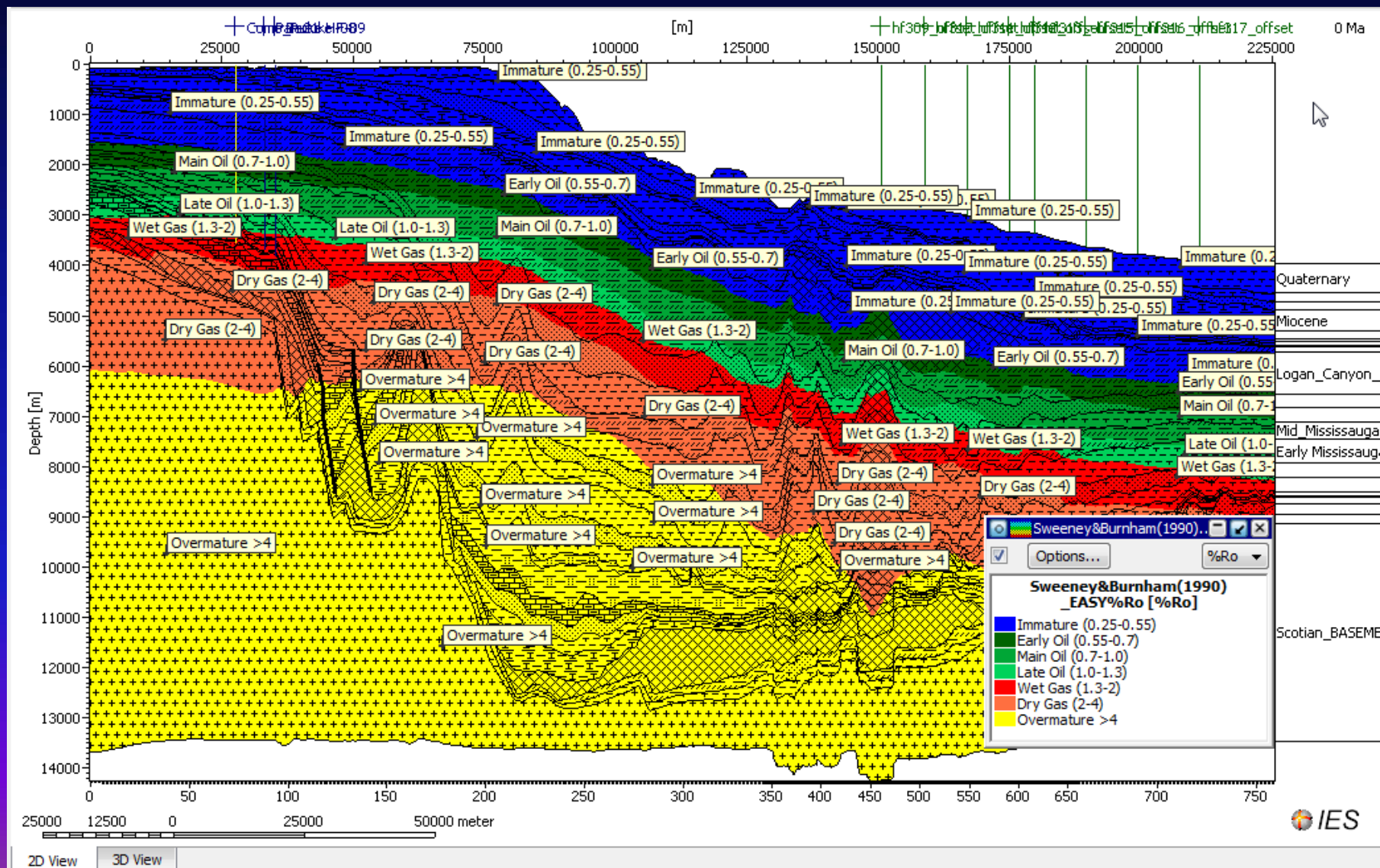


Figure 3c-viii

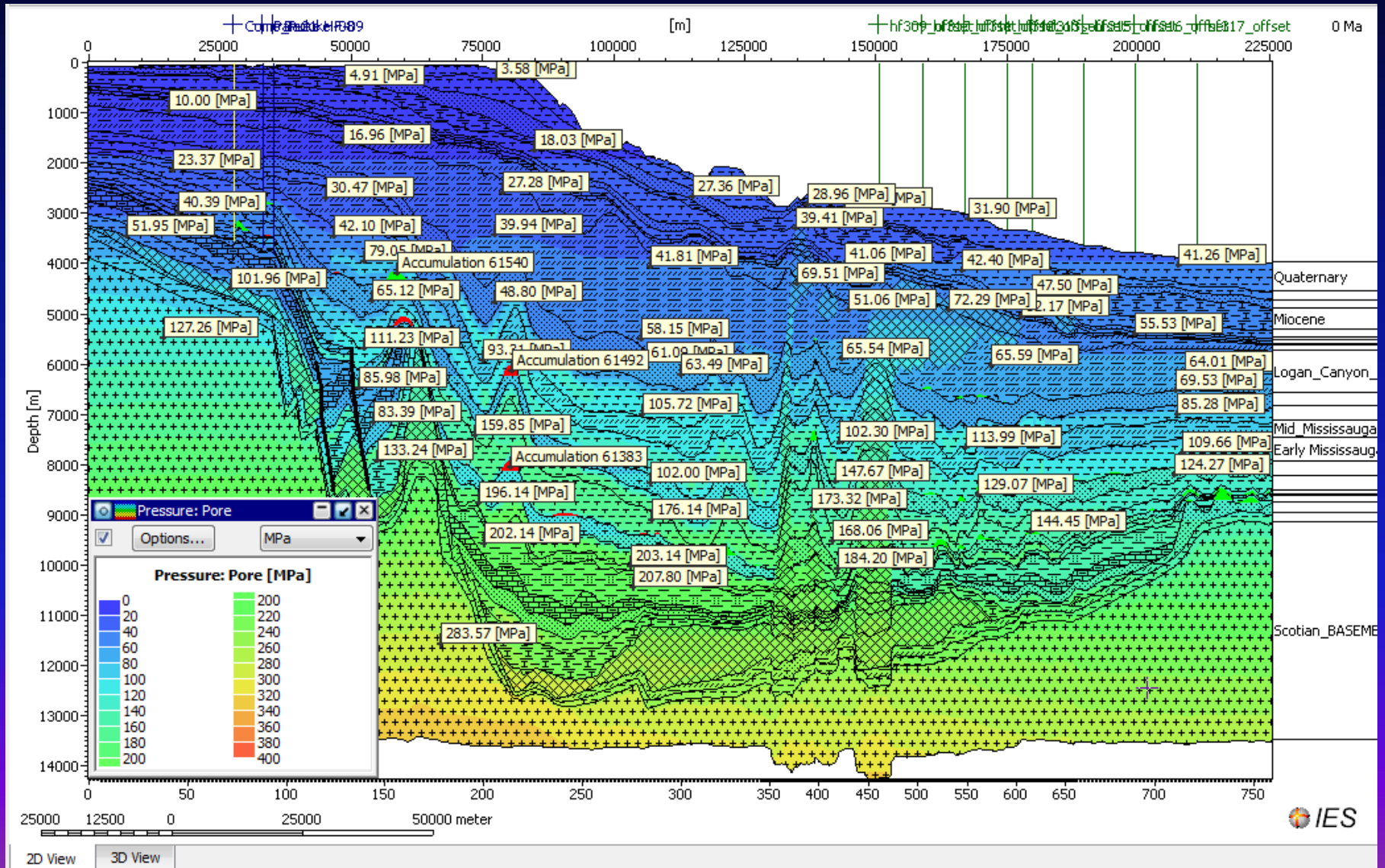
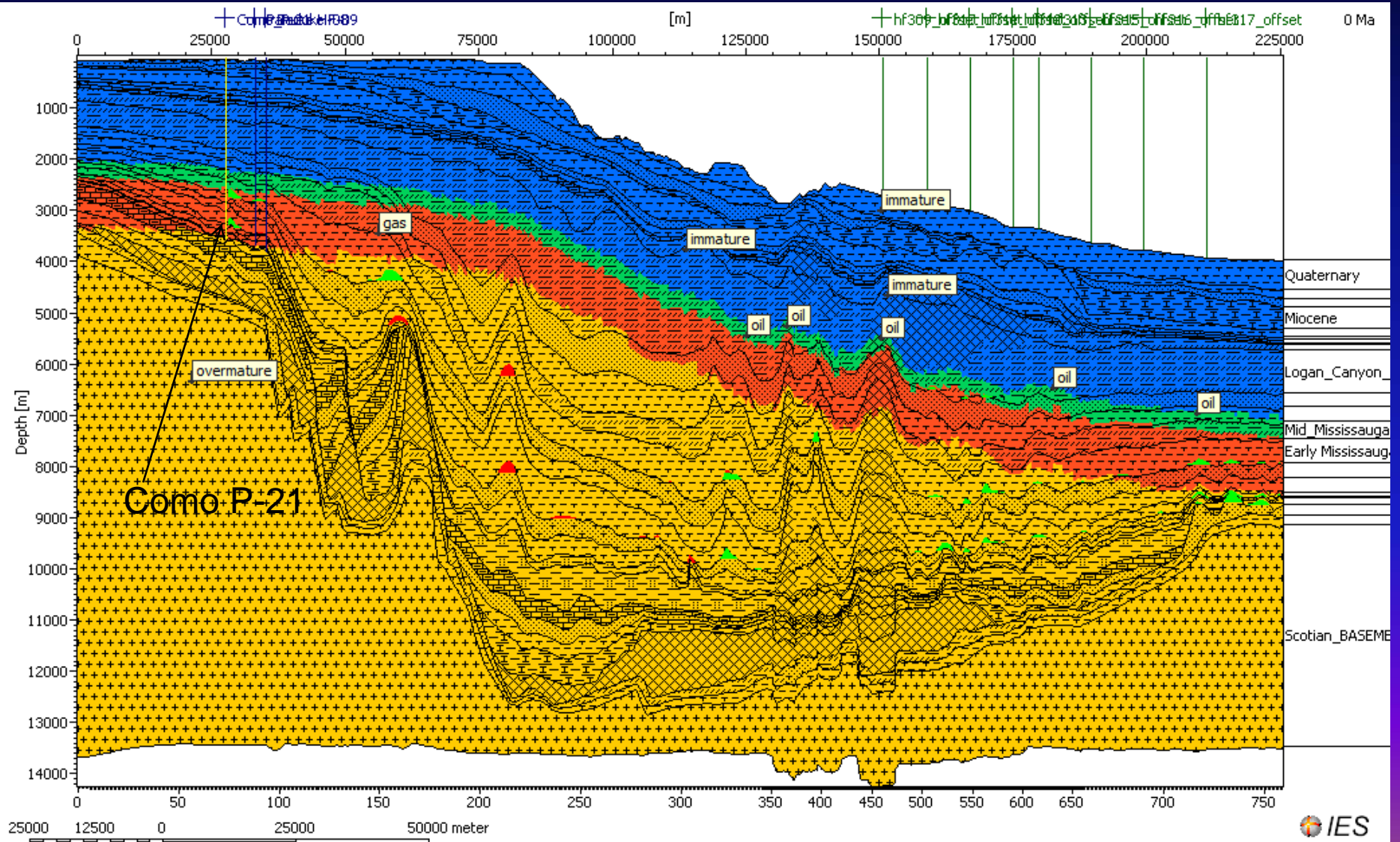


Figure 3c-ix



- immature
- oil
- gas
- overmature

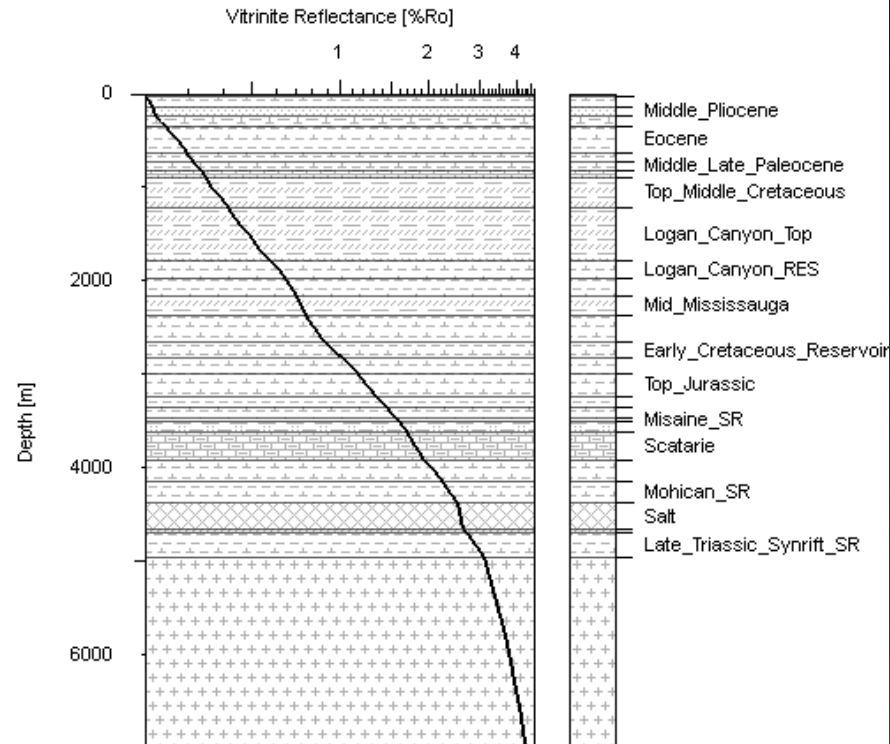
Figure 3c-x



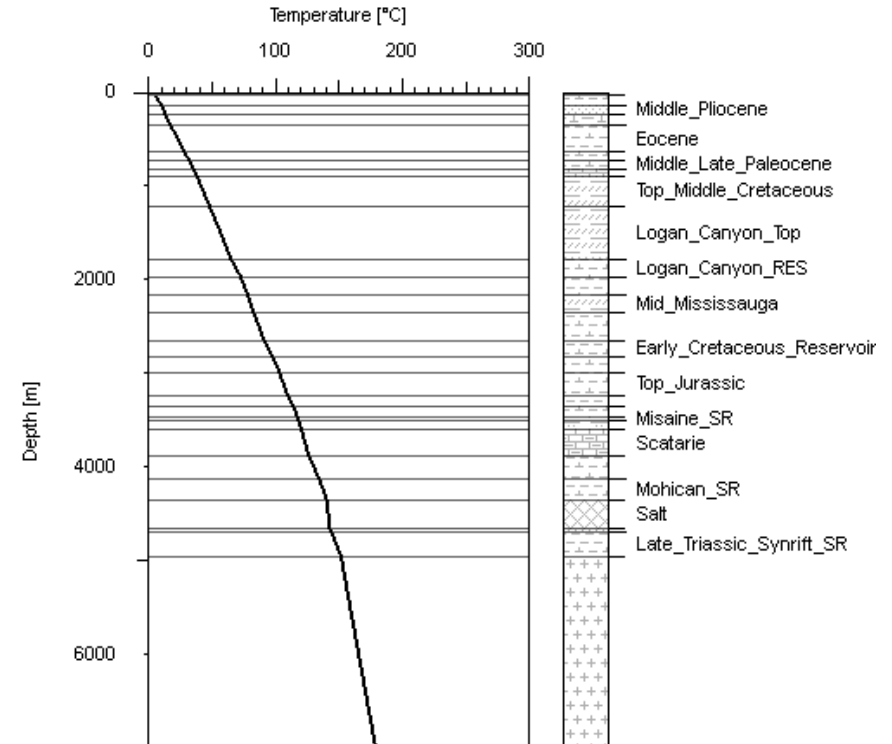
Line NOVASPAN 1600: 1-D Extraction at Como P-21 well – Maturity and Temperature Plot suggesting Mohican Formation is currently at >2% Ro

Figure 3c-xi

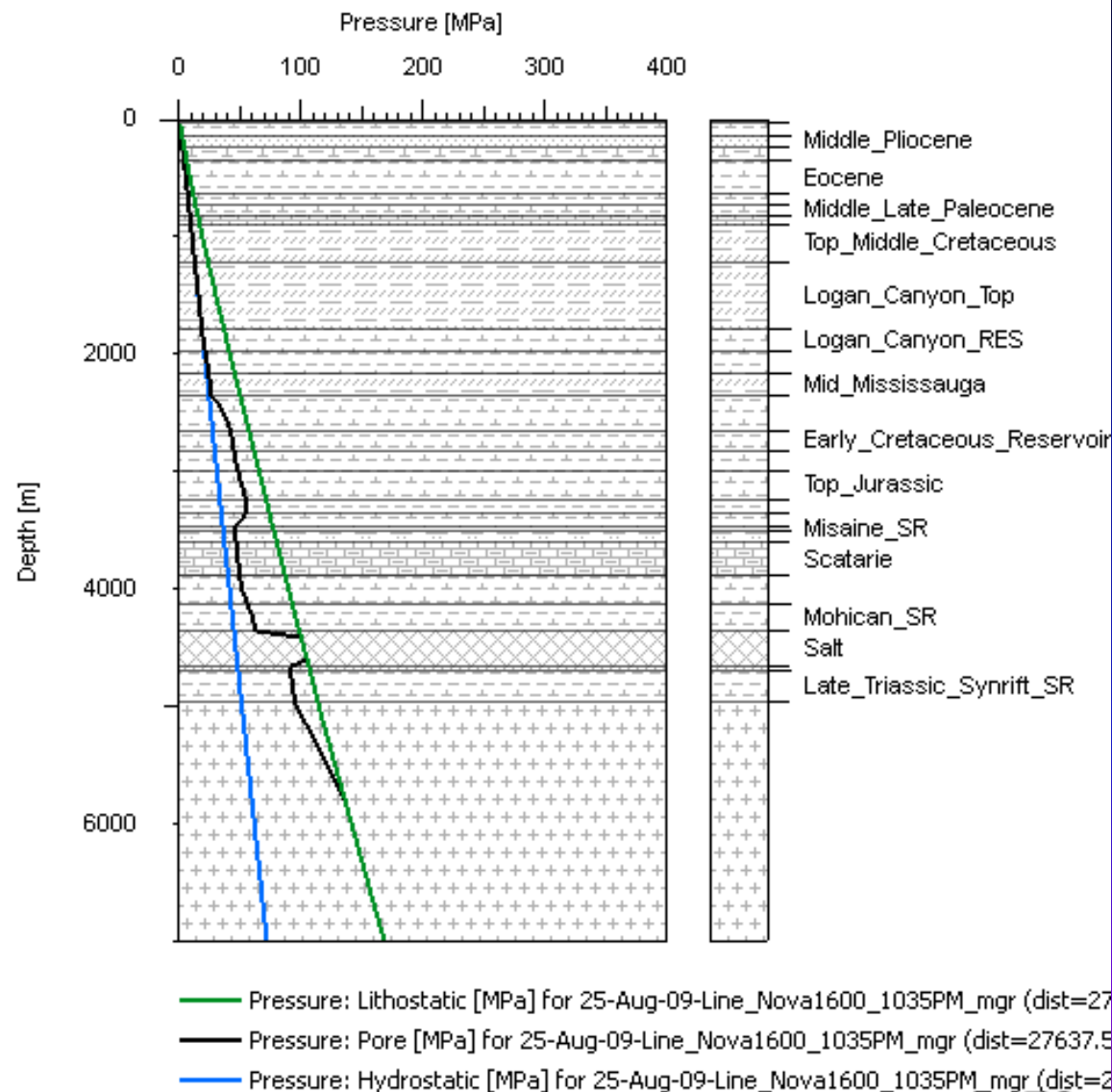
Maturity, 25-Aug-09-Line_Nova1600_1035PM_mgr (dist=27386.2m)



Temperature, 25-Aug-09-Line_Nova1600_1035PM_mgr (dist=27637.5m)



Pressure, 25-Aug-09-Line_Nova1600_1035PM_mgr (dist=27637.5m)



Line NOVSPAN 1600:
1-D Extraction at Como P-21 well
Pressure versus Depth Plot
suggesting a possible overpressure
in the Mohican Formation

Figure 3c-xii

**SEISMIC LINE NOVASPAN 1600
ONSET OF HYDROCARBON
EXPULSION & HC ACCUMULATION**

Line 1600: Onset of Hydrocarbon Expulsion

Figure 3d-i

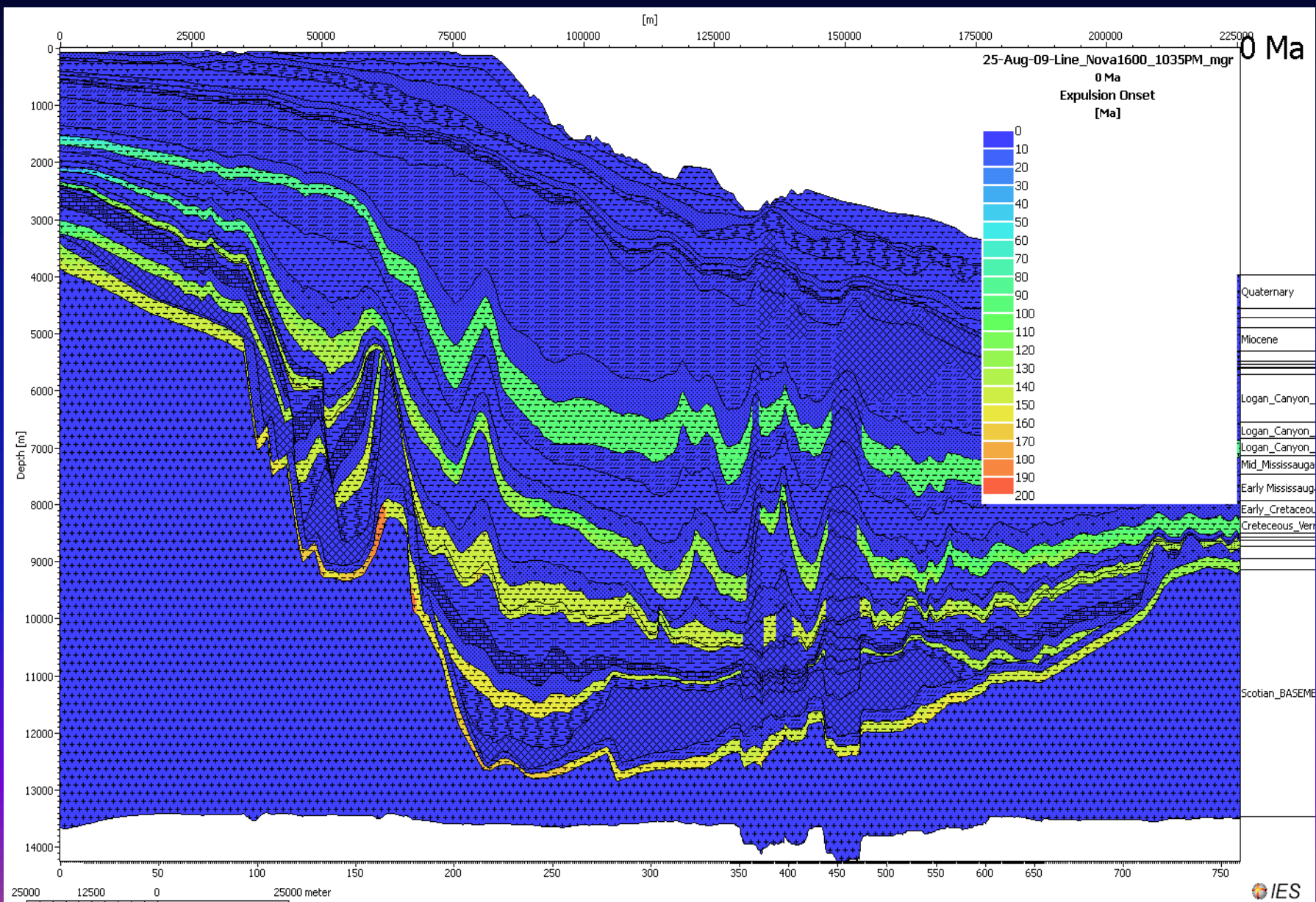


Figure 3d-ii



LINE NOVASSPAN 1600: RESERVOIR HYDROCARBON FINGERPRINTING

TWO EARLY CRETACEOUS RESERVOIRS

Line NOVASPAN 1600: Reservoir Accumulation in various Reservoirs and focussing on Early Cretaceous Researvoir-Shelf 67486

Figure 3e-ia

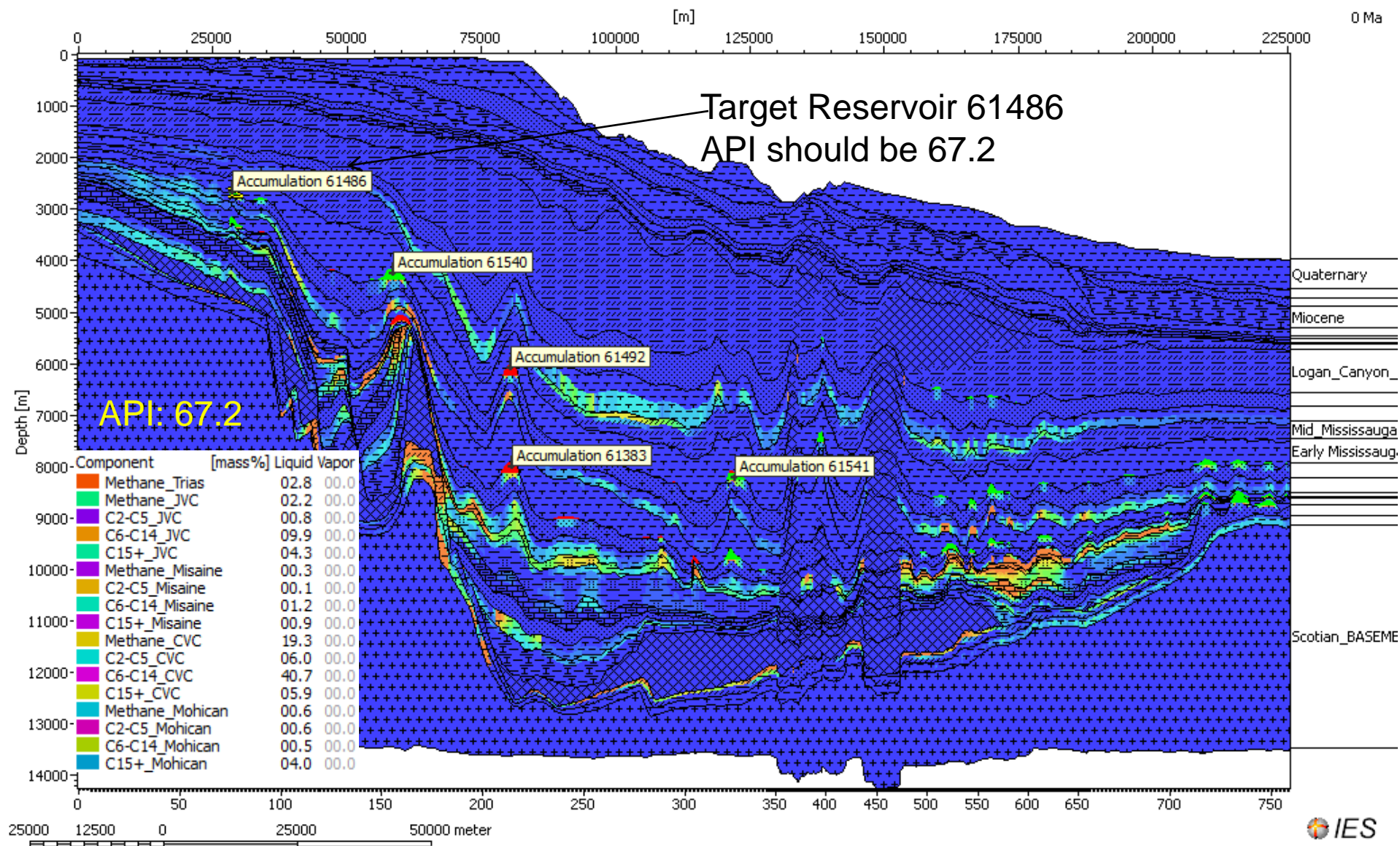
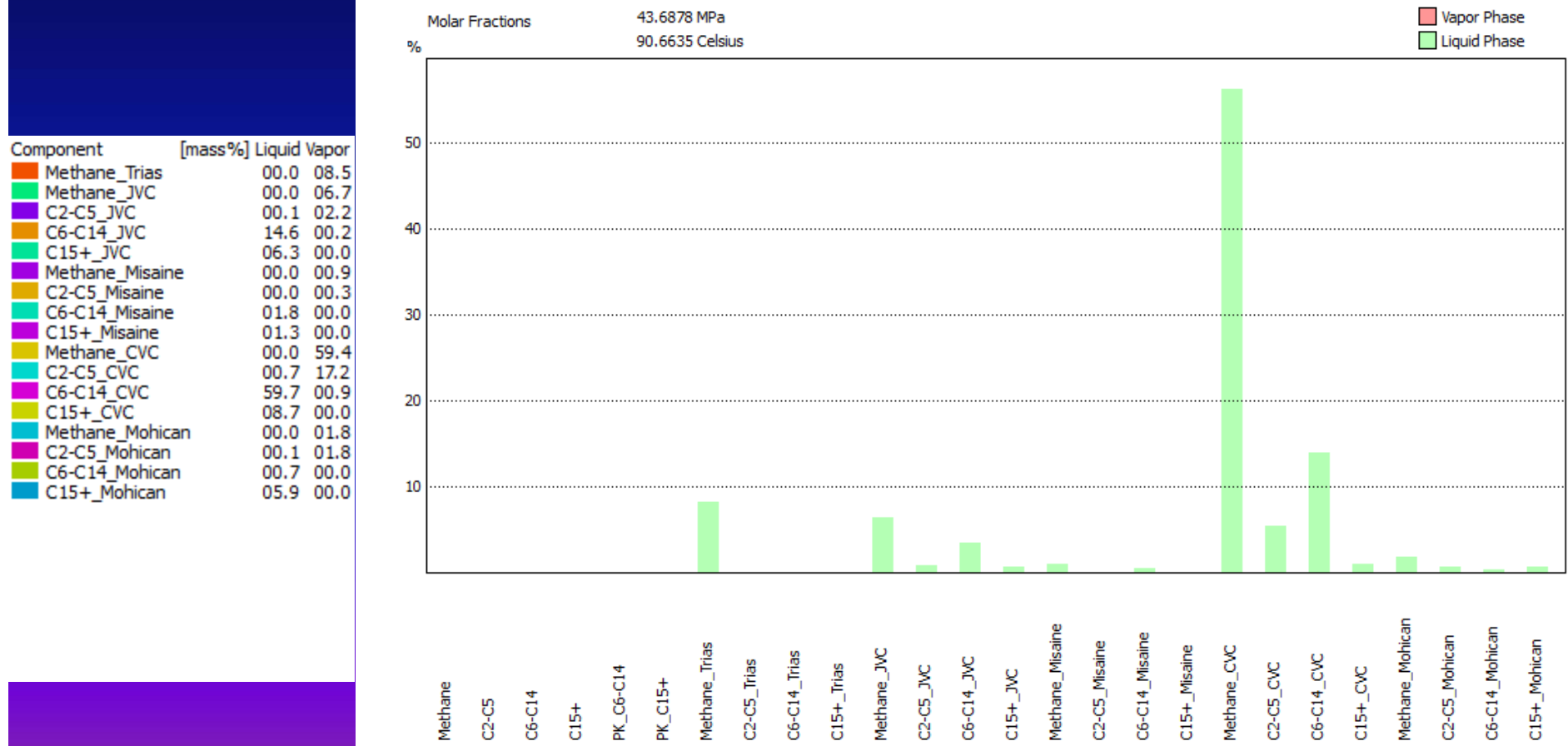
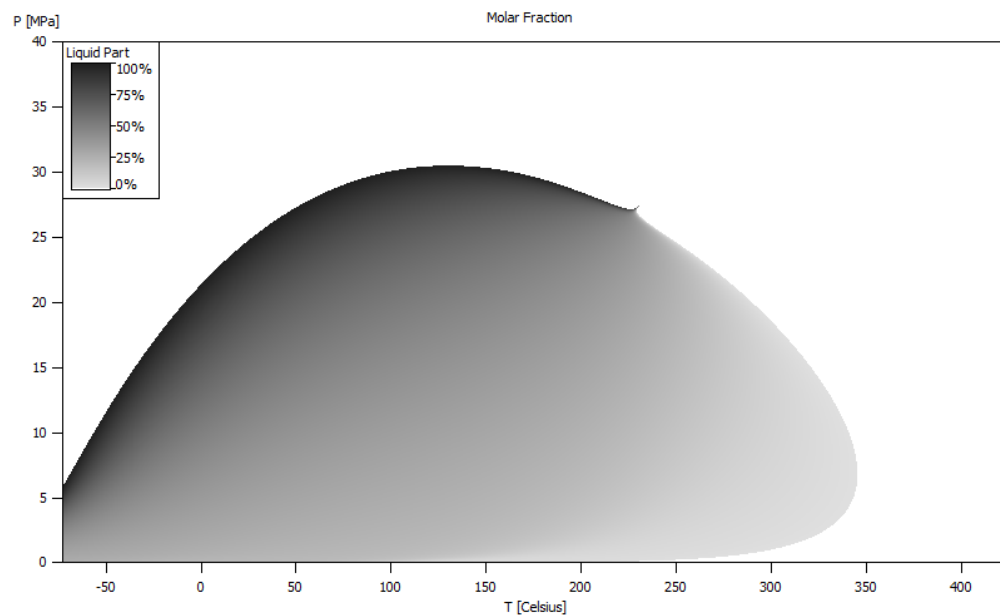


Figure 3e-ib

Line NOVASPAN 1600: Early Cretaceous Researvoir-Shelf 67486 (close to Como P-21 well)
 Source rock fingerprinting suggests the reservoir HCs are mainly composed of condensate
 & methane derived from the Cretaceous Verrill Canyon Source Rock

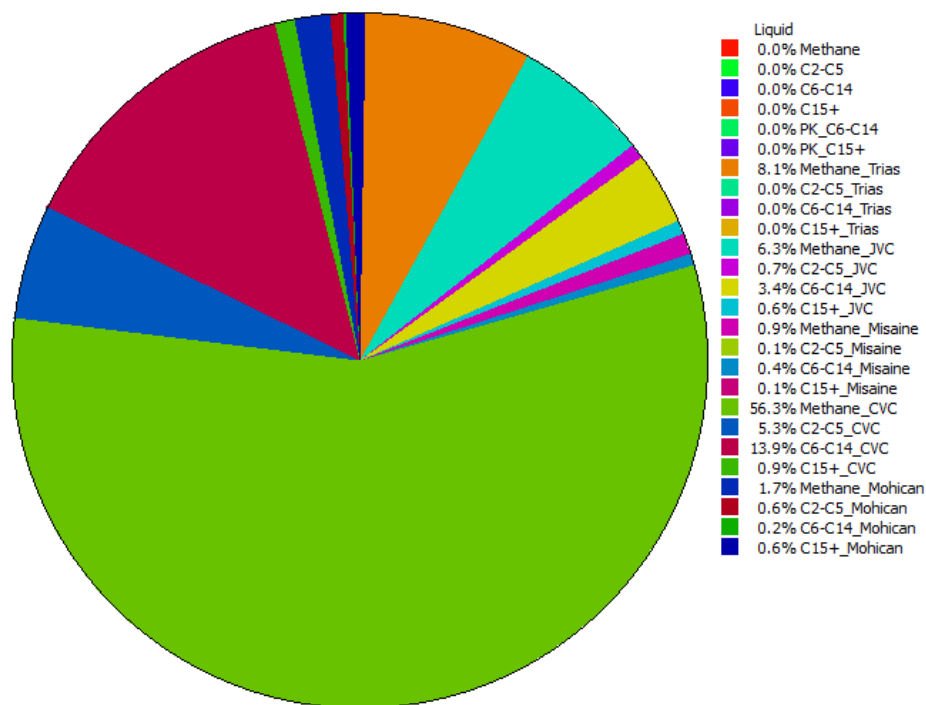




Line NOVASPAN 1600:
Early Cretaceous Reservoir
Shelf 61486 with HC Components
and P-T diagram

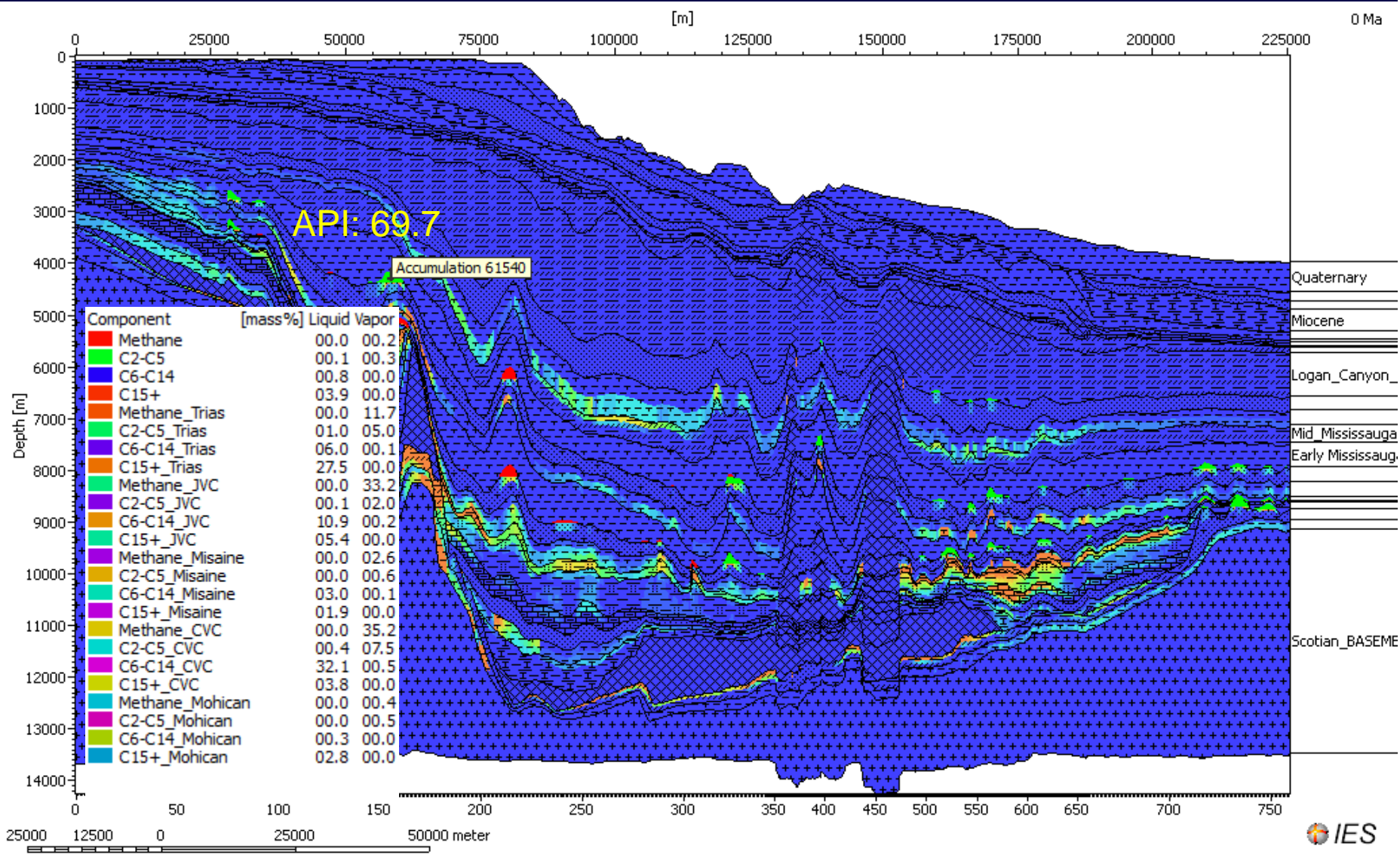
Figure 3e-ic

Molar Fractions 43.6878 MPa 90.6635 Celsius



Line NOVASPAN 1600:Early Cretaceous Reservoir: Accumulation 61540 with API and HC Component Summary

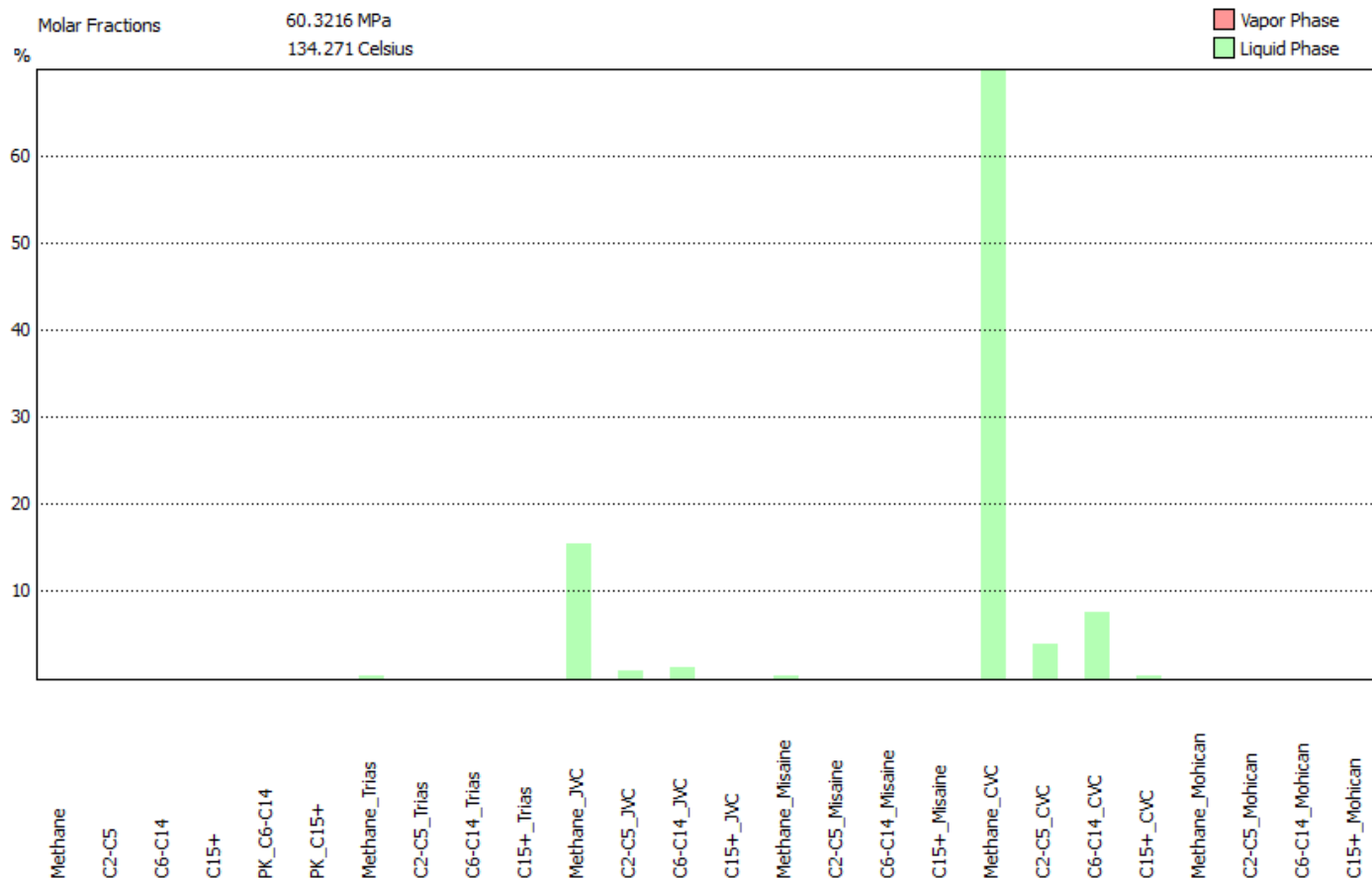
Figure 3e-iiia



Line NOVASPAN 1600: Early Cretaceous Reservoir Accumulation 61540.
Source rock fingerprinting suggests the reservoir HCs are mainly
composed of methane derived from both Cretaceous & Jurassic Verrill
Canyon Source Rock

Figure 3e-iiB

Component	[mass%]	Liquid	Vapor
Methane	00.0	00.2	
C2-C5	00.1	00.3	
C6-C14	00.8	00.0	
C15+	03.9	00.0	
Methane_Trias	00.0	11.7	
C2-C5_Trias	01.0	05.0	
C6-C14_Trias	06.0	00.1	
C15+_Trias	27.5	00.0	
Methane_JVC	00.0	33.2	
C2-C5_JVC	00.1	02.0	
C6-C14_JVC	10.9	00.2	
C15+_JVC	05.4	00.0	
Methane_Misaine	00.0	02.6	
C2-C5_Misaine	00.0	00.6	
C6-C14_Misaine	03.0	00.1	
C15+_Misaine	01.9	00.0	
Methane_CVC	00.0	35.2	
C2-C5_CVC	00.4	07.5	
C6-C14_CVC	32.1	00.5	
C15+_CVC	03.8	00.0	
Methane_Mohican	00.0	00.4	
C2-C5_Mohican	00.0	00.5	
C6-C14_Mohican	00.3	00.0	
C15+_Mohican	02.8	00.0	



Line NOVASPAN 1600:
Early Cretaceous Reservoir
Accumulation 61540
with mixed HC components and
P-T Diagram of the components

Molar Fractions 60.3216 MPa 134.271 Celsius

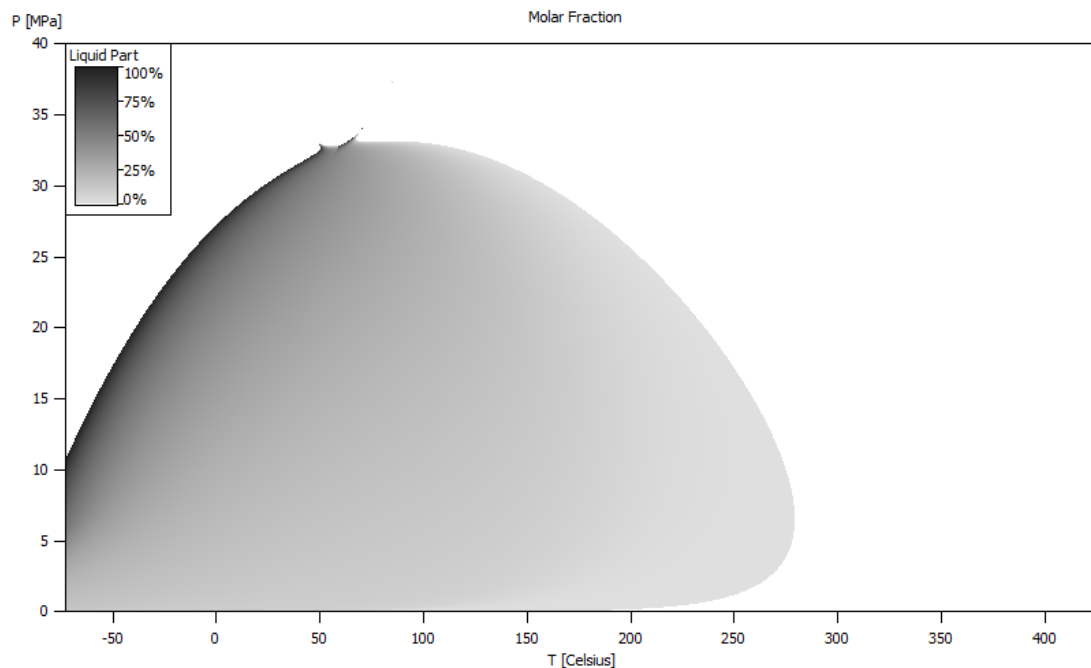
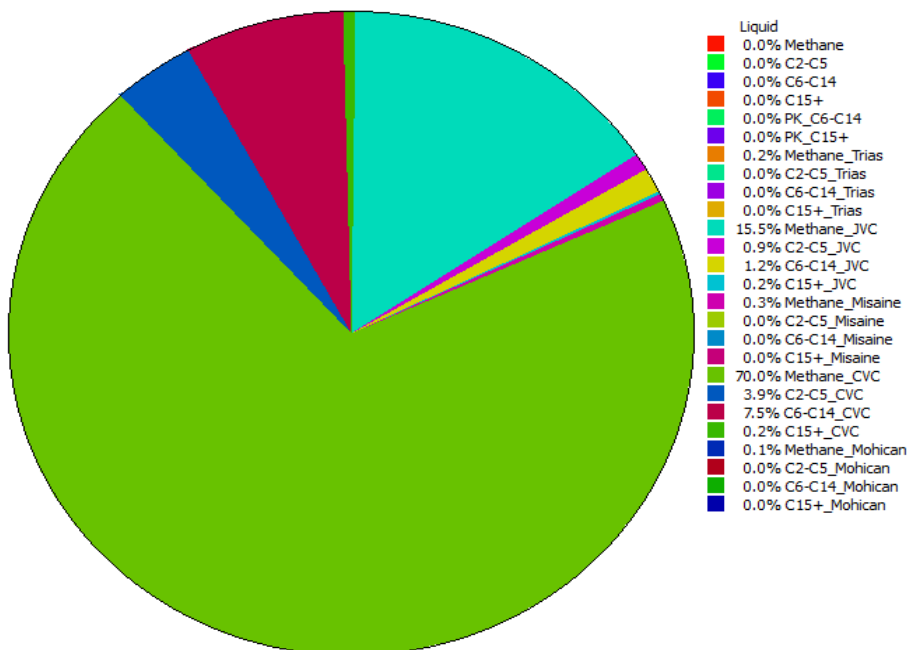
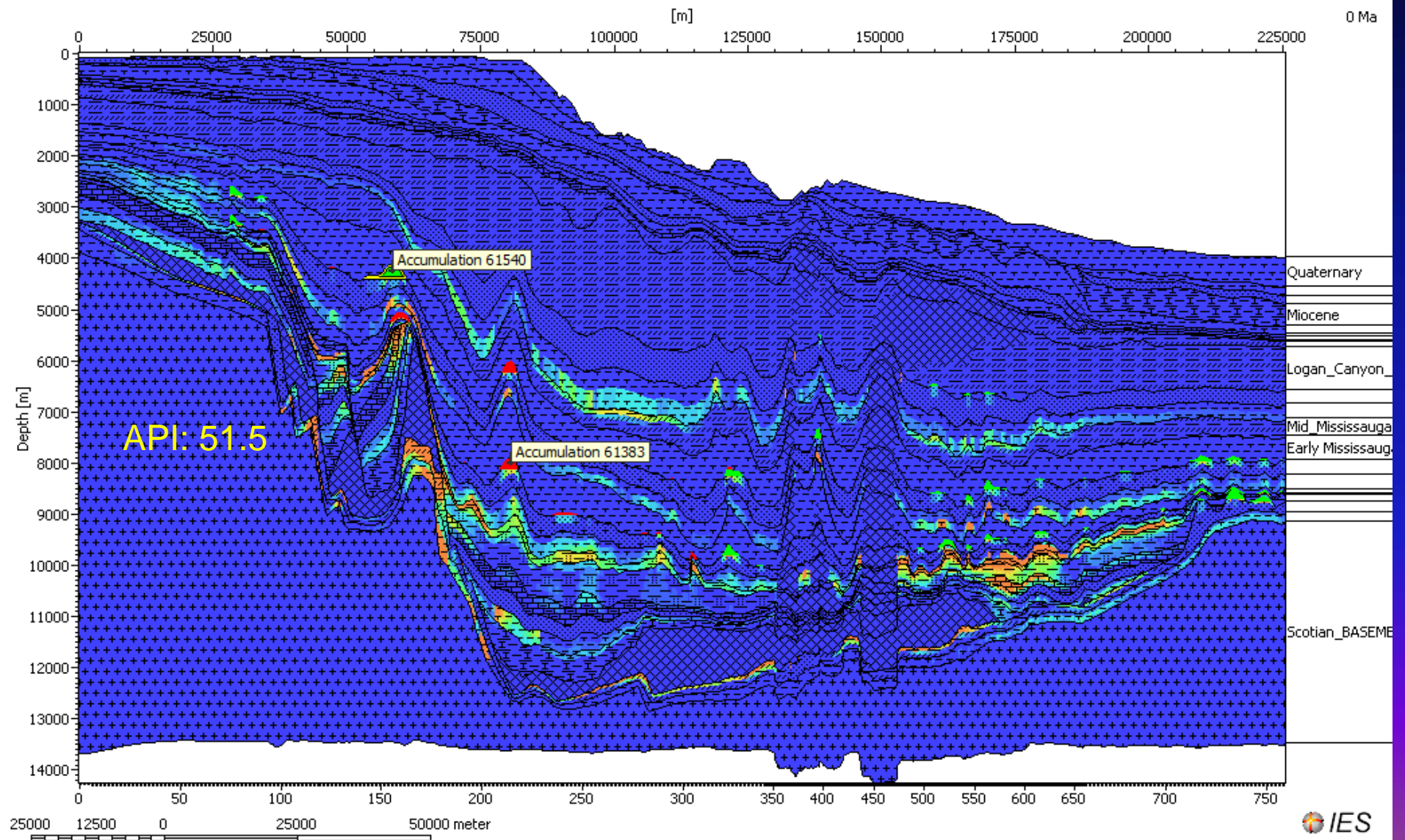


Figure 3e-iic

LATE JURASSIC RESERVOIR SATURATIONS: LINE NOVASPAN 1600

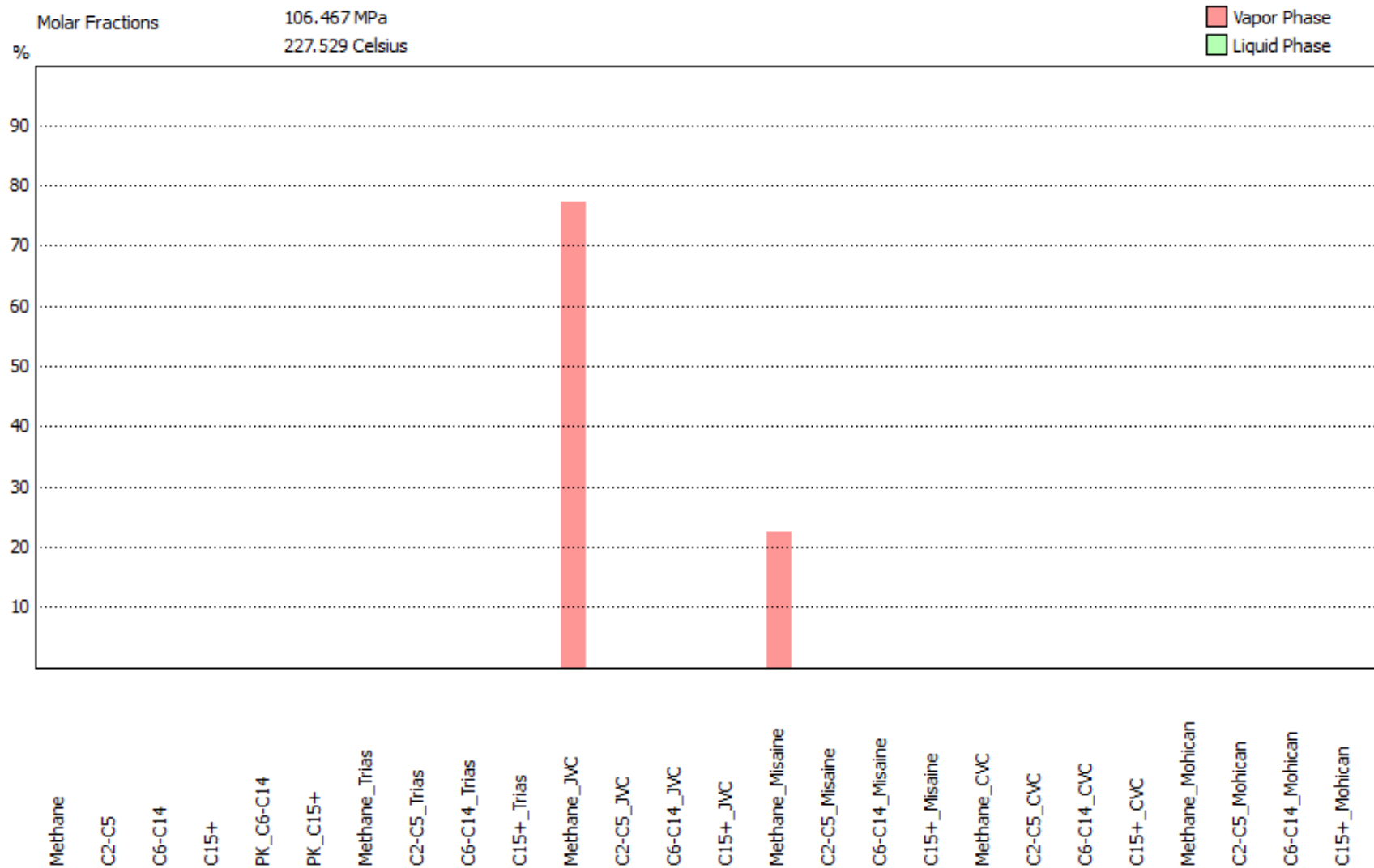
Line NOVASPAN 1600: Late Jurassic Reservoir 61383 with percentages various HC components showing hydrocarbons within the reservoir is amostly methane

Figure 3e-iiia



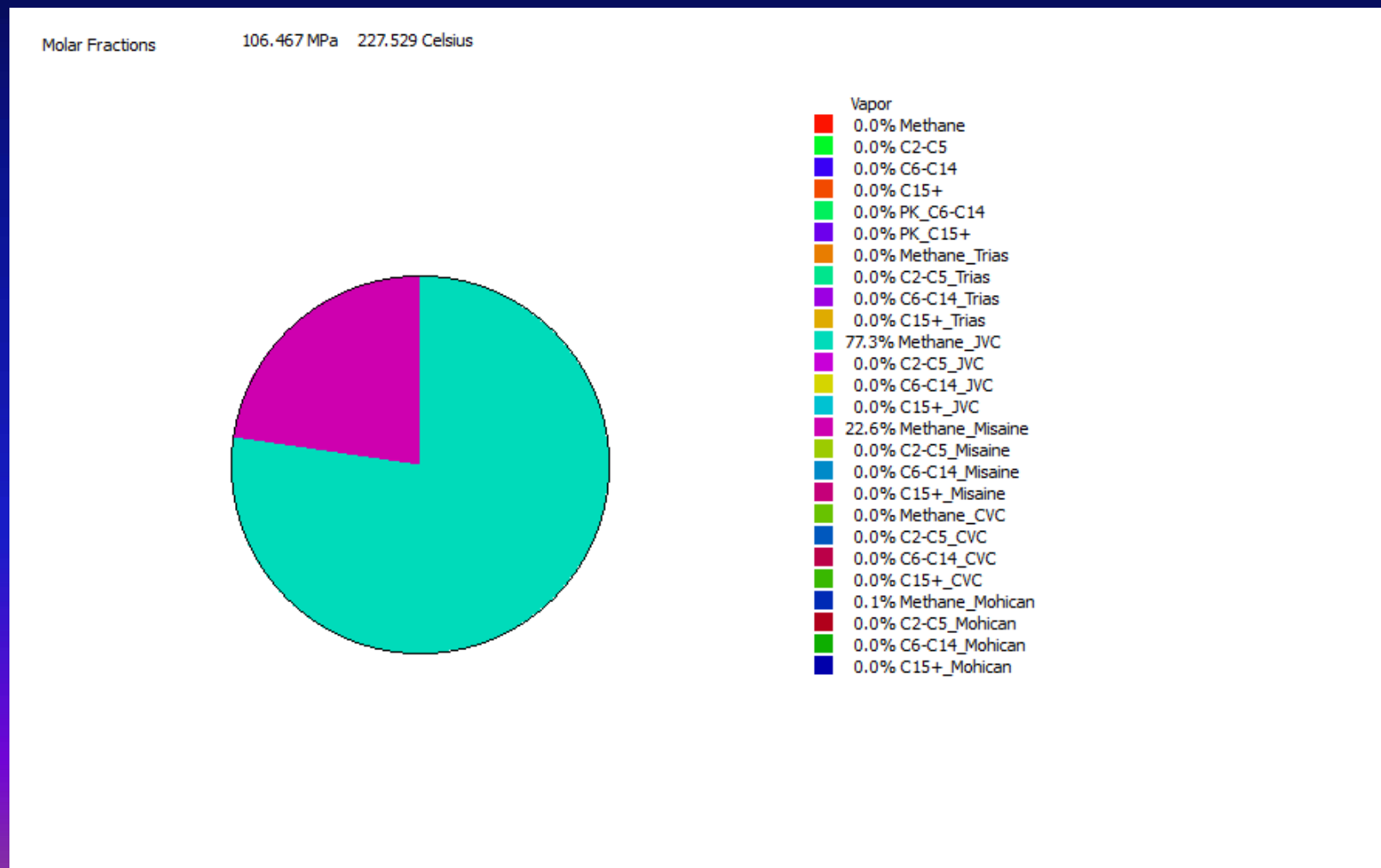
Line NOVASPAN 1600: Late Jurassic Reservoir 61383 with percentages various HC components and source rock fingerprinting

Figure 3e-iiib



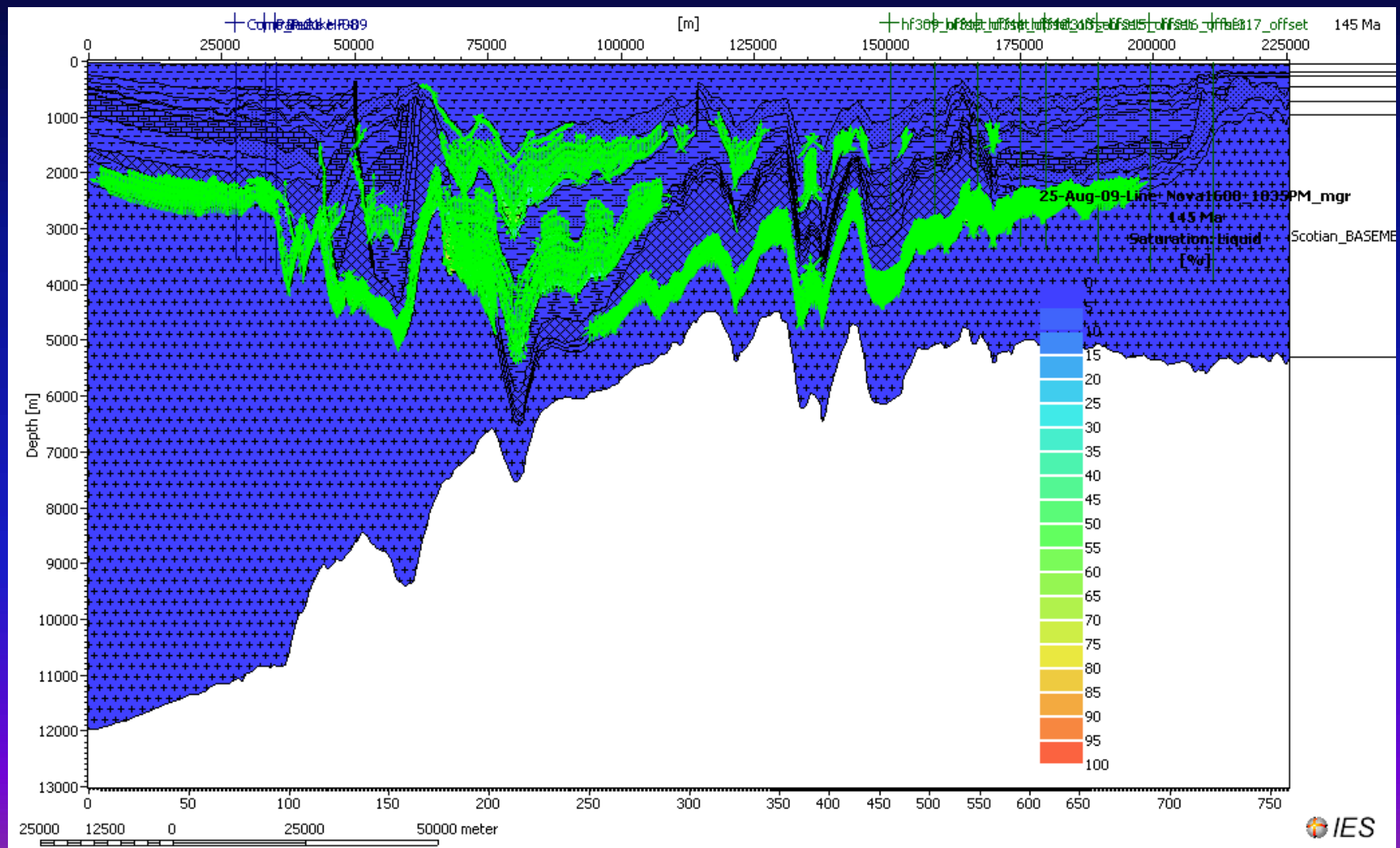
Line NOVASPAN 1600: Late Jurassic Reservoir 61383 with percentages various HC components showing hydrocarbons within the reservoir is mainly methane derived from both JVC and Misaine source rocks

Figure 3e-iiic



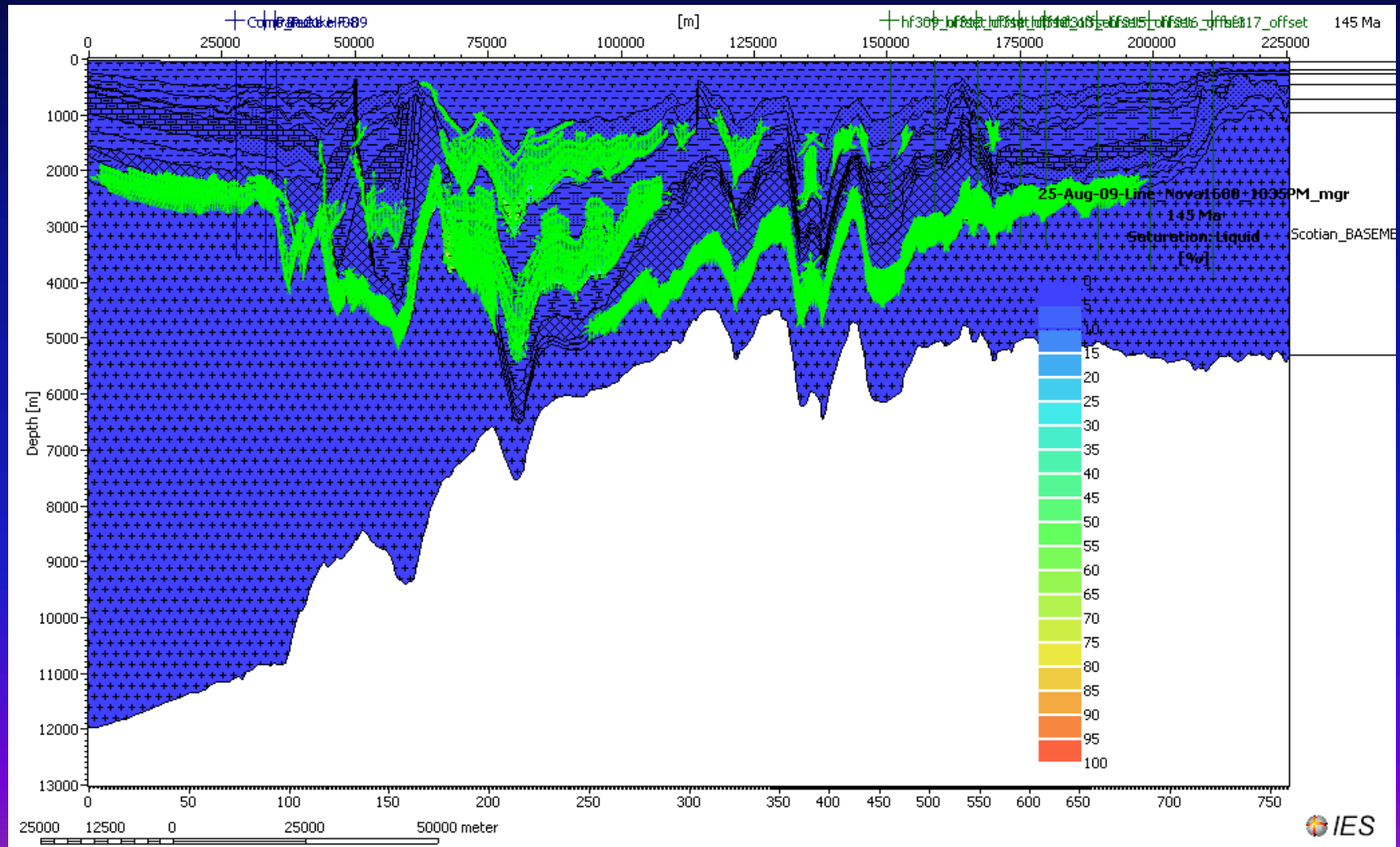
Line 1600- Liquid HC Migration Patterns and Liquid HC Loss 145 Ma

Figure 3f-i



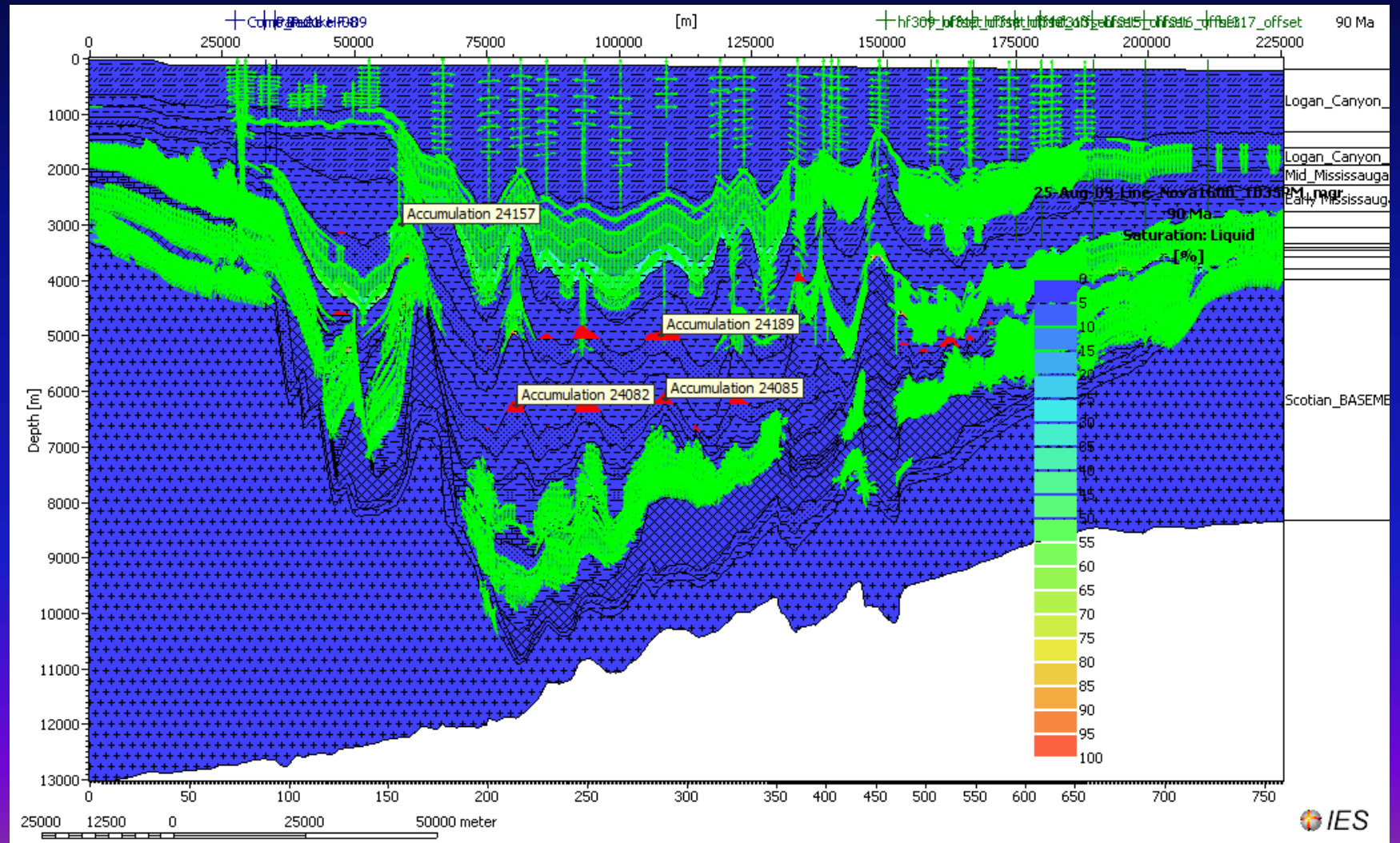
Line 1600- Saturation of Liquids in 112 Ma

Figure 3f-ii



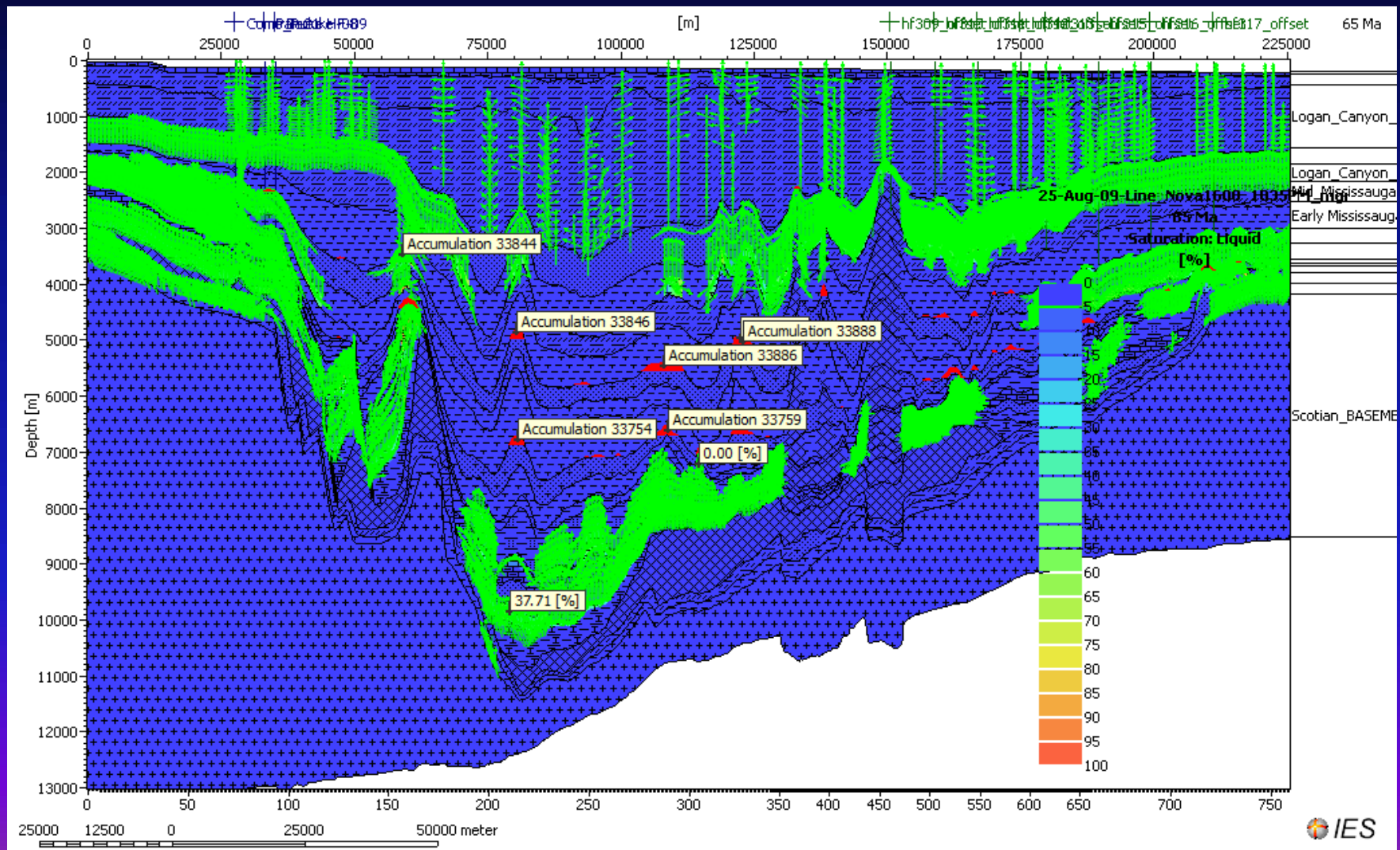
Line 1600- Saturation of Liquids in 90 Ma

Figure 3f-iii



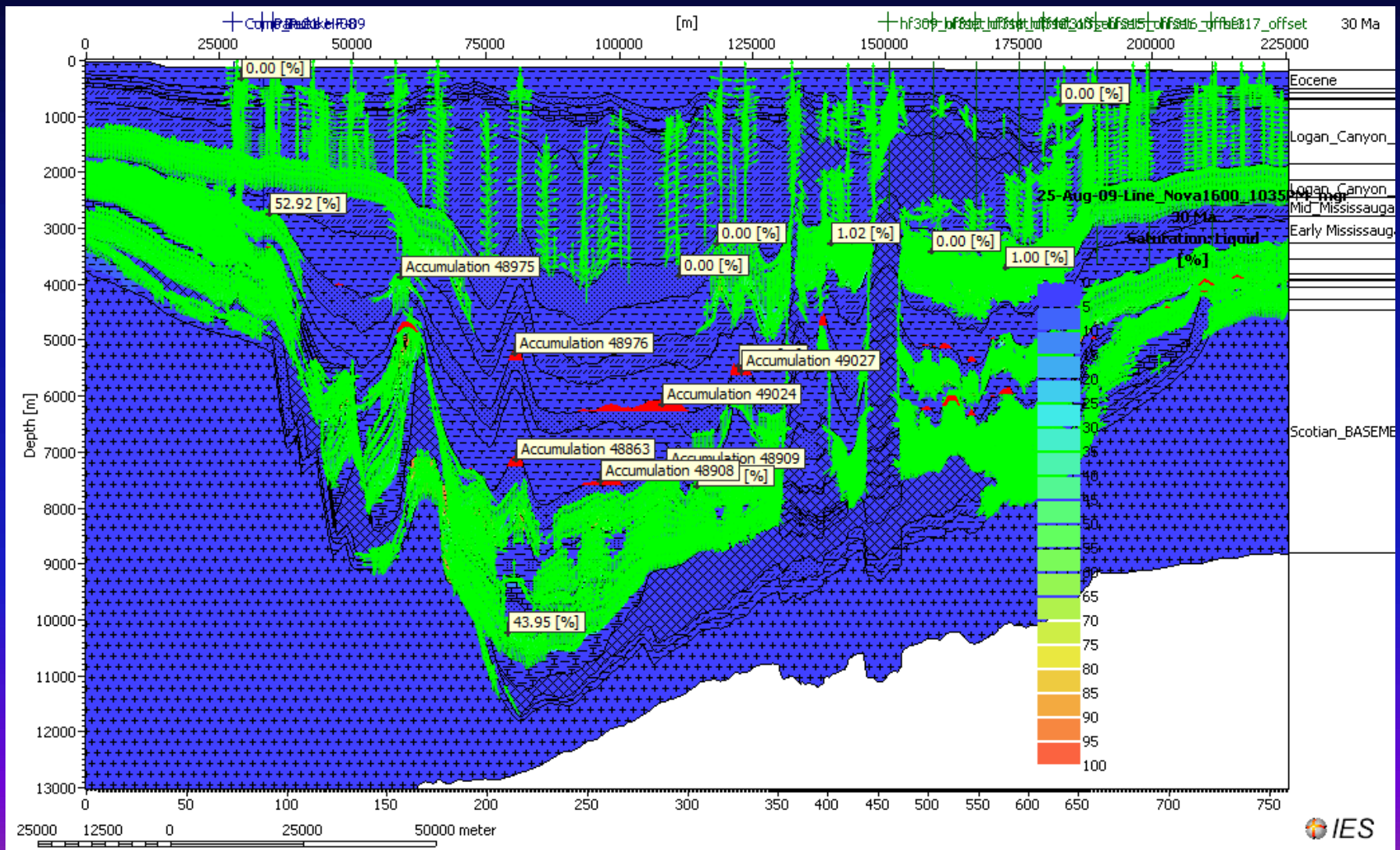
Line 1600- Saturation of Liquids in 65 Ma

Figure 3f-iv



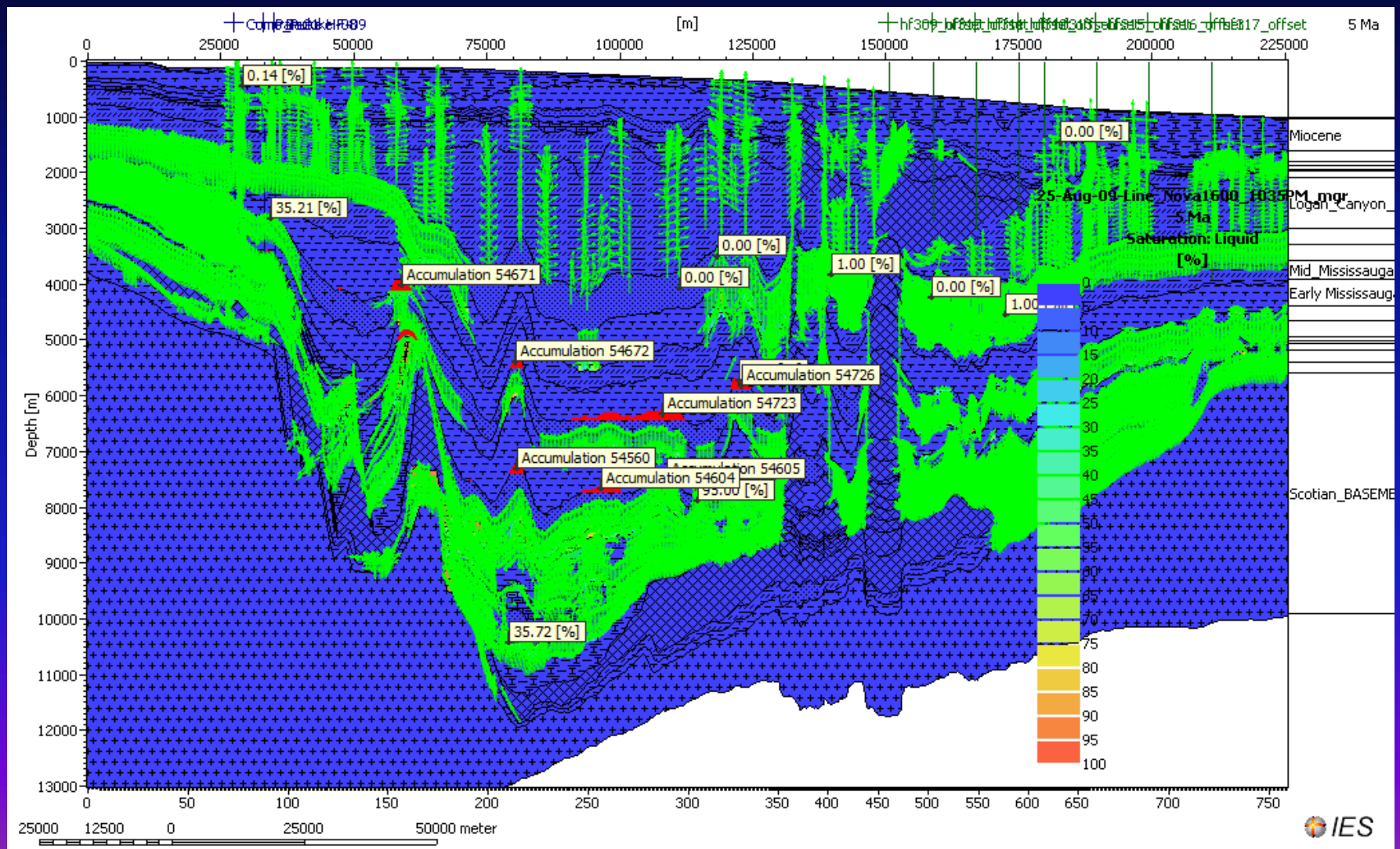
Line 1600- Saturation of Liquids in 30 Ma

Figure 3f-v



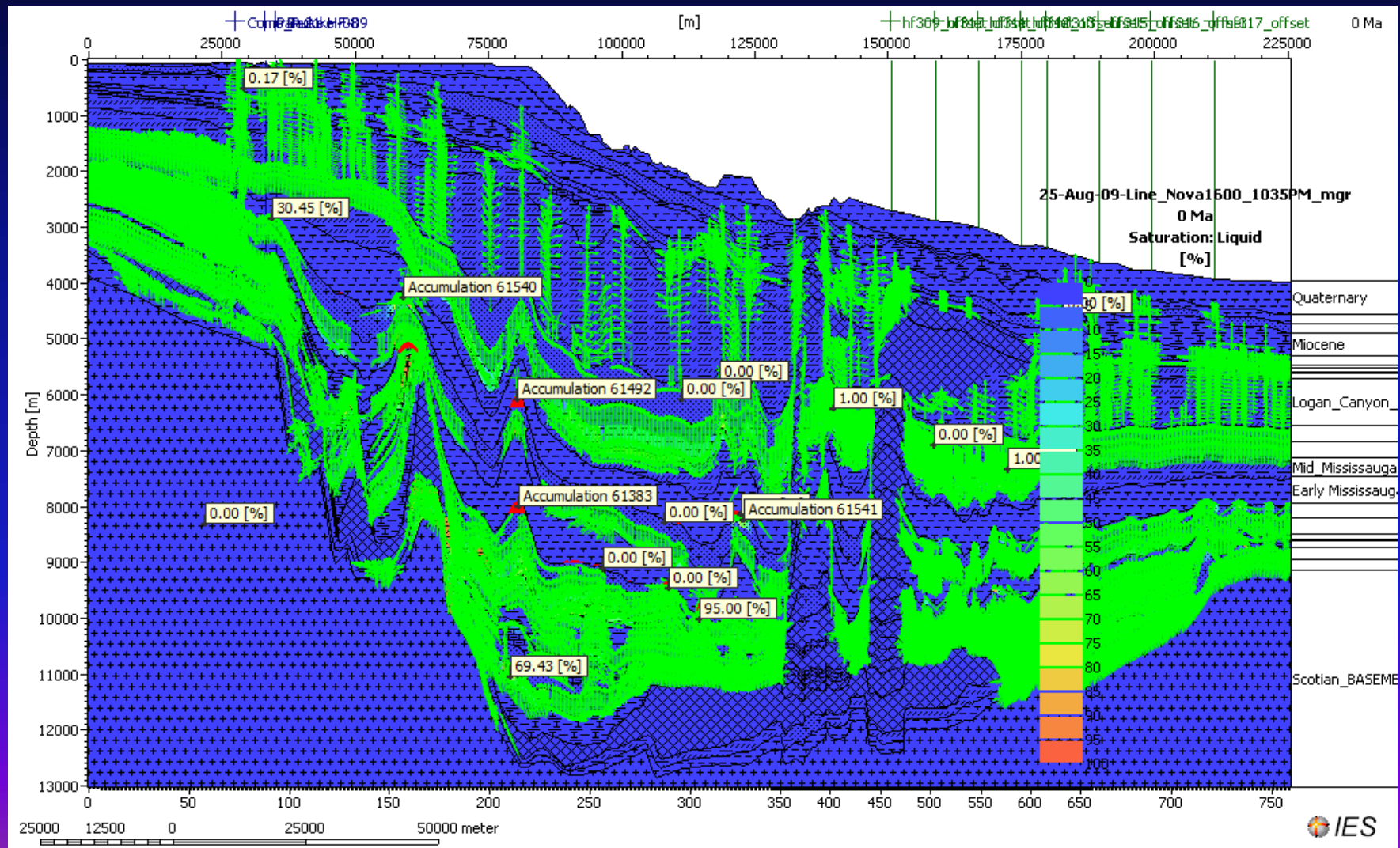
Line 1600- Saturation of Liquids in 5 Ma

Figure 3f-vi



Line 1600- Saturation of Liquids with liquid vectors n present time

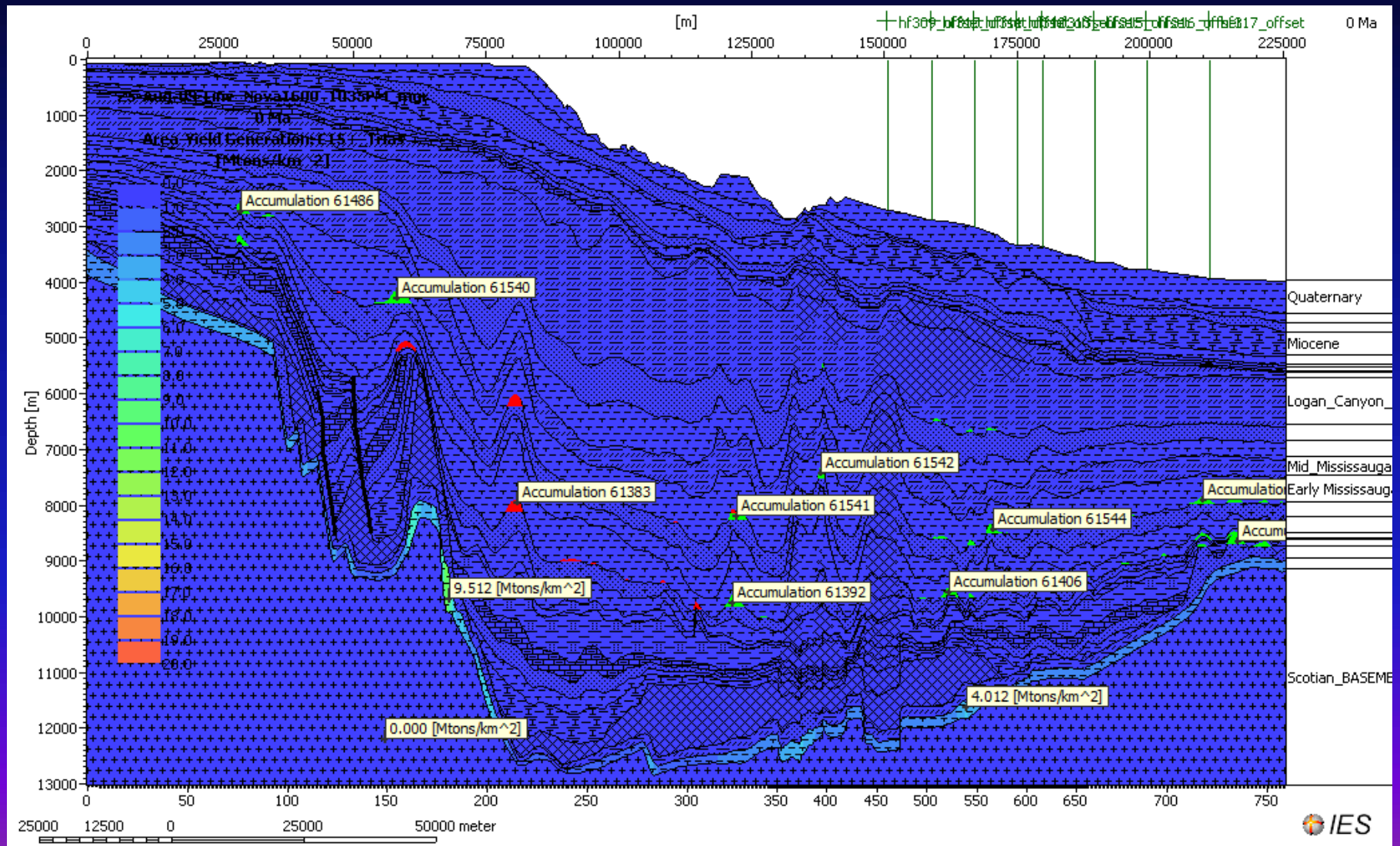
Figure 3f-vii



MASS BALANCE CALCULATION: LINE NOVASPAN 1600

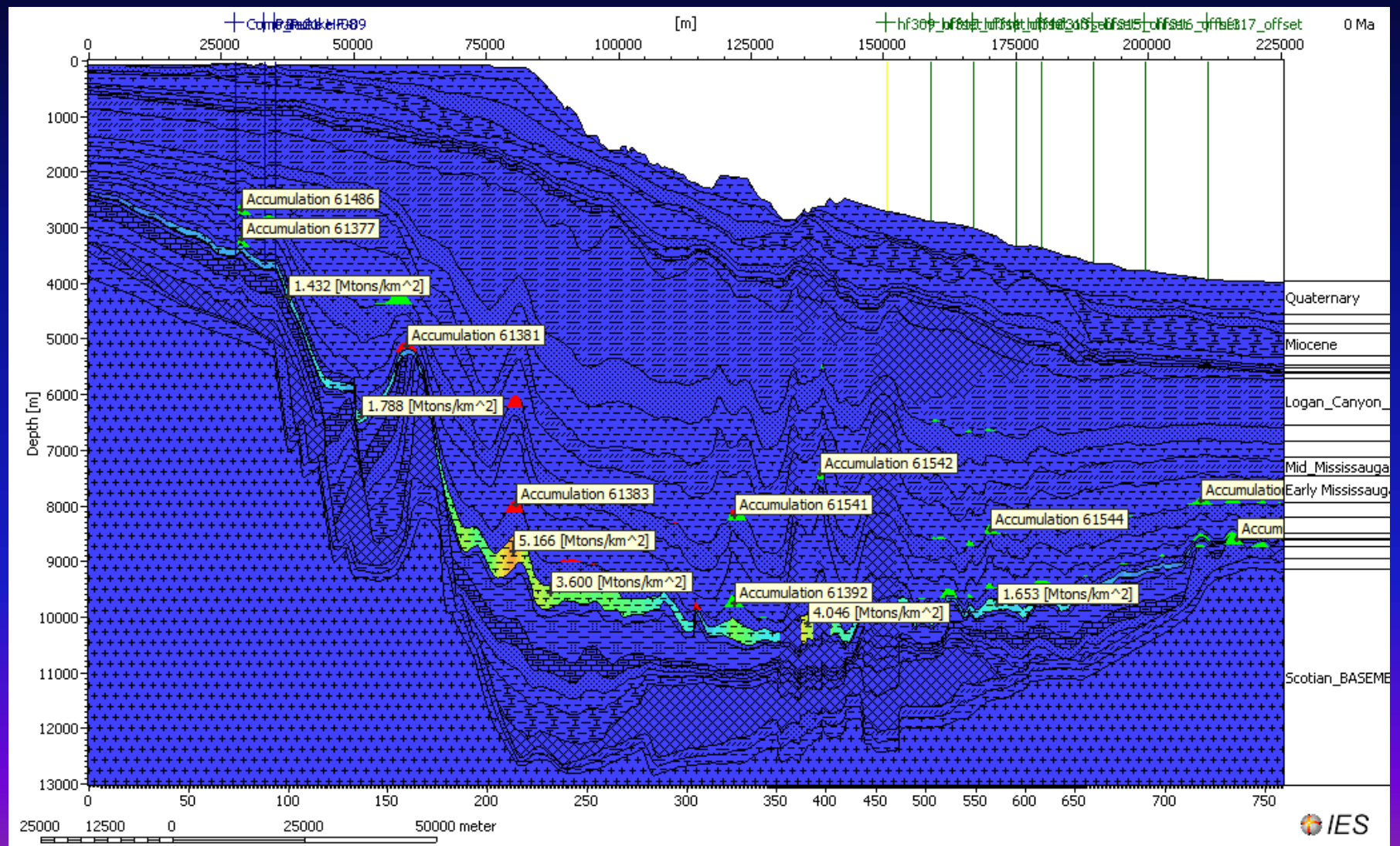
Line 1600 – Amount of hydrocarbon generation along the Late Triassic source Rock

Figure 3g-i



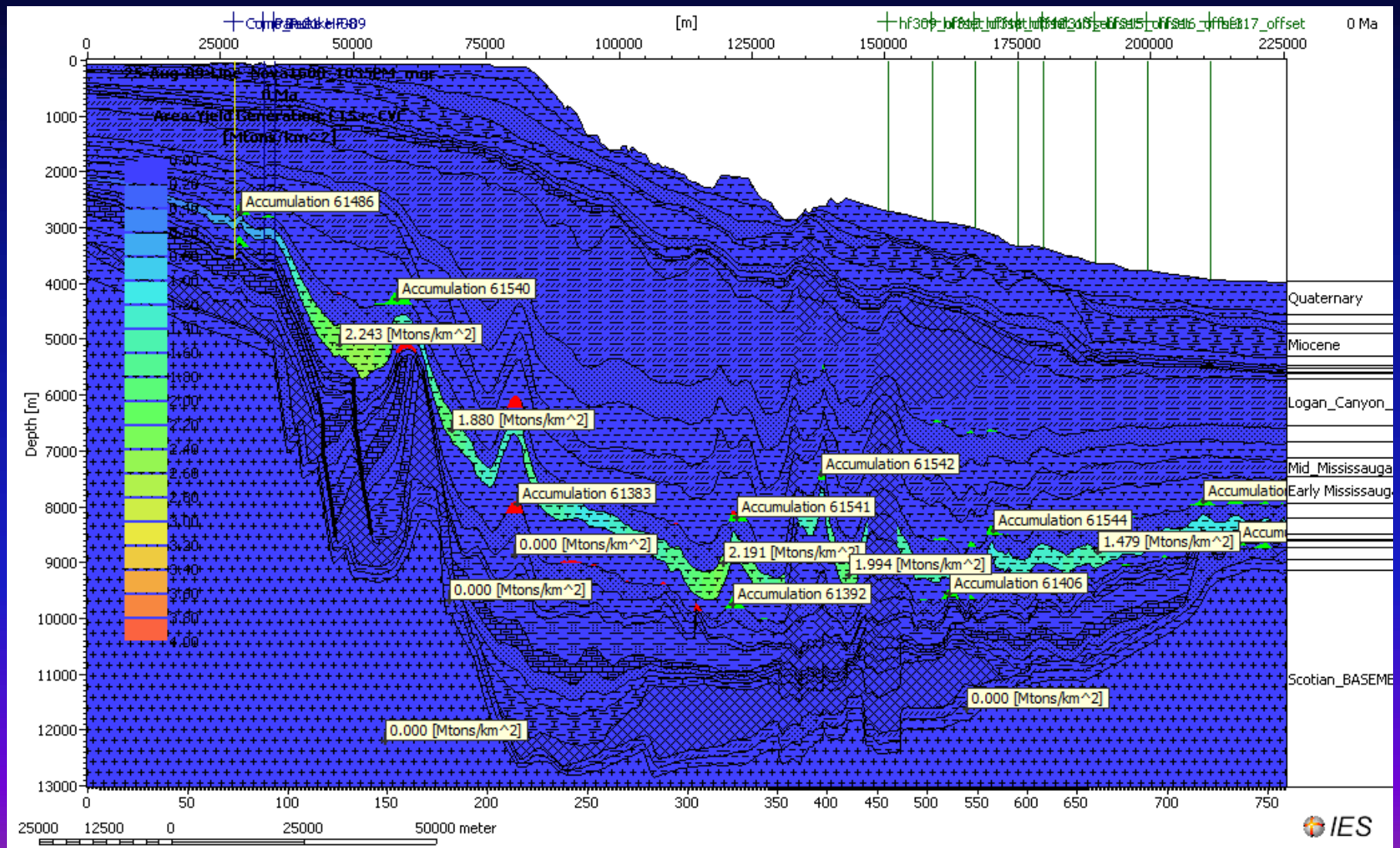
Line 1600: Amount of hydrocarbon generation along the Jurassic Verrill Canyon (JVC) Source Rock

Figure 3g-ii



Line 1600: Amount of hydrocarbon generation along the Cretaceous Verrill Canyon (CVC) Source rock

Figure 3g-iii



Line 1600: Overall mass balance of reservoir hydrocarbons

Info: Only percentages are rounded. Values < 0.005% are displayed as 0.00%!
Volumes/masses calculated for a width of 1 km

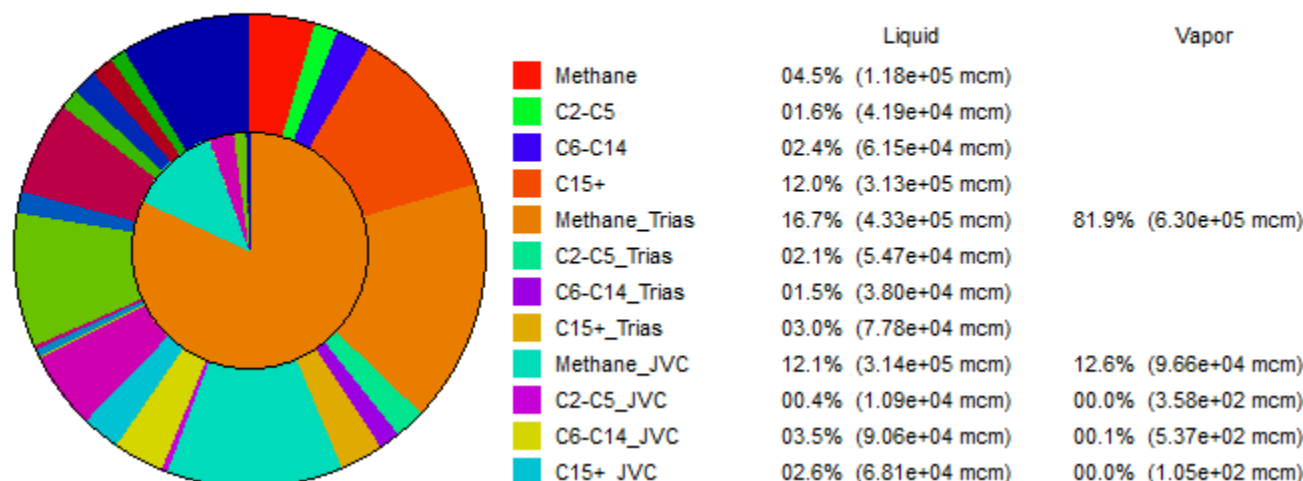
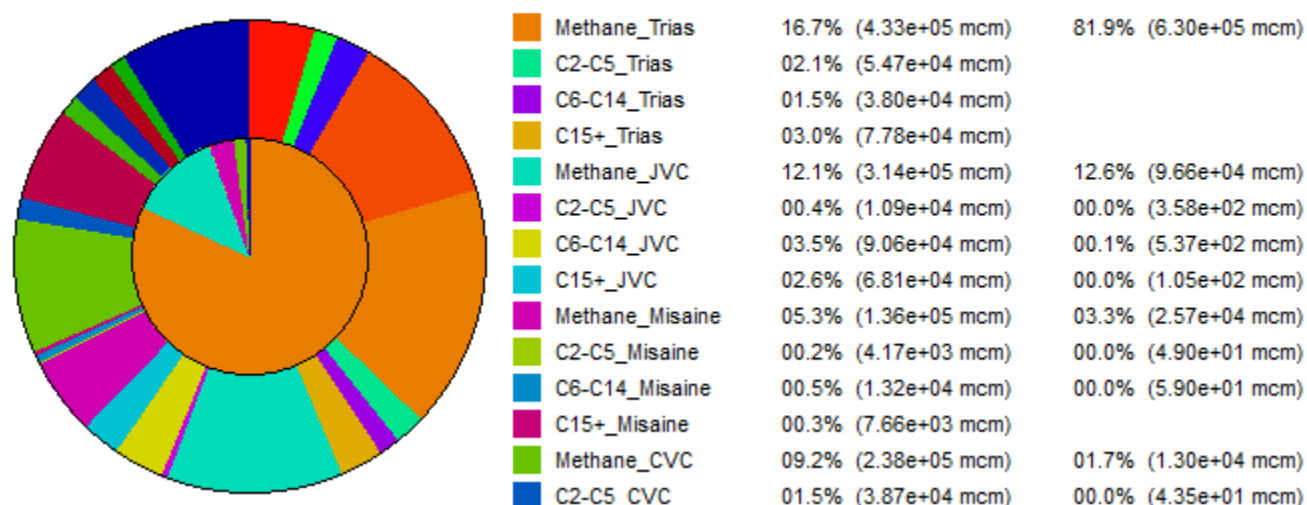


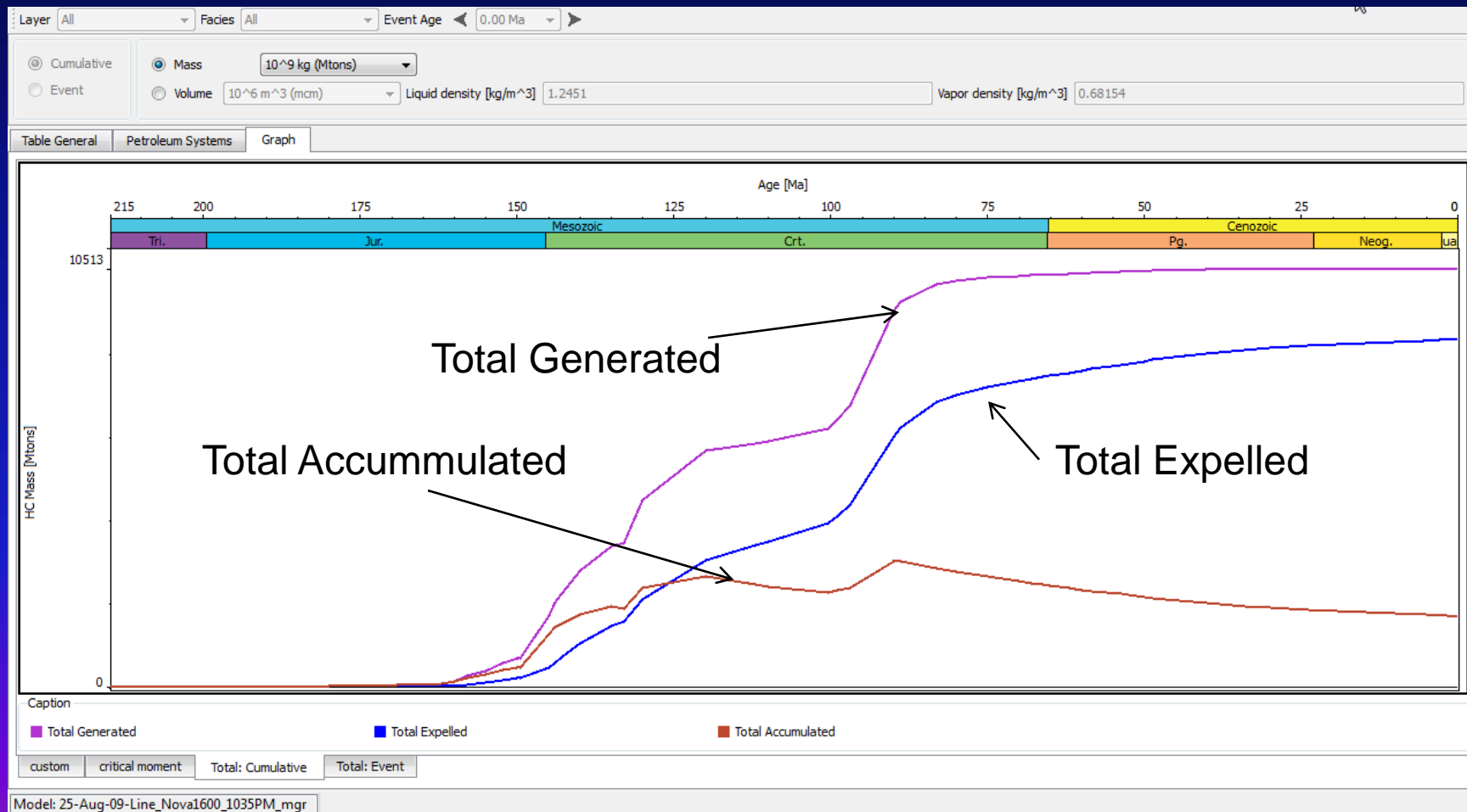
Figure 3h-i

Info: Only percentages are rounded. Values < 0.005% are displayed as 0.00%!
Volumes/masses calculated for a width of 1 km



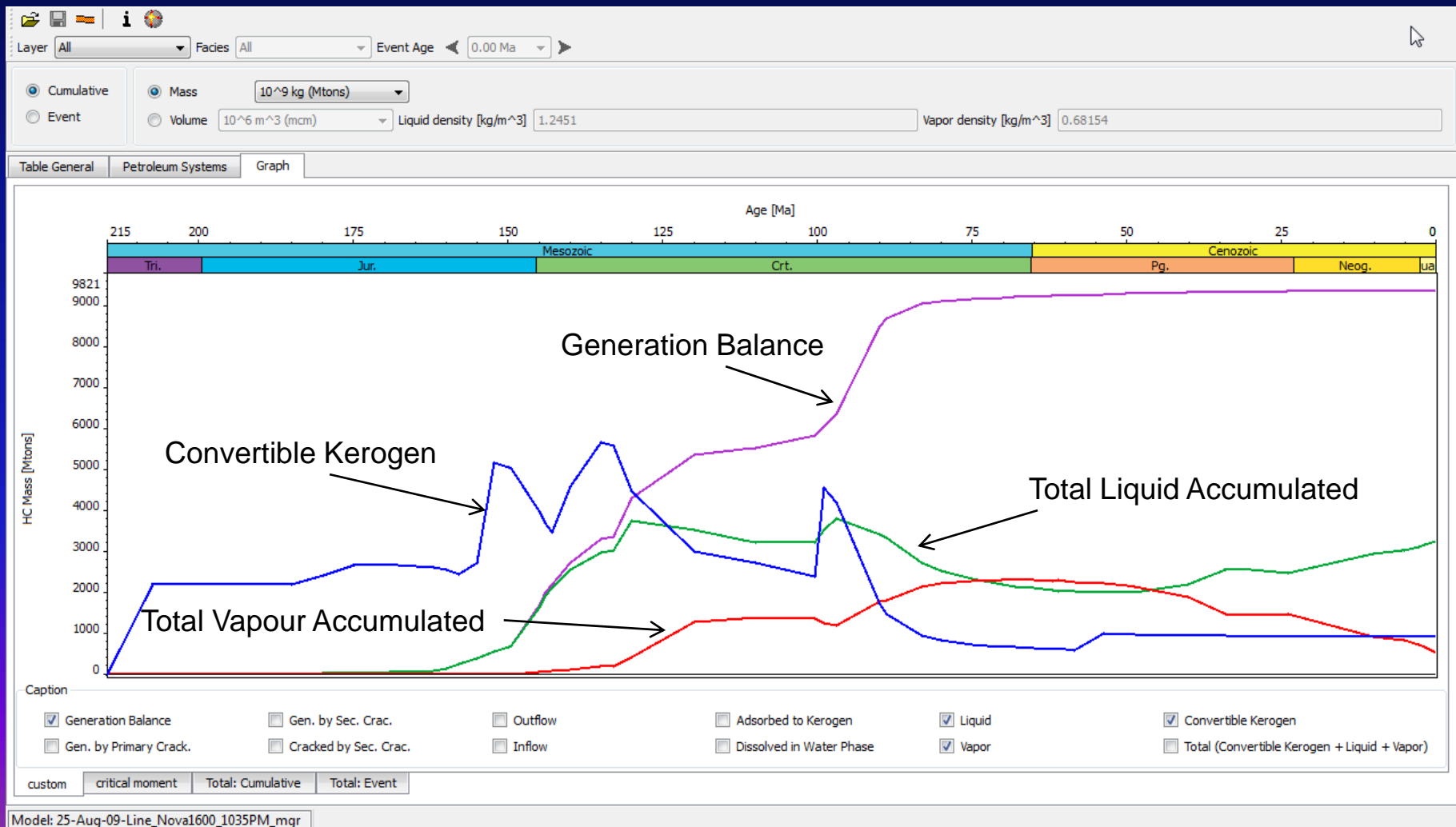
Line 1600: Total HC generated, expelled from various source rocks and accumulated in reservoirs

Figure 3h-ii



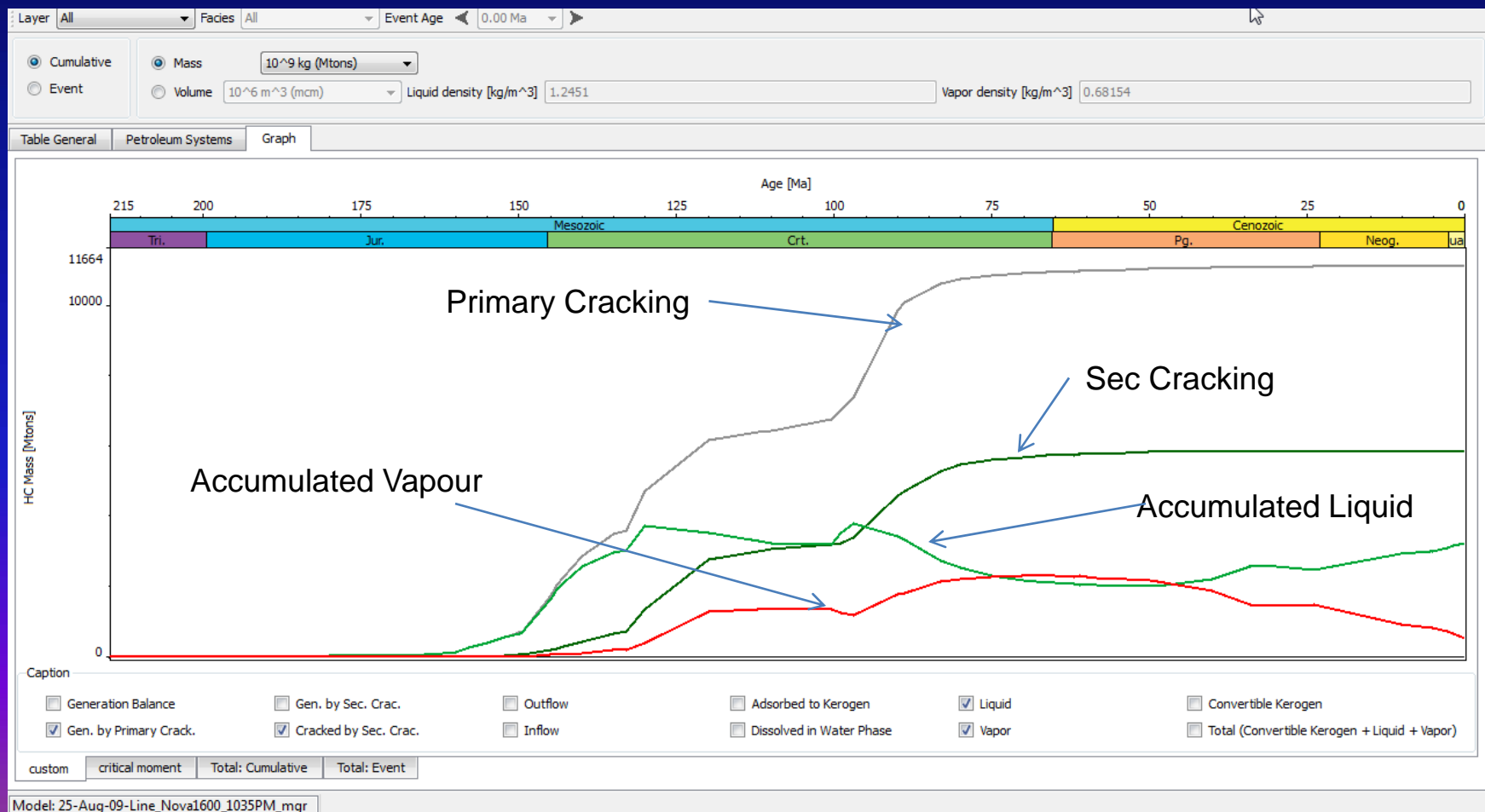
Line 1600: Correlation of generation balance, convertible kerogen, total liquid and total gas accumulated

Figure 3h-iii



Line 1600- Amount of HCs generated from primary and secondary cracking and the amount of liquid and vapour accumulated within various reservoirs

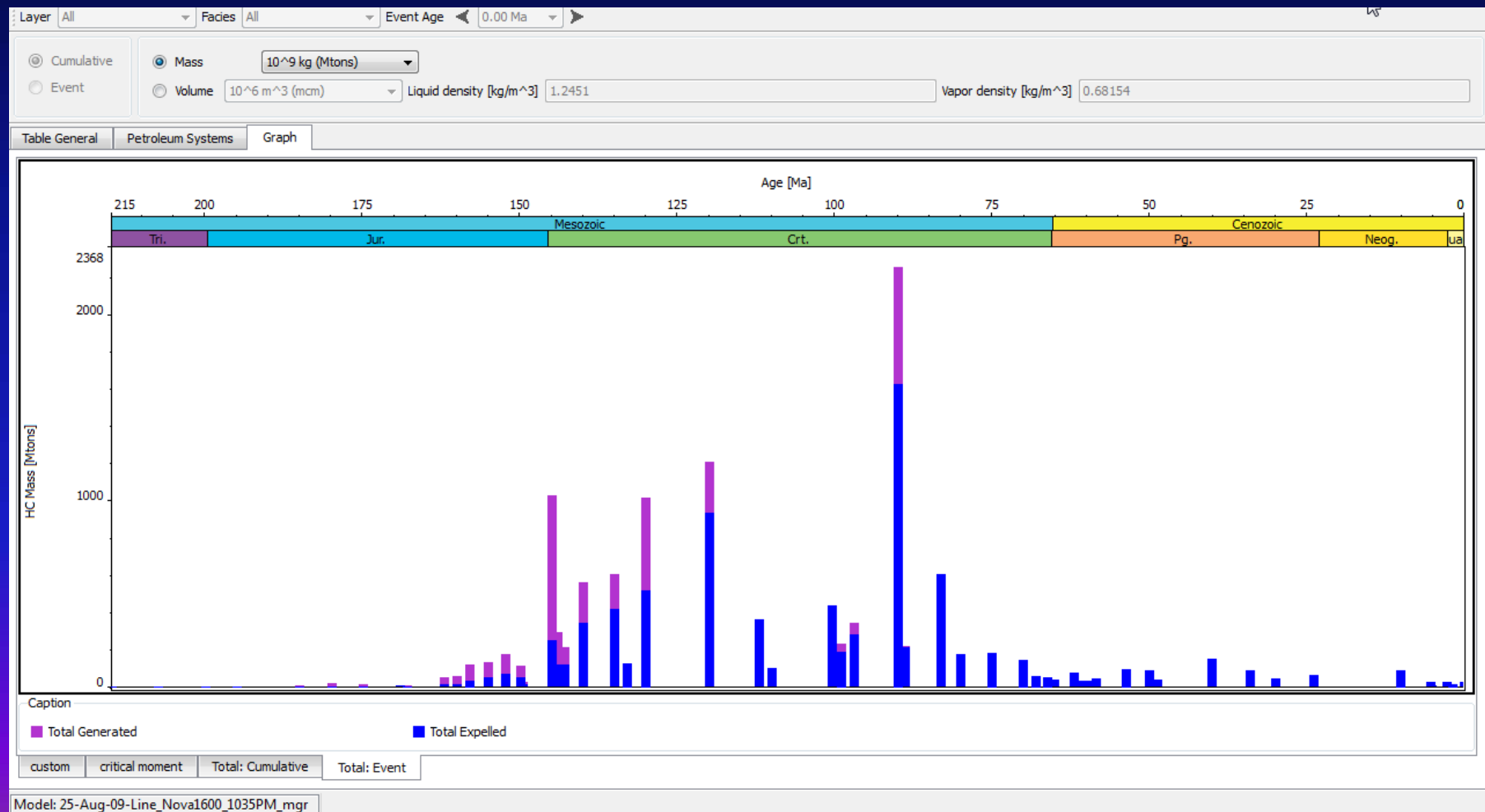
Figure 3h-iv



Line 1600: Petroleum Systems Events Chart

Figure 3h-v

of total generated and expelled HCs



NovaSpan 1600: Conclusion

- The modelled and measured heat flow values have been calibrated as closely as possible changing the transient heat flow trends. With the exception of one value (heat flow line 313), all measured flow values are well calibrated.
- Because the revised model is calibrated with lower heat trends, both Late Jurassic and Early Cretaceous Reservoir in the slope contain a mixture of methane and condensate type of hydrocarbons
- The heat flow values on top of the salt diapir is much hotter compared to the flank of the salt. However, the variation in heat flow values depends on the thickness of the salt diapir and nearness to the surface

Comparative Mass Balance Calculations

Figure 4a

Seismic Line	Total HCs Generated	Source Rock Names
	from SRs	
88-1A	132.3	Middle_Late_Paleocene
	6700.5	Creteceous_Verrill_Canyon
	6374.31	Jurassic_Verrill_Canyon
	1028.3	Misaine
	508.2	Mohican_SR
	4302.7	Late_Tr_Synrift_SR_2
	2164.3	Late_Tr_Synrift_SR_1

Seismic Line	Total HCs Accumulated in Reservoirs	Reservoir Name
88-1A	0.2	Middle_Pliocene
	2599.4	Early_Cretaceous_Reservoir
	895.8	Upper_Jurassic_Reservoir
	212.3	Late_Tr_Synrift_Res_1

Mass Balance of Hydrocarbons: Comparison between Seismic Line 88-1A and 1400

Seismic Line	Total HCs Generated	Source Rock Names
	from SRs	
1400	0.7	Paleocene_Reservoir
	5.9	Middle_Paleocene
	106.5	Cretaceous_VC
	598.3	Jurassic_VerrillCanyon
	367.6	Late_Jurassic
	629.8	Misaine_1
	34.9	Mohican SR
	439.1	E_Jurassic_Lacustrine_SR

Seismic Line	Total HCs Accumulated in Reservoirs	Reservoir Name
1400	6.6	Paleocene_Reservoir
	1.1	Logan_Canyon
	76.3	Early Cretaceous Reservoir
	287.3	Upper_Jurassic_Reservoir

Figure 4b

Seismic Line	Total HCs Generated	Source Rock Names
	from SRs	
1600	0.0	Middle_Late_Paleocene
	2052.0	Logan_Canyon_SR
	3084.8	Creteaceous_Verrill_Canyon
	2343.8	Jurassic_Verrill_Canyon
	231.0	Misaine_SR
	463.2	Mohican_SR
	1837.6	Late_Triassic_Synrift_SR

Mass Balance of Hydrocarbons: Line 1600

Seismic Line	Total HCs Accumulated in Reservoirs	Reservoir Name
1600	42.5	Logan_Canyon_RES
	210.7	Early_Cretaceous_Reservoir
	137.6	Upper_Jurassic_Reservoir
	216.8	Late_Triassic_Synrift_RES

Figure 4c

Mass Balance of Hydrocarbons: Comparison of all Three Seismic Lines

Seismic Line	Total HC Generated from SRs	Total HC Accumulated in Source Rock	Total HC Expelled from SRs	Total HC Accumulated in Reservoirs	Total HC Losses
88-1A	21210.6	3515.93	17694.7	3707.74	13986.9
1400	2182.8	1225.8	956.9	371.5	585.4
1600	10012.4	1658.3	8354.1	607.6	7746.5

2D Waveform Tomography Applied to Long Streamer MCS

Data from the Scotian Slope

Matthias Delescluse^{1*}, Mladen R. Nedimovic² and Keith E. Loudon¹

¹Department of Oceanography, Dalhousie University, Halifax, NS, Canada

²Department of Earth Sciences, Dalhousie University, Halifax, NS, Canada

*Corresponding author. E-mail: mdelescluse@dal.ca

Detailed velocity models of the earth subsurface can be obtained through waveform tomography. The accuracy of the long-wavelength component of such velocity models, which is the background velocity field, is particularly sensitive to modeling low-frequency refracted waves that have long paths through target structures. Thus field examples primarily have focused on the analysis of long-offset wide-angle datasets collected using autonomous receivers, in which refractions arrive at significantly earlier times than reflections. Modern marine acquisition with long streamers now offers the ability to record, both in shallow and deep water, such far offset refracted waves with high spatial density and uniform source. We use 2D MCS data acquired with a 9-km-long streamer over the Scotian Slope in water depths of ~1600 m. The refracted arrivals, although mostly restricted to far offset receivers, provide sufficient information to successfully invert for a high-resolution background velocity field. Using a frequency domain acoustic code over frequencies from 8-24 Hz on two crossing profiles (45 and 30 km long), we detail how the limited refracted waves can constrain the velocity field above the depth of the turning waves (~1.5 km below seafloor). Several important

features are resolved by the waveform velocity model that are not present in the initial travel-time model. In particular, at shallow depth a high velocity layer due to gas hydrates is imaged even where a characteristic BSR is not visible. At greater depth, a strong velocity increase of 300 km/s exists beneath a gently dipping reflector along which low-velocity zones, possibly related to gas, are present. Velocity models are highly consistent at the crossing point between the two profiles. The depth extent of the MCS waveform tomography constrained by refractions could be extended by even longer streamers (e.g. 15 km) or by joint inversion with OBS data.

INTRODUCTION:

Applications of frequency domain 2D acoustic waveform tomography inversion (Pratt and Worthington, 1990; Pratt, 1999) to field seismic data are a few and limited to the two end members of seismic acquisition techniques: (1) long offset wide-angle refraction experiments using individual land or ocean bottom stations (Dessa et al., 2004; Operto et al., 2004; Ravaut et al., 2004; Operto et al., 2006; Bleibinhaus et al., 2007; Bleibinhaus et al., 2009), and (2) high resolution, short streamer marine reflection seismics (Hicks and Pratt, 2001; Shin and Min, 2006; Wang and Rao, 2009). The two cases offer opposite advantages and drawbacks. In the “refraction” case, the validity of the acoustic approximation is questionable, typically limiting the inversion to phase only (Bleibinhaus et al., 2007); while good starting models obtained from traveltimes tomography and low frequencies offer excellent control on the velocity field (Brenders and Pratt, 2007a). In the “reflection” case, small offsets and small-scale targets with

1 simple structures ensure a good validity of the acoustic approximation (Barnes and
2 Charara, 2009; Virieux and Operto, 2009) and the high density of shots and receivers
3 allow very high resolution. However, the background velocity field is not well
4 constrained by reflection waveform tomography and a degree of structural interpretation
5 is necessary to obtain a useful result (Hicks and Pratt, 2001, Wang and Rao, 2009).
6 Although fewer applications to real data have been attempted, reflection seismics is
7 widely used by industry and academic investigators and applicability of the waveform
8 inversion to these datasets should be more studied (a review of industry efforts in
9 applying waveform tomography to field data can be found in Williamson et al., 2010).

10 In this paper, we attempt 2D waveform tomography inversion in frequency
11 domain using a long streamer multichannel seismics (MCS) dataset, which represents an
12 intermediate situation between the two previously cited cases. An earlier attempt to
13 utilize full waveform tomography for long streamer data (Shipp and Singh, 2002) was
14 done in time-space domain but the huge computational cost associated with this method
15 required severe decimation of the input data thus limiting the results.

16 The 2D MCS data with 9 km long streamer acquired on the Scotian Slope (Figure
17 1) and used in this study include refracted waves arriving earlier than the seafloor
18 reflection and later than the direct wave (Figure 2). These waves constrain the
19 background velocity field above their turning depth, while the simple, slowly varying
20 sedimentary environment (Figure 1) minimizes the limitation with the acoustic
21 approximation. This configuration is then likely to combine the strengths of both
22 "reflection" and "refraction" cases of waveform inversion while limiting their drawbacks.
23 We first present the dataset and then describe the preconditioning and inversion strategy.
24 Finally, we discuss the results in terms of limitations of the waveform tomography

method applied to MCS data, possible targets of MCS waveform tomography, and additional information it can provide when compared to a prestack depth migration image.

DATA PRECONDITIONING

Data and Geometry

SHOTS

We use two crossing sections of the Novaspan profiles (lines 1400 and 5300, see Figure 1) acquired by Ion-GXT in 2003. The streamer is composed of 360 receiver groups with 25 m spacing. The shot spacing is 50 m. For the investigated 44 km-long section of the strike Line 5300, we use 231 shots spaced every 150 m (every third shot) and all receivers. For the crossing 29 km-long section of the dip Line 1400, we use 196 shots spaced every 100 m (every second shot) and all receivers. Although 94 m is the ideal spacing to avoid aliasing for our lowest frequency available (8 Hz, and $D_{\text{samp}} = V_{\text{min}}/(2f)$), Brenders and Pratt (2007a) have shown that the sampling theory criterion may be too conservative (see Table 1 for a summary of the sampling of different synthetic and real survey configurations). In practice, our shot domain decimation, undertaken for computing reasons, does not seem to affect our results for the tested frequencies (8 to 24Hz).

RECEIVERS

Feathering of the streamer is limited to a maximum 10 degrees angle, but is generally less. The nominal geometry implies a 170 m minimum offset for the first receiver and consequently a 9145 m maximum offset for receiver 360. However, streamer bending also occurs which shortens the effective maximum offset to an average of 8966 m. To fully take into account the effects of feathering and bending is equivalent to the definition of 83,160 receivers positions for line 5300 (and 70,560 receivers positions for line 1400) and would require 3D codes. Considering the resulting requirement for computer memory and the fact that we need to approximate our geometry to a 2D straight line, we choose to define fixed receivers positions with constant spacing, that will be re-used by different shots. For each shot, only 360 fixed receivers will be active (see sketch on Figure 2). Although the average maximum offset length is only shortened by 2%, this is a very sensitive parameter for both traveltimes and waveform tomography and it is crucial to take this shortening into account. In this respect, focusing on short sections of profiles helps to avoid changes in the geometry approximation due to water currents variations. In our case, an average 24.5 m spacing between receivers is always a good approximation. Finally, for line 5300, the 83,160 independent receiver positions are reduced to 1768 fixed positions (Figure 2).

Amplitudes

The average seafloor depth of the investigated profiles is ~1600 m, which means that multiples are not a problem (Figure 1) because they arrive later than the turning waves and therefore beneath the region where the velocity is constrained (Brenders and Pratt, 2007c). Thus, no multiple attenuation is applied.

Amplitude corrections, however, must be applied, since the observed data are acquired with a point source, corresponding to a 3D geometrical spreading of the acoustic energy, while the acoustic forward modeling code is 2D and assumes a line source with cylindrical spreading. In the near offset domain and for horizontal layers, a simple correction can be applied as a function of $V_{rms}(t) * t^{1/2}$ (Wang and Rao, 2009), or more simply just \sqrt{t} (Hicks and Pratt, 2001). However, our case cannot be considered as a near offset approximation. A simple solution (Ursin, 1990) is to apply an offset dependent correction $(V_{rms}(t) * (t^2 + x^2 / V_{rms}(t)^2)^{1/4})$ where x is the offset) after NMO adjustment to normal incidence traveltimes followed by reverse NMO. In previous large-offset studies, refraction amplitudes are adjusted to the initial smooth forward model (Brenders and Pratt, 2007b). For our dataset, however, this method would also destroy the relative variation of the refraction amplitudes along the profile, which would result in a loss of information.

STARTING MODEL

Seismic source

Once the raw data have been processed to correspond to the 2D acoustic code approximation, the next step is to find a correct initial velocity field in which the modeled first reflection and refraction waves arrive within half a cycle of the observed data at the lowest frequency available (i.e. 8 Hz). If the half-wavelength criterion is not respected, cycle skipping will occur and the waveform inversion will diverge. To obtain the initial forward model, a source wavelet is necessary. Previous studies using frequency domain

1 waveform tomography (Pratt, 1999) usually estimate the source wavelet by solving a
2 linear inverse problem progressively updating the source to fit the data from an initial
3 estimation. This approach is efficient when refraction arrivals are clearly separated from
4 the reflections. In our case, the reflectivity causes a problem. The initial model does not
5 include any reflector except a weak seafloor. Shallow sub-seafloor reflections from the
6 data cannot be correlated with the forward model, which invalidates the method. We
7 consider that the refraction events in our data are limited and not sufficiently correct in
8 terms of amplitude variations in the forward model. Consequently, we use a synthetic
9 source modeled for the 32 airguns, 4258 cu. in. array geometry used during the
10 acquisition (Figure 3). Our tests show that the modeled wavelet has practically the same
11 frequency spectrum as the data (see Figure 3B). We also know that there are no gun
12 malfunction or pressure variation during the acquisition, which yields a constant signal
13 strength from shot to shot.

14 15 *NMO, depth migration and traveltime tomography starting velocity models*

16

17 The two forward models computed using the velocity fields from NMO stack and
18 prestack depth migration fail to produce refracted arrival times within half a cycle of the
19 observed data. Both velocity models are similar and too slow (Figure 4a) and therefore
20 the modeled arrivals are too late (Figure 5a).

21 Starting with the depth migration velocity field, we next use traveltime
22 tomography to obtain a new velocity field (Figure 4b), modeling only the refracted
23 arrivals at far offset. We use the FAST code (Zelt and Barton, 1998), which has been
24 modified to account for direct waves arriving before the refracted arrivals. For this

situation, virtual sources are placed at the seafloor to divide the problem in two parts and bypass the direct paths in the water column (Canales et al., 2008). The resulting velocity field now qualifies as a starting model for waveform tomography as the modeled arrivals now respect the half cycle criterion (Figure 5b). The new starting model includes a velocity increase relative to the initial model of 0-50 m/s in the top 1 km below the seafloor and 50-150 m/s at depths (between 1 and 1.5 km below seafloor) where the refracted rays turn.

INVERSION STRATEGY

Frequency domain inversion

We use the frequency domain waveform tomography approach of Pratt and Worthington (1990) and Pratt (1999). This method is computationally efficient as the data are manipulated in frequency domain and are utilized progressively from lower to higher frequencies. This incremental frequency strategy also helps overcome the non-linearity of the wavefield inversion. The frequency bandwidth is limited by the lowest frequency in the dataset (8 Hz) and also by the size of the forward model grid. The finite difference forward model code needs 4 nodes per spatial wavelength for a 95% accuracy (Brenders and Pratt, 2007b). For the inversion to run within a reasonable computing time (i.e. <24 hours), we limit our velocity grid size to a 3020x333 dimension, which corresponds to a 15 m spacing (45 km x 5 km). The lowest velocity being 1500 m/s, 4 nodes correspond to a $1500 \text{ m/s} / 60 \text{ m} = 25 \text{ Hz}$ maximum frequency. Because structures

are seen through different incident angles, one frequency illuminates a range of spatial wavenumbers (Sirgue and Pratt, 2004), which means that a small number of frequencies cover a continuous range of spatial wavenumbers. With a 9 km streamer, this “efficient waveform tomography” strategy (Sirgue and Pratt, 2004, Brenders and Pratt, 2007a) would result in the use of only 4 frequencies in our 8-25 Hz data. However, real data are noisy and, although the Ion-GXT dataset has a good signal to noise ratio, more frequencies are necessary to create some overlap in the spatial wavenumber coverage and avoid noise artifacts. In our case, 9 frequencies are used from 8 to 24 Hz with a 2 Hz step.

Reflectivity

In an effort to limit the weight of reflections in the inversion, we ignore the 160 first traces of each shot gather and only consider the 200 receivers from offsets of 4 to 9 km. The weight of near offset reflections is high in the inversion gradient, although only poor velocity information exists. The high amplitudes of the near offset sea-bottom reflection are also unlikely to be correctly modeled by the 2D acoustic code (Hicks and Pratt, 2001). The limited frequency bandwidth of the inversion also does not result in a physically meaningful reflectivity image. Even with a higher frequency inversion, the interpretation of reflectivity-related velocity variations are doubtful because impedance contrasts are not the result of variations in velocity alone. We therefore favor the long wavelength, background component of the velocity model by limiting the inversion to only two iterations per frequency. Too many iterations would over-fit the reflectivity, thus emphasizing the short wavelength component without improving the longer wavelength velocity field.

1 The results of the phase and amplitude inversion for line 5300 are shown in
2 Figures 6 and 7. The results for line 1400 are displayed in Figure 8. The velocities at the
3 crossing between the two lines are in very good agreement (Figure 8). The next section
4 will discuss those results in terms of comparison with the migrated section, and the
5 validity of the acoustic approximation in this specific sedimentary environment.

6 7 **DISCUSSION**

8 9 *Interpretation of the results and comparison with the migrated section*

10 11 *LINE 5300:*

12 Figure 6 shows the result of our inversion for line 5300 derived using 9
13 frequencies and a total of 18 iterations. Several significant features are now derived that
14 did not exist in the initial, smooth velocity model from traveltimes tomography. First, a
15 velocity contrast appears around 2 km depth. On the migrated section (Figure 6), it
16 clearly corresponds to the Bottom Simulating Reflector (BSR) visible at the same depth
17 between 5 km and 8 km. A BSR marks the thermal stability limit of gas hydrates, which
18 can trap some free gas underneath. As a result, a velocity inversion is expected to follow
19 the seafloor shape, as hydrates have the effect of increasing velocity (Leblanc et al.,
20 2007) whereas gas lowers it. This is exactly what happens between 5 km and 8 km of line
21 5300 where the velocity drops almost by 200 m/s. Of particular interest is that this low
22 velocity layer continues eastward where the depth image does not show a clear BSR. The
23 contrast between those two velocity zones gradually decreases towards the east (compare

1 velocity profiles A,B,C in Figure 6), but it is still detected by the waveform tomography
2 image.

3 Deeper information can also be extracted from this new velocity field. The gently
4 dipping reflector around 2.4 km depth acts as the ~2000 m/s limit and the sediments
5 below it have a much faster velocity than in the migration velocity field. This is the depth
6 where the refracted rays turn. In the western half of the profile, this dipping reflector has
7 a strong amplitude. In the waveform tomography image, it corresponds to a low velocity
8 zone above it (see velocity profile B, LVZ on Figure 6). The 2.9-km-deep discontinuous
9 reflector is imaged as a low velocity boundary, except towards its eastern extremity
10 where it is imaged as a high velocity (velocity profile C on Figure 6). In general, lower
11 velocities are present to the west of the profile and shallower, higher velocities emerge to
12 the east.

13 On the shot gathers (Figure 7), this lateral evolution is visible with a clear, long
14 refraction event for the western shot gathers (corresponding to profile A) and a later
15 refraction event, with slightly higher velocity (deeper, more compacted high velocity
16 sediments?) for the eastern shot gathers (corresponding to profiles B and C). Lower
17 refraction amplitudes on shot gather B correspond to the low velocity region (Figure 6)
18 just above the 2.4 km deep, high amplitude reflector. The general trend of the cross-over
19 between reflection and refraction phases also varies laterally and is quite closely matched
20 by the inversion. Contrary to traveltimes tomography, waveform tomography is able to use
21 refraction waves even when they are not the first arrival. The extent of the available
22 refraction information can be seen in the starting velocity forward model (Green wiggles
23 in Figure 5).

24

1 LINE 1400:

2
3 Figure 8 shows the result of the same inversion strategy for the crossing profile
4 1400. Fewer shots are available but the crossing point with line 5300 is well imaged and
5 the velocity at that position can be compared on both profiles. The two profiles show
6 nearly identical velocity variations. The high and low velocity contrast corresponding to
7 the gas hydrates stability limit is also present toward the landward part of the profile with
8 the low velocity layer gradually diminishing seaward. Some reflectors cross that high
9 velocity layer between 26 and 35 km, which indicates that this high velocity follows the
10 seafloor and not the lithology (Figure 8). The 2.3-km-deep reflector is also the ~2000 m/s
11 isovelocity limit on this profile. Finally, the 2.9-km-deep reflector is also related to a high
12 velocity at the crossing point, although this same reflector corresponds to a lower
13 velocity just further north. Some dipping artifacts are visible on this profile because the
14 depth of the turning waves varies laterally as a consequence of the non flat bathymetry
15 (Figure 8).

16
17 *Phase and amplitude inversions and the applicability of acoustic waveform*
18 *tomography to long-streamer MCS data.*

19
20 Using long streamer data means using reflection arrivals near or beyond the
21 critical angle, with potentially important P-to-S wave conversions at far offsets. The
22 acoustic code we use does not take into account the energy lost by S-wave conversions
23 and the use of the amplitude information could be affected. It is thus important to check
24 that our results are not significantly impacted by this limitation.

1 To assess the effect of S-wave conversions in our specific marine sedimentary
2 environment, we calculate two forward models (Figure 10) of a shot gather in a 1D
3 velocity model corresponding to profile B (Figure 6). This profile has been chosen
4 because two velocity inversions are present, which represent the most complex features
5 in the section. The first forward model is a purely acoustic response, whereas the second
6 is the acoustic response including P-S conversions (Fuchs and Mueller 1971, Kennett,
7 1974). While we acknowledge that lateral variations of the velocity field could increase
8 P-S conversions, in our case, we are very close to a 1D situation. This area of the Scotian
9 slope is composed of a thick (~ 7km), Triassic to Quaternary, post-rift sedimentary
10 section. The upper two kilometers, covered by our investigations, are composed of
11 interbedded horizontal layers of prodeltaic mudstone, claystone and siltstone deposited
12 since the Miocene as a result of different events such as the late Tertiary sea-level
13 lowstands (Piper and Normark, 1989; Leblanc et al, 2007). Recent mud depositions from
14 the last interglacial period (12 ka, Mosher et al., 1994) were cored and show soft, water
15 saturated seafloor properties ($V_p=1530\pm20$ m/s, $\text{density}=1680\pm50$ Mg/m³; Leblanc et al.,
16 2007).

17 These aspects are compatible with the use of high Poisson's ratios (0.49 at the
18 seafloor to 0.41 at 1km depth, Hamilton, 1979) to determine the S-wave velocity used in
19 the 1D forward model. The difference between the two forward models (Figure 10) is not
20 significant and establishes the applicability of the acoustic waveform tomography to this
21 dataset, corresponding to a smooth S-wave velocity field (Barnes and Charara 2009).

22 When these conditions are not met, this type of test is very useful to determine what part
23 of the wavefield cannot be used for phase plus amplitude inversion. In general, first
24 refraction arrivals have a small incident angle and thus can often be used if there are no

1 strong lateral variations of attenuation, which is a potential problem with OBS datasets
2 (Bleibinhaus et al., 2007,2009), since long profiles may cross very different geological
3 terrains.

4 Figure 9 shows the phase only inversion of Line 5300, with all other parameters
5 unchanged. Comparison with the phase plus amplitude inversion shows a large
6 improvement of the result relative to phase only, which is a another validation of the
7 acoustic approximation in our specific case. We are confident that unmodeled parameters
8 (small lateral variations, higher S-wave velocity contrasts at the BSR) do not significantly
9 impact the validity of the acoustic approximation. Comparing the forward modeled
10 wavefields in the “phase” and “phase plus amplitude” waveform inverted velocities
11 (Figure 7) shows a much better fit of the refraction event when using the amplitude
12 information. This improvement of the modeled wavefield corresponds to a clear
13 improvement of the velocity contrast below the hydrate layer (see difference field in
14 Figure 9) and a much more detailed image in general.

16 CONCLUSIONS

18 Waveform tomography applied to MCS data is a promising imaging method when
19 used in a suitable environment. The relatively high starting frequency (~8 Hz) and the
20 limited weight of the refractions in the dataset require a good starting velocity model for
21 a successful inversion. A more complex environment, with all other parameters
22 unchanged, could potentially limit the ability to determine a successful starting velocity
23 model. Longer refracted wavepaths through the target structures would overcome this
24 problem and depending on the velocity structure itself, the refracted waves would then

1 turn at a greater depth. Using a longer streamer (e.g. 15 km) or modeling structures in
2 shallower water depths could help to extend the depth of the inversion, although in the
3 second case the multiple reflections would interfere. Joint inversion of MCS and OBS
4 data would then be the most robust solution to obtain a refraction-based high-resolution
5 velocity model at all depths imaged by the MCS reflection method. OBS data, through
6 the use of lower frequencies and more robust traveltimes inversions, could also cover the
7 low wavenumbers we might miss by using high starting frequencies of the MCS data,
8 even above the depth of the turning waves.

9 In the meantime, the use of MCS waveform tomography appears to be adapted
10 best to studies of shallow sediment such as the characterization of gas hydrate structures.
11 The high resolution background velocity field helps to interpret a low amplitude reflector
12 as the continuation of a strong and well defined BSR. For deeper reflectors, it associates
13 the main sedimentary units to characteristic velocities and detects velocity inversions
14 down to the depth limit of the turning waves (Figure 6).

17 **ACKNOWLEDGMENTS**

18
19 We thank Ion-GXT for use of the NovaSPAN seismic dataset. David Mosher
20 (Geological Survey of Canada, Atlantic Division) kindly allowed us to use the Gundalf©
21 source modeling software. Velocity figures are prepared with GMT software (Wessel and
22 Smith, 1995) and shot gathers are displayed with Paradigm Focus© software.

24 **REFERENCES**

- 1
2 Barnes, C., and Charara, M., 2009. The domain of applicability of acoustic full-waveform
3 inversion for marine seismic data. *Geophysics*, **74(6)**, WCC91-WCC103
- 4 Bleibinhaus, F., Hole, J.A., Ryberg, T., and Guys, G.S., 2007. Structure of the California
5 Coast Ranges and San Andreas Fault at SAFOD from seismic waveform inversion
6 and reflection imaging. *J. Geophys. Res.*, **112**, B06315
- 7 Bleibinhaus, F., Lester, R.W., and Hole, J.A., 2009. Applying waveform tomography to
8 wide-angle seismic surveys. *Tectonophysics*, **472 (1-4)**, 238-248.
- 9 Brenders, A.J., and Pratt, R.G., 2007a. Efficient waveform tomography for lithospheric
10 imaging: implications for realistic, two dimensional acquisition geometries and
11 low-frequency data. *Geophys. J. Int.*, **168**, 152-170.
- 12 Brenders, A.J., and Pratt, R.G., 2007b. Full waveform tomography for lithospheric
13 imaging: results from a blind test in a realistic crustal model. *Geophys. J. Int.*,
14 **168**, 133-151.
- 15 Brenders, A.J., and Pratt, R.G., 2007c. Waveform tomography of marine seismic data:
16 What can limited offset offer? 75th Annual International Meeting, SEG, Expanded
17 Abstracts, **26**, 3024-3029.
- 18 Canales, J. P., B. E. Tucholke, M. Xu, J. A. Collins, and D. DuBois, 2008. Seismic
19 evidence for large-scale compositional heterogeneity of oceanic core complexes,
20 *Geochem., Geophys., Geosyst.* **9**, Q08002, doi:10.1029/2008GC002009
- 21 Dessa, J.-X., Operto, S., Kodaira, S., Nakanishi, A., Pascal. G., Virieux, J., and Kaneda,
22 Y., 2004. Multiscale seismic imaging of the eastern Nankai trough by full
23 waveform inversion. *Geophys. Res. Lett.*, **31**, L18606
- 24 Hamilton, E. L., 1979. Vp/Vs and Poisson's ratios in marine sediments and rocks. *J.*

- 1 *Acoust. Soc. Am.*, **66(4)**, 1093-1101.
- 2 Fuchs, K., and Mueller, G., 1971. Computation of synthetic seismograms by the
- 3 reflectivity method and comparison with observations. *GJRS*, **23**, pp. 417-433
- 4 Hicks, G., and Pratt, R.G., 2001. Reflection waveform inversion using local descent
- 5 methods: Estimating attenuation and velocity over a gas sand deposit. *Geophysics*,
- 6 **66**, 770-780.
- 7 Kennett, B.L.N., 1974. Reflections, rays and reverberations. *Bulletin of the Seismological*
- 8 *Society of America*, 564, 1685-1696
- 9 LeBlanc, C., Louden, K. and Mosher, D., 2007. Gas hydrates off Eastern Canada:
- 10 Velocity models from wide-angle seismic profiles on the Scotian Slope. *Marine*
- 11 *and Petroleum Geology*, **24(5)**, 321-335.
- 12 Mosher, D.C., Moran K., and Hiscott, R.N., 1994. Late Quaternary sediment, sediment
- 13 mass-flow processes and slope stability on the Scotian Slope, *Sedimentology* **41**,
- 14 pp. 1039–1061
- 15 Operto, S., Ravaut, C., Improta, L., Virieux, J., Herrero, A., and Dell'Aversana, P., 2004.
- 16 Quantitative imaging of complex structures from dense wide-aperture seismic
- 17 data by multiscale traveltime and waveform inversions: a case study. *Geophysical*
- 18 *Prospecting*, **52**, 625-651.
- 19 Operto, S., Virieux, J., Dassa, J.X., and Pascal, G., 2006. Crustal seismic imaging from
- 20 multifold ocean bottom seismometer data by frequency domain full waveform
- 21 tomography: Application to the eastern Nankai trough. *J. Geophys. Res.*, **111**,
- 22 B09306
- 23 Piper, D. J. W., and Normark, W. R., 1989. Late Cenozoic sea-level changes and the
- 24 onset of glaciation: impact on continental slope progradation off eastern Canada,

- 1 *Marine Petroleum and Geology*, **6**, pp. 336–348.
- 2 Pratt, R.G., 1999. Seismic waveform inversion in the frequency domain, Part 1: Theory
3 and verification in a physical scale model. *Geophysics*, **64**, 888-901.
- 4 Pratt, R.G. And Worthington, M.H., 1990. Inverse theory applied to multi-source cross-
5 hole tomography. Part I: Acoustic wave-equation method. *Geophysical*
6 *Prospecting*, **38**, 287-310.
- 7 Ravaut, C., Operto, S., Imbrota, L., Virieux, J., Herrero, A., and Dell'Aversana, P., 2004.
8 Multiscale imaging of complex structures from multifold wide-aperture seismic
9 data by frequency-domain full-waveform tomography: application to a thrust belt.
10 *Geophys. J. Int.*, **159**, 1032-1056.
- 11 Shin, C., and Min, D-J., 2006. Waveform inversion using a logarithmic wavefield.
12 *Geophysics*, **71(3)**, R31-R42.
- 13 Shipp, R.M., and Singh, S.C., 2002. Two-dimensional full wavefield inversion of wide-
14 aperture marine seismic streamer data. *Geophy. J. Int.*, **151**, 325-344.
- 15 Sirgue, L., and Pratt, R.G., 2004. Efficient waveform inversion and imaging: A strategy
16 for selecting temporal frequencies. *Geophysics*, **60**, 1870-1874.
- 17 Ursin, 1990. Offset-dependent geometrical spreading in a layered medium. *Geophysics*,
18 **55(4)**, 492-496.
- 19 Virieux, J., and Operto, S., 2009. An overview of full-waveform inversion in exploration
20 geophysics. *Geophysics*, **74(6)**, WCC1-WCC26
- 21 Wang, Y. and Rao, Y., 2009. Reflection seismic waveform tomography. *Journal of*
22 *Geophysical research*, **114**, B03304.
- 23 Wessel, P. and Smith, W.H.F., 1995. New version of the Generic Mapping Tool released,
24 EOS Trans. AGU, **329**.

Williamson, P., Wang, B., Bevc, B., and Jones, I., 2010. Full Wave-equation methods for complex imaging challenges. *The Leading Edge*, **29**(3), pp. 264-268

Zelt, C.A., and Barton, P.J., 1998. 3D seismic refraction tomography: A comparison of two methods applied to data from the Feroe Basin. *Journal of Geophysical Research*, **103**, 7187-7210.

LIST OF FIGURES AND TABLES:

Table 1:

Aliasing number $N_a = 2D_{\text{samp}} * f / V_{\text{min}}$ (where D_{samp} is the source or receiver interval and V_{min} the minimum velocity in the model) in a selection of studies involving different real and synthetic datasets. An aliasing number higher than 1 theoretically produces some aliasing. In practice, inversion results can be satisfying with sparser sampling (Brender and Pratt, 2007b).

Study	Data	Geometry	V_{min} (m/s)	D_{samp} (m)	f (Hz)	N_a
Hicks and Pratt (2001)	real	reflection	1560	12.5	10-60	0.16-1
Operto et al. (2006)	real	refraction	2000	1000	3-15	3-15
Sirgue and Pratt (2004)	synthetic	refraction	1500	100	5-10	0.7-1.3
Ravaut et al. (2006)	real	refraction	2000	90	5.4-20	0.5-1.8
Brenders and Pratt (2007b)	synthetic	refraction	4000	5000	0.8-7	2-18
Bleibinhaus et al. (2009) @ SAF	real	refraction	2000	500-1000	3-14	1.5-14
Bleibinhaus et al. (2009) @ CBI	real	refraction	1500	1000	3-16	4-21
This study L5300	real	MCS	1500	150	8-24	1.6-4.8
This study L1400	real	MCS	1500	100	8-24	1.1-3.2

1

2 *Figure 1:* Location of the Novaspan 2D lines acquired by GXT in 2003 on the Scotian
3 slope using a 9-km-long streamer (dashed lines). The crossing red sections of lines 5300
4 and 1400 are used in this study. White areas represent salt. The seismic profile is a stack
5 section of Line 5300 where seafloor multiples are visible (M). Turning depth of the
6 recorded refraction waves is around 3.5 s TWTT.

7

8 *Figure 2:* (a) Sketch of the streamer geometry in relation with the fixed receiver array.
9 The active receivers for shot 116 are indicated in red. (b) Example of the frequency
10 domain data in a shot-receiver space: the 24 Hz component of the data is displayed and
11 the red dashed line indicates the 24 Hz component of shot 116 for all 360 traces. For each
12 shots, non active receivers have a zero component. (c) Shot gather 116 corresponding to
13 the positions above. Refracted arrivals arriving before the seafloor reflection are indicated
14 as well as the first multiple of the seafloor (M).

15

16

17 *Figure 3:* (a) Modeled source wavelet using Gundalf © software. (b) Frequency
18 spectrums of the field data (red) and of the modeled source wavelet (black).

19

20 *Figure 4:* Starting velocity models for the full waveform tomography. (a) Smoothed
21 prestack depth migration velocity field for line 5300 and (b) the starting velocity model
22 obtained after traveltome tomography. Traveltome tomography updates the velocity only
23 in the highlighted area indicating limited depth penetration as constrained by the 9-km-
24 long streamer. Positions A, B and C approximately correspond to shot gathers displayed

1 in Figure 5.

2
3 Figure 5: Shot gathers corresponding to the positions A, B, C in Figure 4. The wavefields
4 are displayed for every 4th trace with a 2 km/s reduced velocity. Real data is in black and
5 the forward model is in green; common areas are in red, even when the phases are wrong.
6 The modeled refractions arrive too late in the migration velocity case (a). For clarity and
7 homogeneity with the next figures, we display a 8-25 Hz wavefield, and although the
8 match with the far offset refraction arrival is not perfect at 25 Hz for shots A and B, the
9 model clearly fits the data within half a cycle at 8 Hz after traveltimes tomography (b).
10 The seafloor reflection very weak in the models because the velocities are smooth, which
11 makes the part of the refraction event arriving after the seafloor more visible.

12
13 *Figure 6:* Waveform tomography velocity model for GXT line 5300 (top) using 9
14 frequencies (range 8-24 Hz with 2 Hz step). The prestack depth migrated reflection image
15 (bottom) is displayed for comparison. The BSR reflector is visible at 2 km depth between
16 distances of 5-8 km. Red curves show velocity versus depth at three specific locations
17 (A,B,C). These locations correspond to the shot gathers on Figure 7. Position C is the
18 crossing point with profile 1400 (see Figure 9). Shaded areas are not covered by the
19 refracted rays recorded on the 9 km-long streamer. Notice the visible polygonal fault in
20 the waveform velocity model. G. H. indicates the gas hydrates layer (high velocity)
21 below which low velocity free gas is trapped. The high amplitudes at 2.4 km depth on the
22 prestack depth migration profile correspond to the low velocity zone (LVZ) above the
23 reflector in the velocity model.

Figure 7: Observed (black) and modeled (green) shot gathers ($f_{\max}=25$ Hz). The refracted waves on these shot gathers turn approximately at positions A, B and C of Figure 6. Areas where the model and the data agree are shown in red. The wavefields are displayed with a 2 km/s reduced velocity. Shaded receivers for nearest offsets (0-4 km) are not used in the inversion. Only every 4th trace is displayed. Shot gathers on the left (a) are modeled in the phase only waveform velocity model (Figure 9a) and shot gathers on the right (b) are modeled in the phase plus amplitude waveform velocity model (Figure 6 and 9b). Notice how even the phase of the refracted arrivals at far offset are improved by the addition of the amplitudes in the inversion (shots A and B).

Figure 8: (a) Waveform tomography velocity model for GXT line 1400 using 9 frequencies (range 8-24 Hz with 2 Hz step) superimposed on the prestack depth migrated reflection image. Shaded areas are not covered by the refracted rays recorded on the 9 km-long streamer. Dipping artifacts are visible between 25 and 35 km just above the shaded area limit (stars, see text). (b) Velocity at the crossing point C with line 5300 (Figure 6). The NMO (blue), migration (green), traveltime tomography (orange) and waveform tomography velocities for lines 1400 (black) and 5300 (red) are displayed. Note the excellent agreement between the waveform models.

Figure 9: Velocity models after phase only inversion (a) and phase plus amplitude inversion (b). Prestack depth migration profiles are superimposed. The difference field (c) between the two results of the inversions emphasizes how crucial the amplitude information is to retrieve the velocity inversion at the weak BSR. Positions A, B and C approximately correspond to shot gathers displayed on Figure 7.

1

2 Figure 10: Acoustic synthetic shot gather (gray) forward modeled in a 1D velocity model
3 corresponding to profile B in Figure 6. The red wiggles are the difference field between
4 the purely acoustic case and the acoustic part of the full seismic case including S wave
5 conversion at the horizontal layer interfaces. The part of the wavefield where the
6 difference is noticeable, but not significant, is contoured. The critical angle for the
7 seafloor is 74 degrees using velocities and densities derived from cores, corresponding to
8 an offset of 11 km.

9

10

11

12

13

14

15

16

17

18

19

20

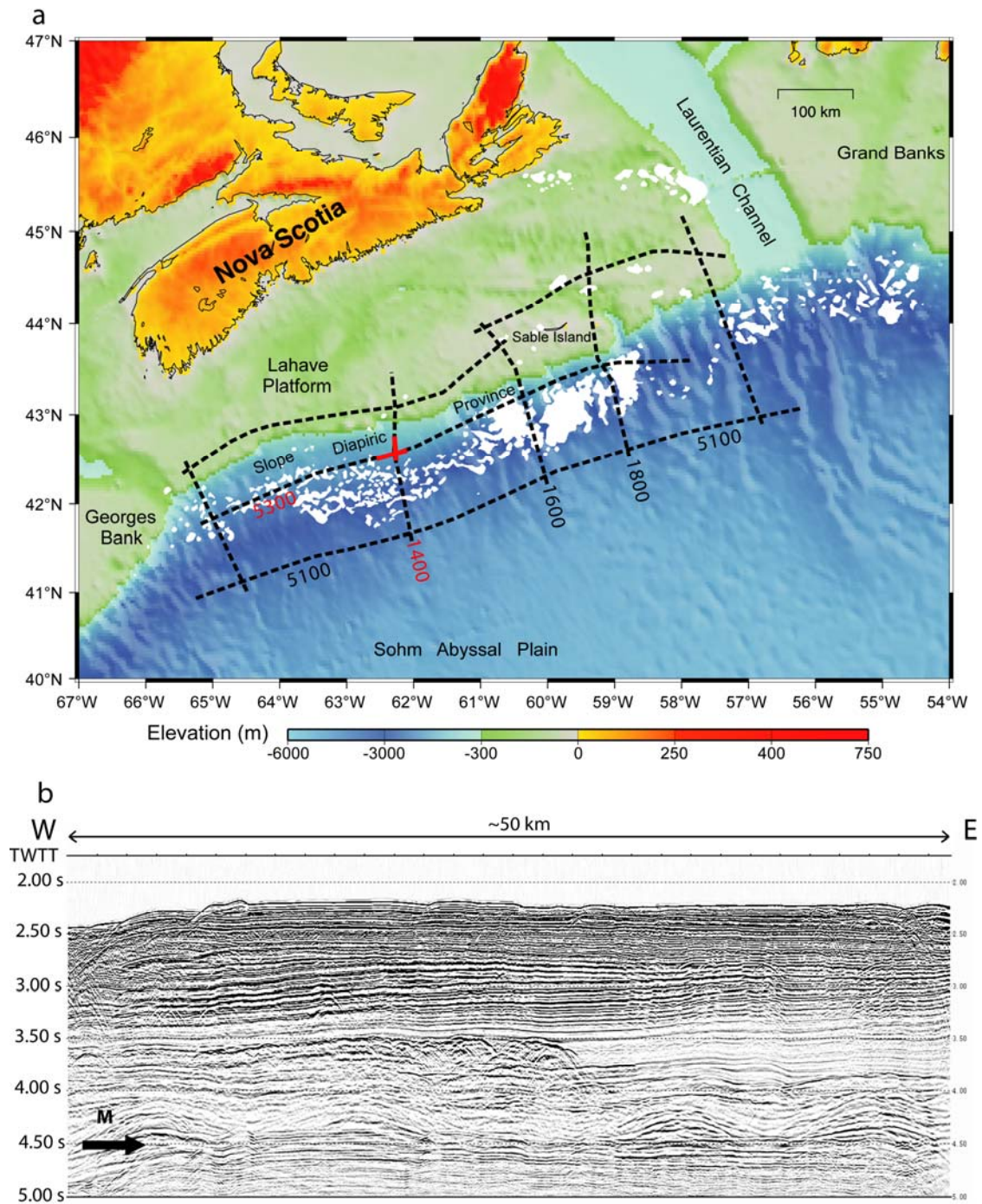
21

22

23

24

1 FIGURES



2

3 Figure 1

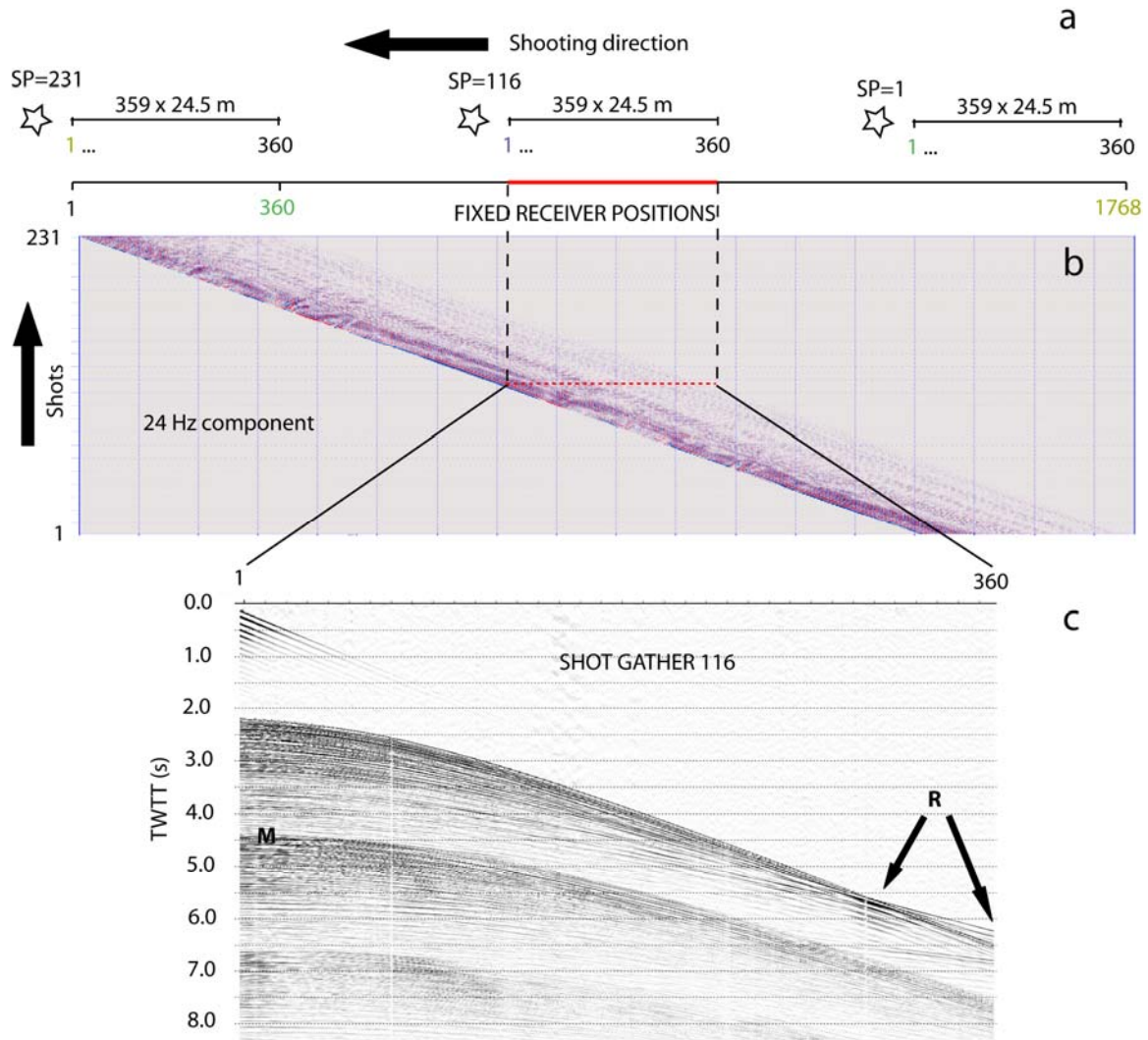
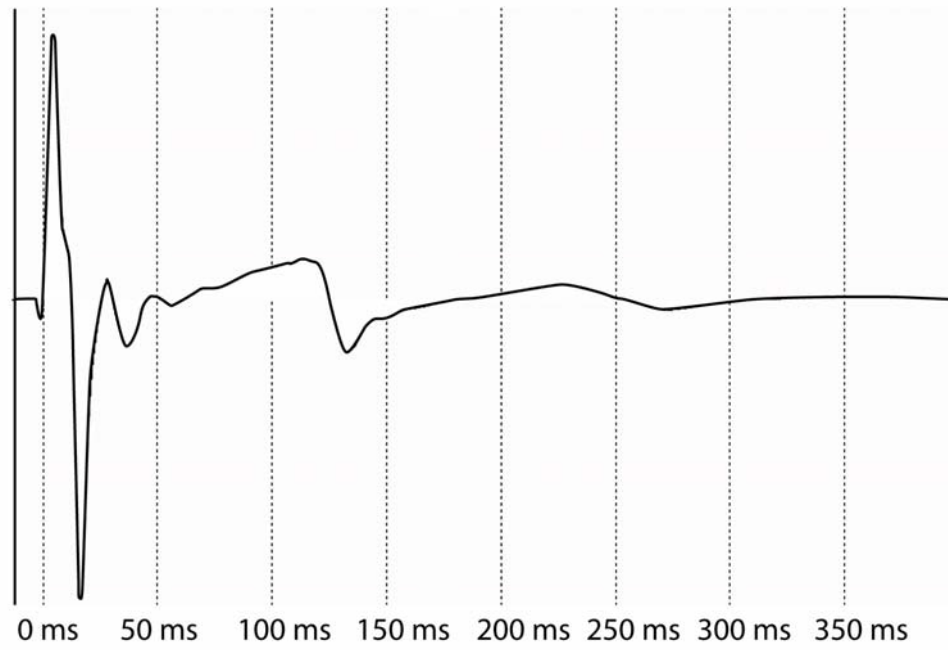
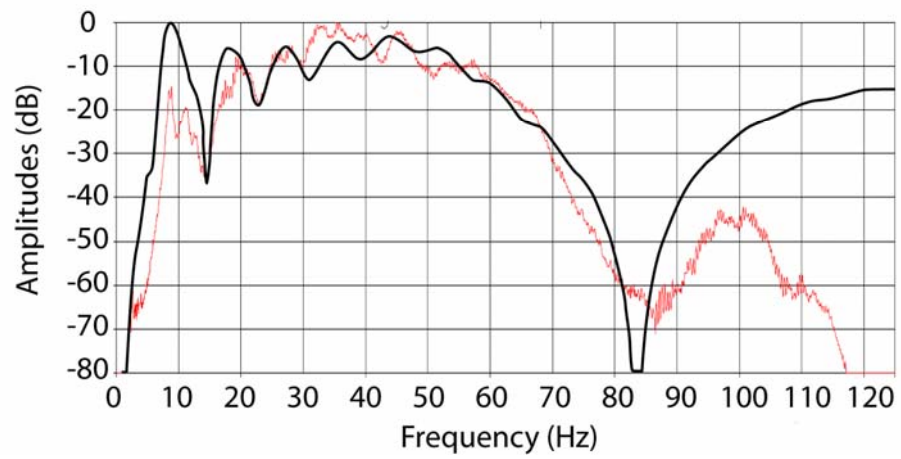


Figure 2

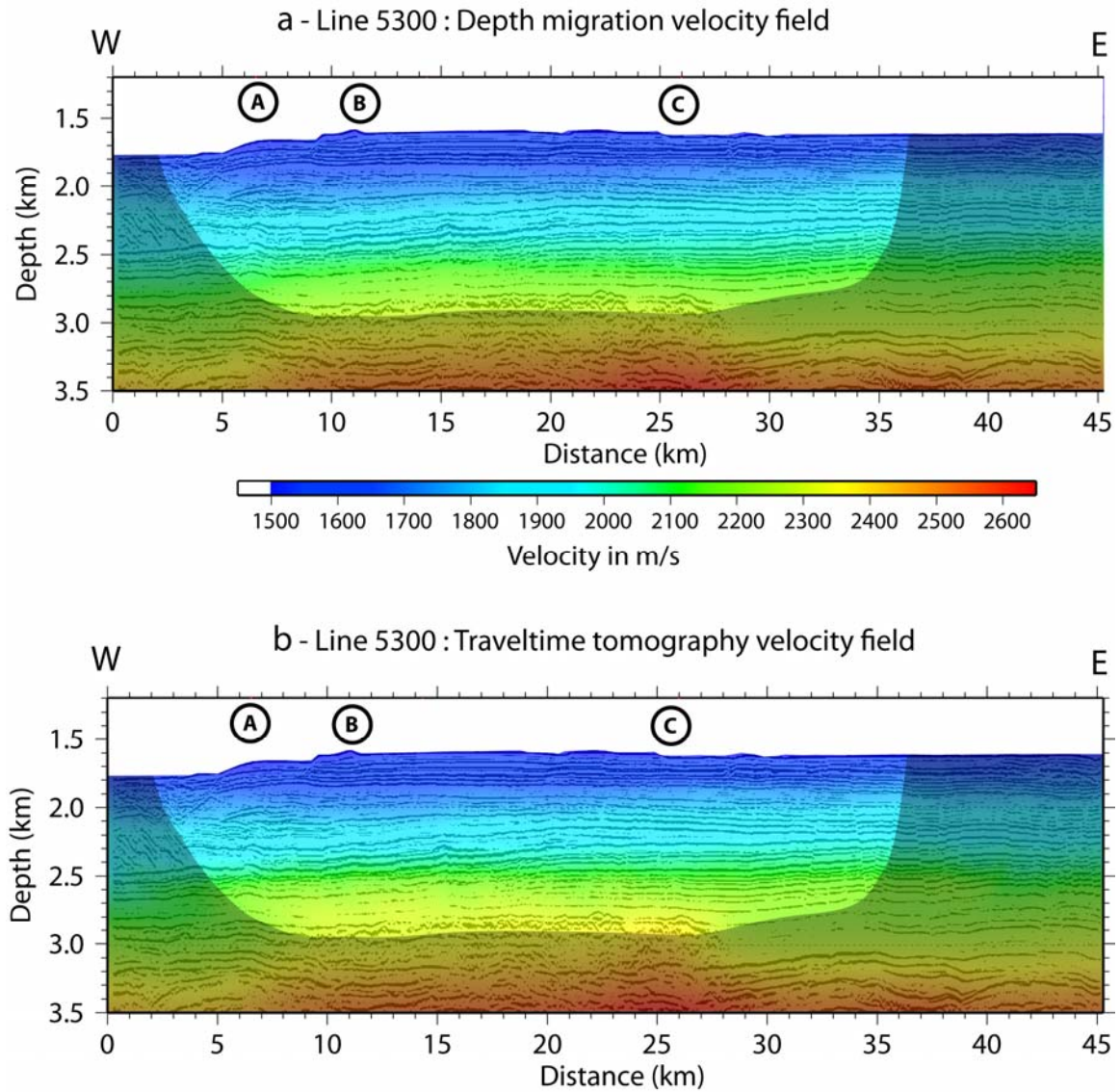
a - MODELED SOURCE WAVELET**b - DATA & SOURCE FREQUENCY SPECTRUMS**

1

2

3 *Figure 3*

4



1

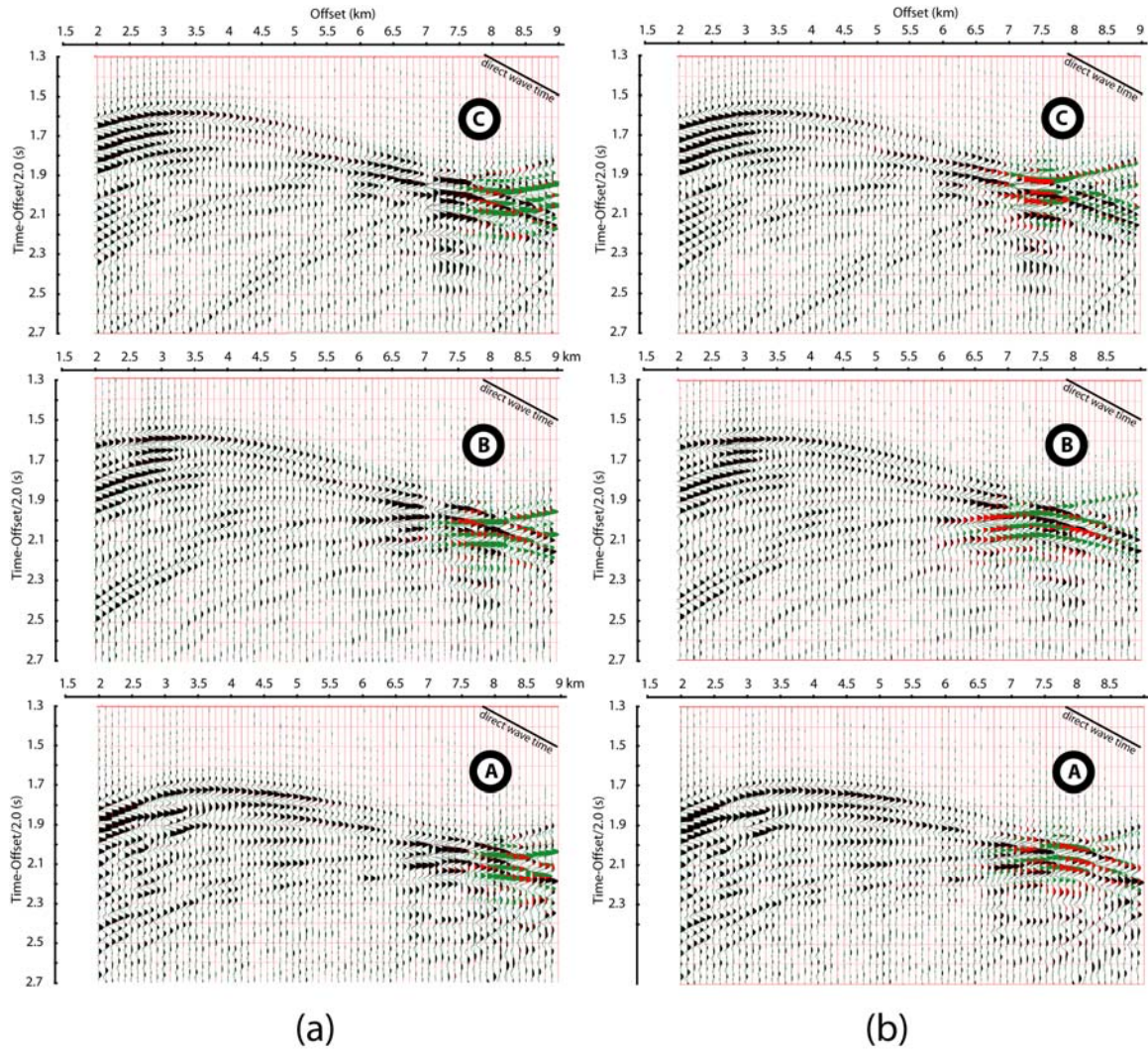
2 *Figure 4*

3

4

5

6



1
2
3
4
5
6
7

Figure 5

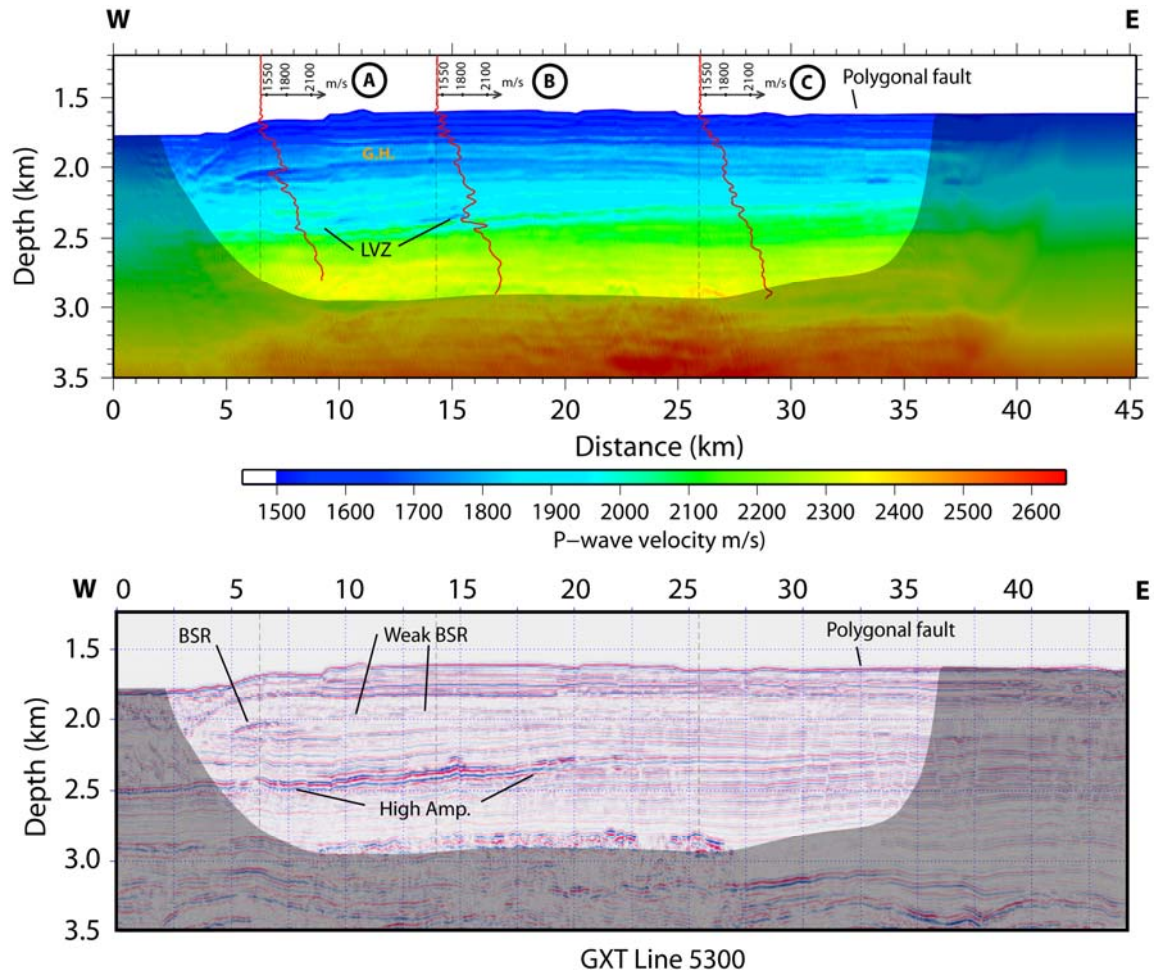


Figure 6

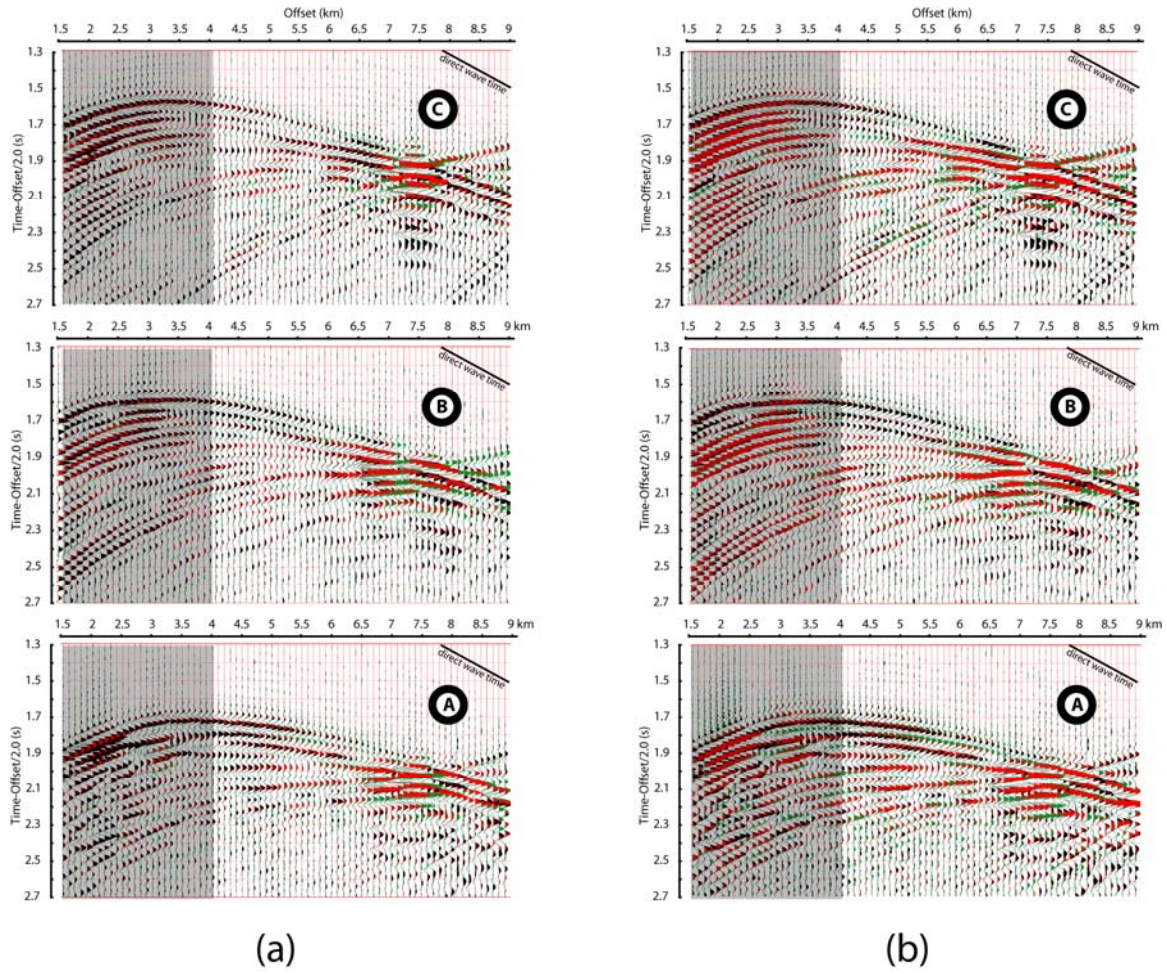


Figure 7

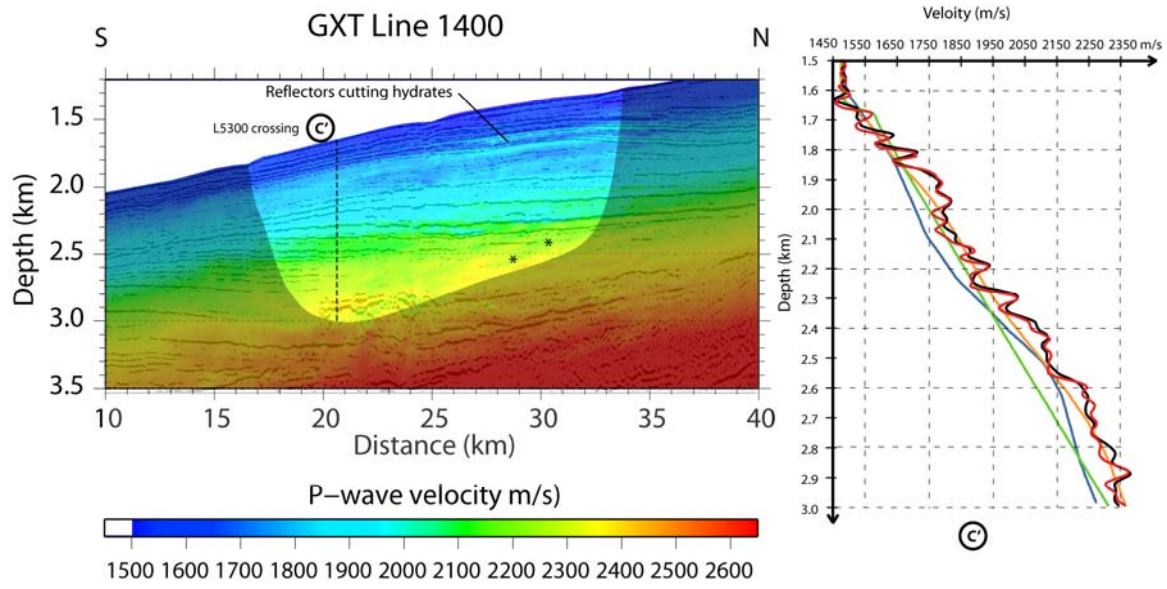
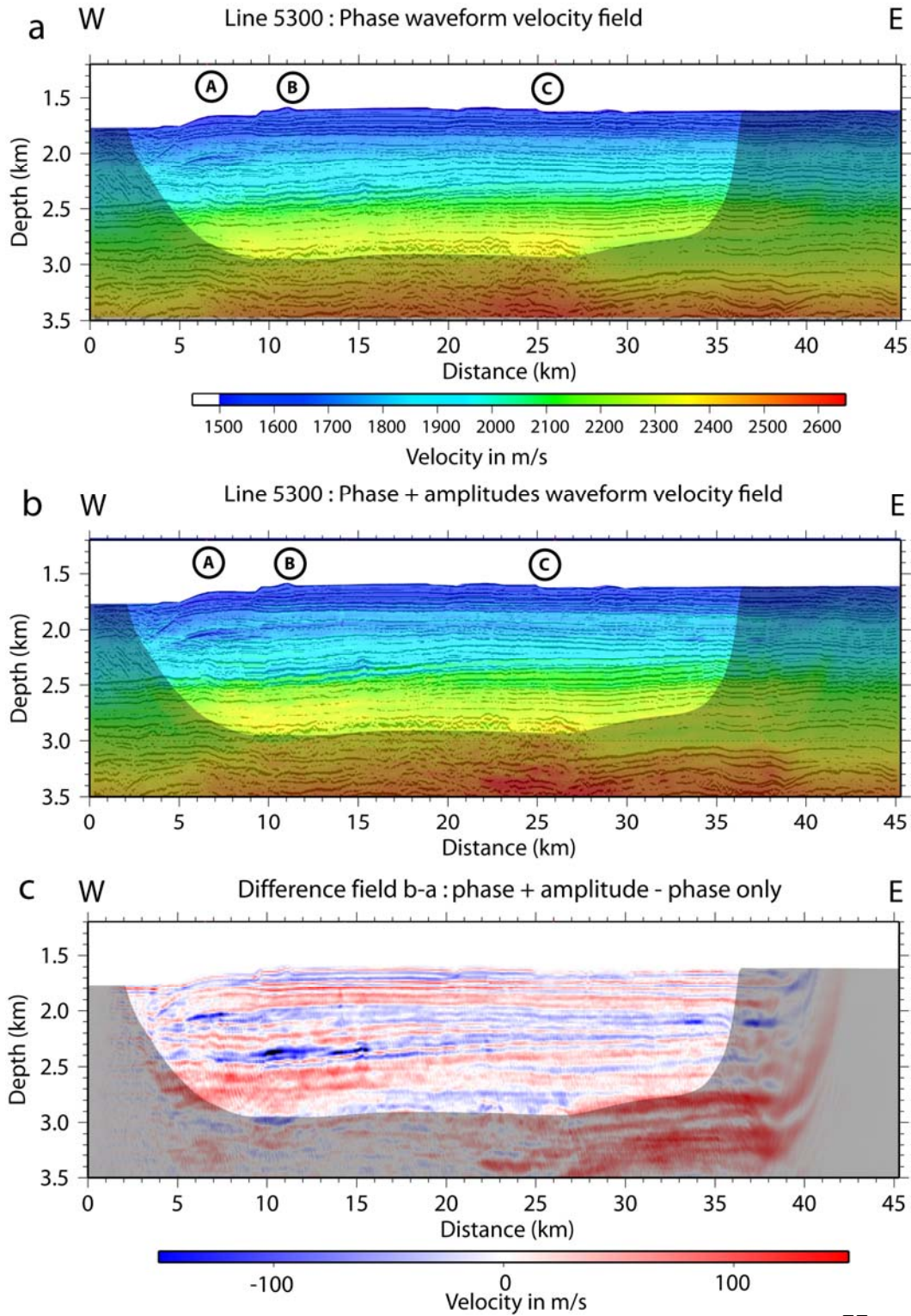


Figure 8



23

24 *Figure 9*

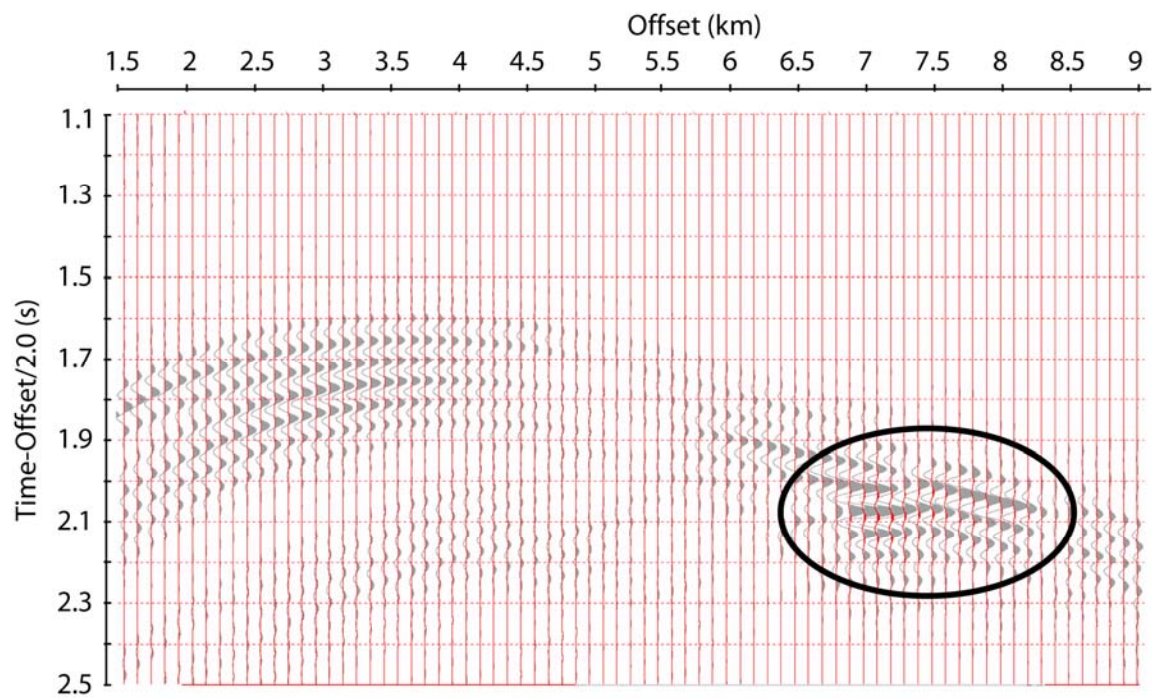


Figure 10

Proposal to ION GX Technology
Dr. Keith Loudon and Dr. Mladen Nedimović,
Dalhousie University

Proposal title: Joint analysis of the NovaSpan Line 2000 MCS and OETR Line OBS data using traveltimes and waveform tomography

Summary:

We seek to further develop our relationship with ION GX Technology, which started in 2006, by proposing to jointly analyze NovaSpan MCS Line 2000 and OETR OBS line data using traveltimes and full waveform tomography. For this, we request that ION GX Technology provide us with the NovaSpan Line 2000 navigation and raw shot gathers in SEG-Y format. We have the necessary funding needed for data analysis through our other research grants. If possible, we would also appreciate receiving the new prestack depth migrated images of the NovaSpan 2003 lines.

Completed work:

Detailed velocity models of the earth subsurface can be obtained through waveform tomography. The accuracy of the long-wavelength component of such velocity models, which is the background velocity field, is particularly sensitive to modeling low-frequency refracted waves that have long paths through target structures. Thus field examples primarily have focused on the analysis of long-offset wide-angle datasets collected using autonomous receivers, in which refractions arrive at significantly earlier times than reflections. Modern marine acquisition with long streamers now offers the ability to record, both in shallow and deep water, such far offset refracted waves with high spatial density and uniform source. During the past two years, we focused our exploratory waveform tomography work on two small crossing sections of Nova Span lines 5300 and 1400. These 2D MCS data were acquired with a 9-km-long streamer over the Scotian Slope in water depths of ~1600 m. The refracted arrivals, although mostly restricted to far offset receivers, provide sufficient information to successfully invert for a high-resolution background velocity field. Using a frequency domain acoustic code over frequencies from 8-24 Hz on the two crossing profiles (45 and 30 km long), we detail how the limited refracted waves can constrain the velocity field above the depth of the turning waves (~1.5 km below seafloor). Several important features are resolved by the waveform velocity model that are not present in the initial travel-time model. In particular, at shallow depth a high velocity layer due to gas hydrates is imaged even where a characteristic BSR is not visible. At greater depth, a strong velocity increase of 300 km/s exists beneath a gently dipping reflector along which low-velocity zones, possibly related to gas, are present. Velocity models are highly consistent at the crossing point between the two profiles. After review by ION GXT, we submitted a manuscript on this work to *Geophysics*.

Proposed work:

A dense wide-angle refraction profile using 100 ocean bottom seismometers (OBS) was collected in Fall 2009 for OETR Association at a location coincident with the ION GXT Line 2000. We have the collected data in our lab. These data, combined with the ION GXT Line 2000 data, open up new opportunities with respect to the quality and resolution of the velocity profiles that can be produced. The large number of OBSs on the OETR line have densely sampled the deep structures providing excellent velocity constraints on the deep sediments, crystalline crust and uppermost mantle, but do not constrain well the velocities of the uppermost sediments. In order to produce a highly detailed and accurate velocity image at all depths, velocities in the uppermost few km of sediments must first be constrained by applying waveform tomography to the ION GXT Line 2000 data. This result can then be combined with the traveltimes tomography model formed using the wide angle data to form the starting velocity model for the full waveform tomography of the dense OBS data. We believe that through this process we can form the first highly detailed velocity images of a passive margin setting, where the detailed velocity profile would extend to approximately the same depth as does the prestack depth reflection image. We expect the newly formed detailed velocity images to provide significant new insight into the rifting processes at the north-central Scotian margin.

Costs:

We would be pleased to cover all the costs incurred by ION GXT in preparing and sending us the requested data. Please let us know if there is any additional information we can provide.